



The
University
Of
Sheffield.

Department
Of
Mechanical
Engineering

Investigating Fundamental Processes in Erosive Wear of Titanium Alloys by Water Droplets

Alan Terry **MARTIN** MEng

August 2020

Supervisors: Adrian Leyland, Rob Dwyer-Joyce

Thesis submitted to The University of Sheffield for the degree of
Doctor of Philosophy

SUMMARY

Water droplet erosion (WDE) occurs when water droplets impact a surface at high speed, causing erosive wear, in areas such as aerospace engine fan blades, steam turbine blades and wind turbine blades. WDE resistant materials have previously been identified and used to prolong component life, such as cobalt overlays on steam turbine blades, but these can fail dramatically. A fundamental understanding of the wear mechanism is required to effectively design a surface which can resist WDE for longer.

This project sought to better understand the fundamental mechanisms of water droplet erosion through the use of a literature review and experiments.

Two titanium alloys were used in this investigation; Ti-15Mo and Ti-6Al-4V. Ti-15Mo was developed for biomedical applications such as dental implants, while Ti-6Al-4V is the most commonly used titanium alloy, appearing in areas such as aero-engine fan blades and offshore components. Since the Ti-15Mo had a grain size around twenty times larger than the Ti-6Al-4V, some Ti-6Al-4V was annealed to a larger grain size, to provide a means of comparison between the two differing alloys.

Several models are suggested in the literature to describe the physical phenomena of WDE, such as direct deformation, stress wave propagation, hydraulic penetration, and lateral outflow jetting. WDE is likely produced as a synergy of these effects, however the relative importance of each is still poorly understood. Direct deformation and stress wave propagation cause initial roughening and (near) surface cracking. Hydraulic penetration and lateral outflow jetting are secondary in widening cracks or interacting with uneven surface material. Ultimately, large spalls of material are removed due to cyclic fatigue and cumulative damage caused by repeated droplet impact.

In this work, WDE experiments conducted on a whirling arm-type test machine showed good agreement with the literature. Advanced erosion was characterised by deep craters and quantified by mass loss-time plots. Initial erosion showed characteristic features similar to those already noted by other authors in the published literature; micropits, slip bands, depressions. EBSD was used to aid damage tracking; it's use for the evaluation of WDE damage has previously not been reported in the literature.

Several characteristic WDE material deformation phenomena noted by other researchers are fatigue related, including slip bands, striations, and twinning. Despite noting such features, few researchers conduct comparative studies between WDE and fatigue. Low cycle fatigue tests were planned, and tensile tests

were carried out to help plan the fatigue tests. Some material mechanical properties - such as resilience - have been reported in the literature to correlate to improved WDE performance (again, few have researched this area), therefore tensile testing was also useful in recording other characteristic material properties.

WDE tends to occur at high strain rate, though there are limited WDE studies which seek to also investigate the materials in dedicated high strain rate tests. Split Hopkinson pressure bar (SHPB) testing was conducted to obtain material properties at high strain rates. The results showed the Ti-alloys could withstand much higher stresses than under conventional quasi-static loading. Deformation occurred by a combination of slip and twinning, as characterised by SEM and EBSD analysis.

It is likely that cavitation within an impinging droplet contributes to the erosion of surfaces. Some authors in the literature have found that the initial stages of cavitation erosion and the early damage seen in WDE are similar. Cavitation erosion tests were therefore also performed in this work, producing grain tilting and micropitting features similar to those seen in the early stages of WDE by other authors.

By considering how the WDE test materials behaved in other experiments with known conditions, notably high strain rate tests, certain deformations could be compared. The findings of this thesis will be of use for researchers and manufacturers when considering materials to withstand erosion.

Recommendations arising from the work performed in this thesis are to investigate the early stages of erosion with further analysis techniques, including low voltage SEM, FIB sectioning, XRD, TEM, and XCT, and to fully investigate low cycle fatigue. This would give further insights into how materials behave in the early stages of WDE. Cavitation erosion could be used as a simple test for ranking candidate substrate and/or coating materials, before committing to full-scale WDE tests.

CONTENTS

Summary	ii
Contents	iv
List of figures	vii
List of tables	xv
Acknowledgements	xvi
1 Introduction	1
1.1 The problem	1
1.2 Aims and objectives	2
1.3 Novelty and impact of work	2
1.4 Structure of thesis	3
2 Titanium alloys	7
2.1 Background	7
2.2 Alloys used in this study	8
2.2.1 Annealing of Ti-6Al-4V	10
2.3 Characterisation of the alloys by EBSD	14
2.3.1 A note on sample orientations cut from the material stock	14
2.3.2 Background	16
2.3.3 EBSD of as-received Ti-15Mo	17
2.3.4 EBSD of as-received Ti-6Al-4V	20
2.3.5 EBSD of annealed Ti-6Al-4V	24
2.4 Discussion	25
3 Water droplet erosion	27
3.1 Literature review	27
3.1.1 Proposed mechanisms of water droplet erosion	27
3.1.2 Relating water droplet erosion to material properties	36
3.1.3 Test rigs	38
3.1.4 Initiation of water droplet erosion	41
3.2 Experimental methods	47
3.2.1 Characterisation of droplet size	50
3.3 Analysis	53
3.4 Results	53
3.4.1 Advanced erosion – 36 hours Ti-15Mo & Ti-6Al-4V	53
3.4.2 Incubation period	68
3.4.3 10 seconds as-received Ti-6Al-4V	69
3.4.4 5 minutes as-received Ti-15Mo	78
3.4.5 5 minutes annealed Ti-6Al-4V	85

3.4.6	10 minutes annealed Ti-6Al-4V	90
3.5	Discussion.....	97
4	Quasi-static material tests.....	100
4.1	Background.....	100
4.2	Experimental methods	100
4.3	Analysis	102
4.4	Results	103
4.5	Discussion.....	104
5	High strain rate mechanics.....	105
5.1	Background.....	105
5.2	Literature review	106
5.2.1	High strain rate tensile testing	106
5.2.2	Split Hopkinson pressure bar	107
5.2.3	Other high-strain rate tests.....	107
5.3	Experimental methods	108
5.4	Analysis	112
5.5	Results	113
5.5.1	Test 5 – annealed Ti-6Al-4V at ‘high’ strain rate.....	119
5.5.2	Test 6 – Ti-15Mo at ‘high’ strain rate	130
5.5.3	Test 2 – Ti-15Mo at ‘high’ strain rate.....	136
5.5.4	Test 10 – Ti-15Mo at ‘low’ strain rate	137
5.5.5	Test 12 – Ti-15Mo at ‘medium’ strain rate	138
5.6	Discussion.....	139
6	Cavitation erosion.....	141
6.1	Literature review	141
6.2	Experimental methods	141
6.2.1	Submerged impingement jet	141
6.2.2	Sonotrode	142
6.3	Results	143
6.3.1	Submerged impingement jet	143
6.3.2	Sonotrode.....	145
6.4	Discussion.....	151
7	Strain rates in this investigation	152
7.1	Summary table	152
7.2	Supporting calculations.....	153
8	Conclusions.....	154
8.1	Water droplet erosion	154
8.2	Quasi-static material tests	155

8.2.1 Tensile test	155
8.3 High strain rate tests	155
8.4 Cavitation erosion	155
8.5 Further work	156
References.....	157

LIST OF FIGURES

Figure 1.1 – Flowchart of planned work.	4
Figure 2.1 – Slip planes in alpha phase titanium [36].	7
Figure 2.2 – Twins in alpha phase brass [38].	8
Figure 2.3 – As-received Ti-15Mo under low magnification light microscopy, with 500 μm scale bar.	9
Figure 2.4 – As-received microstructure of Ti-6Al-4V at under high magnification light microscopy.	10
Figure 2.5 – Ti-6Al-4V annealed at 900 $^{\circ}\text{C}$ for 4 hours then furnace cooled. High magnification light microscope with 20 μm scale bar. N.B. the white flecks are artefacts; colloidal silica polishing compound which has not fully cleaned off.	11
Figure 2.6 – Ti-6Al-4V annealed at 1100 $^{\circ}\text{C}$ for 2 mins, then held at 960 $^{\circ}\text{C}$ for 1 hour then furnace cooled. High magnification light microscopy with 500 μm scale bar. .	12
Figure 2.7 – Ti-6Al-4V annealed at 1050 $^{\circ}\text{C}$ for 5 mins, then held at 960 $^{\circ}\text{C}$ for 1 hour, then furnace cooled. Low magnification light microscopy with 300 μm scale bar. ...	13
Figure 2.8 – Ti-6Al-4V annealed at 1050 $^{\circ}\text{C}$ for 5 mins, then held at 960 $^{\circ}\text{C}$ for 1 hour, then furnace cooled. Low magnification light microscopy with 500 μm scale bar. ...	14
Figure 2.9 – Coupon orientations relative to bar processing direction.	15
Figure 2.10 – Coupon orientations and grain orientations relative to bar processing direction.	15
Figure 2.11 – IPF and IQ maps for Ti-15Mo (ND).	17
Figure 2.12 – IPF and Misorientation map for Ti-15Mo ND.	18
Figure 2.13 – IPF of Ti-15Mo ND. Scanned with a 2x2 binning rate and a step size of 20 μm . Grains of size less than 2 pixels removed.	19
Figure 2.14 – IPF and IQ maps for as-received Ti-6Al-4V (ND).	20
Figure 2.15 – IPF and Misorientation maps for as-received Ti-6Al-4V (ND).	21
Figure 2.16 – IPF of as-received Ti-6Al-4V (ND). Scanned with a 4x4 binning rate and a step size of 1 μm . Grains of size less than 2 pixels removed. Data cleaned up by Kuwahara filter applied to first neighbour for one iteration.	22
Figure 2.17 – SEM images of the as-received Ti-6Al-4V (RD) microstructure, showing the duplex globular and lamellar α phase embedded in a β phase matrix.	23
Figure 2.18 – IPF and IQ maps for annealed Ti-6Al-4V (ND).	24
Figure 2.19 – IPF and IQ maps for annealed Ti-6Al-4V (ND).	25
Figure 3.1 – Erosion on the leading edge of wind turbine blades [18].	27
Figure 3.2 Stress of a 570 $\text{m}\cdot\text{s}^{-1}$ water jet “slug” impinging on a PVDF pressure gauge [29].	28

Figure 3.3 – Hardness of TiAl and Ti64 at the surface exposed to WDE at 350 m·s ⁻¹ with 464 μm droplets [47].	28
Figure 3.4 - Wave generation from liquid droplet impact [2].	29
Figure 3.5 – A 10 mm droplet impacted by a metal slider at 110 m·s ⁻¹ . Interframe time 1 μs [16].	30
Figure 3.6 - Computational simulation of a 100 μm water droplet impact at 500 m·s ⁻¹ with increasing time, t [13].	31
Figure 3.7 – Possible mechanism of cavitation in a collapsing droplet [52].	32
Figure 3.8 – A 5 mm droplet impacted at 60 m·s ⁻¹ [53].	32
Figure 3.9 – Hydraulic penetration.	33
Figure 3.10 - A 2 mm diameter water droplet impacting a surface at 70 m·s ⁻¹ producing lateral outflow jets [53].	33
Figure 3.11 - Springer's schematic of a lateral outflow jet interacting with surface roughness [54].	34
Figure 3.12 - FEM of a 2 mm diameter water droplet impact at 305 m·s ⁻¹ , 1 μs after impact [31].	34
Figure 3.13 – 100 μm diameter water droplet impacting at 500 m·s ⁻¹ . Left: enlarged detail of the lateral jets produced when the shockwave overtakes the contact patch area. Right: the entire model, illustrating the region of interest [13].	35
Figure 3.14 – (Left) Polak's model of extruded slip bands [56] and (right) how Mahdipoor et al. think lateral jets could interact with such a feature [55].	36
Figure 3.15 – The rotating sample set-up which Cook utilised [33].	38
Figure 3.16 – The rocket sled used at Holloman air base [63].	39
Figure 3.17 – Schematic of the pulsed jet erosion rig at EADS [14].	40
Figure 3.18 – Mass loss with “impingement number” (number of revolutions) for a whirling arm water droplet erosion test of Ti-6Al-4V at 350 m·s ⁻¹ impact velocity [57].	41
Figure 3.19 – Raised features on a Ti-6Al-4V surface after 1,000 revolutions through a water droplet stream and a subsurface crack found when FIB sectioning one [57].	42
Figure 3.20 – Grain tilting of the polished Ti-6Al-4V surface after 20,000 revolutions [57].	42
Figure 3.21 - Cracks begin to grow in between grains after 20,000 revolutions [57].	43
Figure 3.22 – As cracks propagate and join, small chunks of material begin to tear off leaving micro-voids [57].	43
Figure 3.23 - Deep craters are formed as hydraulic penetration forces material to detach from the bulk [57].	44

Figure 3.24 – (Left) the edge of an eroded crater in Ti-6Al-4V [75]. (Right) slip bands at the edge of an erosion crater during advanced erosion of untreated Ti-6Al-4V [48]	44
Figure 3.25 - (Left) three advanced erosion tracks caused by the three nozzles Kamkar used and (right) a cross section of an advanced erosion track highlighting sub-tunnels with arrows [57].	45
Figure 3.26 – A crack leading down at 45° from the eroded surface following the directionality of primary alpha lamellar colonies in TiAl [47].	45
Figure 3.27 – (Left) γ -TiAl after a single pass of a 730 MPa jet [76]. (Right) Ti-6Al-4V after three passes of a 940 MPa jet [9].	46
Figure 3.28 – Microcracks and micro-voids forming following initial damage in deep-rolled Ti-6Al-4V [48].	46
Figure 3.29 – Plan-view schematic of the rotating arm test rig at NPL.	47
Figure 3.30 - Water Droplet Erosion test coupon dimensions (in mm).	48
Figure 3.31 – Two sequential photos of droplets travelling from right to left. Field of view is 6.056mm in width. Taken 100 microseconds apart.	50
Figure 3.32 – Original brass nozzle with some corrosion product or other debris inside the bore (300 μ m scale bar).	51
Figure 3.33 – 0.15 mm stainless steel syringe nozzle (200 μ m scale bar).	52
Figure 3.34 – 0.16 mm “diaphragm” nozzle (200 μ m scale bar).	52
Figure 3.35 – Mass loss with WDE exposure time for the two as-received alloys, Ti-15Mo & Ti-6Al-4V.	54
Figure 3.36 Photograph of as-received Ti-6Al-4V after 36 hours of exposure to WDE, with millimetre graduated ruler.	54
Figure 3.37 – Alicona image of as-received Ti-6Al-4V after 36 hours of exposure to WDE. The image is across the entire 8 mm coupon width.	55
Figure 3.38 – SEM image of as-received Ti-6Al-4V after 36 hours of exposure to WDE. An area is circled where higher magnification analysis was investigated further....	56
Figure 3.39 – SEM image of as-received Ti-6Al-4V after 36 hours of exposure to WDE.	57
Figure 3.40 – Alicona image of as-received Ti-15Mo after 36 hours of exposure to WDE. The image is across the entire 8mm coupon width.	58
Figure 3.41 – SEM image of as-received Ti-15Mo after 36 hours of exposure to WDE. An area is marked where higher magnification was conducted.	59
Figure 3.42 – SEM image of as-received Ti-15Mo after 36 hours of exposure to WDE.	60
Figure 3.43 – Photograph of 36-hour WDE Ti-15Mo sample mounted and polished, with millimetre graduated ruler.	61

Figure 3.44 – SEM image showing EBSD scan regions of 36-hour WDE Ti-15Mo sample.....	61
Figure 3.45 – IQ and IPF for 36-hour WDE Ti-15Mo sample, scanned with a 4x4 binning rate and a step size of 1.5 μm . Grains of less than 2 pixels removed.....	62
Figure 3.46 – IPF and Misorientation map for 36-hour WDE Ti-15Mo sample, scanned with a 2x2 binning rate and a step size of 0.5 μm	63
Figure 3.47 – IPF and IQ map for 36-hour WDE Ti-15Mo sample, scanned with a 4x4 binning rate and a step size of 1 μm	64
Figure 3.48 – IPF and Misorientation map for 36-hour WDE Ti-15Mo sample, scanned with a 2x2 binning rate and a step size of 1 μm	65
Figure 3.49 – IPF and Misorientation map for 36-hour WDE Ti-15Mo sample, scanned with a 4x4 binning rate and a step size of 0.2 μm	67
Figure 3.50 – Erosion wear scar in as-received Ti-6Al-4V RD following 10 s exposure to WDE.	69
Figure 3.51 – SEM image of deformation features in erosion wear scar in as-received Ti-6Al-4V RD following 10 s exposure to WDE.	70
Figure 3.52 – SEM and EBSD of “EBSD 1” highlighted in Figure 3.51. 10 s WDE in as-received Ti-6Al-4V RD.....	71
Figure 3.53 – EBSD misorientation maps of the “EBSD 1” region highlighted in Figure 3.51. 10 s WDE in as-received Ti-6Al-4V RD. Scanned with a 2x2 binning rate and a step size of 0.025 μm	72
Figure 3.54 – SEM and EBSD of the “EBSD 2” region of Figure 3.51. 10 s WDE in as-received Ti-6Al-4V RD.....	73
Figure 3.55 – IPF and misorientation maps of the “EBSD 2” region in Figure 3.51. 10 s WDE in as-received Ti-6Al-4V RD. Scanned with a 4x4 binning rate and a step size of 0.2 μm	74
Figure 3.56 – IQ and Phase maps of the “EBSD 3” region of Figure 3.52. 10 s WDE in as-received Ti-6Al-4V RD. Scanned with a 4x4 binning rate and a step size of 0.025 μm	75
Figure 3.57 – IPF and misorientation maps of the “EBSD 3” region of Figure 3.55. 10 s WDE in as-received Ti-6Al-4V RD. Scanned with a 4x4 binning rate and a step size of 0.025 μm	76
Figure 3.58 – SEM of a micropit.....	77
Figure 3.59 – IQ and IPF maps of a micropit. Scanned with a 2x2 binning rate and a step size of 0.2 μm . 10 s WDE in as-received Ti-6Al-4V RD.	77
Figure 3.60 – IQ and phase maps of a micropit. 10 s WDE in as-received Ti-6Al-4V RD. Scanned with a 2x2 binning rate and a step size of 0.2 μm	78
Figure 3.61 – Left: Ti-15Mo TD before WDE. Right: 5 minutes WDE.....	79

Figure 3.62 – Mid-section of coupon, edge furthest from nozzle. Ti-15Mo TD before WDE testing.....	80
Figure 3.63 – Mid-section of coupon, edge furthest from nozzle. Ti-15Mo TD after 5 minutes WDE.	81
Figure 3.64 – SEM & EBSD images of erosion scar at edge furthest from nozzle. Ti-15Mo TD after 5 minutes WDE.....	82
Figure 3.65 – Ti-15Mo TD after 5 minutes WDE. EBSD results with 2x2 binning rate, step size 0.5 μm . Top: IPF. Bottom: Misorientation map of the scan using Kernel Average 1st neighbour. Overlaid on IQ map.	83
Figure 3.66 – Ti-15Mo TD after 5 minutes WDE. SEM & EBSD at a higher magnification of an area of slip bands.	84
Figure 3.67 –Left: annealed Ti-6Al-4V RD before testing. Right: after 5 minutes WDE.	85
Figure 3.68 – Mid-section of coupon, 3 mm from edge nearest to nozzle. Annealed Ti-6Al-4V RD before WDE testing.	86
Figure 3.69 – Mid-section of coupon, 3 mm from edge nearest to nozzle. Annealed Ti-6Al-4V RD after 5 minutes WDE testing. Light microscope at low magnification. Scale bar is 1000 μm	87
Figure 3.70 – SEM & IPF images of mid-section of coupon, 3 mm from edge nearest to nozzle. Annealed Ti-6Al-4V RD after 5 minutes WDE testing.	88
Figure 3.71 – IPF and Misorientation map for 5 minute WDE Annealed Ti-6Al-4V RD sample, scanned with a 2x2 binning rate and a step size of 0.1 μm	89
Figure 3.72 – Mid-section of coupon, edge nearest to nozzle. Annealed Ti-6Al-4V RD before WDE testing.	90
Figure 3.73 – Mid-section of coupon, edge nearest to nozzle. Annealed Ti-6Al-4V RD 10 minutes after WDE testing.	91
Figure 3.74 – Erosion features at “SEM 1” region of Figure 3.73. Annealed Ti-6Al-4V RD 10 minutes after WDE testing.....	92
Figure 3.75 – IPF and IQ maps scanned with a 2x2 binning rate and a step size of 0.5 μm . EBSD of the higher magnification region of Figure 3.71. Annealed Ti-6Al-4V RD 10 minutes after WDE testing.....	93
Figure 3.76 – SEM & EBSD images from “EBSD 2” region of Figure 3.73. Approximately 2.5 mm from the edge of the coupon. Annealed Ti-6Al-4V RD 10 minutes after WDE testing.....	94
Figure 3.77 – Increased magnification SEM & EBSD images of erosion features. Approximately 2.5 mm from the edge of the coupon. Annealed Ti-6Al-4V RD 10 minutes after WDE testing.....	95
Figure 3.78 – Higher magnification images of the “SEM 2” area highlighted in Figure 3.77. Annealed Ti-6Al-4V RD 10 minutes after WDE testing.....	96
Figure 3.79 – Mass loss curves for various materials [77]......	97

Figure 4.1 – Dimensions of the tensile test and low cycle fatigue test specimens (in mm).....	101
Figure 4.2 – Stress versus strain for the tensile test of annealed Ti-6Al-4V.....	103
Figure 5.1 – Varying strain rate regimes, typical tests, and typical examples [83]–[85].	105
Figure 5.2 – Lost motion device or “slack adapter” used to attain higher strain rates [88].....	106
Figure 5.3 – Compressive Split Hopkinson Bar set-up [84].....	107
Figure 5.4 – A specimen mounted on a thick flyer plate, fired at an inclination to impact a parallel anvil [84].	108
Figure 5.5 – Compressive Split Hopkinson Bar set-up.	109
Figure 5.6 – Tensile SHPB set-up.....	109
Figure 5.7 – The ‘long’ and ‘short’ SHB compressive test coupons.....	111
Figure 5.8 – SHB tensile test coupon dimensions.	111
Figure 5.9 – Strain measurements from the strain gauges on the Hopkinson bars.	112
Figure 5.10 – Ti-15Mo samples tested at various strain rates.....	113
Figure 5.11 – Strain rate with time for the Ti-15Mo samples.....	114
Figure 5.12 – Annealed Ti-6Al-4V samples tested at various strain rates.....	115
Figure 5.13 – Strain rate with time for the annealed Ti-6Al-4V samples.	116
Figure 5.14 – Annealed Ti-6Al-4V and Ti-15Mo tested in tensile Split Hopkinson Pressure Bar. The result of the quasi-static tensile test is also included for comparison.	117
Figure 5.15 – Strain rate with time for the Ti-15Mo and annealed Ti-6Al-4V tensile SHPB tests.	118
Figure 5.16 – Photographs of test number 5. Annealed Ti-6Al-4V tested at a peak strain rate of 7700 s ⁻¹ . Peak strain 22 %. Peak stress 1750 MPa.	119
Figure 5.17 – Confocal microscopy of test number 5. Annealed Ti-6Al-4V tested at a peak strain rate of 7700 s ⁻¹ . Peak strain 22 %. Peak stress 1750 MPa.....	120
Figure 5.18 – SEM images of test number 5. Annealed Ti-6Al-4V tested at a peak strain rate of 7700 s ⁻¹	121
Figure 5.19 – Increased magnification images of “SEM 3” region in Figure 5.18. Annealed Ti-6Al-4V tested at a peak strain rate of 7700 s ⁻¹	122
Figure 5.20 – Sectioning test number 5. Annealed Ti-6Al-4V tested at a peak strain rate of 7700 s ⁻¹	123
Figure 5.21 – EBSD near surface of “front” face of test number 5. Annealed Ti-6Al-4V tested at a peak strain rate of 7700 s ⁻¹	124

Figure 5.22 – IPF and IQ maps of “front” face of test number 5. Annealed Ti-6Al-4V tested at a peak strain rate of 7700 s ⁻¹ . Scanned with a 2x2 binning rate and a step size of 0.5 μm. Grains of less than 2 pixels size removed from the IPF.	125
Figure 5.23 – EBSD of a location within the sample, ~1 mm from the loading face, of test number 5. Annealed Ti-6Al-4V tested at a peak strain rate of 7700 s ⁻¹	126
Figure 5.24 – EBSD of a location deeper in the sample, away from the loading faces, of test number 5. Annealed Ti-6Al-4V tested at a peak strain rate of 7700 s ⁻¹	127
Figure 5.25 – SEM and EBSD of another location in the sample, away from the loading faces, of test number 5. Annealed Ti-6Al-4V tested at a peak strain rate of 7700 s ⁻¹	128
Figure 5.26 – IPF and IQ maps of the region highlighted in Figure 5.25. Scanned with a 2x2 binning rate and a step size of 0.2 μm, Pixels of less than 0.1 confidence index removed from the IPF map.....	129
Figure 5.27 – Photographs of test number 6. As-received Ti-15Mo tested at a peak strain rate of 7800 s ⁻¹ . Peak strain 27 %. Peak stress 1800 MPa.	130
Figure 5.28 – Alicona image of side 1 of test number 6. As-received Ti-15Mo tested a peak strain rate of 7800 s ⁻¹ . Peak strain 27 %. Peak stress 1800 MPa.....	131
Figure 5.29 – Photographs & SEM images of test number 6 sectioned. As-received Ti-15Mo tested at a peak strain rate of 7800 s ⁻¹	132
Figure 5.30 – IPF maps “stitched” together, taken in the regions highlighted in Figure 5.29. Scanned with 2x2 binning rate, step size 8 μm. Pixels of less than 0.1 confidence index removed. Test number 6 - as-received Ti-15Mo tested at a peak strain rate of 7800 s ⁻¹	133
Figure 5.31 – IPF scanned with a 2x2 binning rate, step size 0.7 μm. Pixels of less than 0.1 confidence index removed. Test number 6 - as-received Ti-15Mo tested at a peak strain rate of 7800 s ⁻¹	134
Figure 5.32 – IQ and Misorientation map. Scanned with 2x2 binning rate, step size 0.7 μm. Test number 6 - as-received Ti-15Mo tested at a peak strain rate of 7800 s ⁻¹ .	135
Figure 5.33 – Alicona results of the “front” of sample 2. As-received Ti-15Mo tested at a peak strain rate of 6000 s ⁻¹ . Peak strain 21 %. Peak stress 1800 MPa.....	136
Figure 5.34 – Photographs of test number 10. As-received Ti-15Mo tested at a peak strain rate of 2000 s ⁻¹ . Peak strain 2.5 %. Peak stress 1000 MPa.	137
Figure 5.35 – Photographs of test number 12. As-received Ti-15Mo tested at a peak strain rate of 2400 s ⁻¹ . Peak strain 3 %. Peak stress 1200 MPa.	138
Figure 5.36 – Profile path from left to right of the sample. The red cross is where the profile measurement begins, corresponding to the left of the diagram.	139
Figure 6.1 – Schematic of the submerged impingement jet (SIJ) rig.	142
Figure 6.2 – Light microscope images stitched together of a stainless steel sample after 30 min in SIJ rig.....	143

Figure 6.3 – Annealed Ti-6Al-4V after 10 minutes in SIJ rig. Wear scar is approximately 4 mm in diameter.....	144
Figure 6.4 – Annealed Ti-6Al-4V before and after 10s in SIJ rig.....	145
Figure 6.5 – Annealed TI-6Al-4V after 1 hour in sonotrode rig.....	146
Figure 6.6 – Alicona image of annealed Ti-6Al-4V sample after 1 hour in cavitating sonotrode rig.....	147
Figure 6.7 – Alicona image of annealed Ti-6Al-4V sample after 2 hours in cavitating sonotrode rig. 2mm scale bar.....	148
Figure 6.8 – SEM image of annealed Ti-6Al-4V sample after 2 hours in cavitating sonotrode rig.....	149
Figure 6.9 – SEM image of annealed Ti-6Al-4V sample after 2 hours in cavitating sonotrode rig.....	149
Figure 6.10 – SEM image of annealed Ti-6Al-4V sample. 2 hours in cavitating sonotrode rig.....	150
Figure 6.11 – SEM image of annealed Ti-6Al-4V sample. 2 hours in cavitating sonotrode rig.....	150
Figure 7.1 – Schematic for the calculation of the strain rate of a droplet impacting a coupon.....	153

LIST OF TABLES

Table 3.1 – Water droplet erosion test plan.....	49
Table 4.1 – Experimentally derived material properties of annealed Ti-6Al-4V, and properties of the as-received Ti-15Mo and Ti-6Al-4V from technical data sheets [79], [80].	103
Table 5.1 – SHB test plan for the strain rates possible.	110
Table 7.1 – Maximum strain rates, stresses and microstructural features observed for the experiments in this investigation.....	152

ACKNOWLEDGEMENTS

Thanks are given to my academic supervisors Adrian Leyland and Rob Dwyer-Joyce, and also to my industrial supervisor; Mark Gee of National Physical Laboratory (NPL). NPL also provided resources throughout the project, and part sponsorship, alongside the EPSRC and The University of Sheffield. Several other academics have helped or offered input and are also thanked, including Martin Jackson, Brad Wynne and Andy Tyas. The split Hopkinson pressure bar experiments would not have been possible without the great help of Andrew Barr, whose MATLAB script and advice also pointed me in the right direction for the data analysis. Great thanks also go to Ken Mingard at NPL for EBSD training and guidance, and others who helped with microscopy, general sample preparation, and experimental procedures such as Linda Orkney, Eric Bennett, Helen Jones, and Mark Stewart. Thanks are also given to University of Leeds, for the use of (and training in) a submerged impingement jet rig. Finally, thanks also to my family and friends for supporting and encouraging me throughout my PhD, with a special mention to Tom and Liv for putting me up so many times while visiting NPL, and with particular thanks to my long-suffering wife!

1 INTRODUCTION

1.1 The problem

Erosive wear may occur by solid particle impingement, liquid impingement, slurry erosion or cavitation [1]. Water droplet erosion (WDE) presents a challenge for several advanced engineering applications. WDE occurs when water droplets impact on components moving at high surface speeds. On aerospace turbofan engines, the leading edges of the fan blades suffer WDE damage, due to rain droplets impacting the fan surface [2]. The fan tip can be moving as fast as $400 \text{ m}\cdot\text{s}^{-1}$ tangential velocity. WDE reduces aerodynamic efficiency and, in the worst case, initiates a larger structural failure. Similarly steam turbine blades are damaged by WDE [3], [4], [13]–[16], [5]–[12]. Water droplets condense on the trailing edges of stators in the low-pressure turbine. Droplets eventually fall on to the leading edges of the downstream turbine blades, which can reach $500 \text{ m}\cdot\text{s}^{-1}$ tip speeds. More recently, WDE of wind turbine blades has been identified as a life-limiting factor; given overall turbine life should be around 20 years, but severe WDE can degrade a blade within 5 years [2], [17]–[22]. Wind turbines are often sited in areas of high velocity wind. These sites often coincide with areas of high precipitation. Large diameter wind turbines could experience surface speeds greater than $80 \text{ m}\cdot\text{s}^{-1}$ at the tip.

WDE changes the blade geometry thus reducing efficiency, but WDE is often considered unavoidable given the operating environment. Therefore coatings are applied to prolong the component life, allowing for longer service intervals [2], [8], [28], [20]–[27]. Coating designs have been improved incrementally, but it is not clear why or how the coating architectures resist WDE. The coating will still fail eventually, but it is difficult to track damage or to understand where failure initiated. The fundamental mechanisms of WDE remain unclear.

The main body of research into WDE mechanisms has been undertaken over the past fifty or so years, with several theories in the literature addressing some (but not all) of the different types of damage mechanism that are said to exist [9], [11], [13], [29]–[33]. To design a surface capable of resisting WDE requires a fundamental understanding of the damage mechanisms and their prevalence, which is currently not clear from the available literature.

Two titanium alloys were investigated. Ti-15Mo, a β phase alloy originally developed for biomedical applications, and the two-phase $\alpha + \beta$ alloy, Ti-6Al-4V, which is used for several industrial applications, including in aerospace fan blades. The Ti-6Al-4V alloy was investigated in both its as-received, equiaxed duplex structure; and an annealed

state of larger α lamellae which, although not typical of industrial applications, allowed comparisons between the two chosen alloys to be made at a similar grain size.

1.2 Aims and objectives

The overall aim of the project was to investigate the fundamental mechanisms which occur at the initial stages of water droplet erosion. This was achieved using the following objectives:

- review the WDE mechanisms proposed in the literature
- research, prepare and characterise titanium alloys for experiments
- investigate the early stages of WDE experimentally, using a range of analysis methods such as optical microscopy, focus variation microscopy, secondary electron microscopy (SEM), and electron backscatter diffraction (EBSD)
- explore relations between certain material properties and WDE performance by using mechanical tensile tests to characterise materials
- research the similarities between WDE features and low cycle fatigue (LCF) deformations in a material
- investigate high strain rate loading in WDE by examining the high strain rate response of the test materials via split Hopkinson pressure bar (SHPB) experiments
- experimentally compare the early stages of WDE with other similar, but simpler, representative tests such as cavitation erosion.

1.3 Novelty and impact of work

The mechanisms which cause the advanced stages of erosion are well documented, but the early stages of erosion remain less clear, so investigating the initial stages was a focus of this work. Many researchers test materials to the advanced stages of erosion in a somewhat trial-and-error approach, to find one which has the longest incubation period. However material selection should be made based on the properties required to resist erosion mechanisms.

Although many studies on WDE exist, none appear to use EBSD as a method of characterising erosion. At time of writing, it appears this thesis is novel for using EBSD to analyse WDE.

Few studies appear to link deformation from WDE to deformation caused by material characterisation tests such as tensile, fatigue or high strain rate tests. In particular,

testing of materials at high strain rates alongside WDE tests does not appear in the literature. The results indicate that high strain rate deformation mechanisms are an important consideration in WDE material selection. Materials are likely to see loading above the elastic yield limit, so strain hardening offers a route to accommodate further strain.

By considering how the WDE test materials behaved in other experiments with known conditions, notably high strain rate tests, certain deformations could be compared. This indicated the mechanisms present in erosion (for instance, high strain rates, fatigue, stress waves). The findings of this thesis will be of use for researchers and manufacturers when considering materials to withstand erosion.

Representative WDE testing requires complex equipment. Early stage cavitation erosion demonstrated similar damage to initial WDE. A recommendation is to use this simpler benchtop equipment, representative of early stage WDE, to rank materials ahead of WDE testing, or even for the study of early stage erosion.

1.4 Structure of thesis

The thesis is divided into chapters for each research area, which are further subdivided into topics such as literature review, methodologies, analyses, discussion.

Figure 1.1 is a flowchart illustrating the plan of work, why certain methods were used and how different methods and analyses relate to each other.

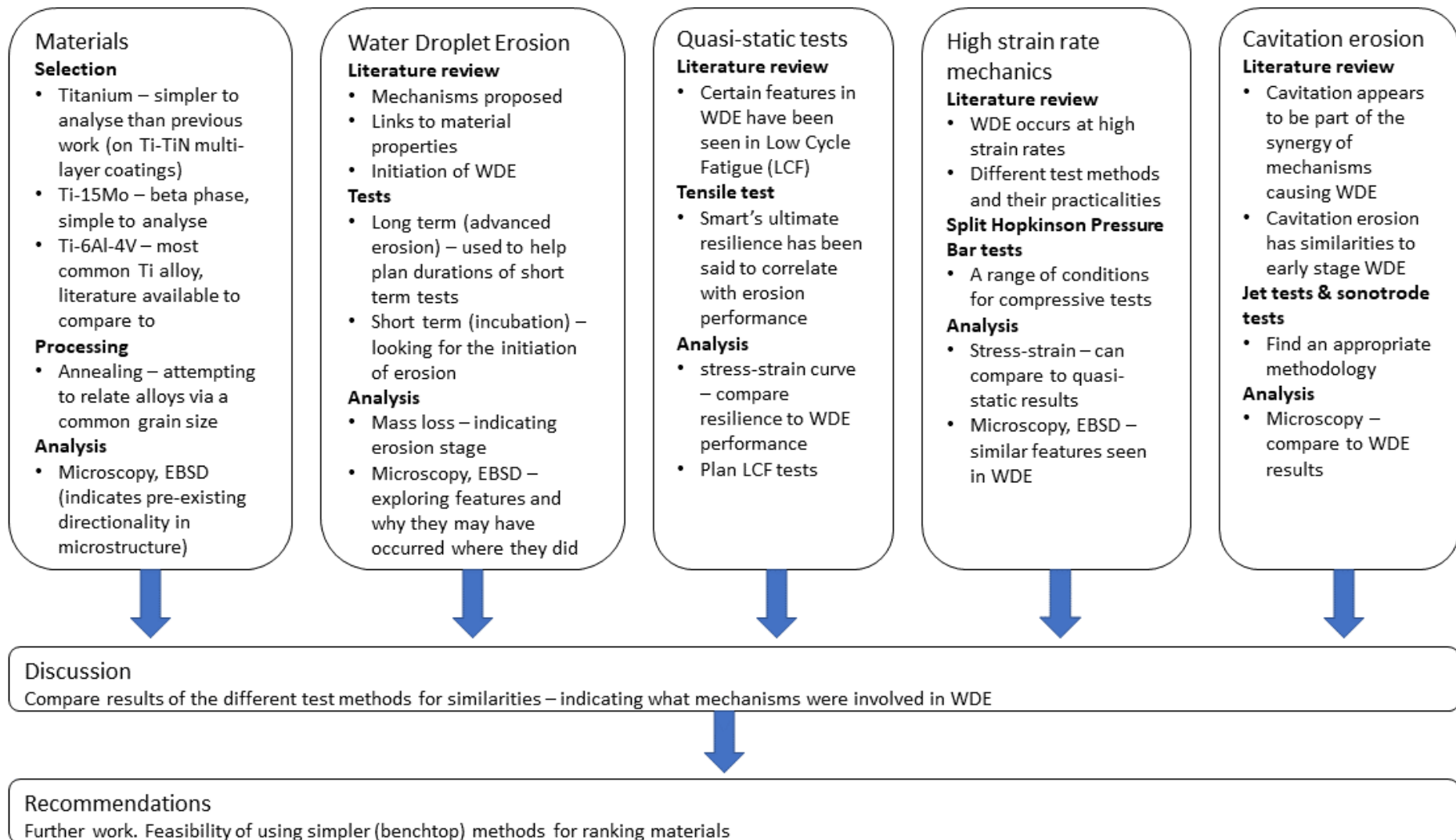


Figure 1.1 – Flowchart of planned work.

The Titanium alloys chapter looks at the selection, preparation, and characterisation of test materials. Having selected two titanium alloys, grain size was used as a basis of comparison, therefore one alloy was annealed to a larger grain size to be more similar to the other. Characterisation of the alloys was mainly done with EBSD, so the technique is explained in this chapter.

The Water droplet erosion chapter includes a literature review, which considers the main models of erosion, how material properties relate to water droplet erosion, and the early stages of erosion. This chapter also describes the experimental equipment, and how water droplet size was measured. Advanced erosion tests were weighed for mass-loss analysis, helping plan how long to run incubation phase tests. Incubation stage erosion tests were run for short time periods. Erosion samples were analysed by optical and SE microscopy, and often also EBSD. The discussion notes similarities between the results and literature. Material failure mechanisms are also discussed, with fatigue and high strain rate deformations notable. Relations between erosion mechanisms and material properties are also examined.

The Quasi-static material tests chapter examines the properties of the test materials, including a tensile test of one alloy. Relations between material properties and WDE are examined. Low cycle fatigue (LCF) is also discussed, because some authors cite certain WDE features as being similar in appearance to damage seen in LCF.

WDE strain rate is difficult to measure, but other strain rate specific test methods can more easily be configured for this purpose. The results can then be compared to give an indication of deformation mechanisms driven by high strain rates in WDE. The High strain rate mechanics chapter begins by researching techniques to produce high strain rate deformation. The test equipment is described, and a test matrix illustrates how the materials were tested under the varying high strain rates achievable. The strain gauge results needed to be processed to determine sample stresses and strains so this is explained in a short analysis section. Stress-strain results are presented as well as various microscopy results, illustrating deformation mechanisms such as slip and twinning. The discussion notes how both materials tested could accommodate high strain rates and load, and the limitations of the test method.

The Cavitation erosion chapter looks at the similarities between the early stages of WDE and cavitation erosion. Some comparison work has been done by other researchers, so this is reviewed. Two experimental methods were available and used so the two procedures are described. The submerged impingement jet (SIJ) test rig contained sand, residual from slurry erosion testing, so results were heavily contaminated by this. Sonotrode testing proved much more reliable and produced

initial cavitation erosion. Light and SE microscopy results reveal erosion features similar to WDE.

A further chapter, Strain rates in this investigation, attempts to relate the several experiments conducted in the thesis by strain rate. Additionally, maximum stresses experienced in the tests and microstructural deformation mechanism are listed as a further means of comparison.

Finally, the Conclusions chapter discusses why the results are significant. WDE features in the literature were reproduced experimentally. Some microstructural deformations (such as slip) were seen in other experiments (e.g. high strain rate tests). This indicated the processes present in erosion (for instance, high strain rate loading). Recommendations for future work were also made, among them were using cavitation erosion to produce representative early stage WDE, as an alternative to WDE test rigs.

2 TITANIUM ALLOYS

2.1 Background

Titanium alloys are of interest due to their strain rate sensitivity – at high strain rates the material can accommodate a higher stress to failure than at quasi-static strain rates. Titanium is also of importance due to ongoing work to develop Titanium/Titanium-Nitride (Ti/TiN) metallic/ceramic multilayered coatings, deposited by Physical Vapour Deposition (PVD) [34]. These coatings have complex failure mechanisms which are difficult to study. Titanium is also useful as it can exist in different phases which have differing properties, while the material similarity still allows for a useful comparison. Though this is also possible in say, steel; purely α or purely γ phase steels are more difficult to obtain.

Titanium alloys can have a complex microstructure depending on processing routes and alloy composition, but they can also have a relatively simple microstructure. The metal exists in two different phases, α and β , which may be controlled by various alloying additions.

Alpha phase titanium is a hexagonal close packed (hcp) crystal structure. The hcp structure has a c/a ratio of 1.587, whereas the ideal hcp structure has a c/a ratio of $\sqrt{3}$ [35]. This means a greater spacing between the prism planes, allowing prismatic slip, but otherwise limiting basal slip. Prismatic slip cannot happen instantaneously, hence the material is strain rate sensitive, meaning a sudden brittle failure of the material at high strain rates can occur. The prismatic slip plane ($\{10\text{-}10\}\langle 11\text{-}20\rangle$) is illustrated in Figure 2.1 below.

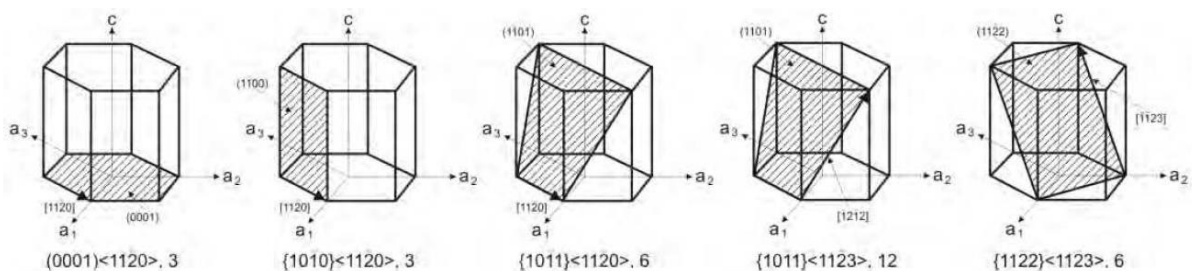


Figure 2.1 –Slip planes in alpha phase titanium [36].

Beta phase titanium has no such constraint and additionally can spontaneously twin to accommodate high-stress deformation. Twinning is often described as a military-like movement of atoms through a crystal plane [37]. The atoms mirror their previous positions so they are symmetric to the original crystal. Twinning does not require

dislocation movement along slip planes and is therefore less strain-rate sensitive. Example twins running across several grains are visible in Figure 2.2 below.

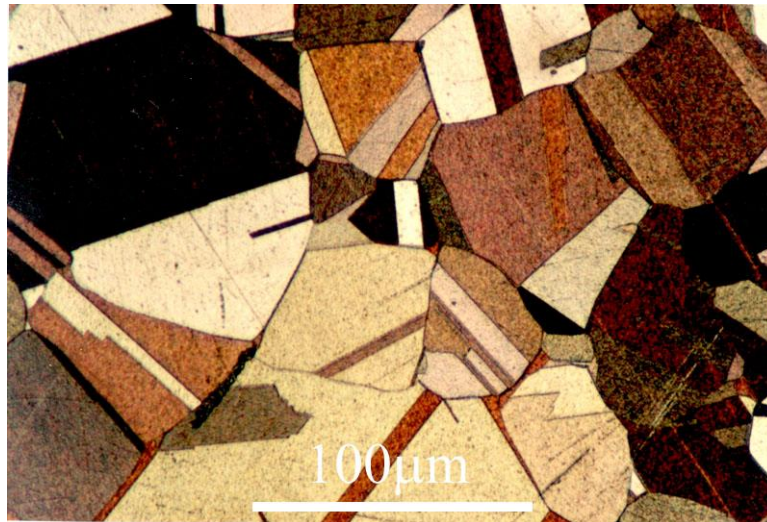


Figure 2.2 – Twins in alpha phase brass [38].

2.2 Alloys used in this study

Beta phase titanium is a bcc structure which is simple to study, relative to other material options such as the abovementioned multi-layered coatings currently used for aircraft engine titanium-alloy fan blade protection – and under investigation for steam turbine and other WDE applications [34]. Some β phase alloys with low elastic modulus and high ductility such as Ti-Nb-Ta-Zr (TNTZ, a.k.a. gum metal), Ti-Nb-Mo, Ti-V, and Ti-Nb were considered before a simple, metastable titanium molybdenum alloy (originally designed for use in biomedical implant applications) was chosen [39]–[43]. It was anticipated that Ti-Mo may be less susceptible to a brittle failure caused by the high-strain-rate impacting droplets. Of the titanium alloys, the beta-alloys have higher impact toughness and increased strain to failure (i.e. increased work of fracture) - and also superior corrosion resistance.

Ti-15Mo provided by TIMET was prepared for metallography and the microstructure imaged with white light microscopy. Figure 2.3 shows the grain size is around 100 μm .

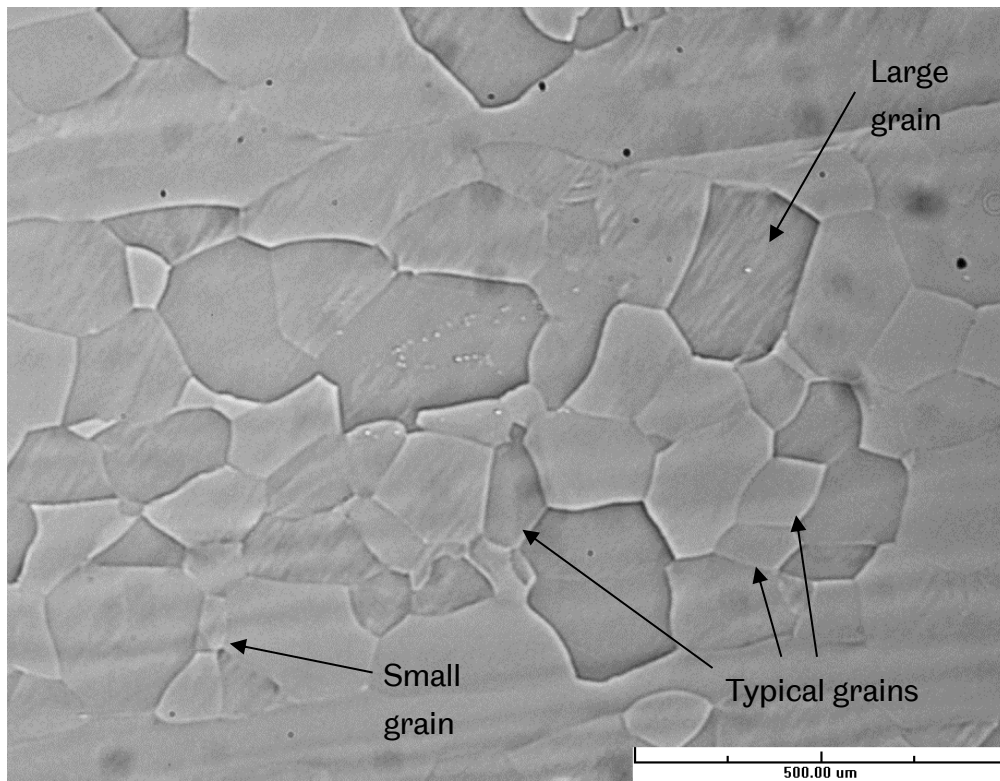


Figure 2.3 – As-received Ti-15Mo under low magnification light microscopy, with 500 μm scale bar.

Only a limited amount of the β -phase Ti-15Mo alloy could be obtained. A larger amount of a more readily available alloy could be obtained as a stock of additional material. A two-phase $\alpha + \beta$ titanium alloy, Ti-6Al-4V, is also investigated as a comparison, since it is a commonly used alloy for gas turbine fan and compressor blades – hence literature data is widely available.

Aerospace grade Ti-6Al-4V bar was supplied by TIMET. The as-received microstructure, imaged with a white light microscope, is shown in Figure 2.4 below. The alpha grain size is approximately 5 μm , observed by utilising a polarising filter with contrast enhanced and brightness reduced.

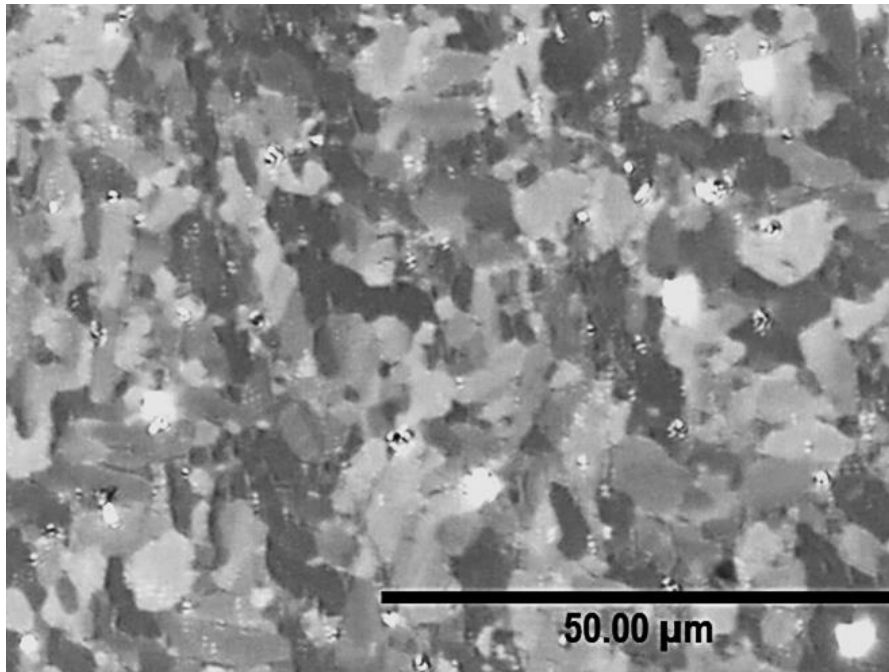


Figure 2.4 – As-received microstructure of Ti-6Al-4V at under high magnification light microscopy.

2.2.1 Annealing of Ti-6Al-4V

With a limited stock of the specialist Ti-15Mo alloy, and a large amount of the more readily available Ti-6Al-4V, it was decided to anneal some of the Ti-6Al-4V to a larger grain size, more similar to that of Ti-15Mo, to provide some basis of comparison between the two alloys. It was initially thought that annealing the Ti-6Al-4V at 800 °C for 1 hour, 4 hours and at 900 °C for 1 hour would increase primary α grain sizes to 25 μm , 50 μm and 100 μm , based on results from previous work nitriding the alloy. It was thought that to increase the primary α grain size, annealing should take place below 992 °C, the β -transus of the alloy, to limit β phase growth. However α grain sizes did not increase much beyond 10 μm . Attempting to hold the anneal for longer at 900 °C for 2 hours, 4 hours and 8 hours did not increase the grain size beyond 20 μm .

Figure 2.5 shows a typical 900 °C anneal and furnace cool microstructure.

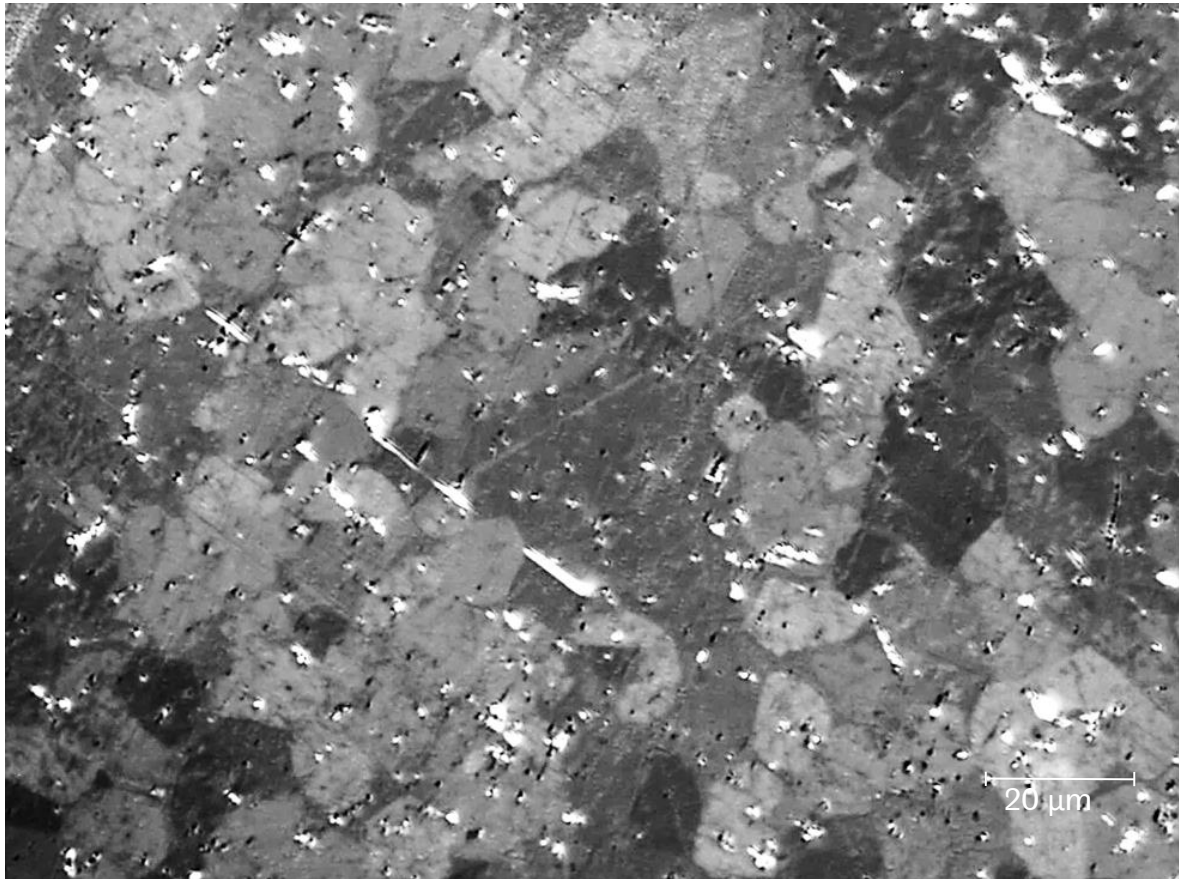


Figure 2.5 – Ti-6Al-4V annealed at 900 °C for 4 hours then furnace cooled. High magnification light microscope with 20 μm scale bar. N.B. the white flecks are artefacts; colloidal silica polishing compound which has not fully cleaned off.

By consulting titanium experts, it became clear that a super β -transus anneal followed by a sub β -transus hold would be required. This would transform primary α grains to large β phase colonies, which can then transform back to α phase in the sub β -transus hold. Figure 2.6 shows the microstructure from such a procedure, the primary α colonies are many 100's of micrometres in size.

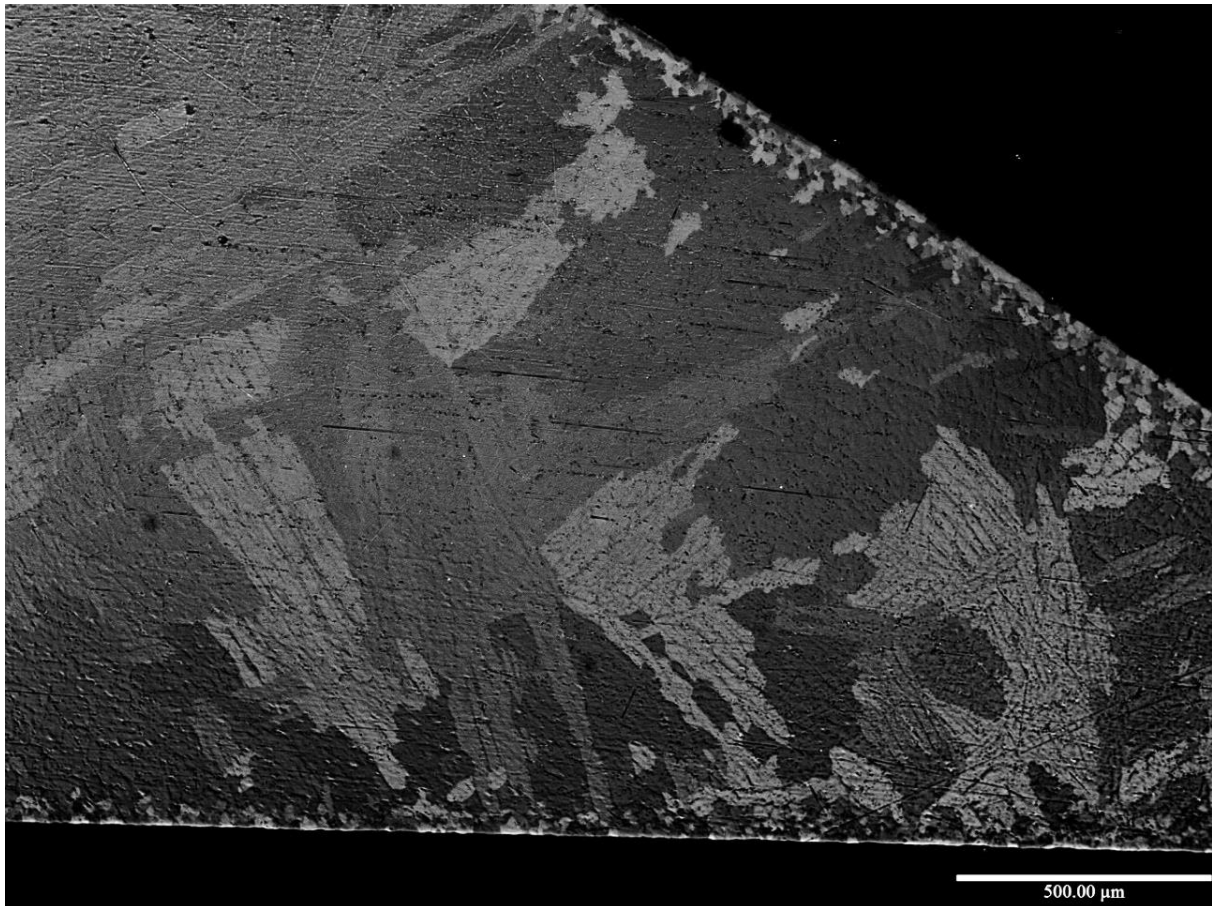


Figure 2.6 – Ti-6Al-4V annealed at 1100 °C for 2 mins, then held at 960 °C for 1 hour then furnace cooled. High magnification light microscopy with 500 μm scale bar.

By changing the super β -transus annealing temperature and hold time it was possible to produce a nearly equiaxed microstructure of large primary α colonies, comparable to the size of the as-received Ti-15Mo β grains. Figure 2.7 shows the microstructure following annealing just above the β -transus for 5 minutes, followed by a hold just below the β -transus for an hour, then furnace cooling. The finer microstructure at the surface would be machined off in sample manufacturing.

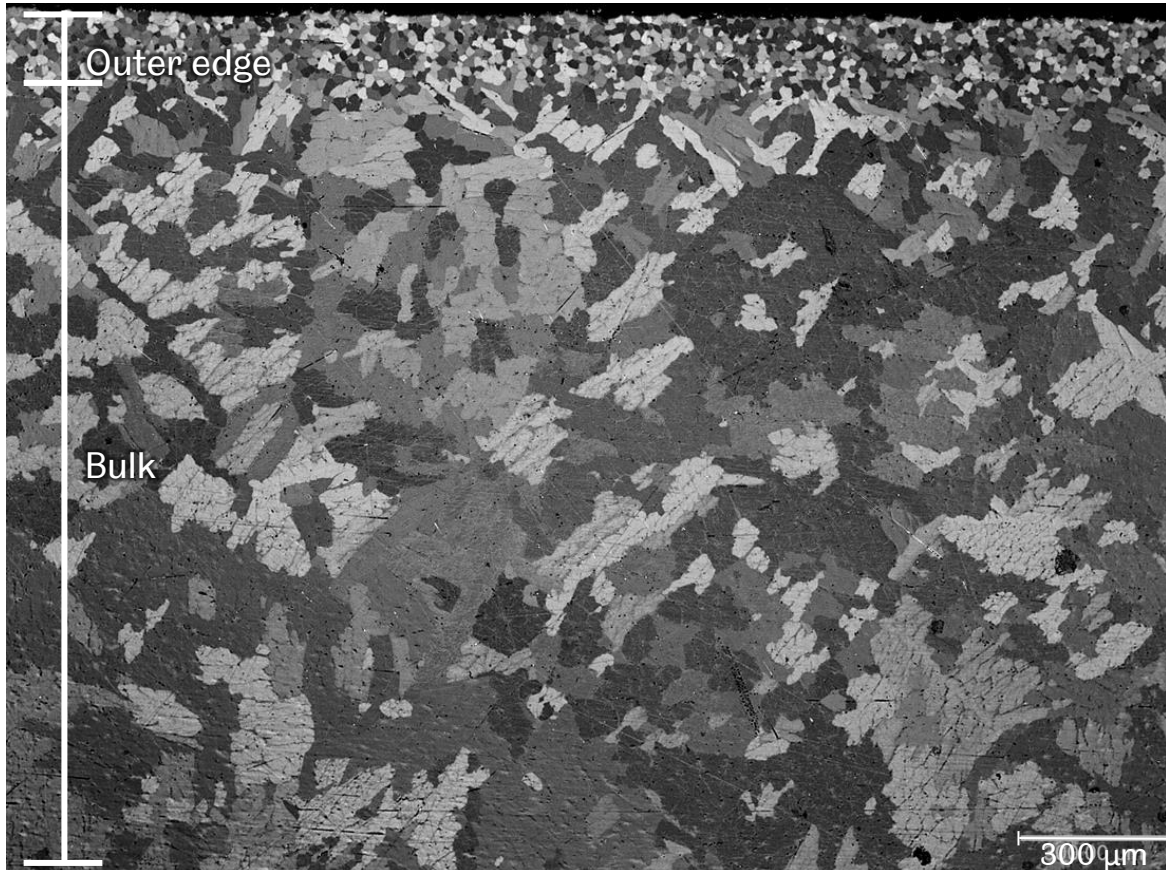


Figure 2.7 – Ti-6Al-4V annealed at 1050 °C for 5 mins, then held at 960 °C for 1 hour, then furnace cooled. Low magnification light microscopy with 300 μm scale bar.

Finally, a batch of as-received Ti-6Al-4V was annealed at these parameters, though unknowingly this was done in a different, larger furnace which appears to have had different characteristics. The final microstructure produced by the batch anneal resulted in colonies of lamellar α laths $\sim 500 \mu\text{m}$ in size, much larger than planned, as illustrated in Figure 2.8.

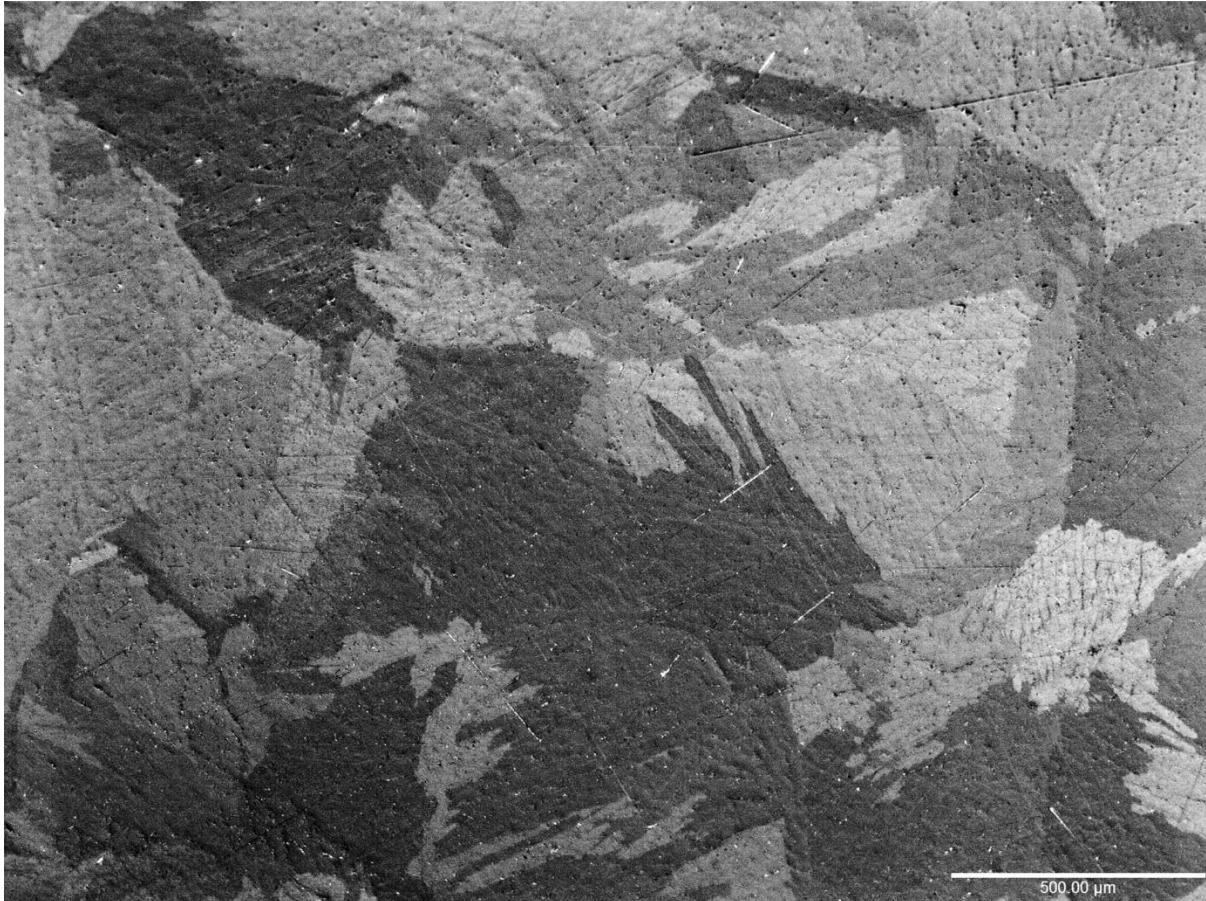


Figure 2.8 – Ti-6Al-4V annealed at 1050 °C for 5 mins, then held at 960 °C for 1 hour, then furnace cooled. Low magnification light microscopy with 500 μm scale bar.

2.3 Characterisation of the alloys by EBSD

2.3.1 A note on sample orientations cut from the material stock

Metal alloy bar stock often goes through a rolling or forging operation when converting primary billet to customer product for machining into components. This influences the microstructure, so that coupons cut from different locations will have grains of different shape and size. It is therefore important to understand which orientation a coupon has been produced from. Figure 2.9 illustrates how coupons can be cut from a bar, and the notation for this.

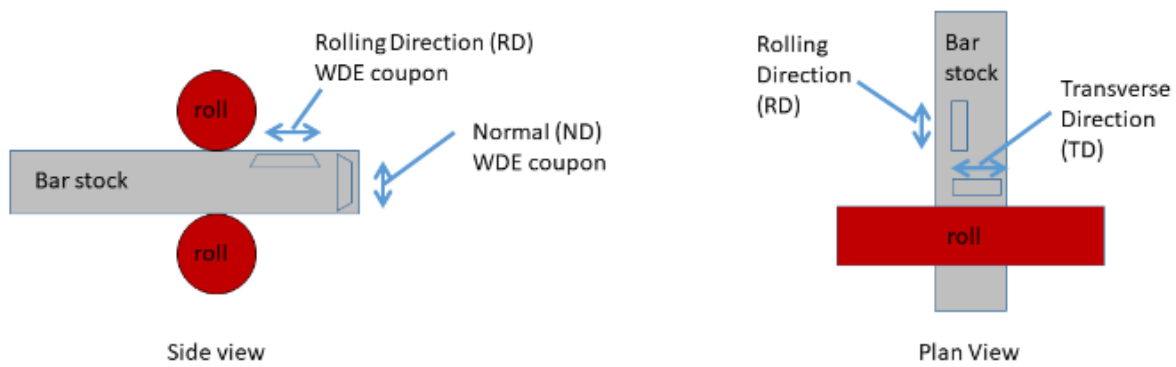


Figure 2.9 – Coupon orientations relative to bar processing direction.

Figure 2.10 demonstrates how processing direction can affect microstructure. Grains viewed in the normal direction (ND) are typically smaller, having been forged or rolled tightly together [44], [45]. Examining coupons taken in the rolling direction (RD) or transverse direction (TD) reveals grains are typically elongated in the processing direction.

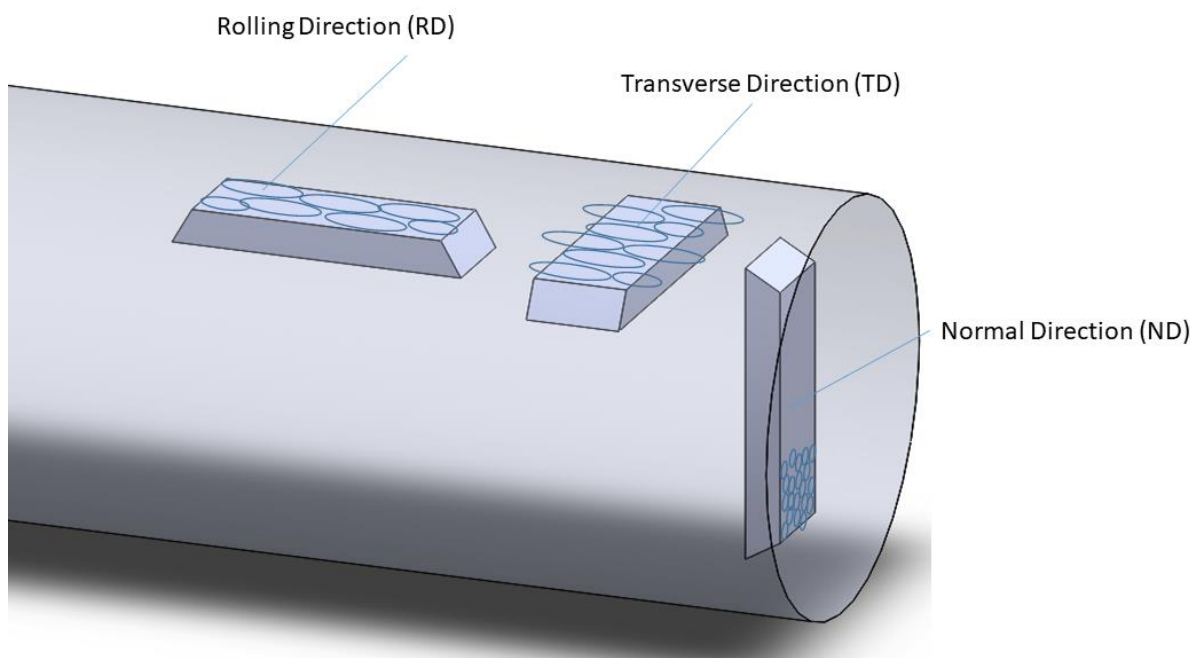


Figure 2.10 – Coupon orientations and grain orientations relative to bar processing direction.

Initially, it was thought WDE samples should be cut from the ND direction, as it was thought to represent the best materials properties. Manufacturing coupons from only one orientation would also reduce confounding effects, since coupons cut from other orientations would have differing properties. Ultimately coupons were cut from all three orientations in an attempt to explore these effects in WDE.

2.3.2 Background

Apart from optical microscopy, electron backscatter diffraction (EBSD) was important when characterising the alloys.

In an electron microscope, electrons are accelerated towards a conductive surface. The electrons excite interatomic bonds, causing the bonds to release electrons to dissipate this energy. Secondary Electrons (SE) can be detected by a CCD and used to produce an image, as in SE microscopy. A few electrons are backscattered. Because there are fewer, the detector needs to be closer to the sample than a SE detector.

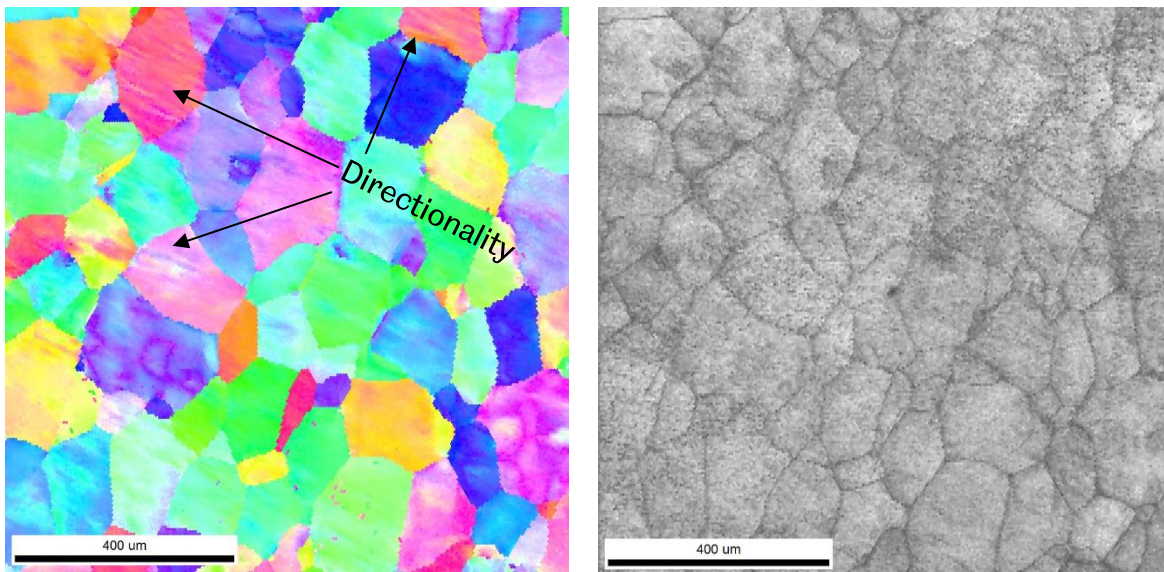
EBSD can provide information about how grains are orientated relative to one another in an Inverse Pole Figure (IPF), such as in Figure 2.11 below. Other useful maps can be produced from the scan data, such as the Image Quality (IQ), also in Figure 2.11 below. This gives an indication of the scan quality. Light regions indicate high confidence in indexing, darker regions indicate poorer indexing. Figure 2.12 shows a misorientation map. This shows misorientation of one pixel relative to its neighbour, so is particularly useful in illustrating local misorientations within a grain.

EBSD is a sensitive technique where dirt, oxides, scratches, or heavy deformation can prevent indexing. Careful sample preparation requires polishing compounds – colloidal silica for titanium, which is difficult to clean off samples. The polishing compounds also risk scratching or mechanically deforming the surface.

EBSD was conducted using an EDAX Hikari detector and TSL software in a Zeiss Supra40 Field Emission SEM at the National Physical Laboratory.

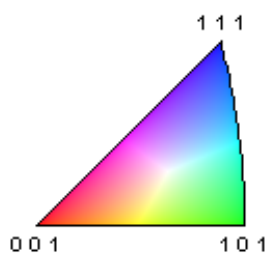
2.3.3 EBSD of as-received Ti-15Mo

Figure 2.11, below, shows an Inverse Pole Figure (IPF) for Ti-15Mo in the ND plane. From Figure 2.11, average grain size is around 100 μm . The IPF also highlights an underlying directionality in the microstructure. This may be from the manufacturing route, likely rolling or forging. It is useful to characterise the alloys before later testing, to help clarify whether microstructural anomalies are caused by testing or are residual from manufacturing.



Color Coded Map Type: Inverse Pole Figure [001]

Titanium (Beta)



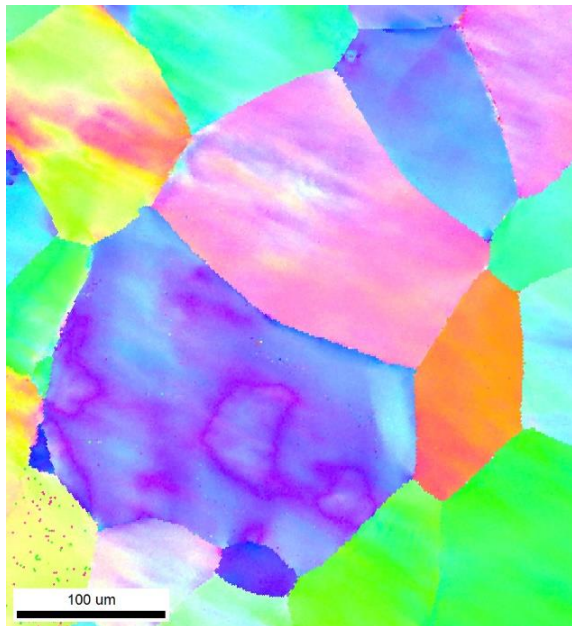
Inverse Pole Figure (IPF) for Ti-15Mo, scanned with a 4x4 binning rate and a step size of 5 μm .

Image Quality (IQ) of the scan. Light regions indicate high confidence in indexing, darker regions indicate poorer indexing.

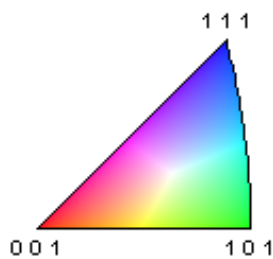
Figure 2.11 – IPF and IQ maps for Ti-15Mo (ND).

Figure 2.12, below, shows a higher-resolution scan of a small region of interest from Figure 2.11. There are unusual ring features in the purple grain. Some other grains contain more than one orientation too. Another useful map which can be produced

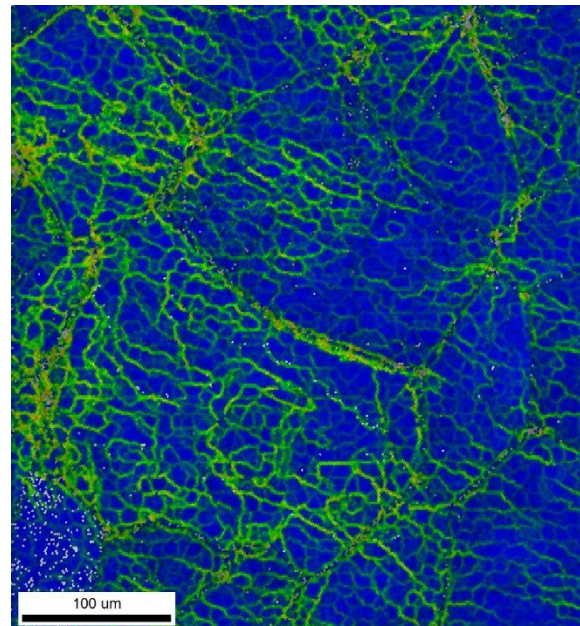
from the EBSD data is one which shows misorientation between neighbouring pixels. A misorientation map is shown for the scan in Figure 2.12. There is significant misorientation at grain boundaries, but also within the grains, particularly at the differently orientated regions noted from the IPF. The misorientation is probably from the manufacturing route, although this sort of patterning does not appear in other rolled or forged materials. The misorientation may be indicative of pre-existing twinning and/or stacking faults, which beta-alloys are susceptible to under mechanical deformation.



Color Coded Map Type: Inverse Pole Figure [001]
Titanium (Beta)



IPF for Ti-15Mo ND, scanned with a 4x4 binning rate and a step size of 1.5 μm



Color Coded Map Type: Kernel Average Misorientation



Misorientation map of the scan using Kernel Average 1st neighbour. Data cleaned up by Kuwahara filter applied to first neighbour for two iterations. Grains of size less than 5 pixels removed. Overlaid on Image Quality map.

Figure 2.12 – IPF and Misorientation map for Ti-15Mo ND.

A larger scale scan taken at a lower magnification in Figure 2.13 reveals that the microstructure also has very large laths running through it.

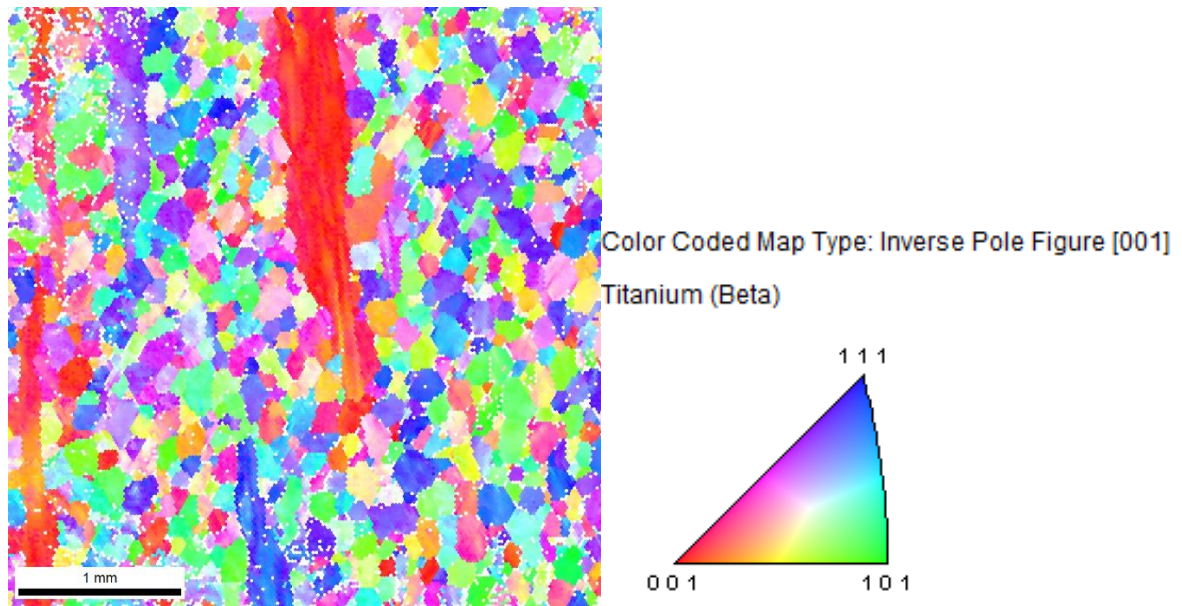


Figure 2.13 – IPF of Ti-15Mo ND. Scanned with a 2x2 binning rate and a step size of 20 μm . Grains of size less than 2 pixels removed.

2.3.4 EBSD of as-received Ti-6Al-4V

Figure 2.14 shows a high resolution EBSD scan of the as-received Ti-6Al-4V microstructure. The image quality (IQ) map is produced from band contrast. High contrast indicates high confidence in indexing, darker areas indicate poor indexing in regions such as grain boundaries, contamination from dirt, polishing scratches or other deformation. The IQ map therefore serves as a useful way of seeing grain boundaries. The IPF indicates some large grains are actually made up of several orientations, and some small grains may in fact be similarly orientated to each other.

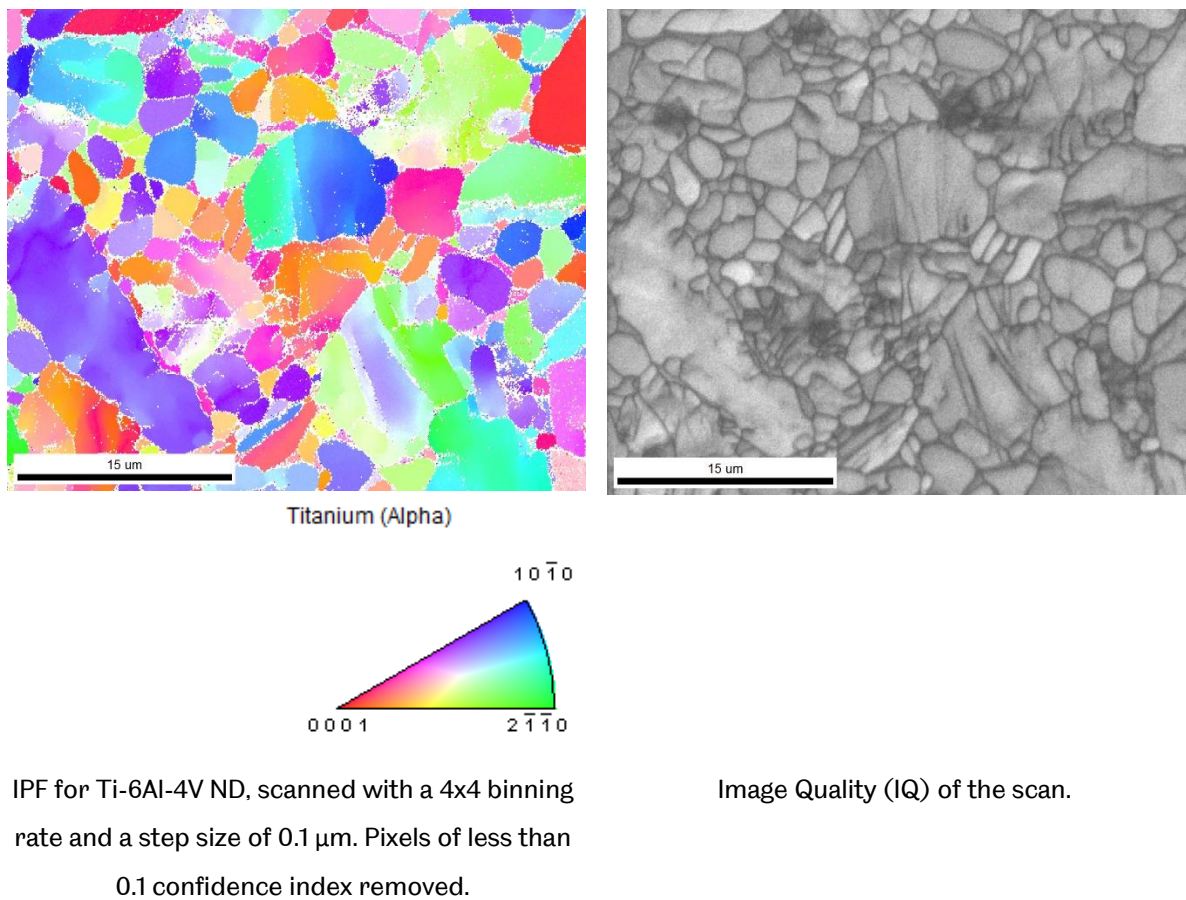
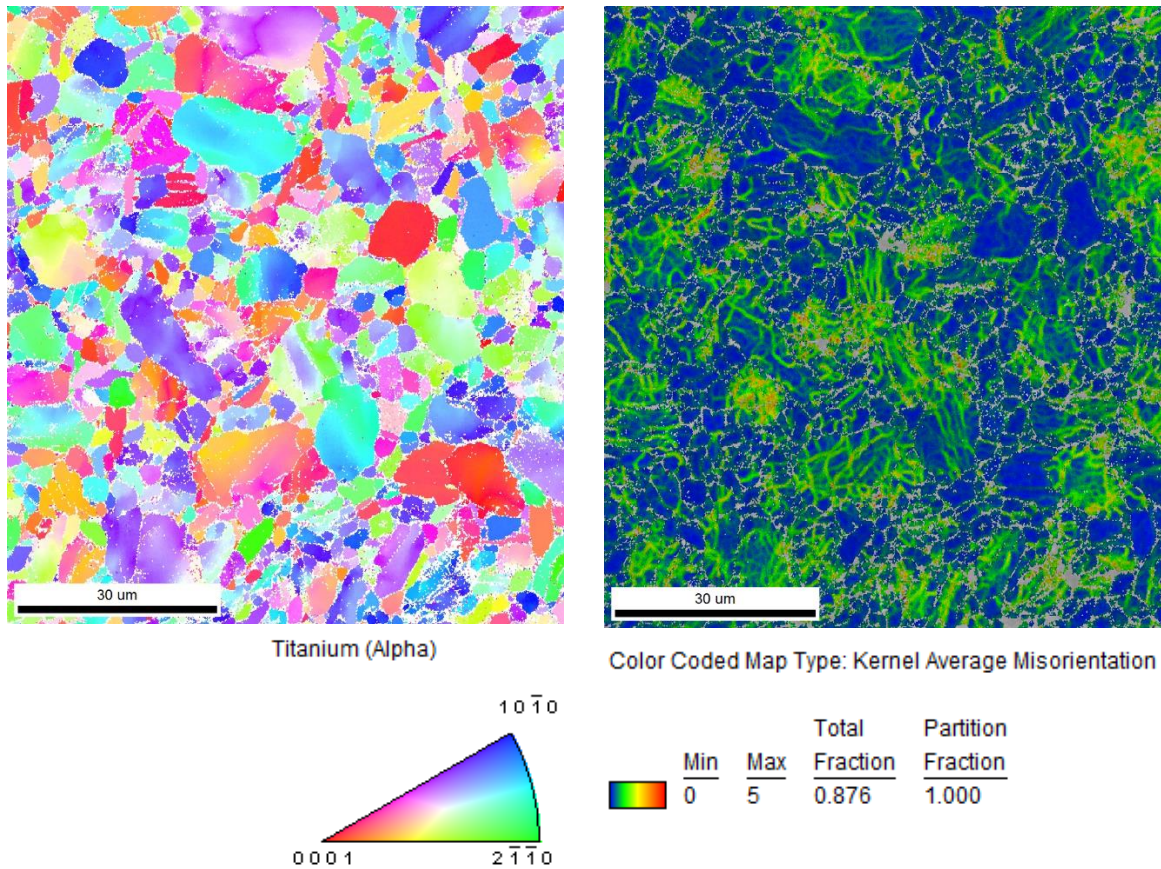


Figure 2.14 – IPF and IQ maps for as-received Ti-6Al-4V (ND).

Figure 2.15 is a scan taken at a lower magnification thus taking in a larger area. The misorientation map suggests a lot of local misorientation, residual from the materials forming route (whether rolled or forged).



IPF for Ti-6Al-4V ND, scanned with a 4x4 binning rate and a step size of 0.2 µm. Pixels of less than 0.1 confidence index removed.

Misorientation map of the scan using Kernel Average 1st neighbour. Data cleaned up by Kuwahara filter applied to first neighbour for two iterations. Pixels of less than 0.1 confidence index removed. Overlaid on Image Quality map.

Figure 2.15 – IPF and Misorientation maps for as-received Ti-6Al-4V (ND).

A larger IPF map in Figure 2.15 demonstrates the microstructure is largely homogenous. Although not visible in this example, macrozones of similarly oriented grains often run through Ti-6Al-4V forged bar.

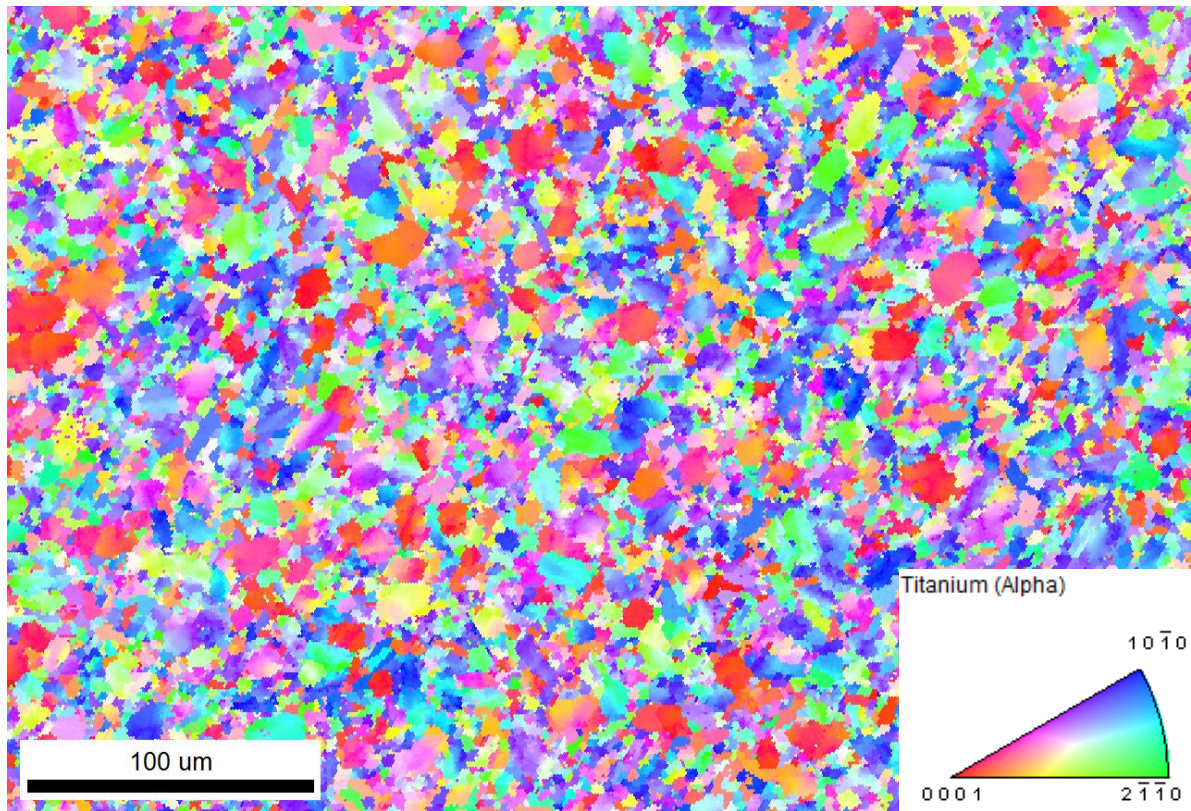


Figure 2.16 – IPF of as-received Ti-6Al-4V (ND). Scanned with a 4x4 binning rate and a step size of 1 μm . Grains of size less than 2 pixels removed. Data cleaned up by Kuwahara filter applied to first neighbour for one iteration.

SEM is also useful for viewing the microstructure. Figure 2.17 shows an equiaxed duplex structure of globular and fine transformed lamellar primary α in prior β grains, typical of a Ti-6Al-4V alloy forged just below the $\alpha+\beta$ transus then air cooled.

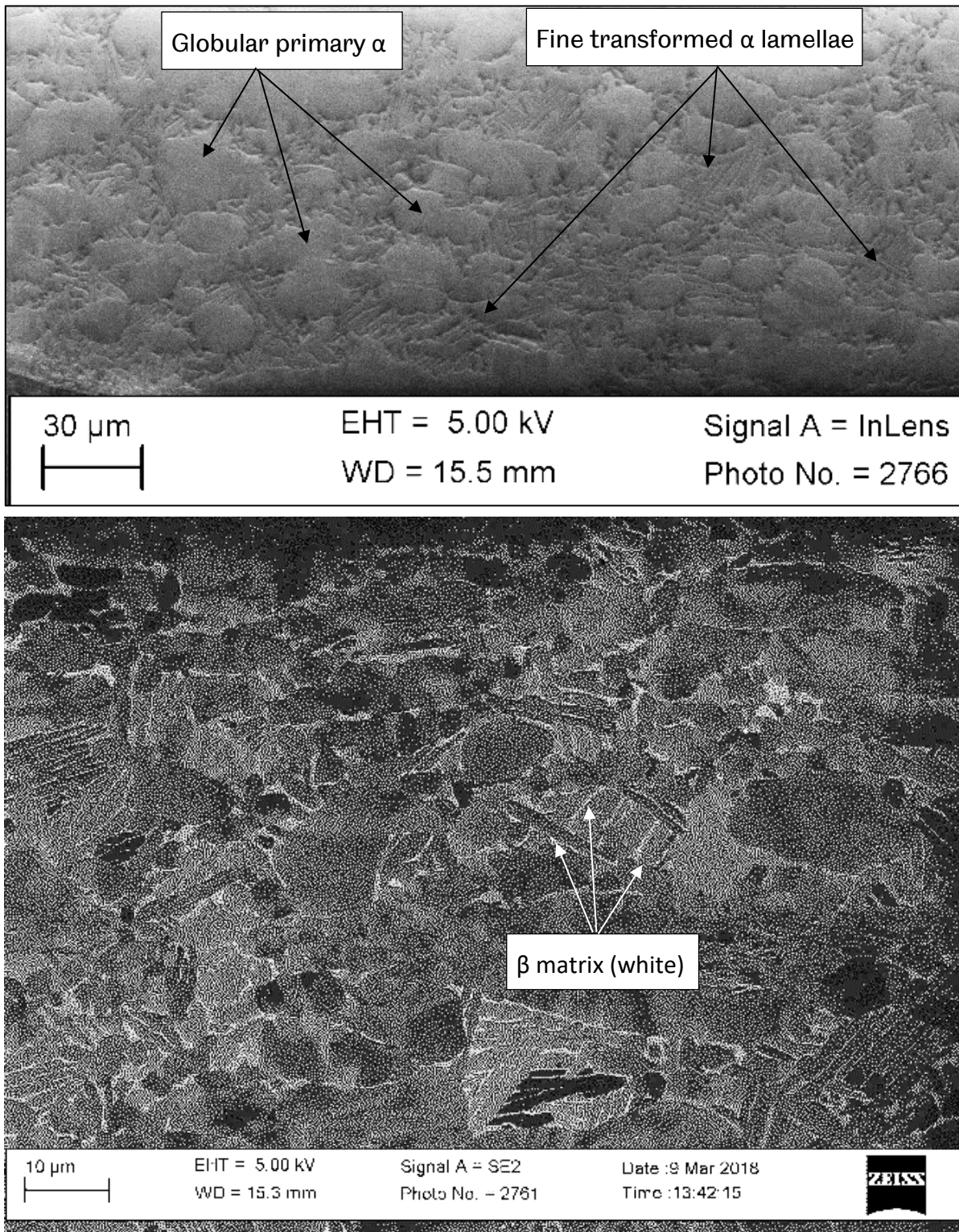
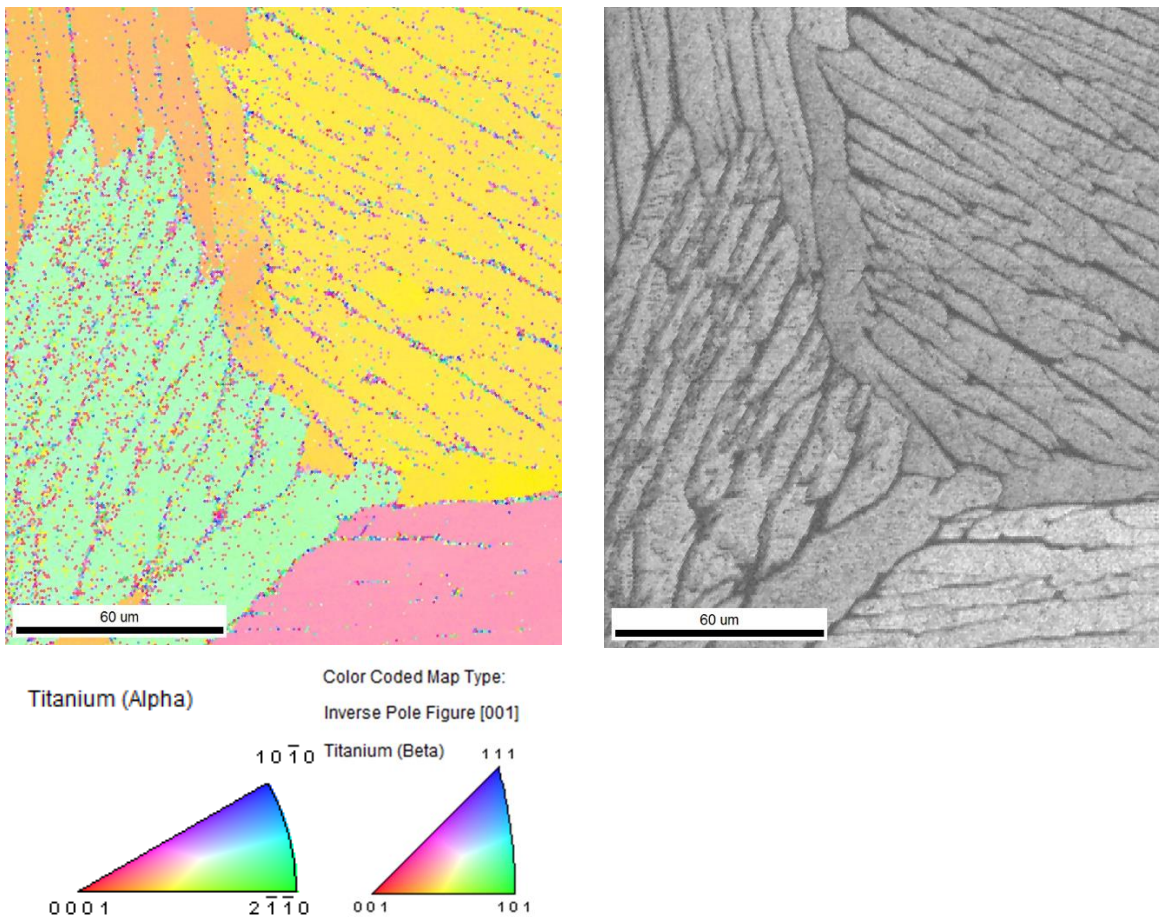


Figure 2.17 – SEM images of the as-received Ti-6Al-4V (RD) microstructure, showing the duplex globular and lamellar α phase embedded in a β phase matrix.

2.3.5 EBSD of annealed Ti-6Al-4V

During the batch anneal of Ti-6Al-4V, the small grains of primary α would have been transformed into β phase, and these β grains grew according to the time held above the β transus. Then, holding the temperature just below the β transus would allow β phase to transform back into α . Figure 2.18 demonstrates the large α laths embedded in a β matrix, grouped in colonies of similarly oriented α laths.

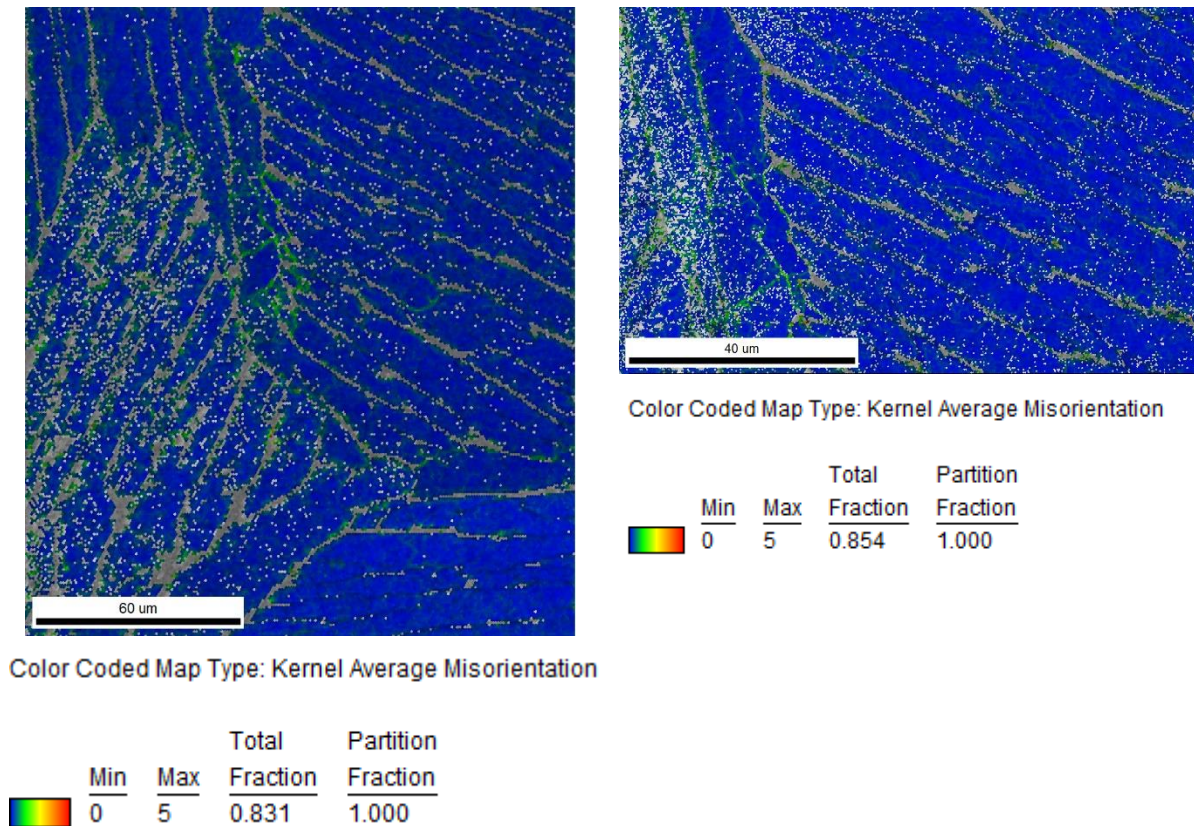


IPF for Ti-6Al-4V ND, scanned with a 2x2 binning rate and a step size of 0.75 μm .

Image Quality (IQ) of the scan.

Figure 2.18 – IPF and IQ maps for annealed Ti-6Al-4V (ND).

Figure 2.19 shows that, in contrast to the as-received alloys, there is little misorientation between neighbouring pixels.



Misorientation map for Ti-6Al-4V ND using Kernel Average 1st neighbour. Scanned with a 2x2 binning rate and a step size of 0.75 μm. Data cleaned up by Kuwahara filter applied to first neighbour for two iterations. Grains of less than 5 pixels removed. Overlaid on Image Quality map.

Misorientation map for Ti-6Al-4V ND using Kernel Average 1st neighbour. Scanned with a 2x2 binning rate and a step size of 0.3 μm. Data cleaned up by Kuwahara filter applied to first neighbour for two iterations. Grains of less than 5 pixels removed. Overlaid on IQ map (50% transparency).

Figure 2.19 – IPF and IQ maps for annealed Ti-6Al-4V (ND).

2.4 Discussion

Ti-15Mo was selected for use in WDE testing as a simple, metastable β -phase alloy with low elastic modulus, long elastic strain to failure, large work of fracture and high ductility. It was expected to deform in a ductile manner, aiding the tracking of droplet impact damage, and the isotropic bcc single-phase composition should allow damage mechanisms to be more readily identified. Ti-6Al-4V was also chosen for study – the

predominantly α -phase alloy was expected to contrast with the β -phase Ti-15Mo and perhaps help to establish if damage mechanisms are driven by crystallographic phase composition, grain size and microstructure – or are largely independent of the alloy material chosen (or its heat treatment path). Ti-6Al-4V is also used in some applications where WDE occurs, such as aero-engine fan blades, so results may be of interest to that industry. Some Ti-6Al-4V was annealed from a 5 μm primary α grain size to a larger size. It was hoped the larger grain size would allow for simpler comparison to the 100 μm β Ti-15Mo.

Although the annealing procedure produced colonies of alpha lamellae in much larger sizes than expected (500 μm), EBSD revealed the annealing process proved very useful in actually removing residual misorientations in the as-received microstructure. This clarified analysis of later tests (e.g. WDE & Split Hopkinson bar tests), as there was less question over whether misorientation was residual or caused by the test in question. Whereas the goal of annealing had been to increase α phase grains to a size more similar to the β phase Ti-15Mo, the range of microstructures (5 μm primary α Ti-6Al-4V, 100 μm β Ti-15Mo, 500 μm primary α Ti-6Al-4V) allowed some investigation between grain sizes and phases.

3 WATER DROPLET EROSION

3.1 Literature review

This literature review aims to understand: where water droplet erosion (WDE) occurs, the process of how a water droplet leads to material loss, material properties relevant to WDE, and how initial erosion begins.

Water droplet erosion (WDE) occurs when water droplets impact a surface at a high velocity. It affects aero-engine fan blades, steam turbine blades and wind turbine blades. This is a problem because erosion, as seen in Figure 3.1 below, reduces aerodynamic efficiency. If left unchecked the roughened surface could also initiate fatigue cracks.



Figure 3.1 – Erosion on the leading edge of wind turbine blades [18].

Cobalt or Nickel overlays may be used on leading edges where erosion is prevalent, such as on steam turbine blades, but this presents a major cost and weight implication for wind turbine blades. Instead, damage to FRP composites may be repaired by conventional wet layup, which is laborious and time-consuming.

3.1.1 Proposed mechanisms of water droplet erosion

Several mechanisms of erosion have been suggested in the literature. Common themes are direct mechanical deformation (by plastic yielding or cracking), stress wave propagation, hydraulic penetration, and lateral outflow jetting (due to droplet compression and collapse), but the relative importance and prevalence of each mechanism remains unclear.

Peak stress due to an impacting droplet can be high enough to cause direct plastic deformation. The “water-hammer” equation, attributed to Cook [33], makes some simplifications, but nonetheless gives a good estimate of this pressure. Assuming a

column of water, rather than a droplet, stopped instantaneously by a surface, the pressure, p , exerted on the surface is $p = \rho cv$ where ρ is fluid density, c is the velocity of a compression wave in the liquid and v is the velocity of the column [33], [46].

Below, Figure 3.2 shows an example of stress which Bourne et al. [29] measured at a surface impacted by a slug of water. The single impact jet apparatus (SIJA) used is designed to be able to accelerate a discrete volume of water at a surface rather than a continuous jet, to be able to simulate the discrete nature of a droplet impact. The measured peak stress is very similar to the calculated water-hammer pressure of 0.85 GPa.

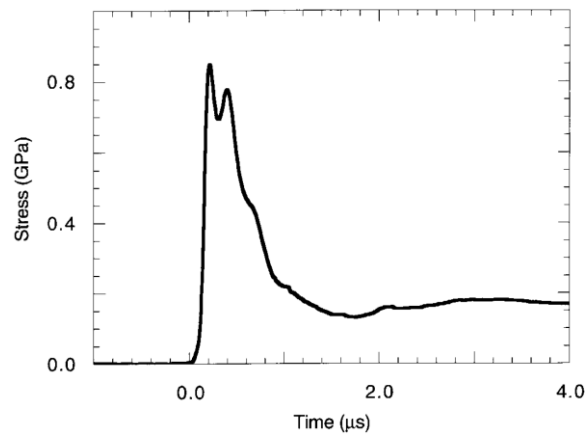


Figure 3.2 Stress of a 570 m·s⁻¹ water jet “slug” impinging on a PVDF pressure gauge [29].

Work hardening at the surface has also been suggested as a relevant factor in WDE. Mahdipoor et al. [47] found hardness increased with 0.5 min WDE exposure times for two Ti alloys, as demonstrated in Figure 3.3 below.

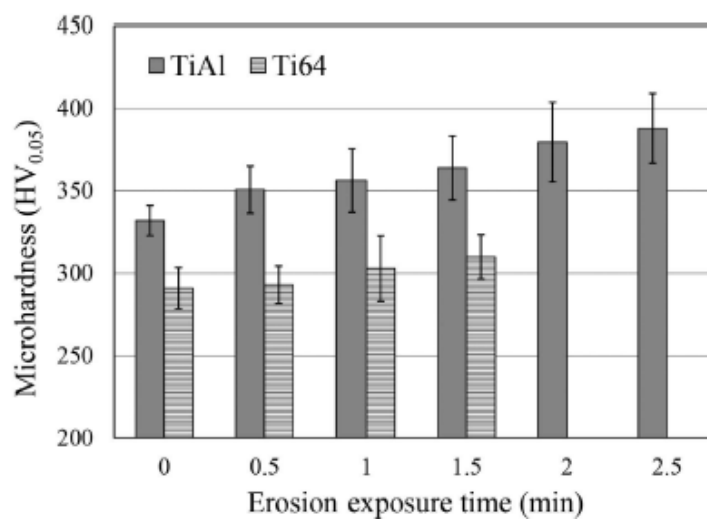


Figure 3.3 – Hardness of TiAl and Ti64 at the surface exposed to WDE at 350 m·s⁻¹ with 464 μm droplets [47].

However, mechanical surface treatments such as shot peening generally do not improve water droplet erosion resistance [48], suggesting work hardening may not be a predominant damage mechanism.

Wave theory has also been prominent in the literature, beginning with Bowden and Field's model from 1964 of Rayleigh waves travelling along the surface of the impacted material and other waves propagating further into the bulk [7]. Bowden and Field used high speed photography to track stress propagation (observable from the resulting fractures) due to water or lead slugs impacting glass specimens. They compared the measured stress propagation wave with the calculated speeds of other waves. The measured wave speed was $3000 \pm 300 \text{ m}\cdot\text{s}^{-1}$. The calculated longitudinal wave and transverse wave speeds were $5750 \text{ m}\cdot\text{s}^{-1}$ and $3370 \text{ m}\cdot\text{s}^{-1}$, respectively. The calculated Rayleigh wave speed was $3100 \text{ m}\cdot\text{s}^{-1}$; suggesting the measured wave was a Rayleigh wave. In acoustics, Rayleigh waves are known to be the most damaging, carrying greater than 60% of the impact energy [49], [50].

The different waves created in the material are illustrated in Figure 3.4 below.

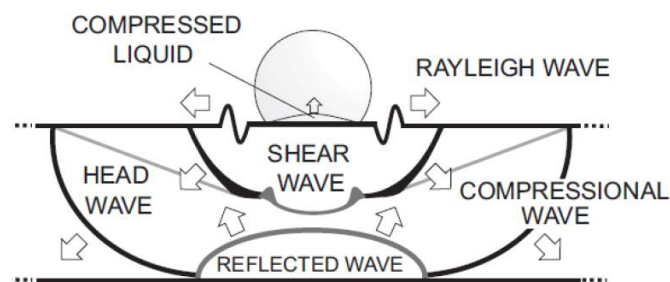


Figure 3.4 - Wave generation from liquid droplet impact [2].

Cavitation has been both observed and modelled within impacting droplets. Pressure waves reflected within the droplet can create cavities which, upon collapsing, can emit shockwaves (i.e. stress waves travelling faster than the speed of sound) which have the potential to damage the surface.

Field, Dear and Ogren [16] photographed a timeseries of an impacting droplet in Figure 3.5 below. A compressive shockwave, S, travels up the droplet, then reflects from the top surface as expansive waves, R. These meet at a focussing region, F, to produce cavities.

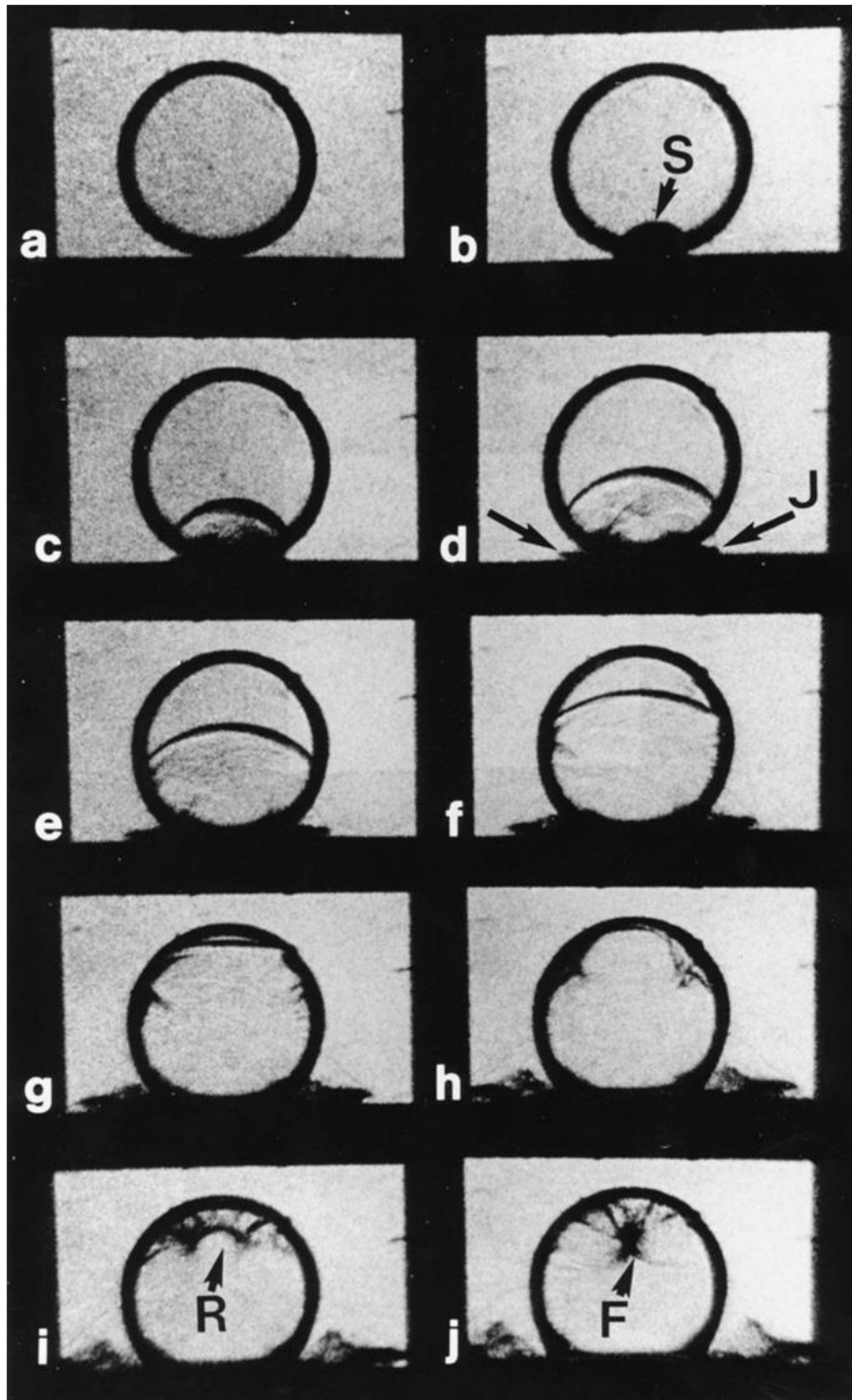


Figure 3.5 – A 10 mm droplet impacted by a metal slider at $110 \text{ m}\cdot\text{s}^{-1}$. Interframe time $1 \mu\text{s}$ [16].

Haller's computational model of an impacting droplet in Figure 3.6 below shows a low pressure cavity forming behind the shockwave, which focuses at the top of the droplet [13].

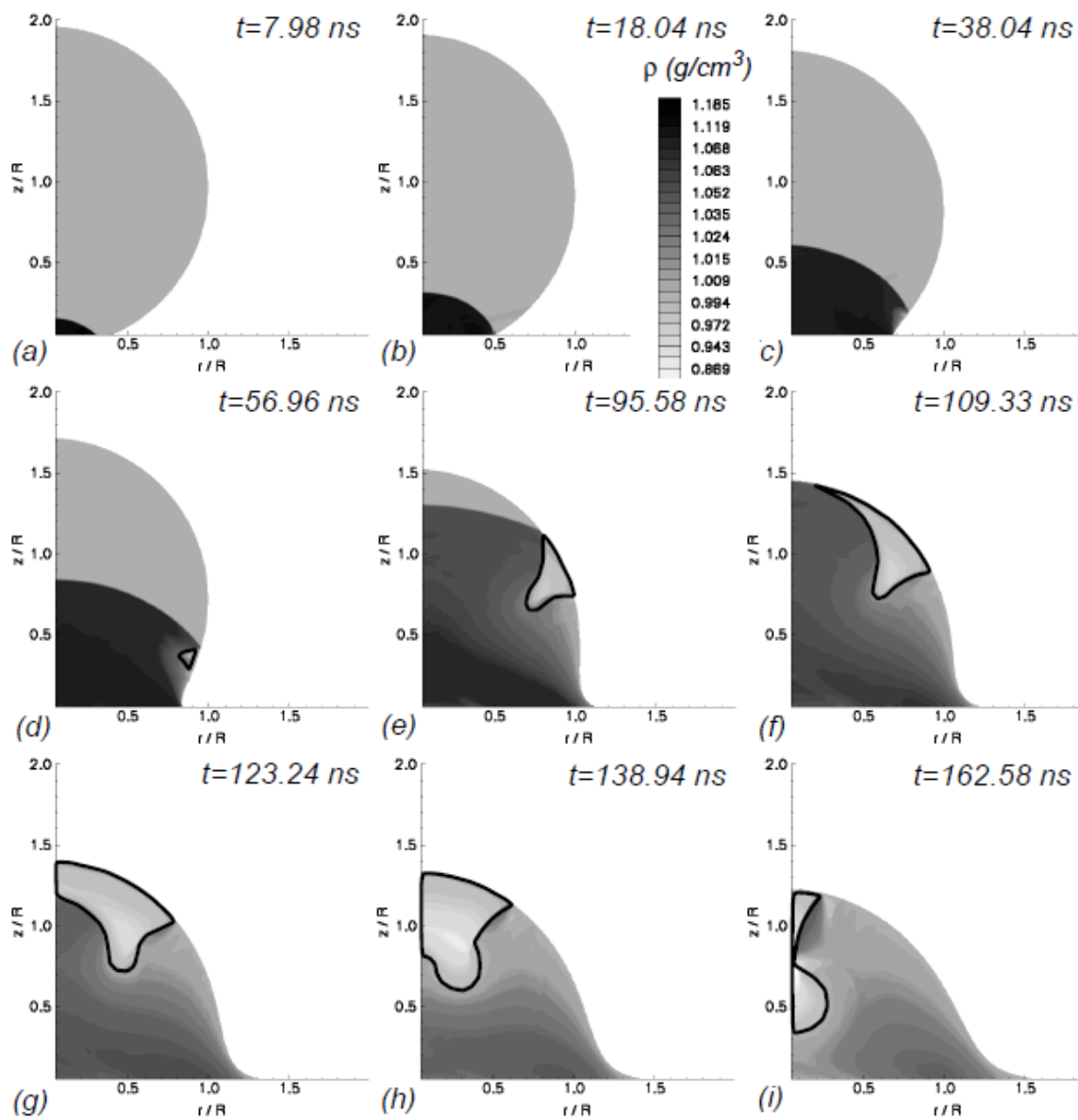


Figure 3.6 - Computational simulation of a 100 μm water droplet impact at $500 \text{ m}\cdot\text{s}^{-1}$ with increasing time, t [13].

Cavities at the top of the droplet may not actually be close enough to the material surface to produce cavitation erosion [51]. However, Obreschkow et al. suggest how these cavities might move nearer to the surface in Figure 3.7 [52].

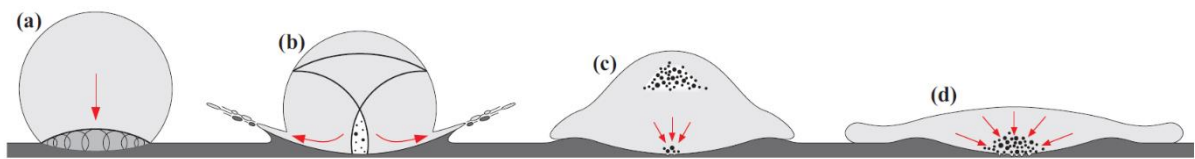


Figure 3.7 – Possible mechanism of cavitation in a collapsing droplet [52].

Cavitation closer to the material surface has also been observed, such as the cavities photographed by Camus [53] in Figure 3.8, one of which collapses and produces a shockwave, labelled S in the second frame.

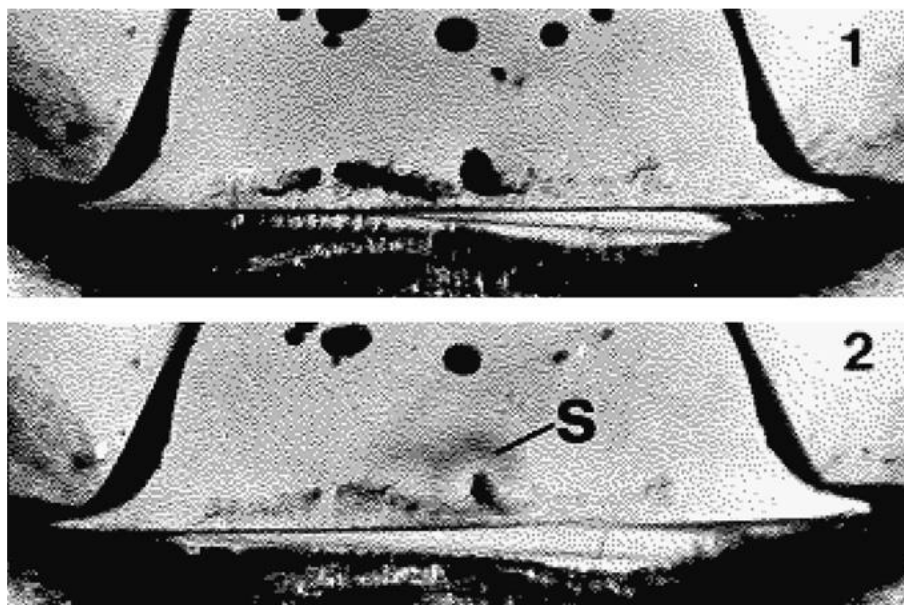


Figure 3.8 – A 5 mm droplet impacted at $60 \text{ m}\cdot\text{s}^{-1}$ [53].

Hydraulic penetration is when fluid is forced into existing cracks, or troughs in surface roughness, as illustrated in Figure 3.9 below. The incompressible fluid will force troughs and cracks wider. This is a secondary WDE mechanism as it requires the surface to have been initially roughened or cracked by other mechanisms.

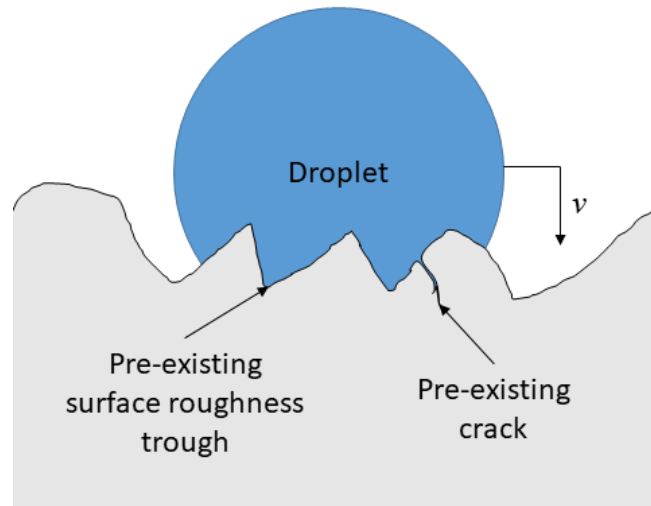


Figure 3.9 – Hydraulic penetration.

Lateral outflow jets have been found in high-speed photographic studies of water droplet impacts, as Camus observed in Figure 3.10 [53].

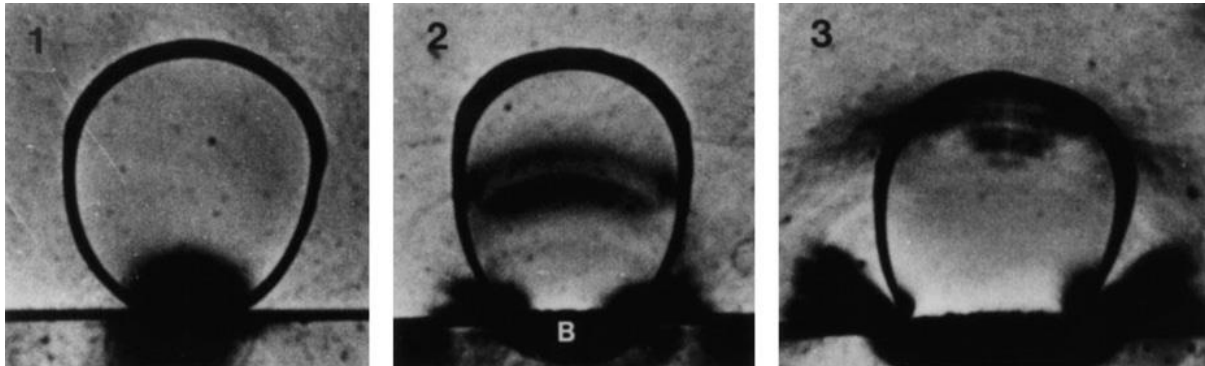


Figure 3.10 - A 2 mm diameter water droplet impacting a surface at $70 \text{ m}\cdot\text{s}^{-1}$ producing lateral outflow jets [53].

Springer's schematic in Figure 3.11 shows how lateral outflow jets produced by a water droplet impact would interact with surface flaws and cause damage [54].

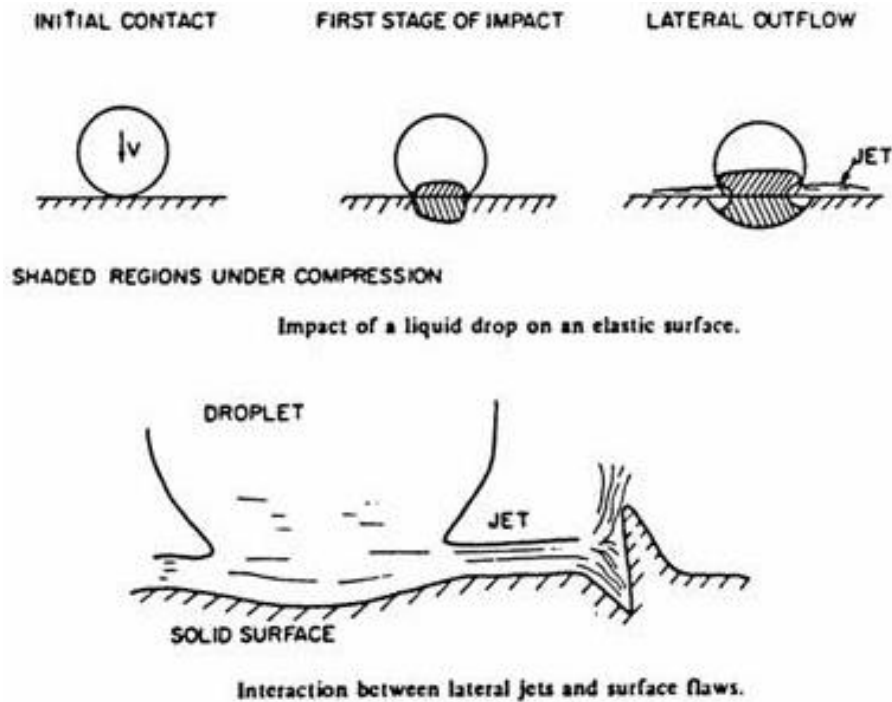


Figure 3.11 - Springer's schematic of a lateral outflow jet interacting with surface roughness [54].

Adler's computational model of a single water droplet impact (Figure 3.12, below) also found water jets were present at the edges of the droplet impact, although no quantitative results were published [31].

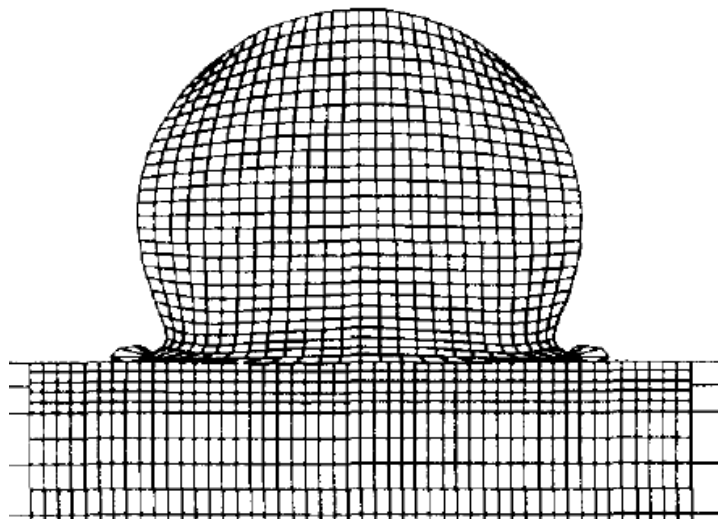


Figure 3.12 - FEM of a 2 mm diameter water droplet impact at $305 \text{ m}\cdot\text{s}^{-1}$, $1 \mu\text{s}$ after impact [31].

Haller's numerical model found lateral jets with velocities as high as $6000 \text{ m}\cdot\text{s}^{-1}$ as Figure 3.13 demonstrates.

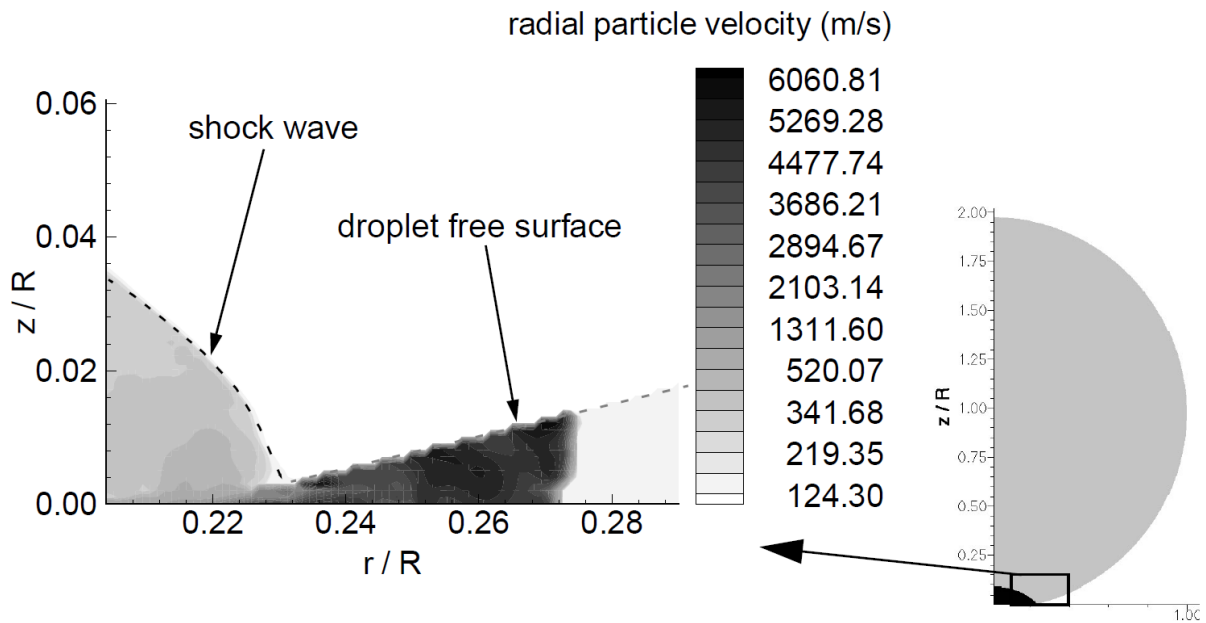


Figure 3.13 – $100 \mu\text{m}$ diameter water droplet impacting at $500 \text{ m}\cdot\text{s}^{-1}$. Left: enlarged detail of the lateral jets produced when the shockwave overtakes the contact patch area. Right: the entire model, illustrating the region of interest [13].

Damage by lateral jetting requires pre-existing flaws, such as surface roughness peaks. In theory a smooth, polished surface would not be damaged by hydraulic penetration or lateral outflow jetting. Mahdipoor et al. [55] suggest Polák's [56] model of fatigue-driven extruded slip bands, as shown in Figure 3.14, could cause the surface flaws which Springer's model requires.

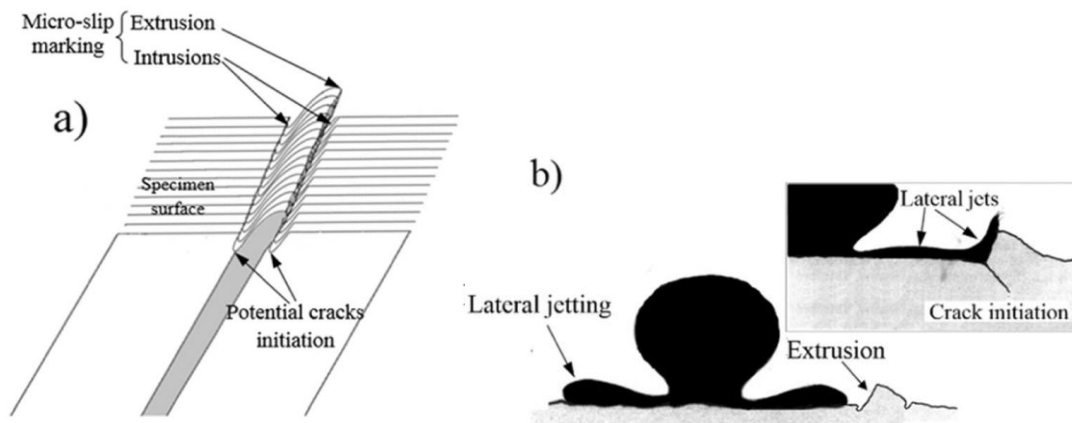


Figure 3.14 – (Left) Polak's model of extruded slip bands [56] and (right) how Mahdipoor et al. think lateral jets could interact with such a feature [55].

Damage associated with fatigue has been observed in water droplet erosion tests. Kamkar [57] reported that striations and slip bands could indicate WDE material removal mechanisms are fatigue related. Momber et al. [58] had previously suggested low cycle fatigue was the mechanism responsible for removing material by water jetting. Twinning, a microstructural deformation and hardening mechanism associated with low cycle fatigue, has also been reported in WDE [47], [51].

It's important to note that no one damage mechanism is solely responsible for WDE – it is known that a synergy of several mechanisms contribute to WDE. For example, materials which resist cavitation erosion well do not necessarily resist WDE. Thomas and Brunton [59] found that erosion can take place at impact pressures below the metals yield strength, suggesting direct deformation alone does not account for erosion. Brunton and Camus [11] suggest cavitation can account for the deficit, as they observed cavitation shockwaves to be larger than impact shockwaves. Thomas and Brunton [59] conducted experiments to recreate the early stages of erosion using compression waves propagated through a liquid column onto a specimen. They went a step further by then using high velocity jetting to simulate lateral outflow jets seen in advanced erosion.

3.1.2 Relating water droplet erosion to material properties

Ma et al. [48] investigated if the compressive residual stresses from surface laser shock peening had any effect on WDE, but concluded fatigue wasn't a dominating mechanism. Richman and McNaughton [60] had previously correlated cavitation erosion resistance with fatigue resistance.

Thomas and Brunton [59] correlated erosion endurance with strain energy to fracture. Strain energy to fracture, also called toughness or fracture toughness, is the integral

of a stress-strain curve. Smart used the UTS as a limit of strain energy (also known as resilience) and suggested high ultimate resilience was preferred to resist cavitation erosion [61].

Some researchers have suggested certain droplet sizes produce the greatest erosion, however this is more likely due to interaction with a particular material. Osgerby suggested 50 μm droplets were “the most damaging” [62], but this was likely influenced by the material under investigation (stainless steel for steam turbine blades – which would have a grain size of around 50 μm). In general, larger droplet size will increase erosion rate, but droplets on a similar order to the materials grain size may have some interaction to result in a greater erosion rate than expected.

Generally, tough and hard materials resist water droplet erosion, such as stellites (cobalt-based metal matrix composites, alloyed with a hard material like tungsten carbide) [47].

3.1.3 Test rigs

There are different methods for experimentally generating water droplet erosion. In his seminal 1928 paper on Erosion by Water-hammer, Cook notes that water jetting stationary or revolving samples is not representative of actual droplet-in-turbine conditions, asserting the continuous stream likely misses the repeated effect of the water hammer pressure [33]. Instead, Cook mounted turbine blade materials on a rotating shaft, achieving $233 \text{ m}\cdot\text{s}^{-1}$ tip speed, and misted the blades with water. Cook's test rig is shown in Figure 3.15.

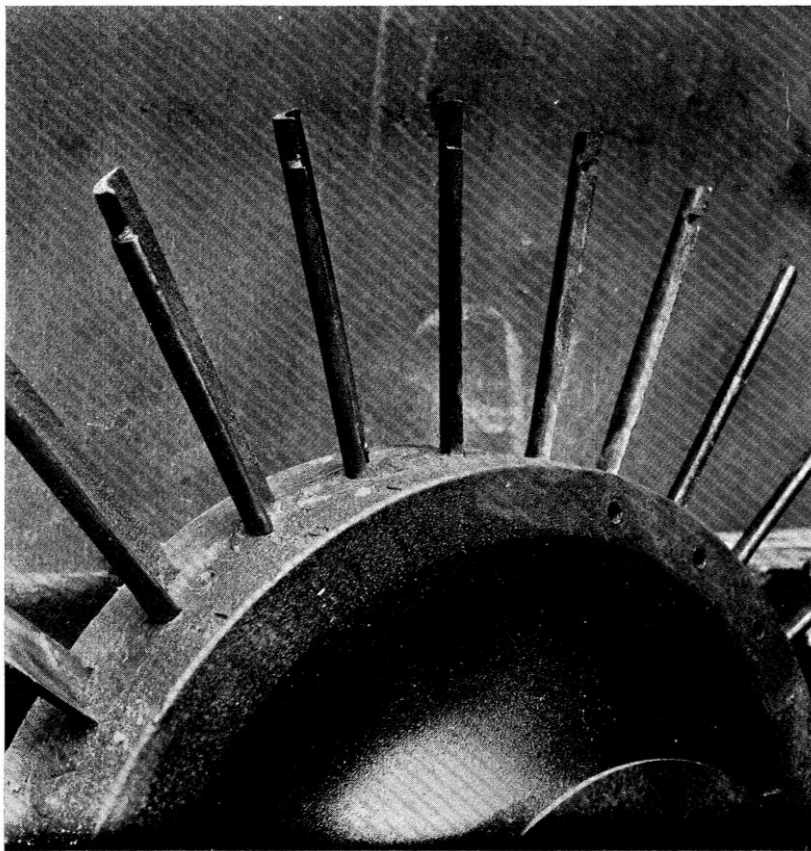


Figure 3.15 – The rotating sample set-up which Cook utilised [33].

Rotating or whirling arm rigs can provide representative results, but can be relatively complex, with associated costs and difficult maintenance requirements.

A high pressure water jet may be the simplest way of producing erosion damage. Oka, Shipway and others have produced erosion damage [8]–[10], though the continuous nature of the water jet lacks both the rounded geometry of impinging droplets, and the repetitive nature of erosion.

Another method to generate WDE is to accelerate samples through a field of water droplets. Figure 3.16 shows samples mounted on the front of a sled at Holloman airbase, New Mexico, which is rocket-propelled along a track surrounded by a sprinkler system. The test can provide results representative of erosion of aircraft components at speeds up to $1830 \text{ m}\cdot\text{s}^{-1}$ [63], but requires a large footprint, is expensive to run, and results can become contaminated by external media such as sand, insects and bird strikes.

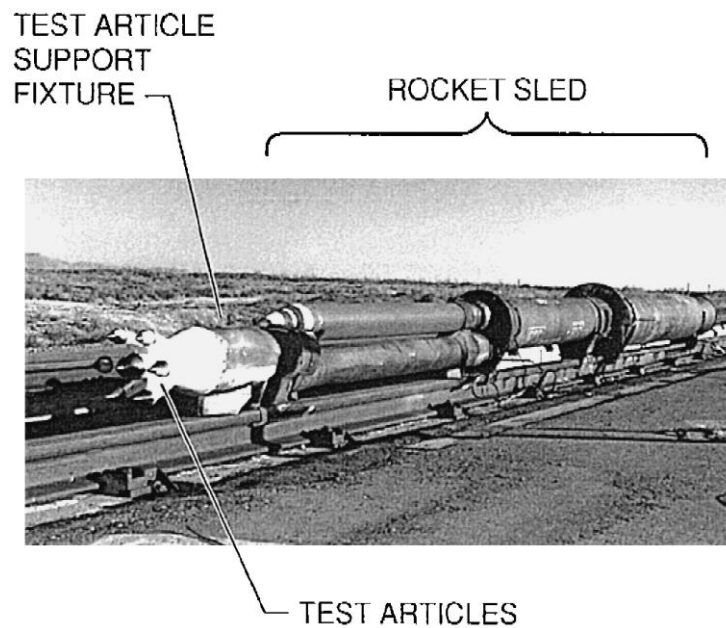


Figure 3.16 – The rocket sled used at Holloman air base [63].

A large body of WDE research was conducted by the Cavendish Laboratory, Cambridge using Single Impact Jet Apparatus (SIJA) [7], [11], [66]–[73], [16], [29], [46], [51], [53], [59], [64], [65]. The advantages of this method are being able to study the effects of single jet impacts, that high velocities can be achieved ($1200 \text{ m}\cdot\text{s}^{-1}$), and that the apparatus are relatively simple. However the nature of small droplet impacts is not well replicated, particularly the repeated nature of impacting droplets.

More recently, the Cavendish Laboratory have utilised another set-up, firing a test sample through a high velocity jet stream, which produces lateral jets, stress waves and cavitation [51].

Pulsed jet test rigs have been utilised to mimic the SIJA high velocity, rounded-front “slugs” but with a repetitive loading cycle. Figure 3.17 illustrates schematically a rig developed for EADS in which a water jet is allowed to pass through holes in a rotating disc, periodically chopping the jet into discrete pulses. A disadvantage of this set-up is that the rotating disc suffers erosion damage, parts of which may impact on the sample.

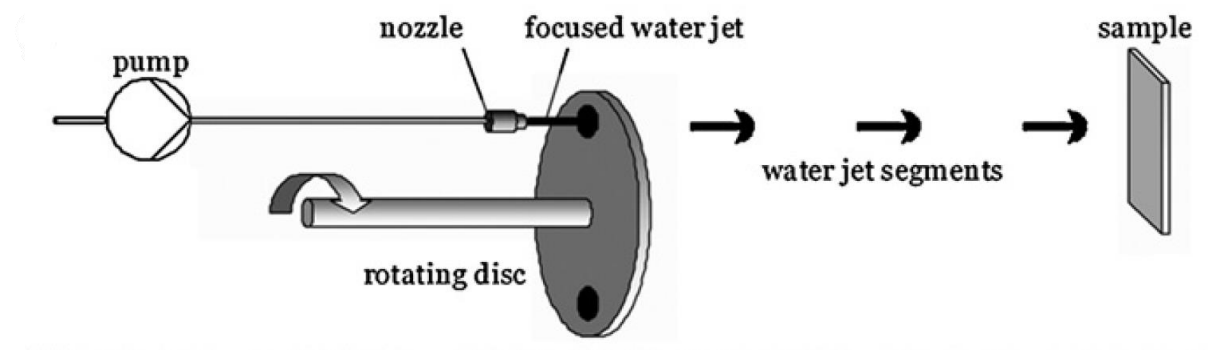


Figure 3.17 – Schematic of the pulsed jet erosion rig at EADS [14].

3.1.4 Initiation of water droplet erosion

The process of erosion is often broken down into three stages; incubation, advanced erosion and terminal erosion rate [57], [74]. Figure 3.18, below, shows that initially erosion is slow. Once incubation is overcome and advanced erosion begins, material removal rate increases sharply. The rate of erosion may decrease following advanced erosion to a more steady, terminal erosion rate.

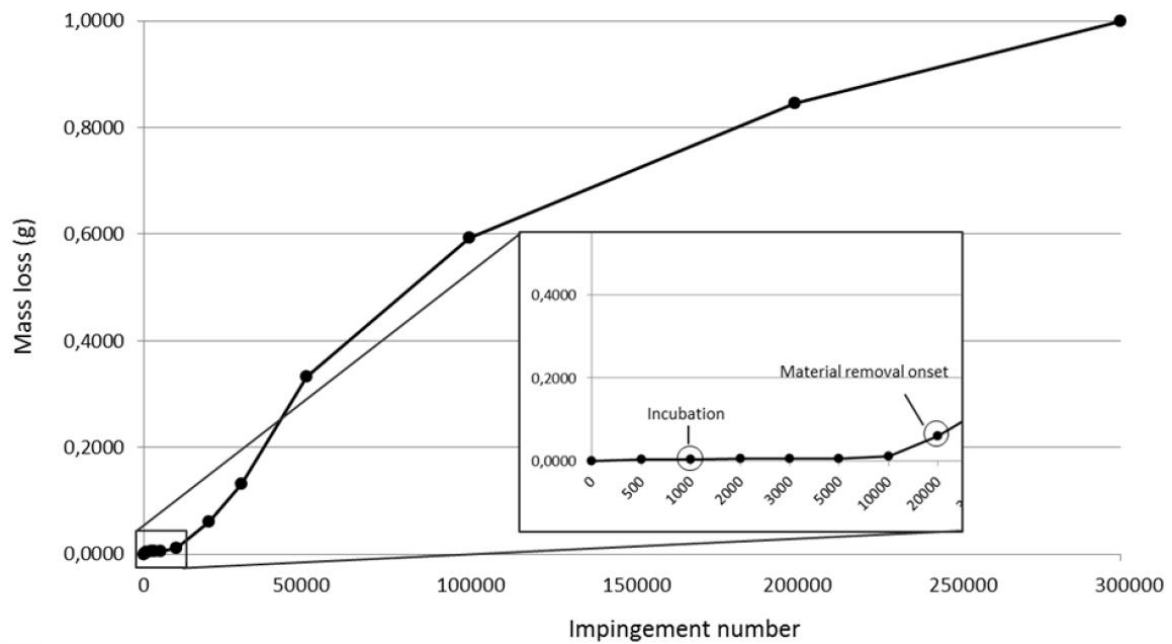


Figure 3.18 – Mass loss with “impingement number” (number of revolutions) for a whirling arm water droplet erosion test of Ti-6Al-4V at 350 m·s⁻¹ impact velocity [57].

Kamkar [57] studied the transitional period between incubation and advanced erosion in polished Ti-6Al-4V using a rotating arm test machine. For a mean droplet diameter of 0.6 mm and impact velocity of $350 \text{ m}\cdot\text{s}^{-1}$, she found initial damage in the form of raised features in an otherwise polished surface at around 1,000 arm revolutions (Figure 3.19). Some of these raised surface features contained cracks that extended in the order of hundreds of micrometres below the surface.

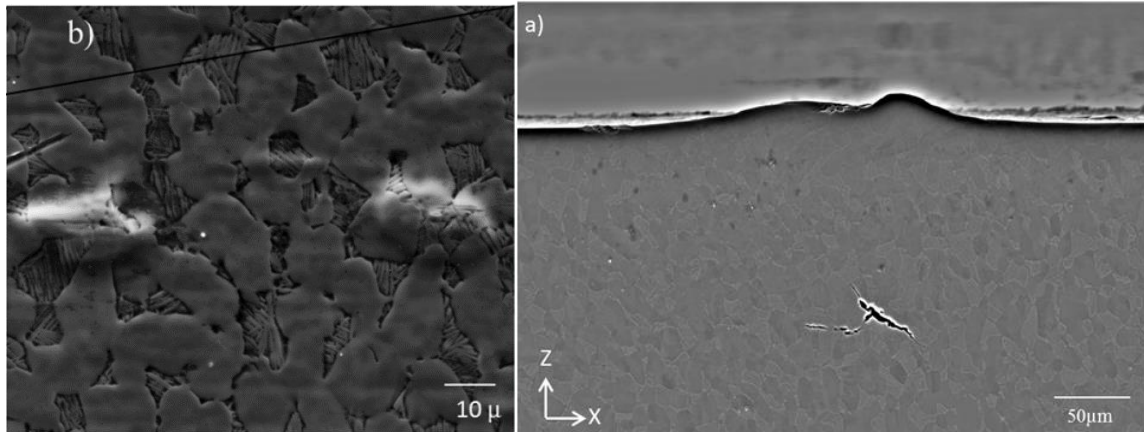


Figure 3.19 – Raised features on a Ti-6Al-4V surface after 1,000 revolutions through a water droplet stream and a subsurface crack found when FIB sectioning one [57].

Next, “grain tilting” (Figure 3.20) occurred after a total of 20,000 arm revolutions. This consists of the expected grain structure, except for slight tilting of the grains in random orientations to each other. The maximum degree of tilt in an analysed area was reported as 2.3° , which meant steps between adjacent grains.

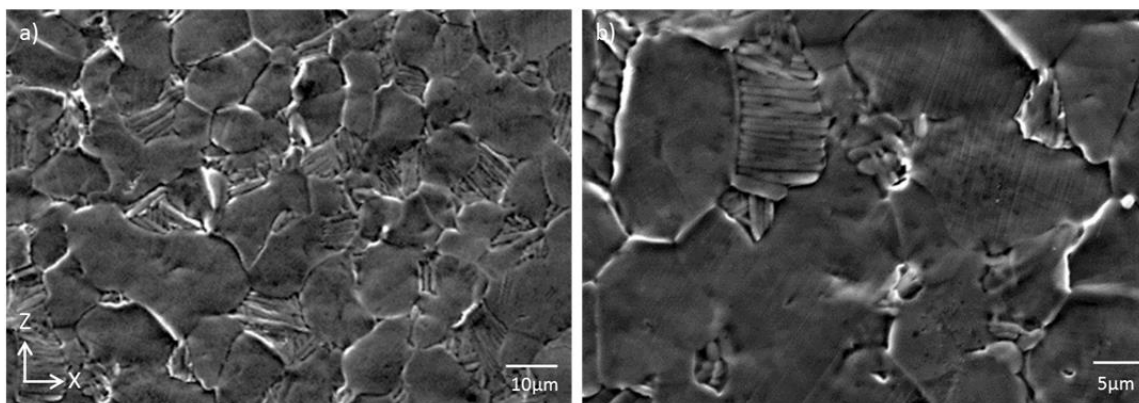


Figure 3.20 – Grain tilting of the polished Ti-6Al-4V surface after 20,000 revolutions [57].

Grain tilting had earlier been noted by Thomas & Brunton [59] and Huang, Folkes, Kinnell, & Shipway [9].

Figure 3.21 shows that minor defects at the edges of tilted grains appear to act as initiators for intergranular cracks to begin. It is hard to define when this process starts in terms of number-of-arm-rotations, as it appears to follow on from grain tilting quite rapidly.

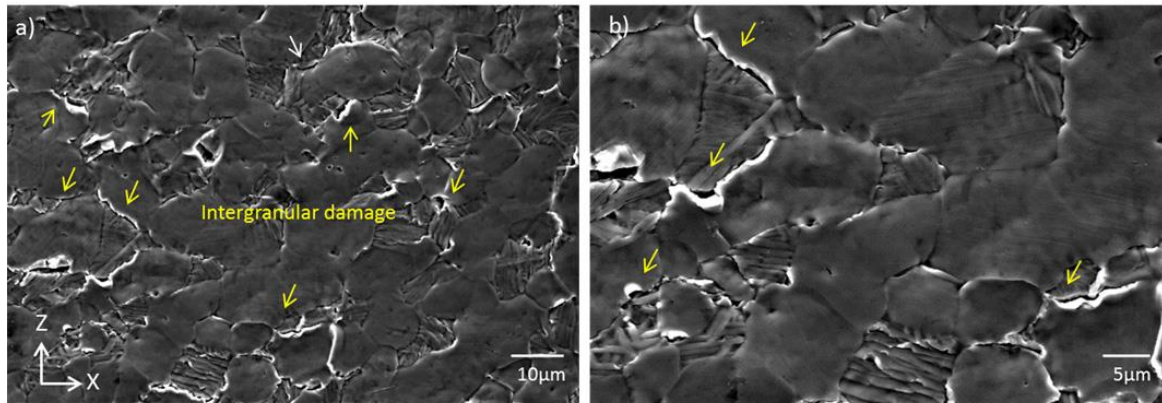


Figure 3.21 - Cracks begin to grow in between grains after 20,000 revolutions [57].

As cracks grow in length they begin to intersect one another, leading to material tearing off and micro-voids forming, as in Figure 3.22.

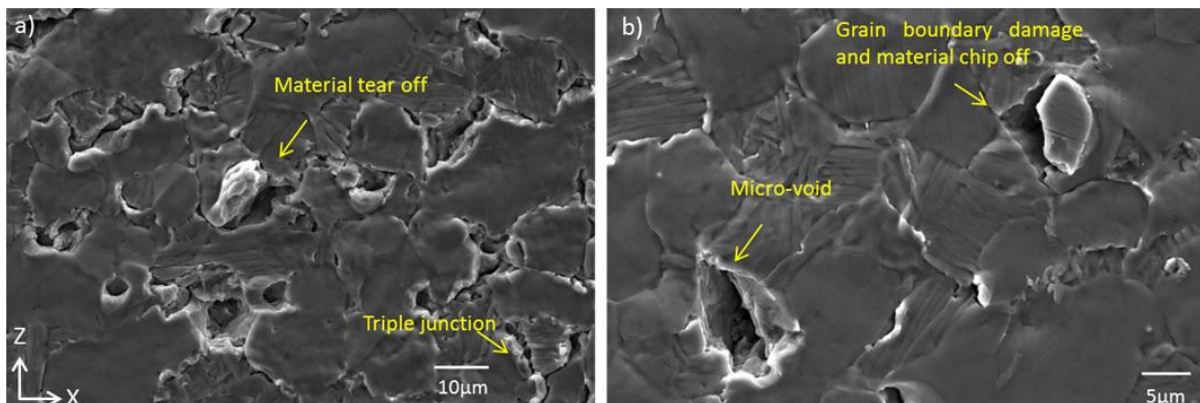


Figure 3.22 – As cracks propagate and join, small chunks of material begin to tear off leaving micro-voids [57].

It is likely that hydraulic penetration expands these micro-voids into the deep craters characteristic of advanced water droplet erosion, as Figure 3.23 shows.

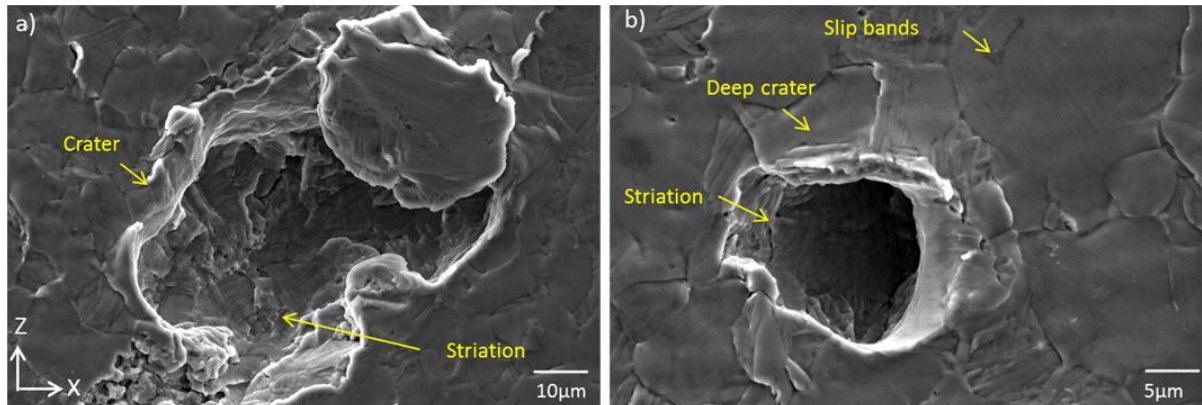


Figure 3.23 - Deep craters are formed as hydraulic penetration forces material to detach from the bulk [57].

Advanced erosion is characterised by a combination of lateral outflow jetting adding shear stresses to perpendicular surfaces, and hydraulic penetration propagating crack growth (leading to spallation) [51]. Large spalls of material are removed leaving craters 100's of micrometres in depth. Gujba et al. [75] note similar damage features to Kamkar [57] at this stage; fatigue striations and material becoming folded back and extruded, as Figure 3.24 shows. Figure 3.24 also shows slip bands observed by Ma et al. [48] in as-received Ti-6Al-4V as material is upheaved and folded back at the edges of advanced erosion craters.

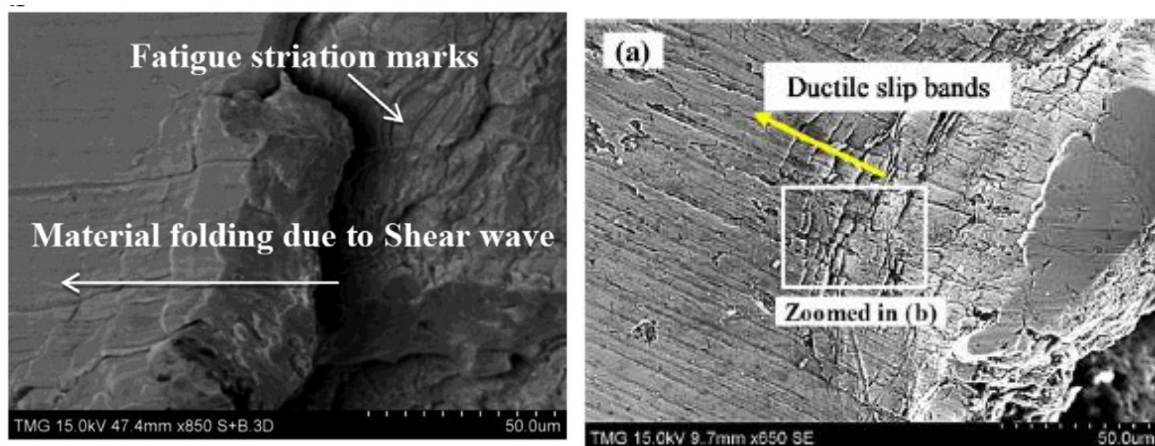


Figure 3.24 – (Left) the edge of an eroded crater in Ti-6Al-4V [75]. (Right) slip bands at the edge of an erosion crater during advanced erosion of untreated Ti-6Al-4V [48]

These craters feature “sub-tunnels” and cracks at angles of approximately 30° to the plane of the surface, as can be seen in Figure 3.25. The sub-tunnels and cracks are further eroded by hydraulic penetration in a runaway process, at which point erosion rate increases rapidly.

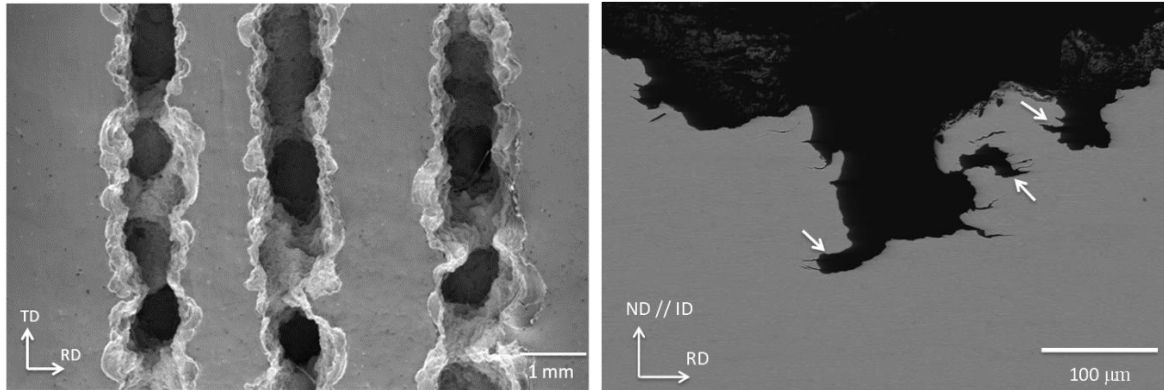


Figure 3.25 - (Left) three advanced erosion tracks caused by the three nozzles Kamkar used and (right) a cross section of an advanced erosion track highlighting sub-tunnels with arrows [57].

Mahdipoor et al. [47] notes that microstructure can influence the erosion mechanism, as Figure 3.26 shows. This suggests a simpler microstructure should be used in a study of the fundamental mechanisms of WDE. A complex microstructure might confound the interpretation of erosion damage mechanisms.

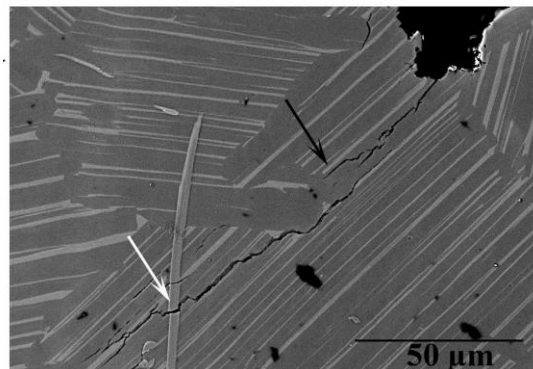


Figure 3.26 – A crack leading down at 45° from the eroded surface following the directionality of primary alpha lamellar colonies in TiAl [47].

Figure 3.27 shows another example of microstructure influencing the damage mechanisms. Two materials are tested under similar water jetting conditions. The γ -TiAl fails in a brittle manner compared to the more ductile Ti-6Al-4V.

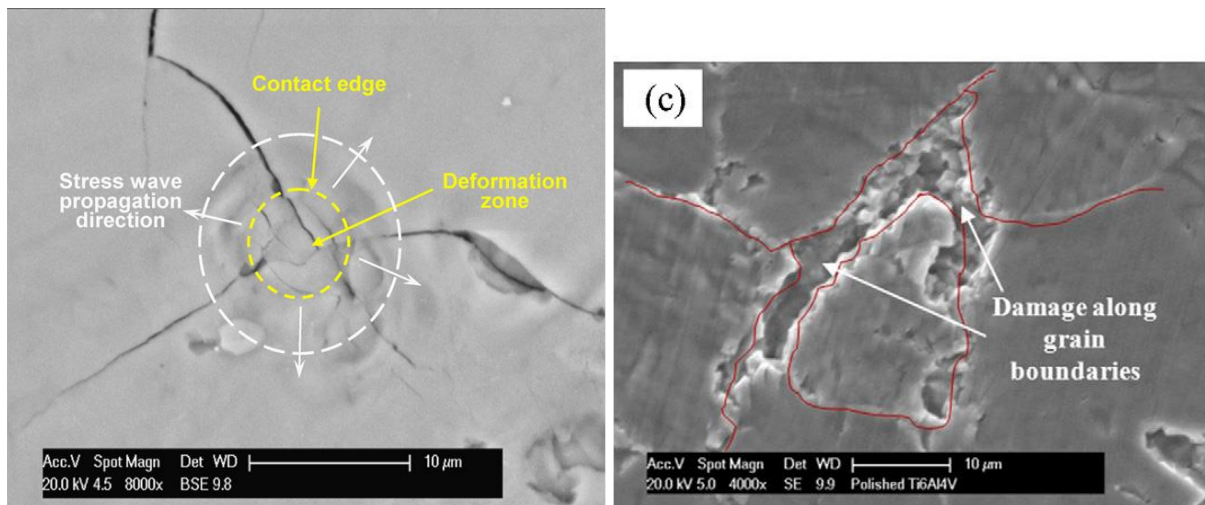


Figure 3.27 – (Left) γ -TiAl after a single pass of a 730 MPa jet [76]. (Right) Ti-6Al-4V after three passes of a 940 MPa jet [9].

Ma et al. [48] investigated the difference between as-received & deep-rolled Ti-6Al-4V, again showing that microstructure plays an important role in damage mechanisms. The cracks in the deep-rolled Ti-6Al-4V in Figure 3.28 below form transversely to the rolling direction, whereas the initial cracks seen in as-received Ti-6Al-4V above begin at grain boundaries.

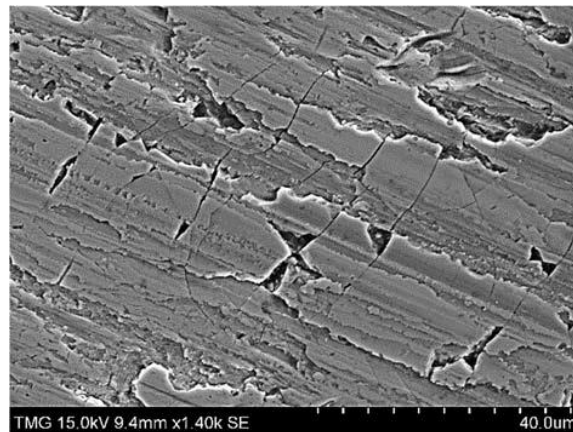


Figure 3.28 – Microcracks and micro-voids forming following initial damage in deep-rolled Ti-6Al-4V [48].

While Kamkar [57] investigated the incubation period to the point of advanced erosion, she could not establish how the initial “grain tilting” occurs. It is likely that direct deformation, stress wave propagation and cavitation begin the process of roughening

the surface and removing small amounts of material, then once surface flaws exist, hydraulic penetration and lateral outflow jetting rapidly remove material. How the primary mechanisms cause grain tilting, slip bands, twinning, surface depressions, raised surface features, and subsurface cracks in the incubation stage is less clear. The purpose of the work reported in this Thesis is to try to elucidate some of these early-stage mechanisms for titanium alloys.

3.2 Experimental methods

In this Thesis, WDE tests were performed on a rotating arm rig which was built in accordance with ASTM G73, located at National Physical Laboratory (NPL), Teddington, UK. The set-up is illustrated by Figure 3.29.

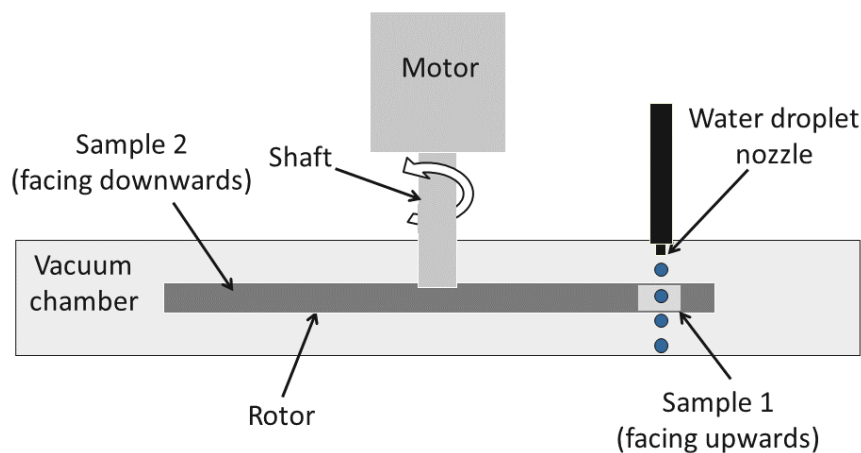


Figure 3.29 – Plan-view schematic of the rotating arm test rig at NPL.

The rotor is 1m in diameter. Two samples are tested at once; secured at either end of the rotor. Frictional heating of the rotor by the air has limited other test rigs in the literature to subsonic speeds, so the chamber is evacuated to attain tangential velocities greater than the speed of sound in air. The partial vacuum also serves to draw water out of the nozzle. The plan was to keep the nozzle size constant for consistency in the tests. The nozzle is discussed below in “Characterisation of droplet size”. High frame-rate photography has been used to confirm that droplets do indeed impinge on the surface, rather than a continuous jet. Coupons are a wedge shape in order to fit into dovetail slots in the rotor, as illustrated by Figure 3.30. This minimises fixturing stresses.

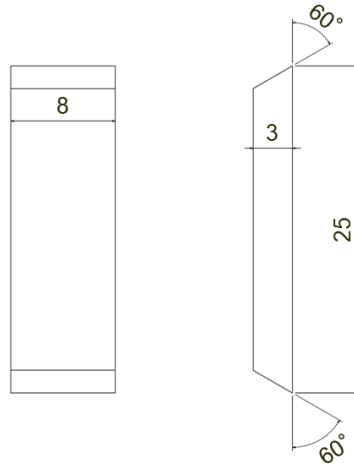


Figure 3.30 - Water Droplet Erosion test coupon dimensions (in mm).

Initially, the plan was to run WDE tests for the different alloys and various grain sizes in long-term tests, through the incubation period and well into advanced erosion, to produce the characteristic erosion rate S-curve. This is obtained by running an erosion test then interrupting it at constant time intervals to weigh the coupons [74]. Shorter term tests within the incubation period could then be planned, to investigate initiation mechanisms of erosion.

Table 3.1 illustrates the test plan for different erosion exposure time and materials, although not all planned tests were completed.

Material	Number of impacts	Time in rig			Tested?	Total coupons	Coupons left
		Hrs	Mins	Secs			
Ti-15Mo (RD 90°)	155,531,456	36			✓	4-off	1-off
	4,320,318	30			✓		
	248,626	5			✓		
Ti-15Mo (RD 0°)	8,288	10			✓	4-off	3-off
	24,863	30			x		
Ti-15Mo (TD)	155,531,456	36			x	4-off	2-off
	9,017	10.88			✓		
	49,725	1			x		
Ti-6Al-4V (RD 90°)	2,983,512	30+30			✓	5-off	3-off
	2,983,512	30+30			✓		
	24,863	30			x		
	49,725	1			x		
	99,450	2			x		
Ti-6Al-4V (RD 0°)	155,531,456	36			✓	5-off	2-off
	149,176	3			x		
	497,252	10			✓		
	12,950	10.48			✓		
Ti-6Al-4V (TD)	12,950	10.48			✓	7-off	4-off
	149,176	3			x		
Ti-6Al-4V (annealed 500µm) (RD 0°)	9,017	10.88			✓	6-off	4-off
	8,288	10			✓		
	248,626	5			✓		
	497,252	10			✓		

Table 3.1 – Water droplet erosion test plan.

The coupon surfaces were highly polished, to minimise the effect of surface roughness on the WDE incubation period (in previous testing, it was found that damage tended to follow the lay produced by machining [30]).

Surface speed was held constant at $300 \text{ m}\cdot\text{s}^{-1}$, as this was high enough to ensure pure erosion (rather than some mixture of corrosion-erosion) and accelerated damage incubation, reducing overall test length. As-received Ti-15Mo, as-received Ti-6Al-4V and Ti-6Al-4V annealed to $500 \mu\text{m}$ grain size were tested.

3.2.1 Characterisation of droplet size

Droplet sizes for a variety of nozzle diameters were characterised using a high-speed camera and strobe-light set-up. Figure 3.31 is two such images.

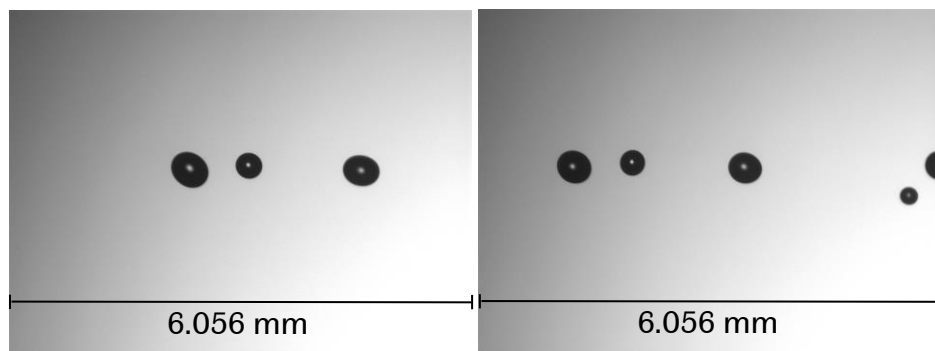


Figure 3.31 – Two sequential photos of droplets travelling from right to left. Field of view is 6.056mm in width. Taken 100 microseconds apart.

Initially, a single brass nozzle was available which was not changed, to ensure consistent test methods. This had previously been characterised to produce an average droplet size of $\sim 300 \mu\text{m}$. It was thought the diameter was originally specified to be $160 \mu\text{m}$, though this was not measured at the time of initial droplet characterisation.

Figure 3.32 is an image of the original brass nozzle. The diameter is larger than the original specification was thought to be. The average droplet diameter was 317 μm . One week later the droplet measurement system was reassembled and the average droplet size was measured to be 590 μm . It is possible that the nozzle bore was cleaned between these measurements, which might account for the large variation in measured droplet diameters.

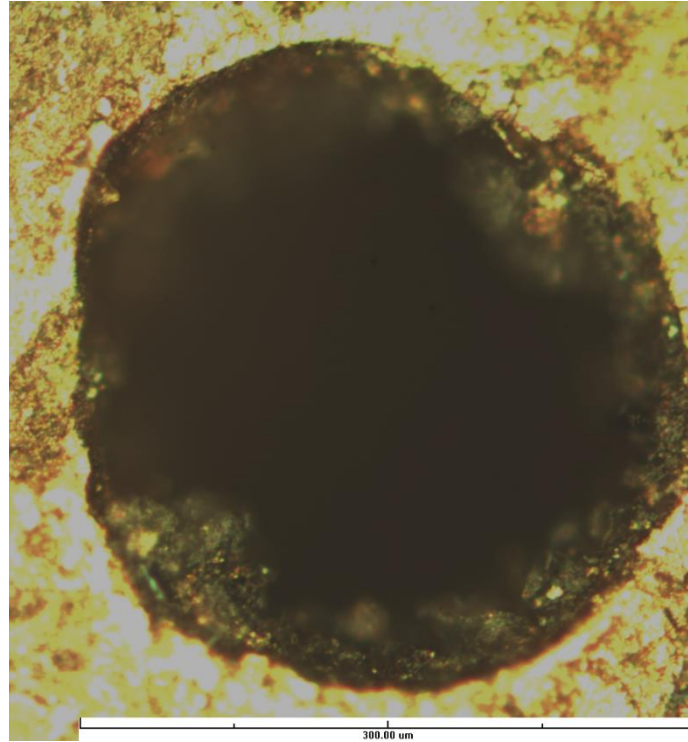


Figure 3.32 – Original brass nozzle with some corrosion product or other debris inside the bore (300 μm scale bar).

Using the width of the field of view and the time interval between photos it is possible to calculate droplet speed as $5.10 \text{ m}\cdot\text{s}^{-1}$. At the top rotational speed of 5730 rpm, there is 5.24 ms between rotor passes. Water droplets travel 27 mm in 5.24 ms. This means the droplet stream is replenished to cover the 8 mm width of the samples between impacts. For an average of 4.46 droplets per frame and a field of view of 6.06 mm, on average 5.89 droplets impact an 8 mm wide coupon per rotation.

Due to corrosion and other debris interrupting the flow, and a long-term goal for the equipment to produce droplets of other sizes, other nozzle sizes were then manufactured. To begin with, stainless steel tubes used for the manufacture of medical syringes were cut to length by EDM and held in an aluminium housing using adhesive. Figure 3.33 is one such nozzle manufactured from 150 μm stainless steel tube, the closest available diameter to the 160 μm diameter specification the brass nozzle was

thought to be originally. Altering the distance from the nozzle to the measurement location, the stand-off distance (S.D.), means droplet size changes somewhat. Droplet diameters at a S.D. of 70 mm were an average size of 369 μm – closest to those of the original brass nozzle.

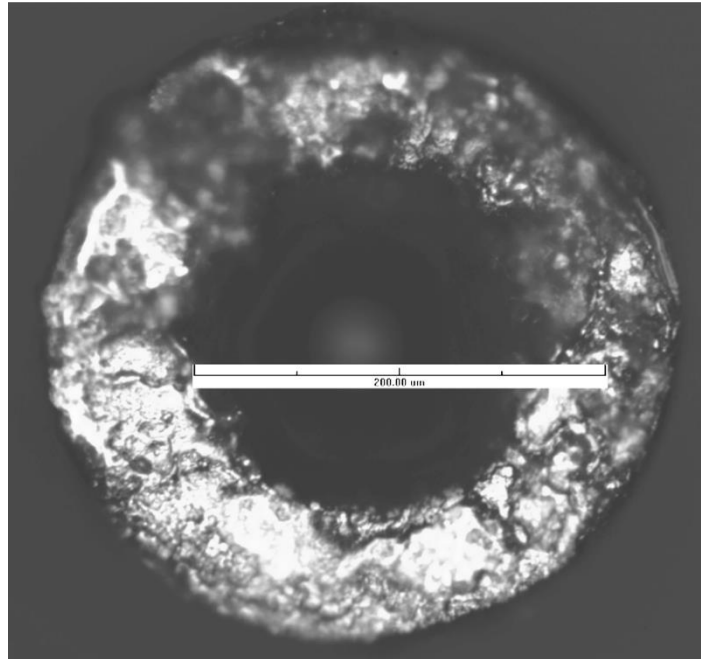


Figure 3.33 – 0.15 mm stainless steel syringe nozzle (200 μm scale bar).

However, the medical syringe nozzles suffered flow issues, which was realised to be due to a an excessively high length-to-diameter ratio. A thin sheet “diaphragm” nozzle was developed to avoid this issue. Figure 3.34 is a 0.16 mm diameter hole in a 0.5 mm thick sheet. A 140 mm S.D. produced 284 μm diameter droplets – closest to the size the original brass nozzle delivered. There was an average of 1.054 droplets per mm, so the average number of impacts across the 8 mm wide sample per rotor revolution is 8.43.

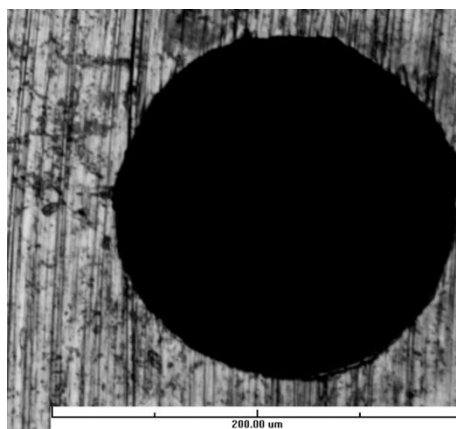


Figure 3.34 – 0.16 mm “diaphragm” nozzle (200 μm scale bar).

3.3 Analysis

Analysis of mass loss was achieved by weighing the test samples at periodic time intervals, as described in ASTM G73 [74]. Plotting the mass loss with exposure time gives an indication of how well a material performs in water droplet erosion. The erosion rate graph is then useful for identifying the incubation period.

Analysis of the tested coupons was conducted by a number of microscopy techniques such as optical, focus variation optical (e.g. Alicona), secondary electron (SEM), and electron backscatter diffraction (EBSD). EBSD is of particular interest here, since it does not appear to have been used previously in the literature to evaluate samples post-WDE testing.

3.4 Results

3.4.1 Advanced erosion – 36 hours Ti-15Mo & Ti-6Al-4V

Initially, the two as-received alloys, Ti-15Mo & Ti-6Al-4V, were tested in a long duration, 36-hour test, which equates to approximately 7.28×10^7 droplet impacts at $300 \text{ m}\cdot\text{s}^{-1}$. Mass measurements were taken every two hours. This established the erosion rate “S-curves” for the two alloys, illustrated in Figure 3.35. These tests were conducted with the original brass nozzle, which was likely to have produced droplets of average diameter $317 \mu\text{m}$, and an average of 5.89 droplet impacts per sample rotation.

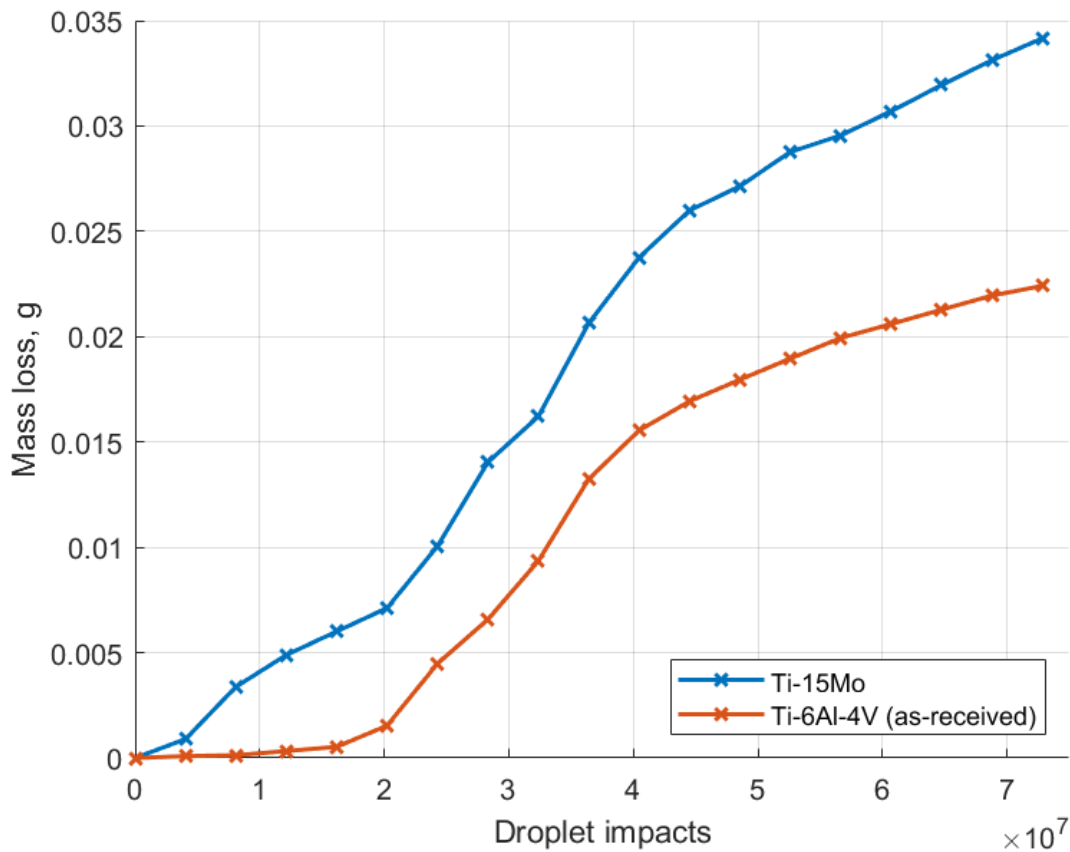


Figure 3.35 – Mass loss with WDE exposure time for the two as-received alloys, Ti-15Mo & Ti-6Al-4V.

Although the overall mass loss was greater for Ti-15Mo than for Ti-6Al-4V in the 36-hour test, the incubation period, advanced erosion and subsequent terminal erosion rates occurred at similar times during the testing.

The wear scar runs across the entire 8 mm width of coupon. The wear craters are 1-2 mm deep. Figure 3.36 shows a photograph of as-received Ti-6Al-4V following the test.

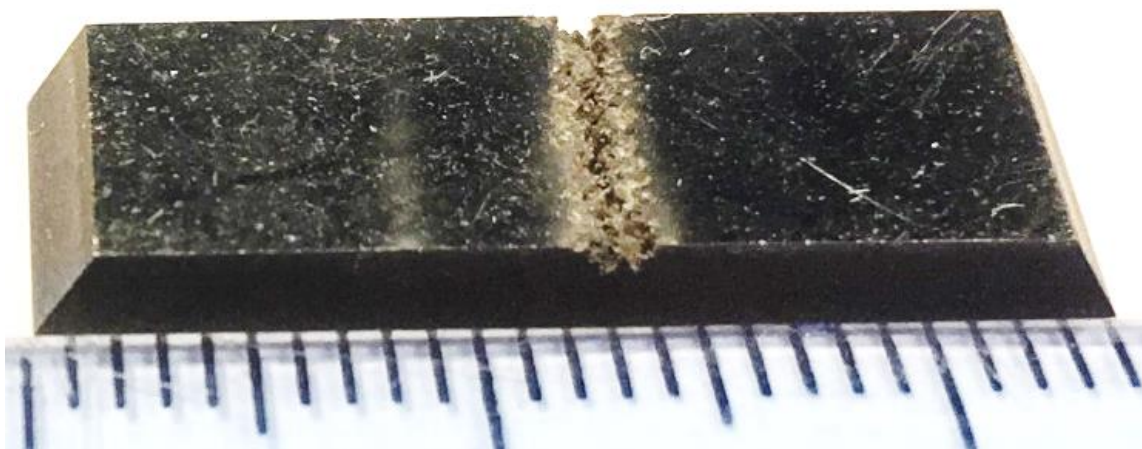


Figure 3.36 Photograph of as-received Ti-6Al-4V after 36 hours of exposure to WDE, with millimetre graduated ruler.

Figure 3.37 shows an optical micrograph of the wear scar, imaged using Alicona focus variation optical microscopy.

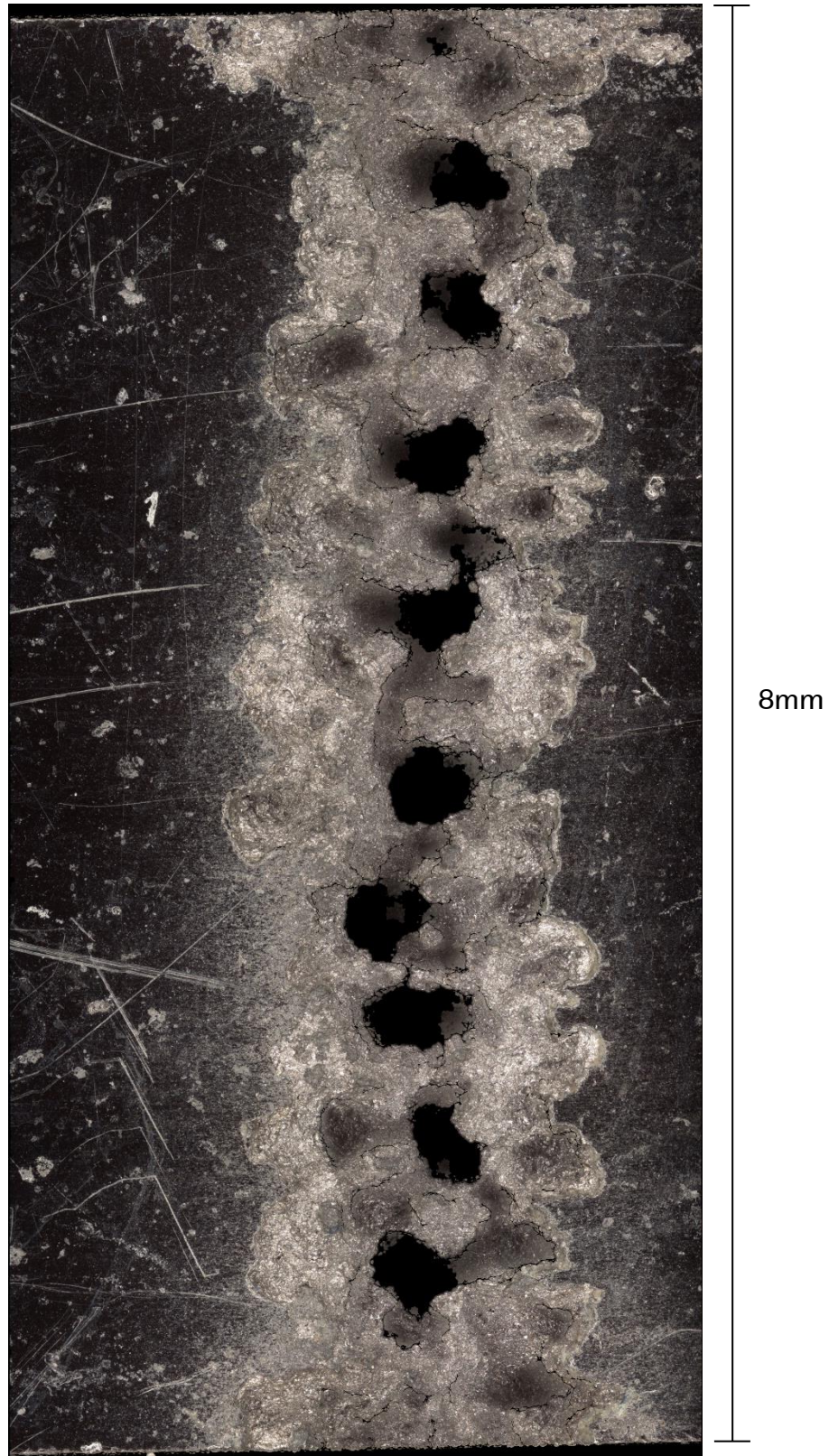


Figure 3.37 – Alicona image of as-received Ti-6Al-4V after 36 hours of exposure to WDE. The image is across the entire 8 mm coupon width.

Figure 3.38 is a SEM image of the erosion scar in Ti-6Al-4V following the 36-hour test.

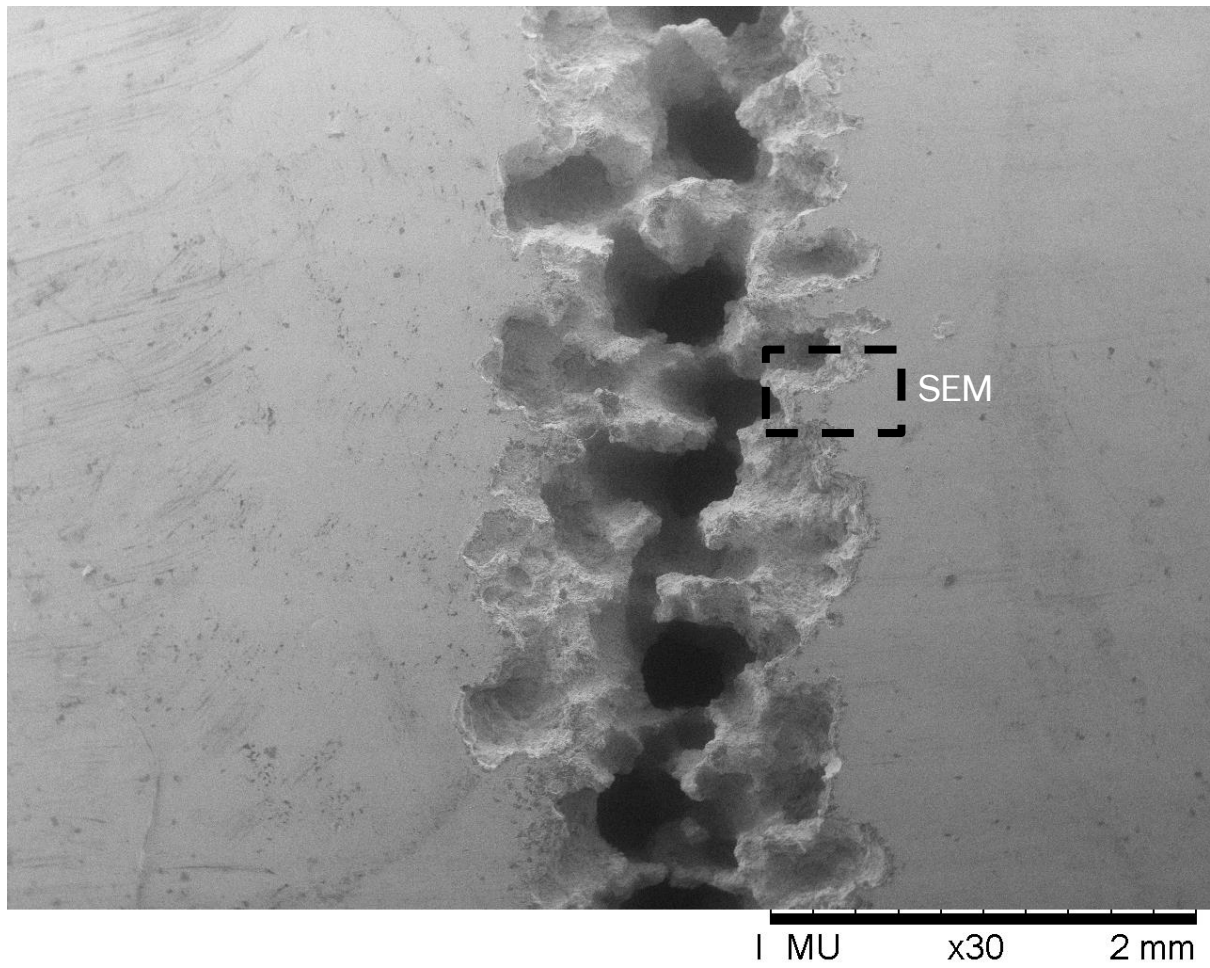


Figure 3.38 – SEM image of as-received Ti-6Al-4V after 36 hours of exposure to WDE. An area is circled where higher magnification analysis was investigated further.

Looking more closely at the edges of the erosion scar in Figure 3.39 below reveals rough fractured surfaces. A brittle failure is perhaps expected from the predominantly alpha-phase Ti-6Al-4V, which is the more strain-rate sensitive alloy of the two tested samples.

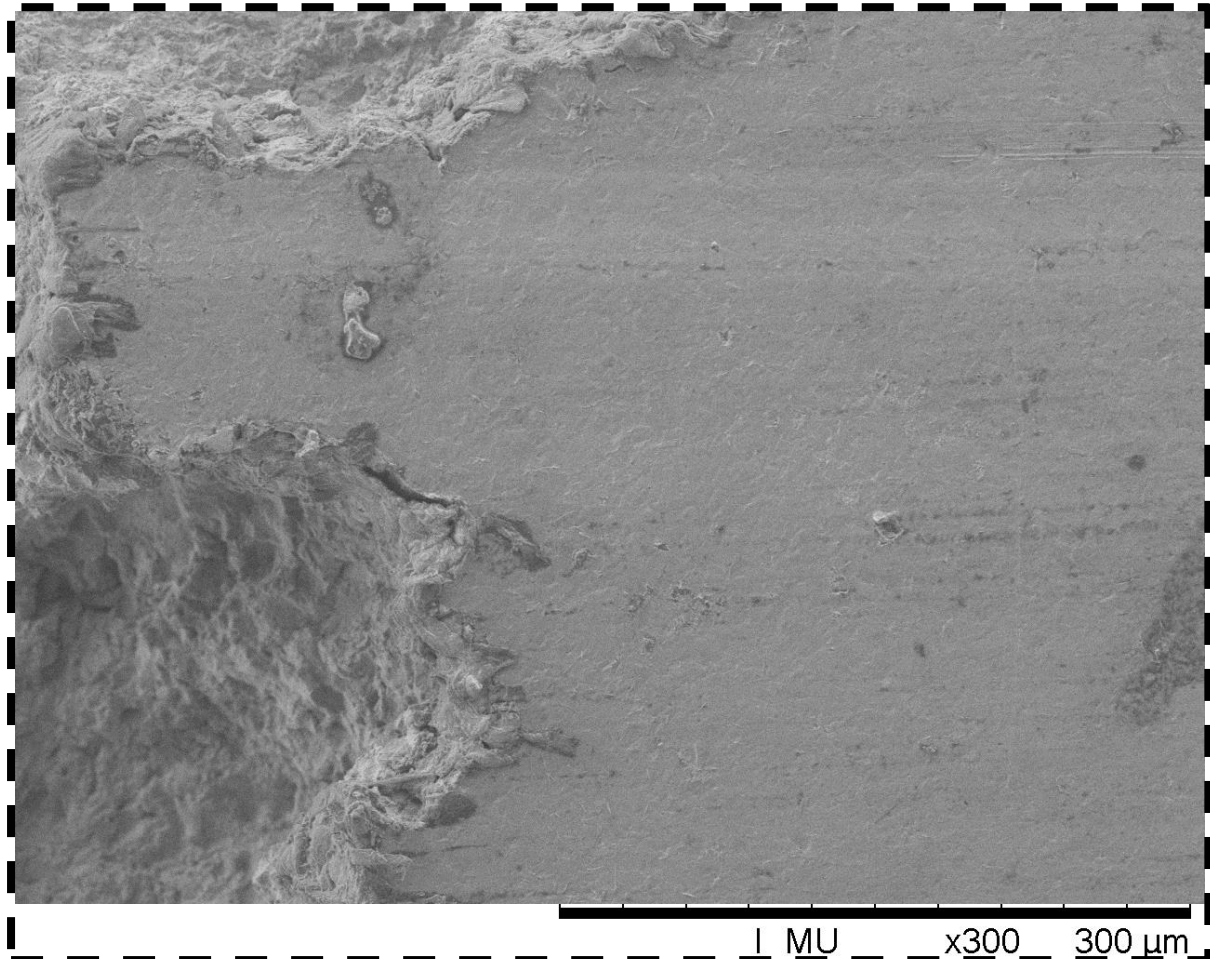


Figure 3.39 – SEM image of as-received Ti-6Al-4V after 36 hours of exposure to WDE.

Figure 3.40 is an Alicona image of the other alloy, the as-received Ti-15Mo, following 36 hours WDE.

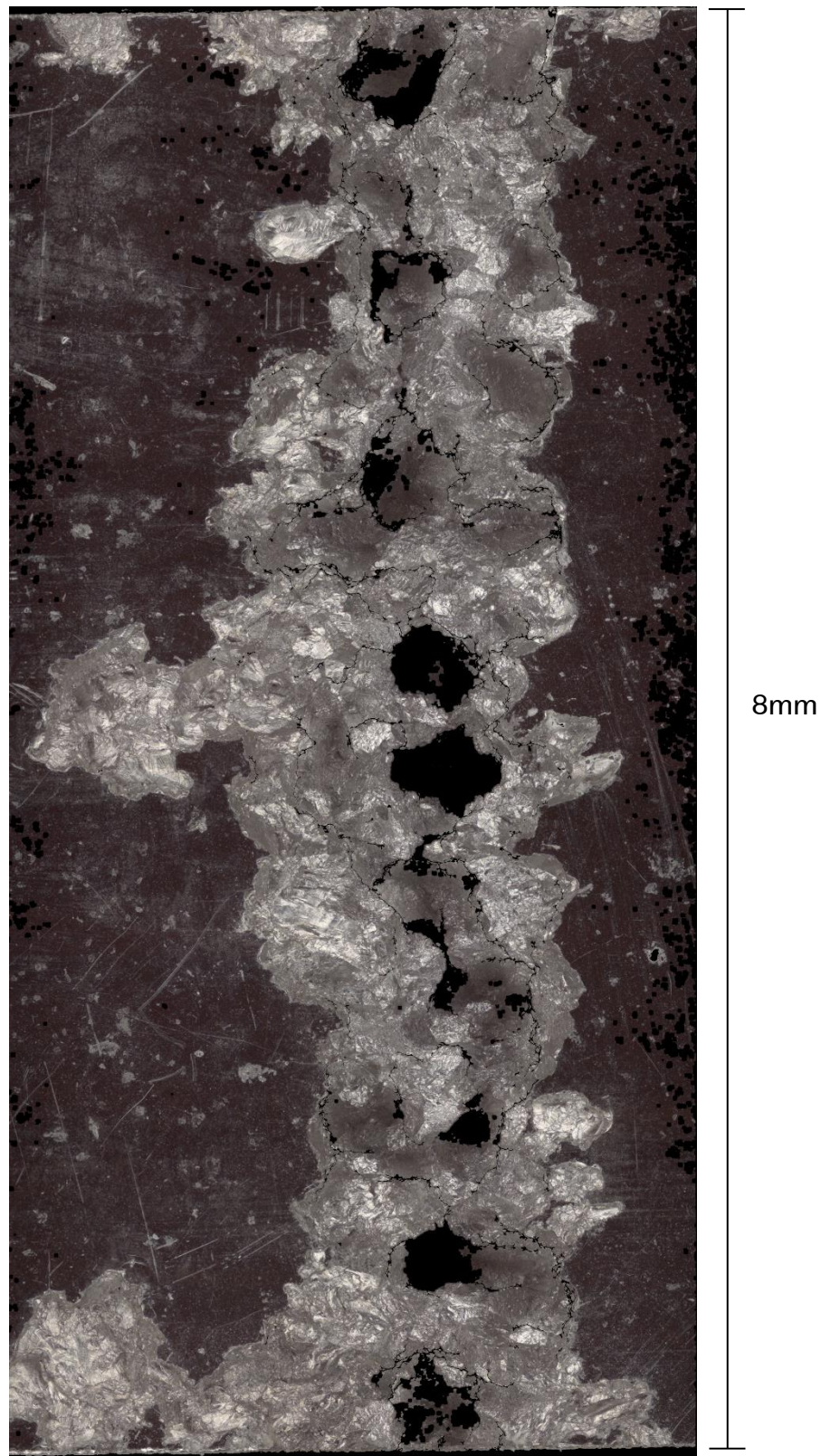


Figure 3.40 – Alicona image of as-received Ti-15Mo after 36 hours of exposure to WDE. The image is across the entire 8mm coupon width.

An SEM image of the Ti-15Mo coupon is shown in Figure 3.41.

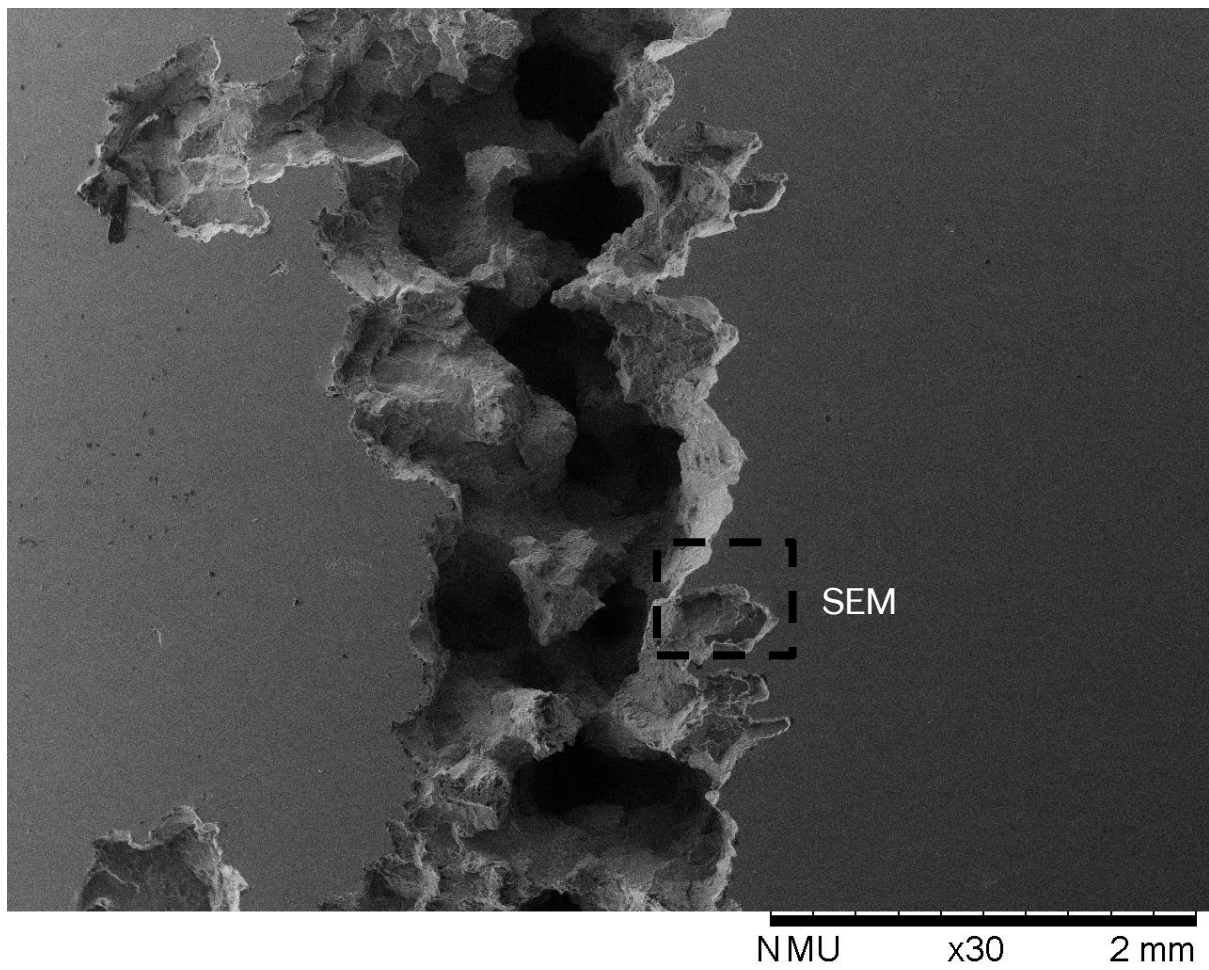


Figure 3.41 – SEM image of as-received Ti-15Mo after 36 hours of exposure to WDE. An area is marked where higher magnification was conducted.

Fatigue striations can be observed in the higher magnification SEM image at the wear scar edge in Figure 3.42. Cracks have expanded gradually and material at the edges is upheaved and folded back, similar to results in the literature, as in Figure 3.24. This more ductile failure mode (than Ti-6Al-4V) could reasonably be expected of the beta-phase alloy.

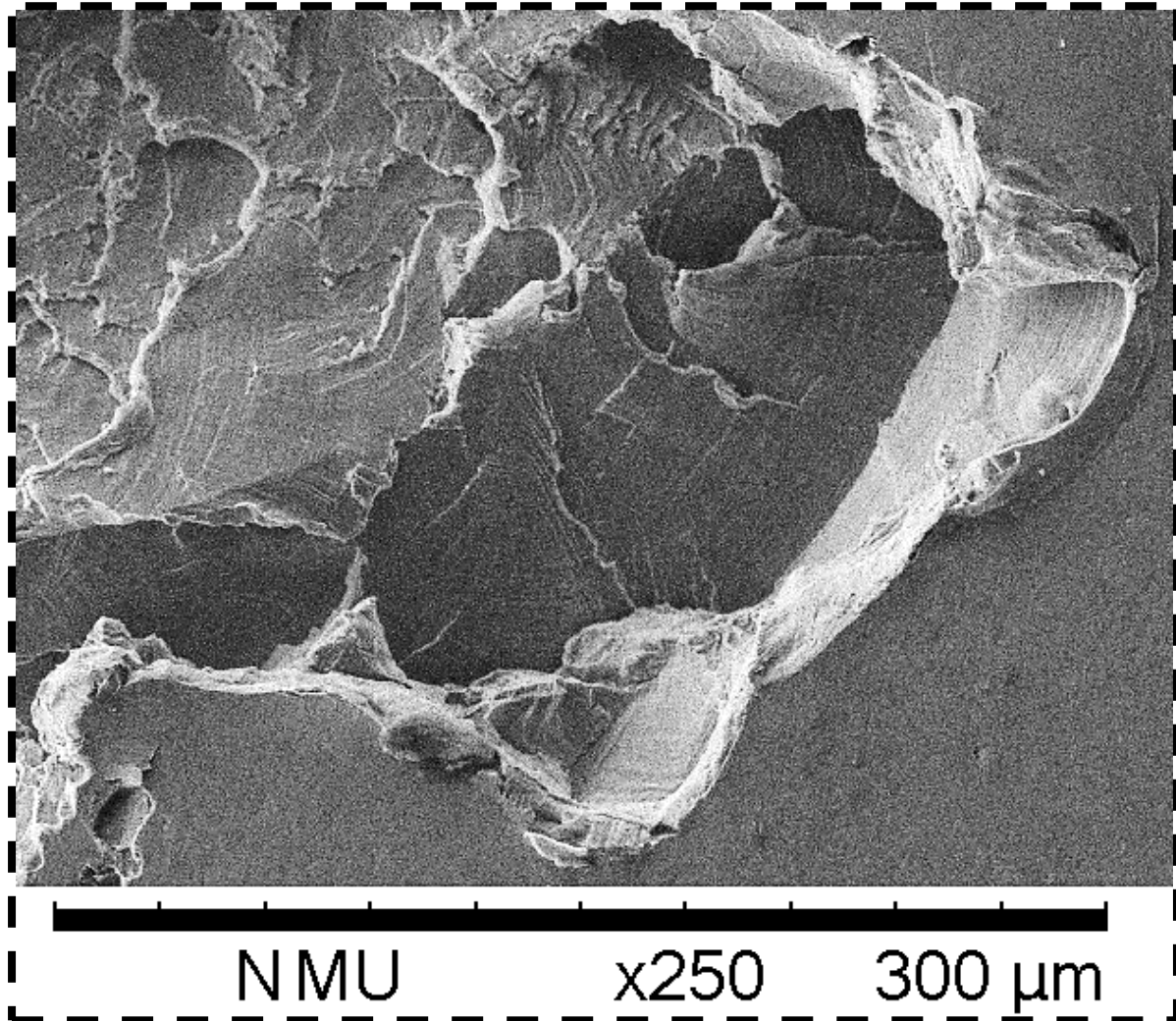


Figure 3.42 – SEM image of as-received Ti-15Mo after 36 hours of exposure to WDE.

The Ti-15Mo sample was mounted in cross-section to the erosion track and polished, as demonstrated in Figure 3.43.

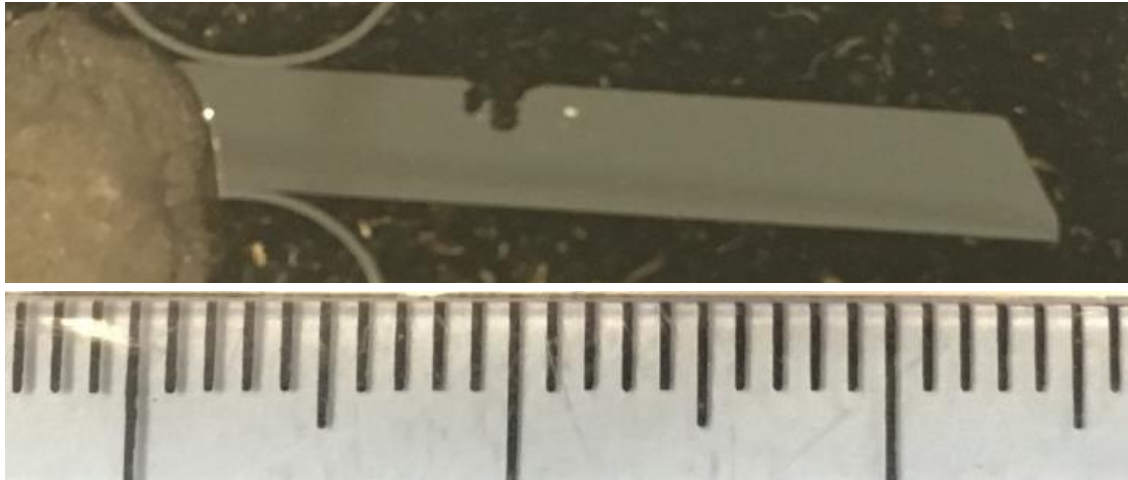


Figure 3.43 – Photograph of 36-hour WDE Ti-15Mo sample mounted and polished, with millimetre graduated ruler.

Figure 3.44 indicates where EBSD scans were conducted on the sample and illustrates how the sample appears upside-down, due to the detector imaging arrangement.

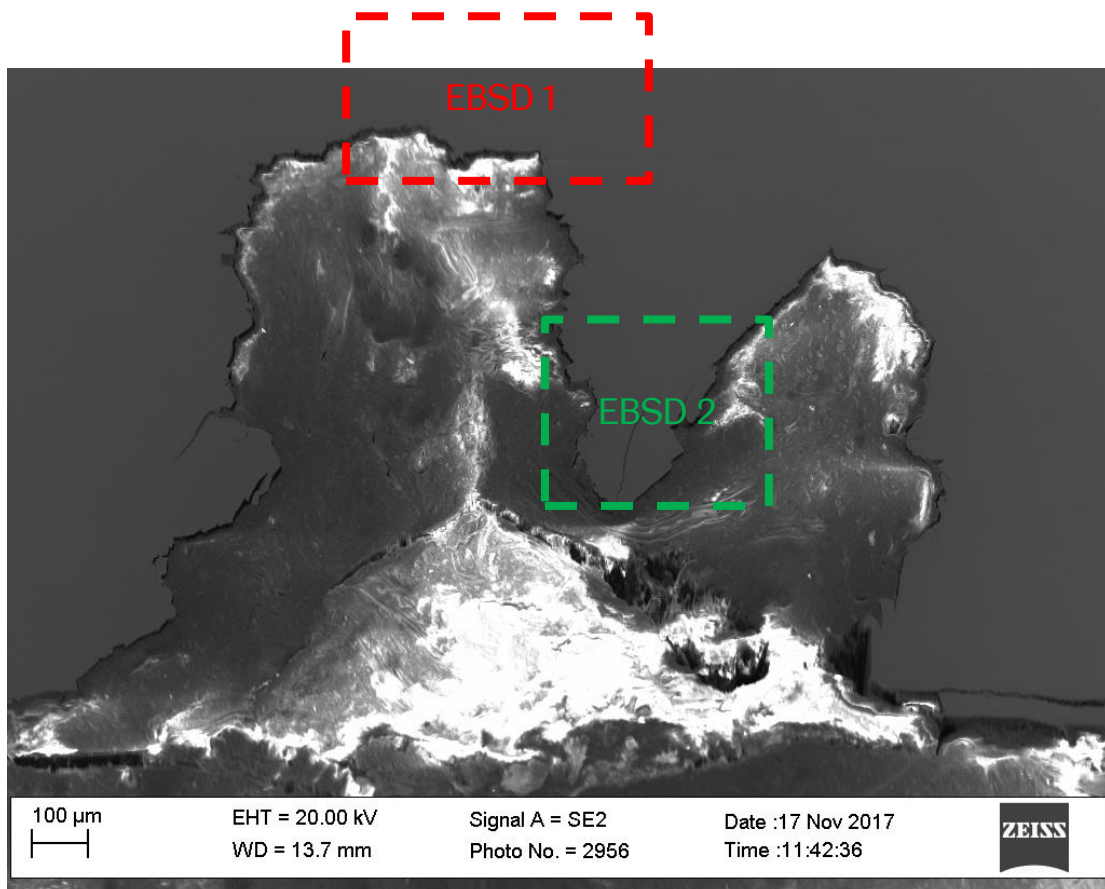


Figure 3.44 – SEM image showing EBSD scan regions of 36-hour WDE Ti-15Mo sample.

The post-processed results from “EBSD 1” in Figure 3.44 are shown Figure 3.45 below. The Image Quality (IQ) map demonstrates where indexing was poor in darker regions. Since grain boundaries are difficult to index, they show up clearly. The Inverse Pole Figure (IPF) shows how grains are oriented. This can aid in tracking damage, such as how a crack interacts with the microstructure. There are significant artefacts (coloured in pink) around the grain boundaries and at the crater edge in a region of non-conductive mounting compound. This suggests the artefact is due to a poor background acquisition when setting up the scan. A small region where several different grain orientations coalesce is highlighted “EBSD 3”, where further analysis was conducted.

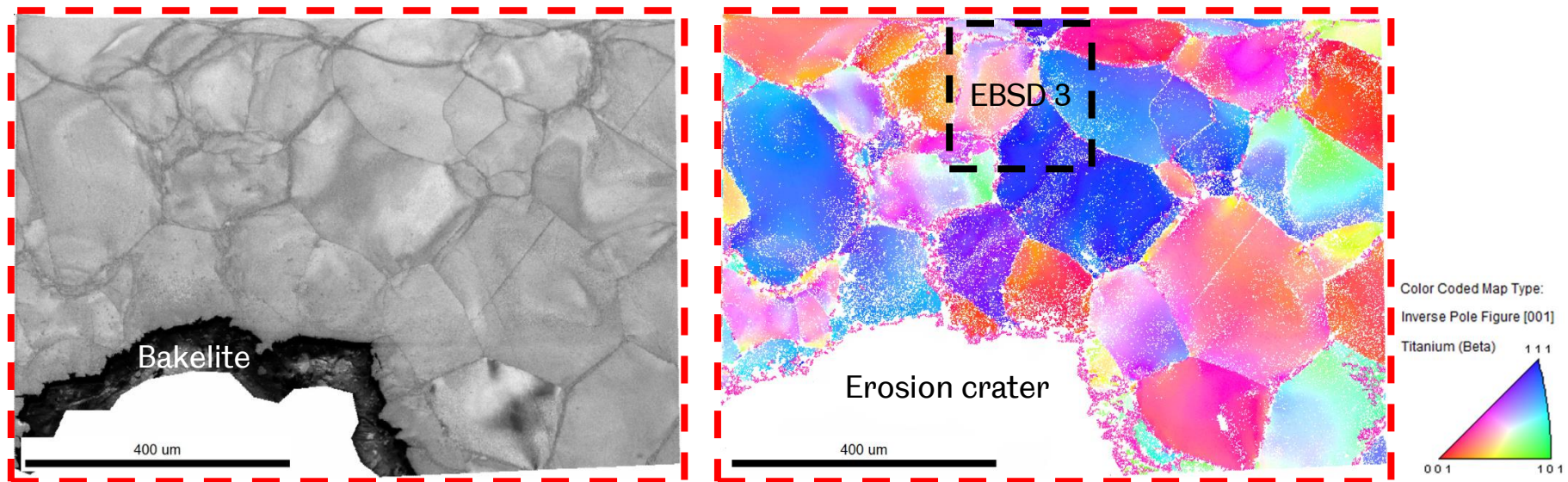
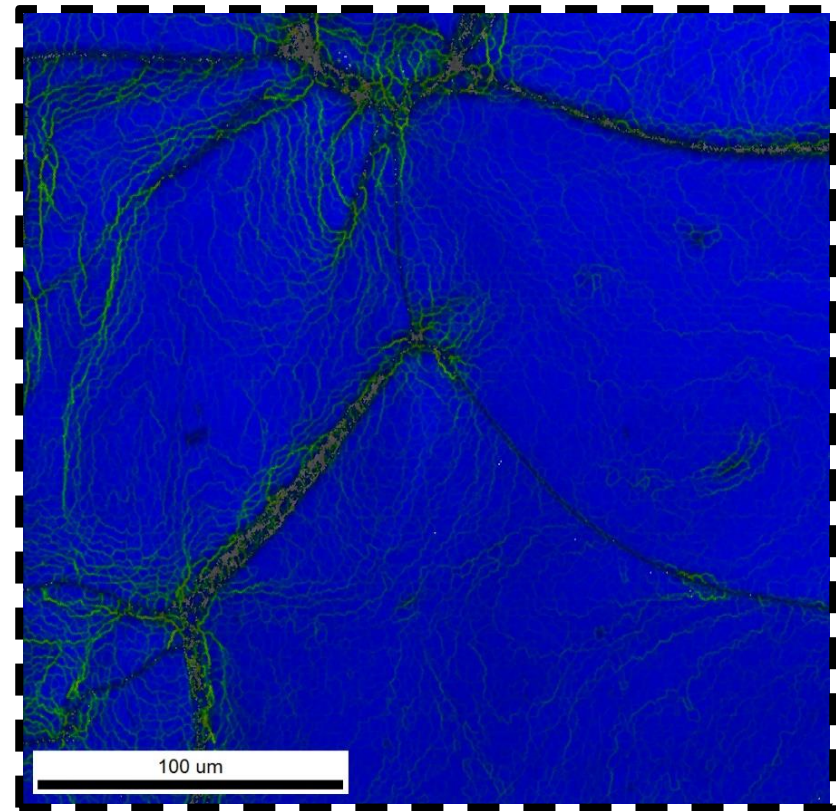


Figure 3.45 – IQ and IPF for 36-hour WDE Ti-15Mo sample, scanned with a 4x4 binning rate and a step size of 1.5 μm . Grains of less than 2 pixels removed.

The results of a higher resolution scan of the “EBSD 3” region from Figure 3.45 are shown in Figure 3.46. The IPF and misorientation map show sub-grains and misorientation, particularly at grain boundaries, but these are common in the untested as-received Ti-15Mo.



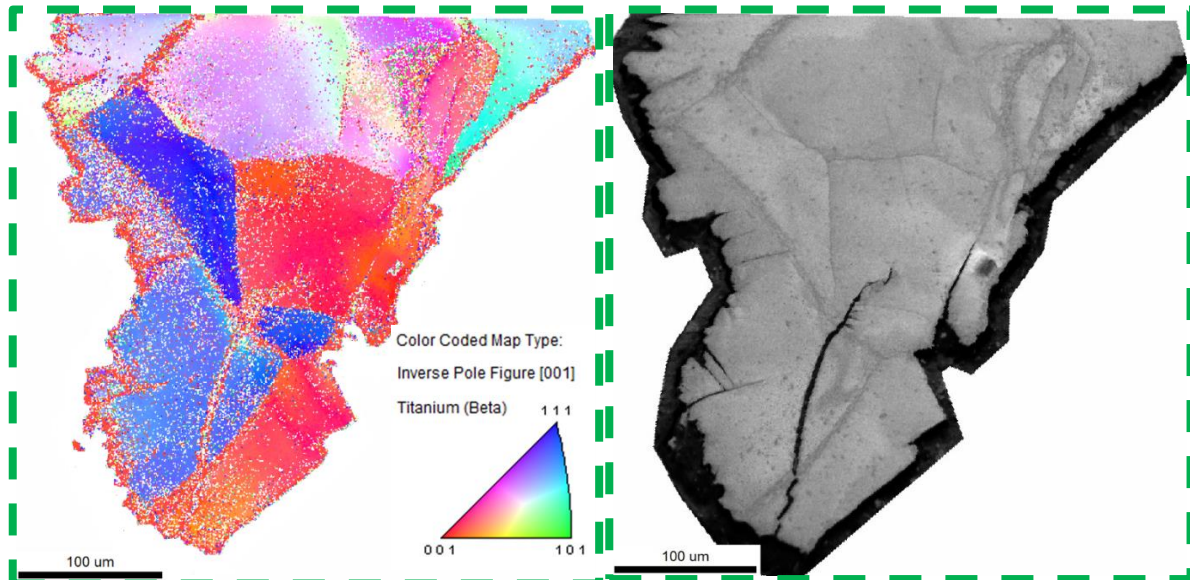
IPF



Misorientation map of the scan using Kernel Average 1st neighbour. Data cleaned up by Kuwahara filter applied to first neighbour for two iterations. Grains of size less than 5 pixels removed. Overlaid on IQ map.

Figure 3.46 – IPF and Misorientation map for 36-hour WDE Ti-15Mo sample, scanned with a 2x2 binning rate and a step size of 0.5 μm.

A crack tip (marked “EBSD 2” in Figure 3.44) was investigated further. The resulting IPF in Figure 3.47 shows poor indexing, particularly at grain boundaries and in the surrounding mounting compound, with red artefacts from a poor background acquisition.

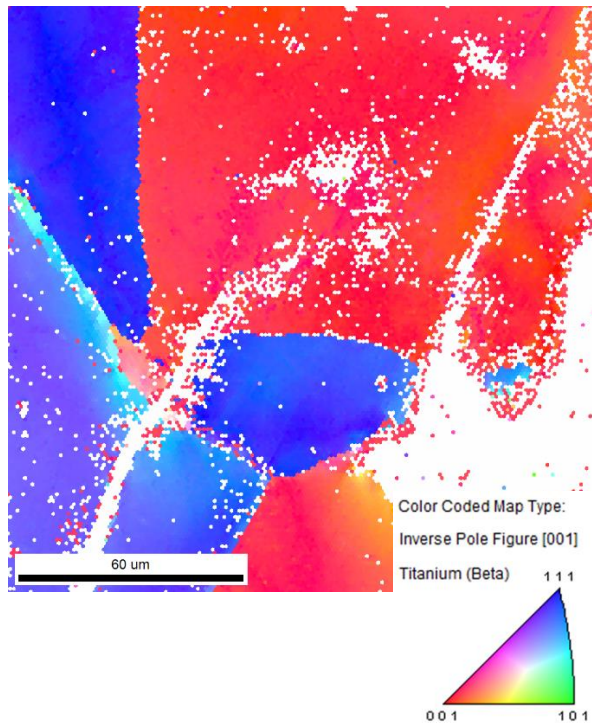


IPF. Pixels of less than 0.005 confidence index removed. Scale bar 100 µm.

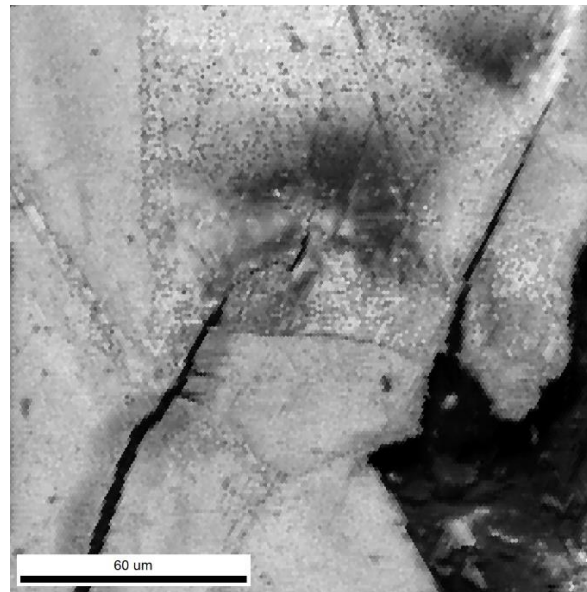
IQ. Scale bar 100µm.

Figure 3.47 – IPF and IQ map for 36-hour WDE Ti-15Mo sample, scanned with a 4x4 binning rate and a step size of 1 µm.

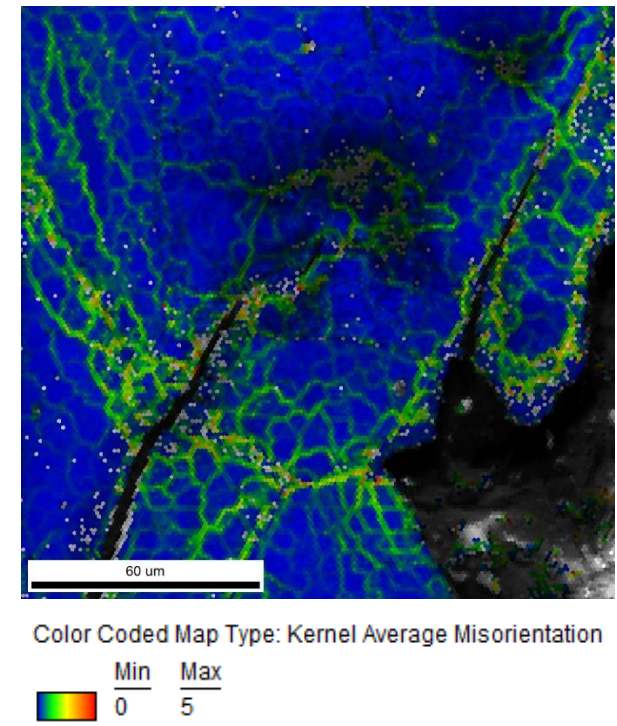
A higher resolution scan was performed by utilising a smaller step size. The results are illustrated in Figure 3.48. However there was poor indexing around the crack, and at the tip - a particular region of interest.



IPF. Pixels of less than 0.025 confidence index removed. Scale bar 60 μm.



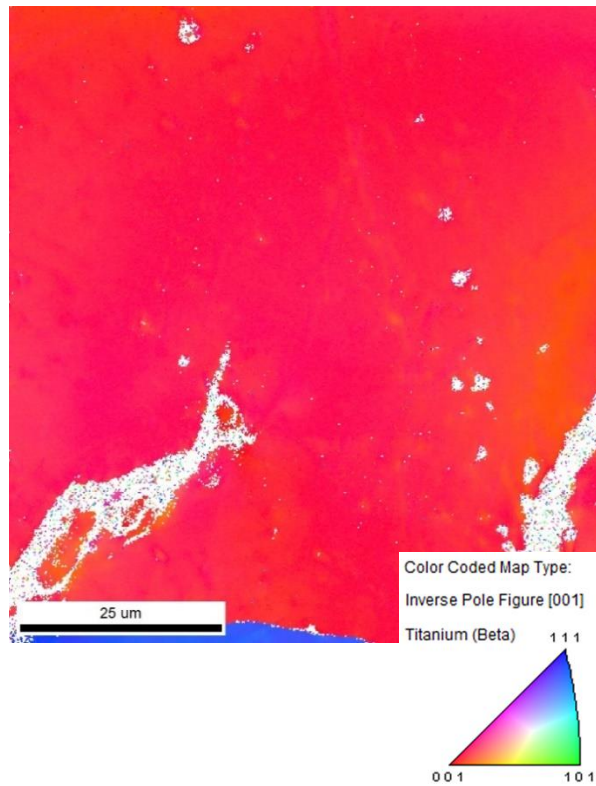
IQ. Scale bar 60 μm.



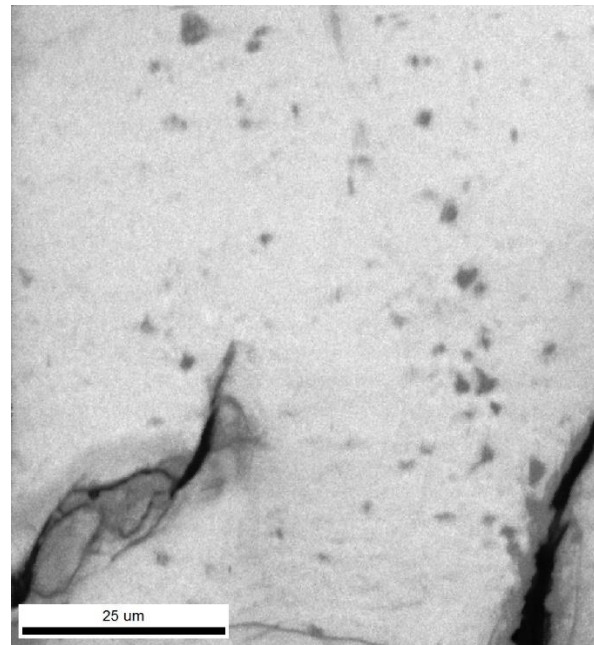
Misorientation map of the scan using Kernel Average 1st neighbour. Data cleaned up by Kuwahara filter applied to first neighbour for two iterations. Grains of size less than 5 pixels removed. Overlaid on IQ map. Scale bar 60μm.

Figure 3.48 – IPF and Misorientation map for 36-hour WDE Ti-15Mo sample, scanned with a 2x2 binning rate and a step size of 1 μm.

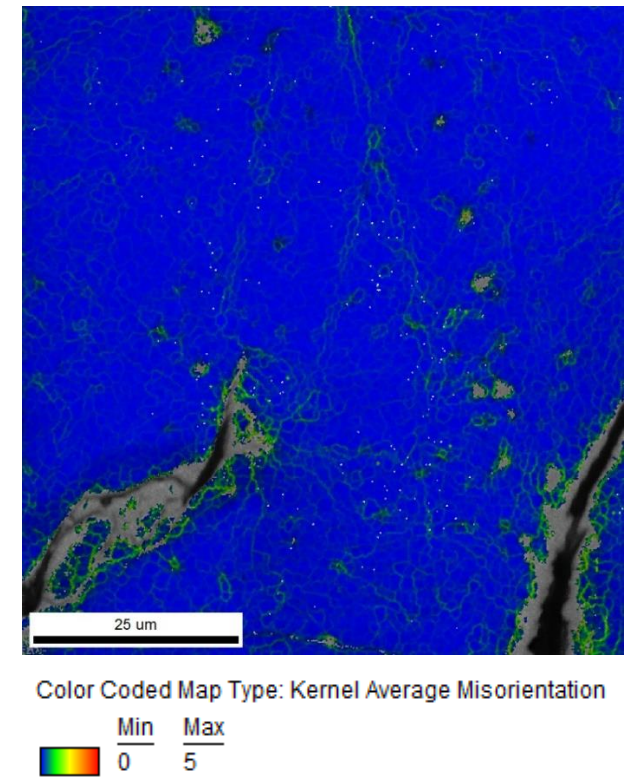
With a smaller step size of 0.2 μm , a higher resolution scan was possible. The results in Figure 3.49 show the indexing has been improved. There does not appear to be any significant misorientation at the crack tip driving its growth. Background acquisition was obtained at a location in the bulk of the material, with no surrounding bakelite mounting compound, which may have helped reduce artefacts.



IPF. Pixels of less than 0.01 confidence index removed. Scale bar 25 μm.



IQ. Scale bar 25 μm.



Misorientation map of the scan using Kernel Average 1st neighbour. Data cleaned up by Kuwahara filter applied to first neighbour for two iterations. Grains of size less than 5 pixels removed. Overlaid on IQ map. Scale bar 25 μm.

Figure 3.49 – IPF and Misorientation map for 36-hour WDE Ti-15Mo sample, scanned with a 4x4 binning rate and a step size of 0.2 μm.

3.4.2 Incubation period

The long-duration test established the erosion “S-curves” for the alloys. This helps identify where the incubation period ends for the alloys and advanced erosion begins. Shorter-duration tests were conducted to investigate material behaviour in the incubation period. In the literature, similar whirling-arm tests performed on Ti-6Al-4V with 600 μm droplets at $350 \text{ m}\cdot\text{s}^{-1}$ found deformation from 1000 rotations, as shown in Figure 3.19 earlier [57]. For the 1 m diameter rotor used in this work, 1000 rotations corresponds to only 10 seconds of exposure when running at top speed (5730 rpm, or $300 \text{ m}\cdot\text{s}^{-1}$ tangential velocity).

3.4.3 10 seconds as-received Ti-6Al-4V

As-received Ti-6Al-4V was tested for 10 s with a 0.16 mm diameter, 0.5 mm thick sheet “diaphragm” nozzle. At a S.D. of 140 mm, droplets produced were an average of 284 μm in diameter. The number of droplet impacts per coupon rotation was 8.43. The total number of droplet impacts for the exposure time was ~ 8700 . There was no measurable mass loss with the $\pm 10^{-5}$ g precision mass balance used. Figure 3.50 shows a light microscope image of the erosion scar, characterised by small dark speckles and lines. A region is highlighted where further SEM and EBSD analysis was done.

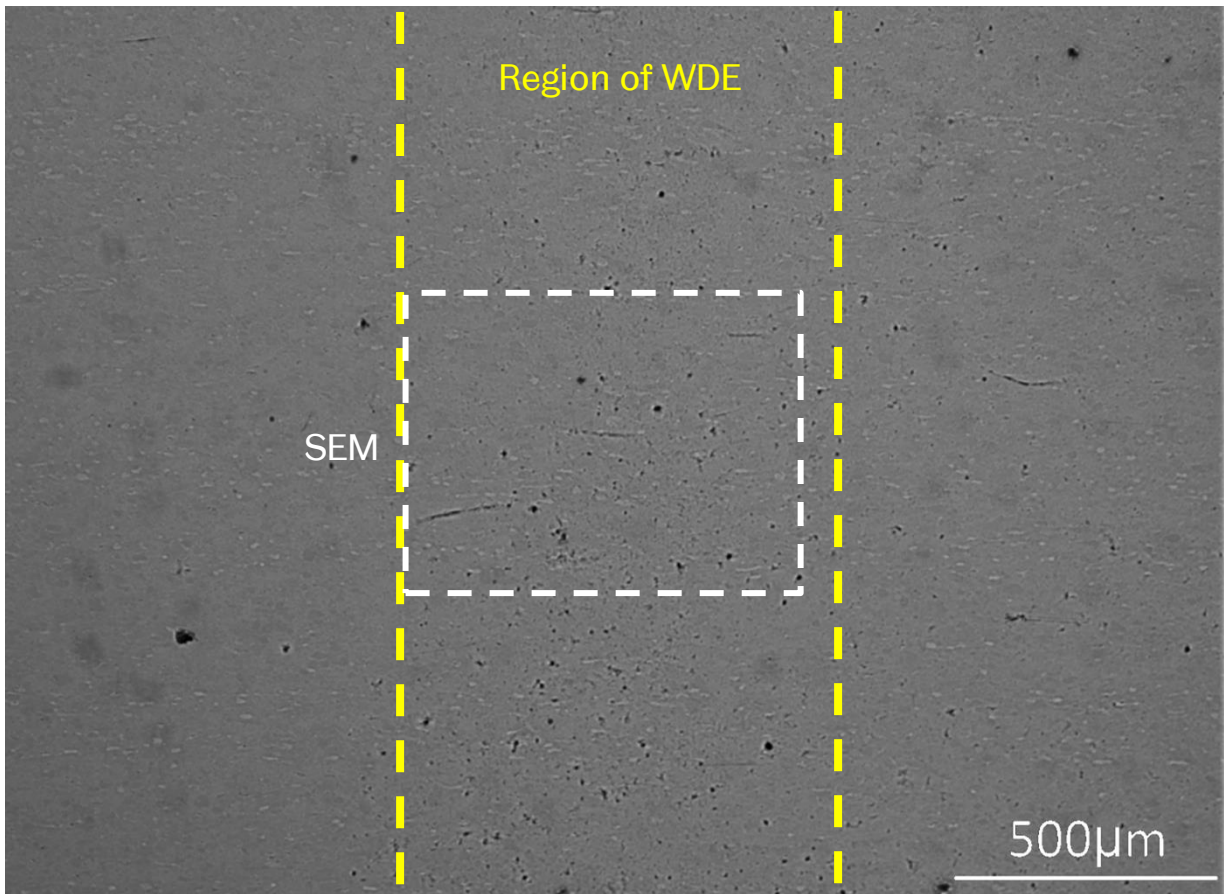


Figure 3.50 – Erosion wear scar in as-received Ti-6Al-4V RD following 10 s exposure to WDE.

Figure 3.51 is a higher magnification SEM image of the region highlighted in Figure 3.50 within the erosion scar. Certain features become easier to identify, such as micropits and indentations.

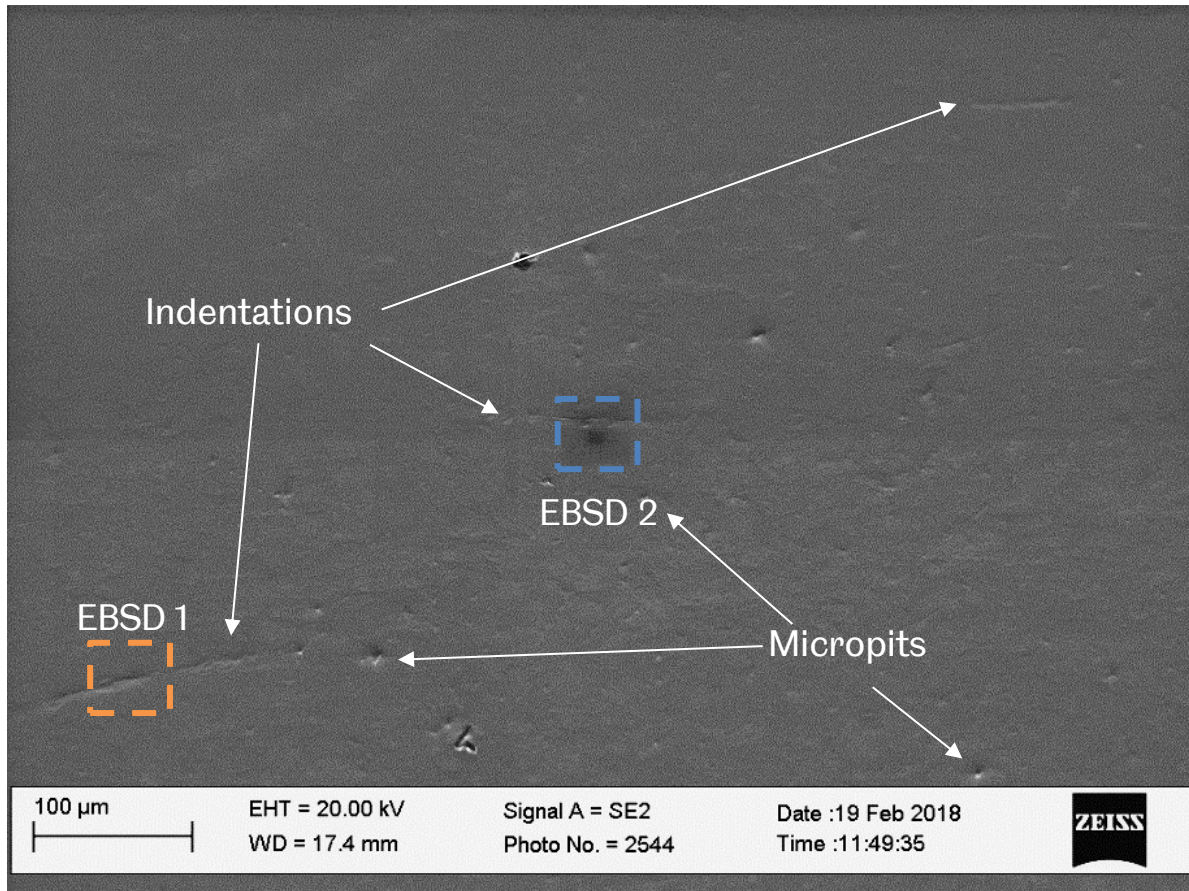
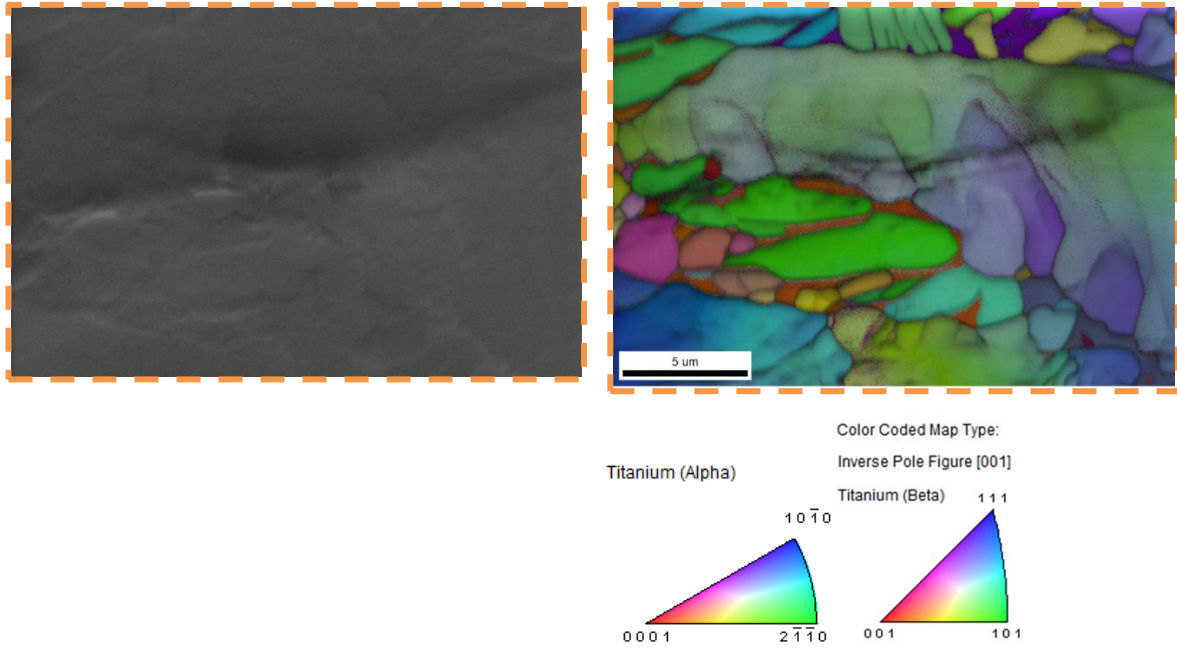


Figure 3.51 – SEM image of deformation features in erosion wear scar in as-received Ti-6Al-4V RD following 10 s exposure to WDE. .

EBSD was conducted on the left most indentation observed in Figure 3.51 (labelled EBSD 1). A higher magnification SEM image in Figure 3.52 shows the indentation in a little more detail. The IPF of the same region is also shown in Figure 3.52. Part of the indentation runs across a large (>20 μm) grain. Elongated grains like these are expected in this orientation of the material, as the coupon was cut parallel to the rolling direction.

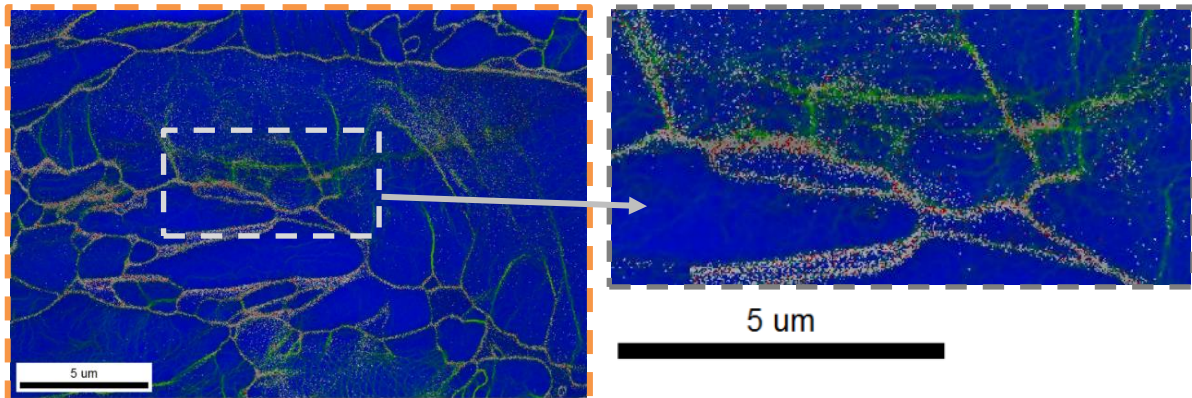


SEM.

IPF overlaid on an IQ map. Scanned with 2x2 binning rate, step size 0.025 μm. Scale bar 5 μm.

Figure 3.52 – SEM and EBSD of “EBSD 1” highlighted in Figure 3.51. 10 s WDE in as-received Ti-6Al-4V RD.

Figure 3.53 is a misorientation map for the “EBSD 1” region. A portion of the scan is enlarged to illustrate the misorientation caused by the indentation.



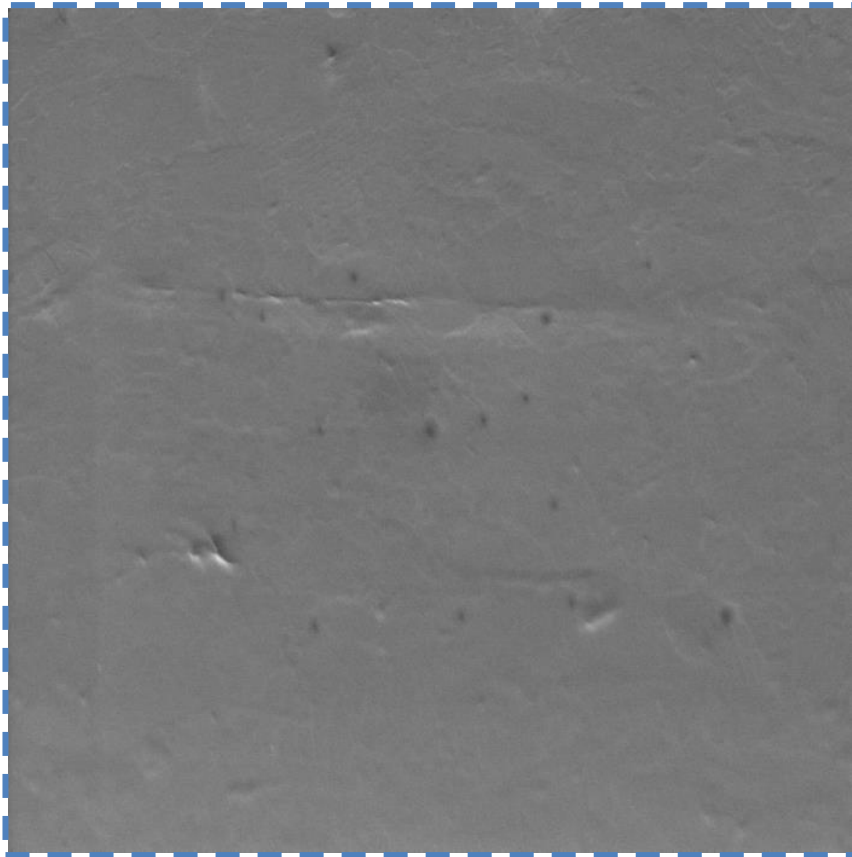
	Min	Max	Total Fraction	Partition Fraction
	0	5	0.932	1.000

Misorientation map of the scan using Kernel Average 1st neighbour. Data cleaned up by Kuwahara filter applied to first neighbour for two iterations. Pixels of less than 0.05 confidence index removed. Overlaid on IQ map. Scale bar 5 μm.

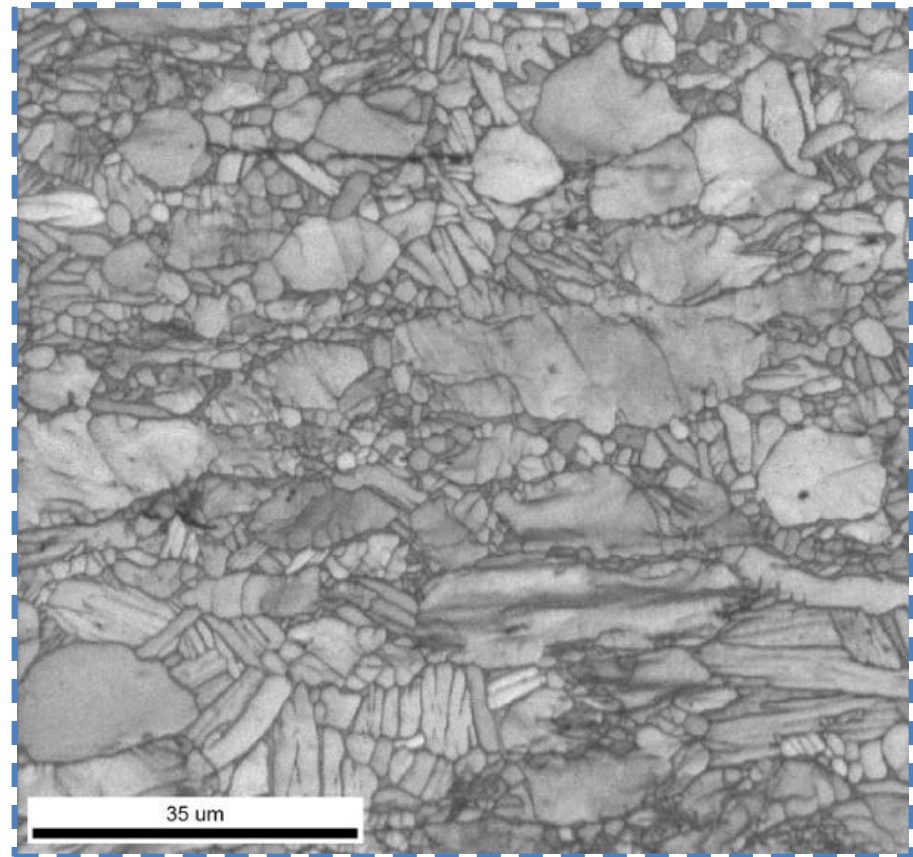
Enlarging the region of the indentation shows local misorientation.

Figure 3.53 – EBSD misorientation maps of the “EBSD 1” region highlighted in Figure 3.51. 10 s WDE in as-received Ti-6Al-4V RD. Scanned with a 2x2 binning rate and a step size of 0.025 μm.

The central indentation labelled “EBSD 2” in Figure 3.51 was also investigated. Figure 3.54 shows an SEM image and IQ map from the EBSD scan.



SEM



IQ scanned with a 4x4 binning rate and a step size of 0.2 μm.

Figure 3.54 – SEM and EBSD of the “EBSD 2” region of Figure 3.51. 10 s WDE in as-received Ti-6Al-4V RD.

The IPF and misorientation maps of the “EBSD 2” scan are shown in Figure 3.55 below. Neither particularly show any microstructural reasons why the indentation might have formed where it did. A location is marked “EBSD 3” where further EBSD was performed on the indentation.

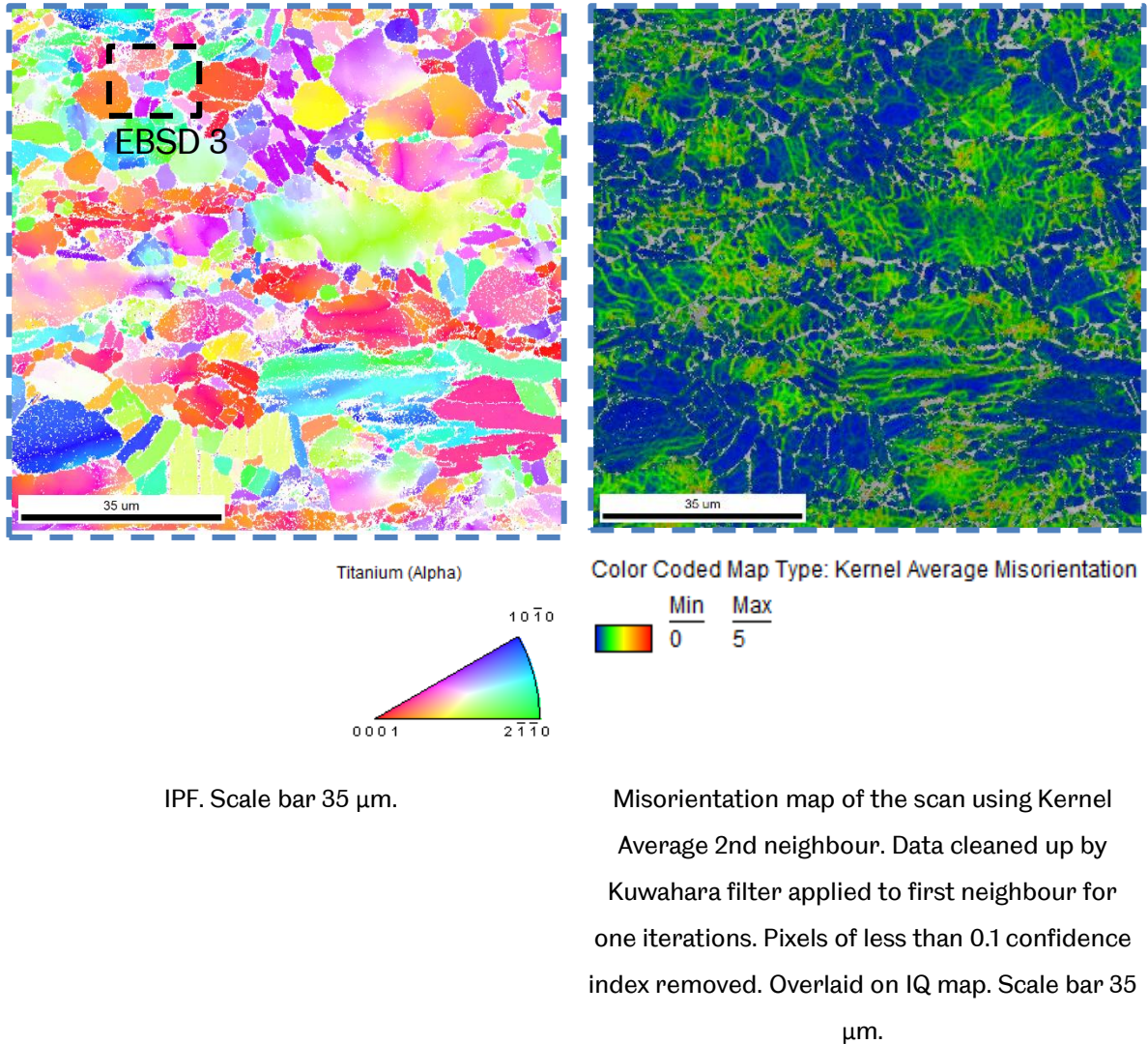
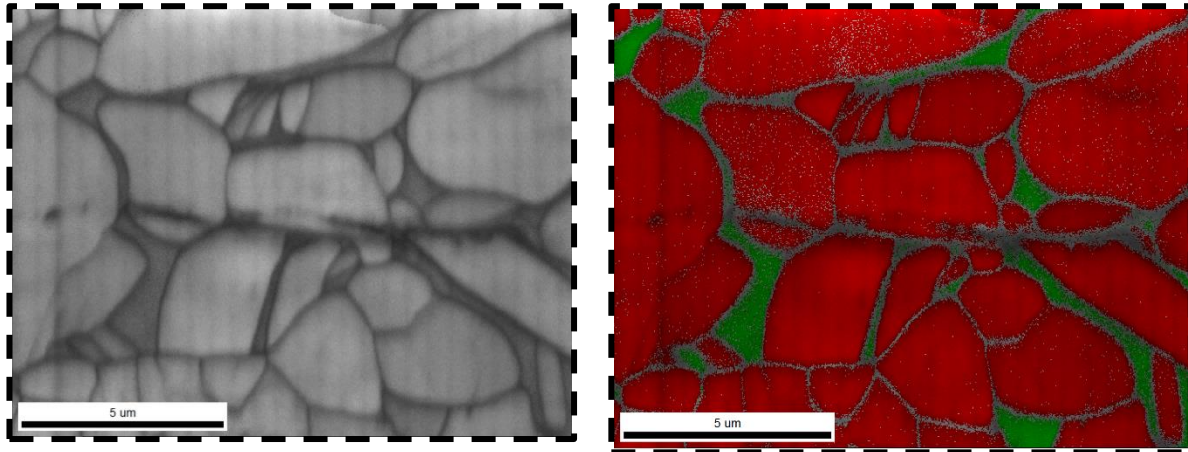


Figure 3.55 – IPF and misorientation maps of the “EBSD 2” region in Figure 3.51. 10 s WDE in as-received Ti-6Al-4V RD. Scanned with a 4x4 binning rate and a step size of 0.2 µm.

The indentation (“EBSD 3” in Figure 3.55) was magnified in the SEM and a higher resolution EBSD scan conducted by utilising a smaller step size. Figure 3.56 shows the IQ and phase maps resulting from the scan. The indentation runs across both alpha-phase grains and the beta-phase matrix.



Color Coded Map Type: Phase

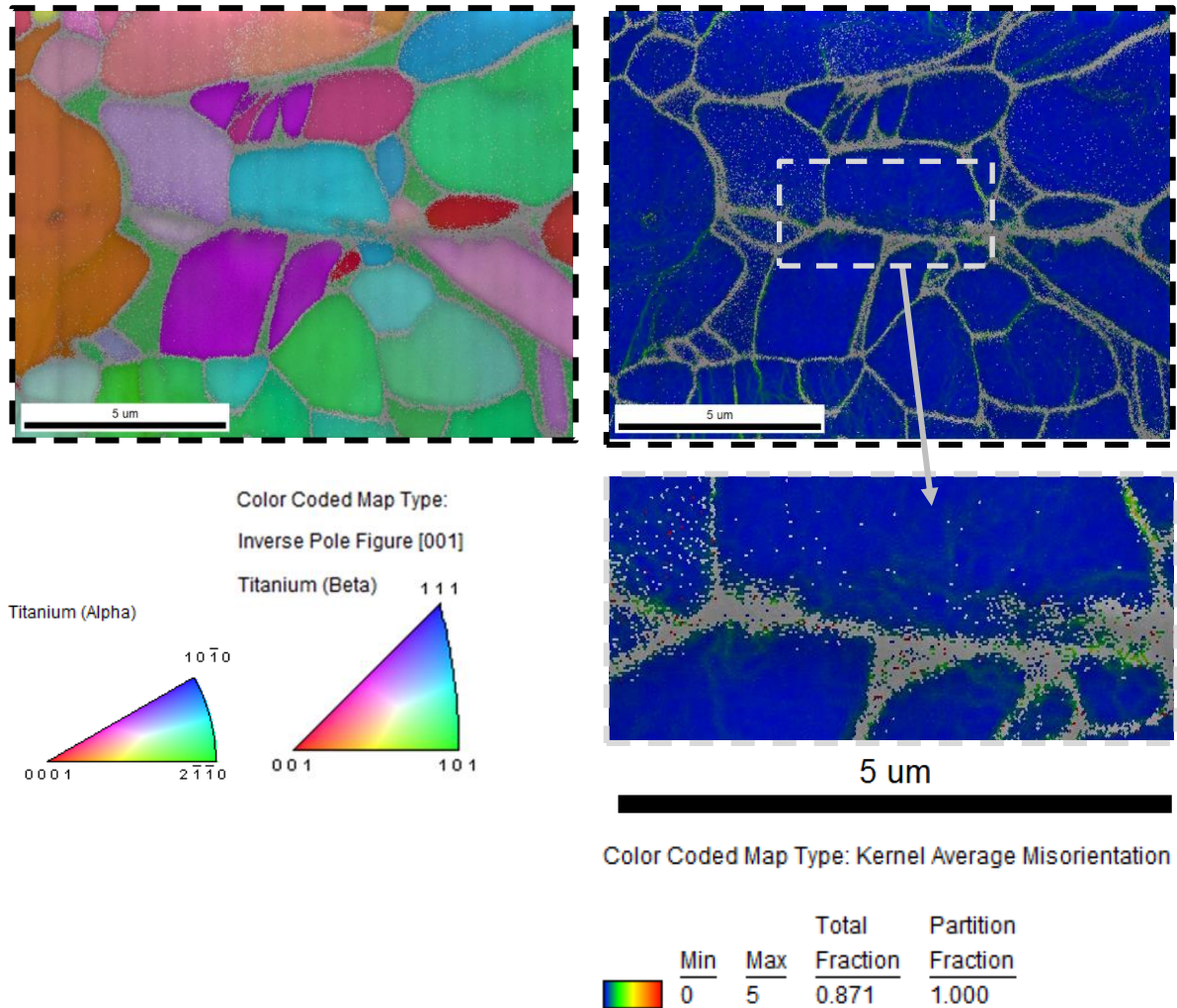
Phase	Total Fraction	Partition Fraction
Titanium (Alpha)	0.820	0.941
Titanium (Beta)	0.051	0.059

IQ. Scale bar 5 µm.

Phase map of the scan. Data cleaned up by Kuwahara filter applied to first neighbour for two iterations. Pixels of less than 0.1 confidence index removed. Overlaid on IQ map. Scale bar 5 µm.

Figure 3.56 – IQ and Phase maps of the “EBSD 3” region of Figure 3.55. 10 s WDE in as-received Ti-6Al-4V RD. Scanned with a 4x4 binning rate and a step size of 0.025 µm.

Figure 3.57 shows the IPF for the “EBSD 3” region marked on Figure 3.55. As was the case in Figure 3.55; the IPF doesn’t give an indication of why an indentation might have formed here. The misorientation map doesn’t show a lot of misorientation between pixels in each grain.



IPF overlaid on IQ map. Pixels of less than 0.1 confidence index removed.

Misorientation map of the scan using Kernel Average 1st neighbour. Data cleaned up by Kuwahara filter applied to first neighbour for two iterations. Pixels of less than 0.1 confidence index removed. Overlaid on IQ map.

Figure 3.57 – IPF and misorientation maps of the “EBSD 3” region of Figure 3.55. 10 s WDE in as-received Ti-6Al-4V RD. Scanned with a 4x4 binning rate and a step size of 0.025 μm .

Figure 3.58 is an SEM image of a micropit. EBSD was performed on the site marked.

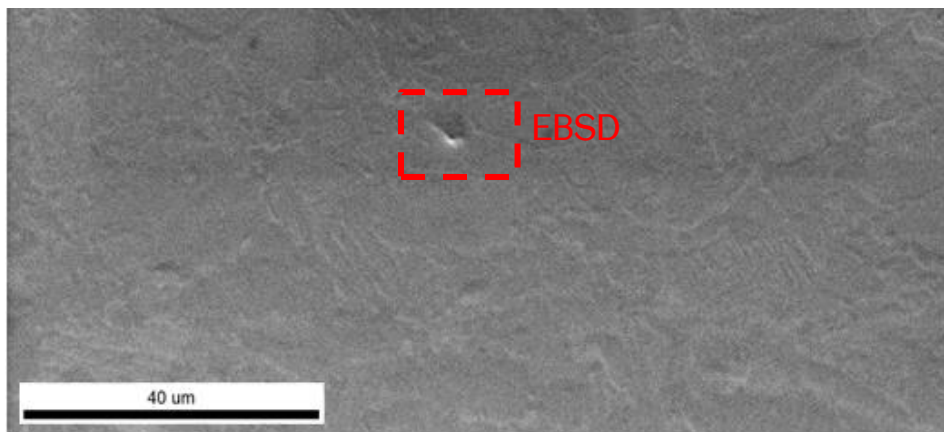
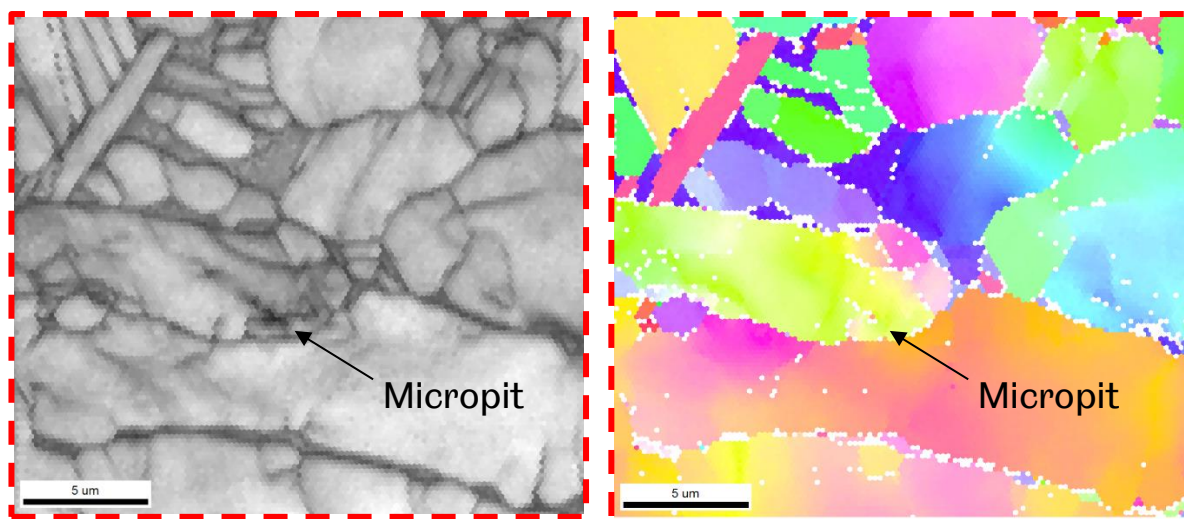
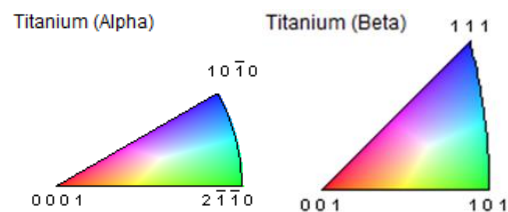


Figure 3.58 – SEM of a micropit.

Results of an EBSD scan of the micropit are shown in Figure 3.59. The micropit shows as a darker region of poorer indexing in the IQ map. It has not started at a grain boundary, but inside a grain. The micropit has spread inside the grain but has not yet crossed the grain boundary into other grains.



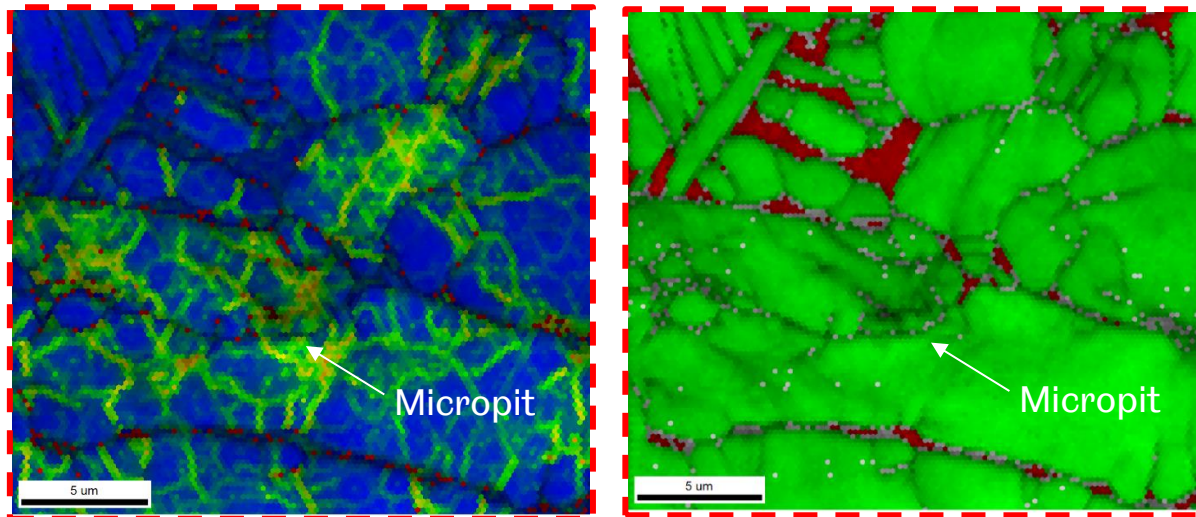
IQ. Scale bar 5 μm.



IPF overlaid on IQ map. Pixels of less than 0.1 confidence index removed. Scale bar 5 μm.

Figure 3.59 – IQ and IPF maps of a micropit. Scanned with a 2x2 binning rate and a step size of 0.2 μm. 10 s WDE in as-received Ti-6Al-4V RD.

There is a lot of misorientation in and around the micropit in Figure 3.60, but it is difficult to tell if some or all of this is not residual from the forming route of the material. The phase map shows this micropit has formed in an alpha grain, but that might not be surprising, given the majority of the material is alpha phase in a secondary beta phase matrix.



Color Coded Map Type: Kernel Average Misorientation

	Min	Max	Total Fraction	Partition Fraction
	0	5	1.000	1.000

Misorientation map of the scan using Kernel Average 1st neighbour. Data cleaned up by Kuwahara filter applied to first neighbour for two iterations. Overlaid on IQ map. Scale bar 5 µm.

Color Coded Map Type: Phase

Phase	Total Fraction	Partition Fraction
Titanium (Beta)	0.043	0.045
Titanium (Alpha)	0.903	0.955

Phase map of the scan. Pixels of less than 0.1 confidence index removed. Overlaid on IQ map. Scale bar 5 µm.

Figure 3.60 – IQ and phase maps of a micropit. 10 s WDE in as-received Ti-6Al-4V RD. Scanned with a 2x2 binning rate and a step size of 0.2 µm.

3.4.4 5 minutes as-received Ti-15Mo

As-received Ti-15Mo was tested for 5 minutes with a 0.16 mm diameter, 0.5 mm thick sheet “diaphragm” nozzle. At a S.D. of 140 mm, droplets produced were on average 284 µm in diameter. The total number of droplet impacts for the exposure time was 2.49×10^5 . There was no detectable mass loss. Using a digital read out (DRO) on the microscope stage it was possible to collect images of the same sample location before

and after testing. Figure 3.61 shows light microscope images taken across the 8 mm width of the coupon at the mid-section, both before and after the experiment.

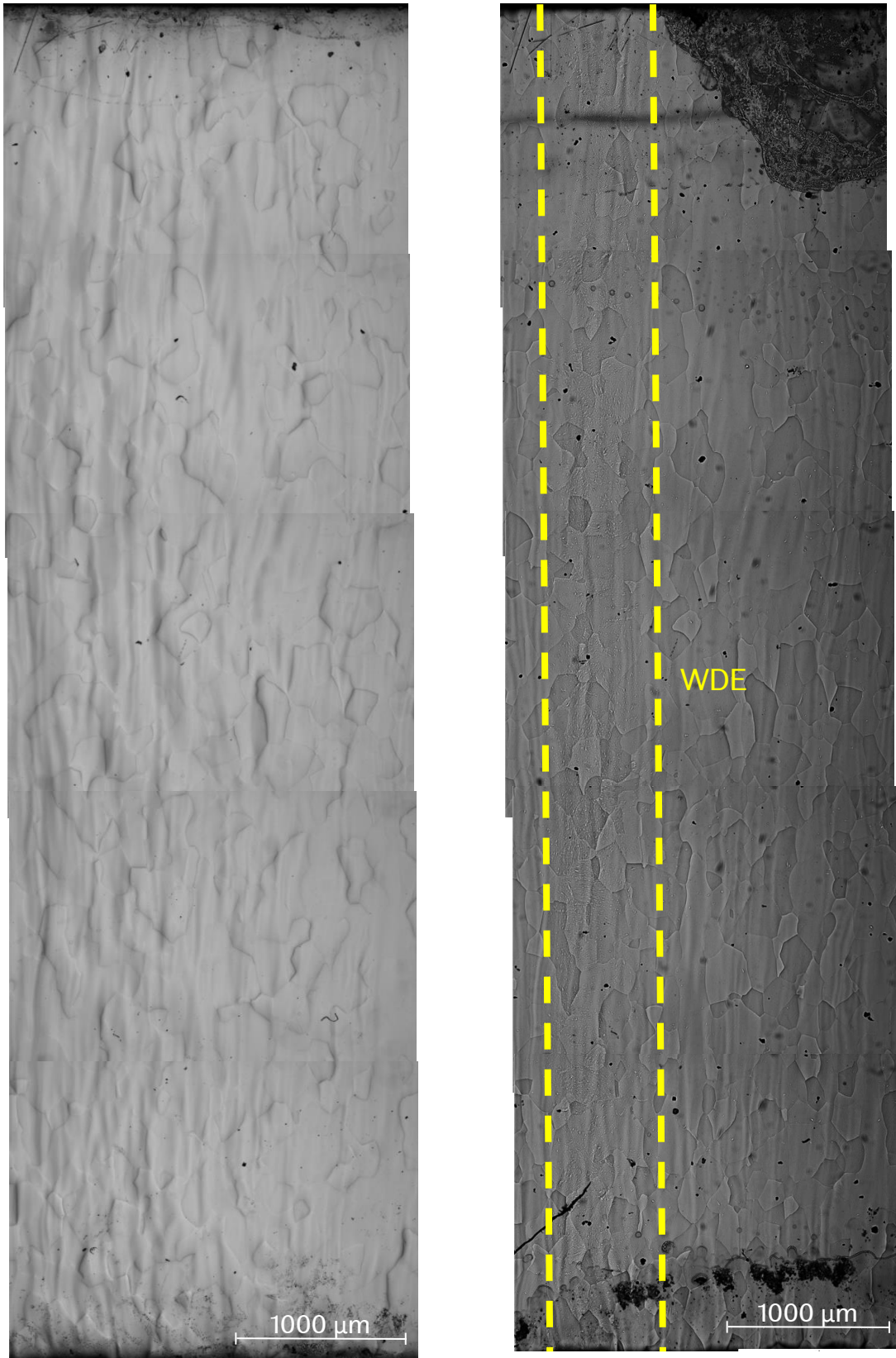


Figure 3.61 – Left: Ti-15Mo TD before WDE. Right: 5 minutes WDE.

Figure 3.62 below is the edge furthest away from the nozzle before testing. There is a slight relief on the surface due to the mechanical polishing technique.

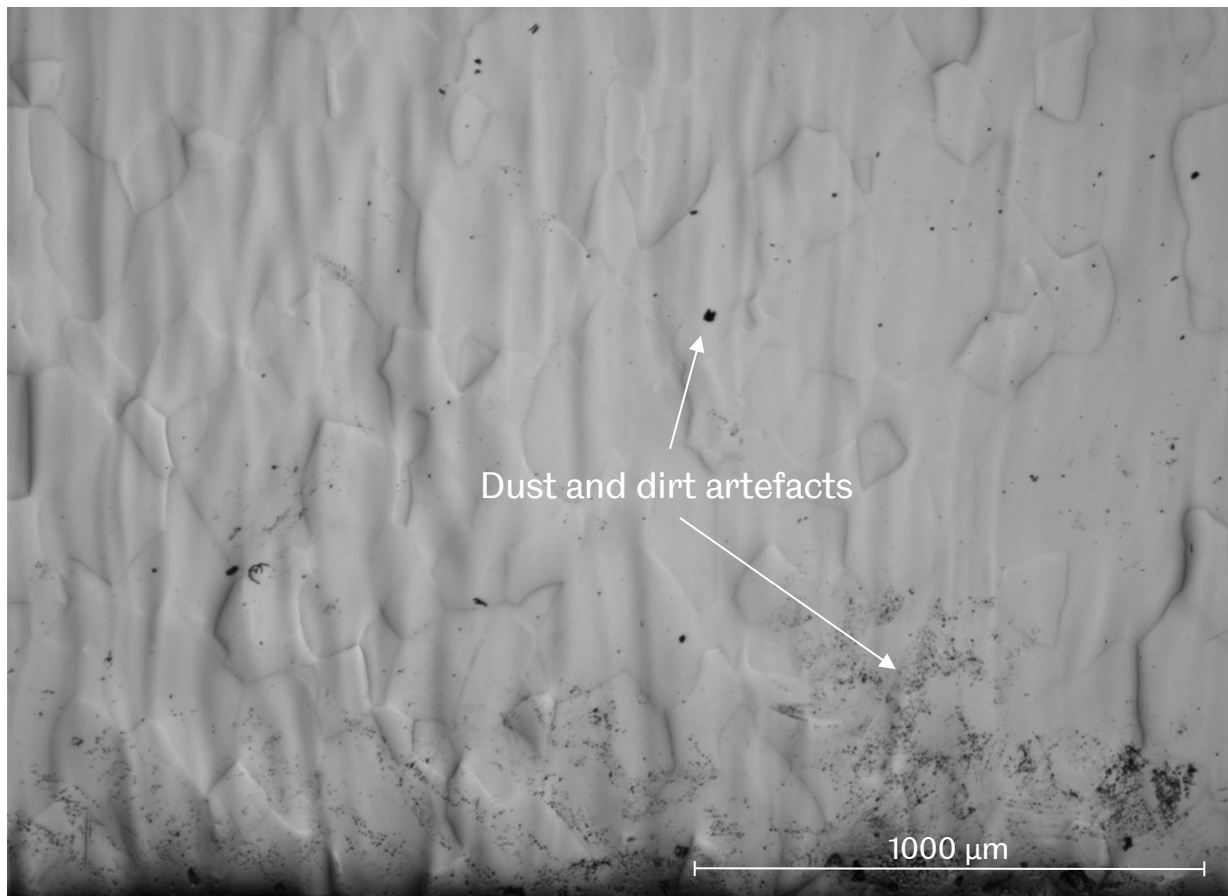


Figure 3.62 – Mid-section of coupon, edge furthest from nozzle. Ti-15Mo TD before WDE testing.

Figure 3.63 shows the same location following the 5-minute test. There is a line on the left of the image of small marks indicating deformation from the water droplets. A region is highlighted where higher magnification SEM and EBSD analysis was conducted.

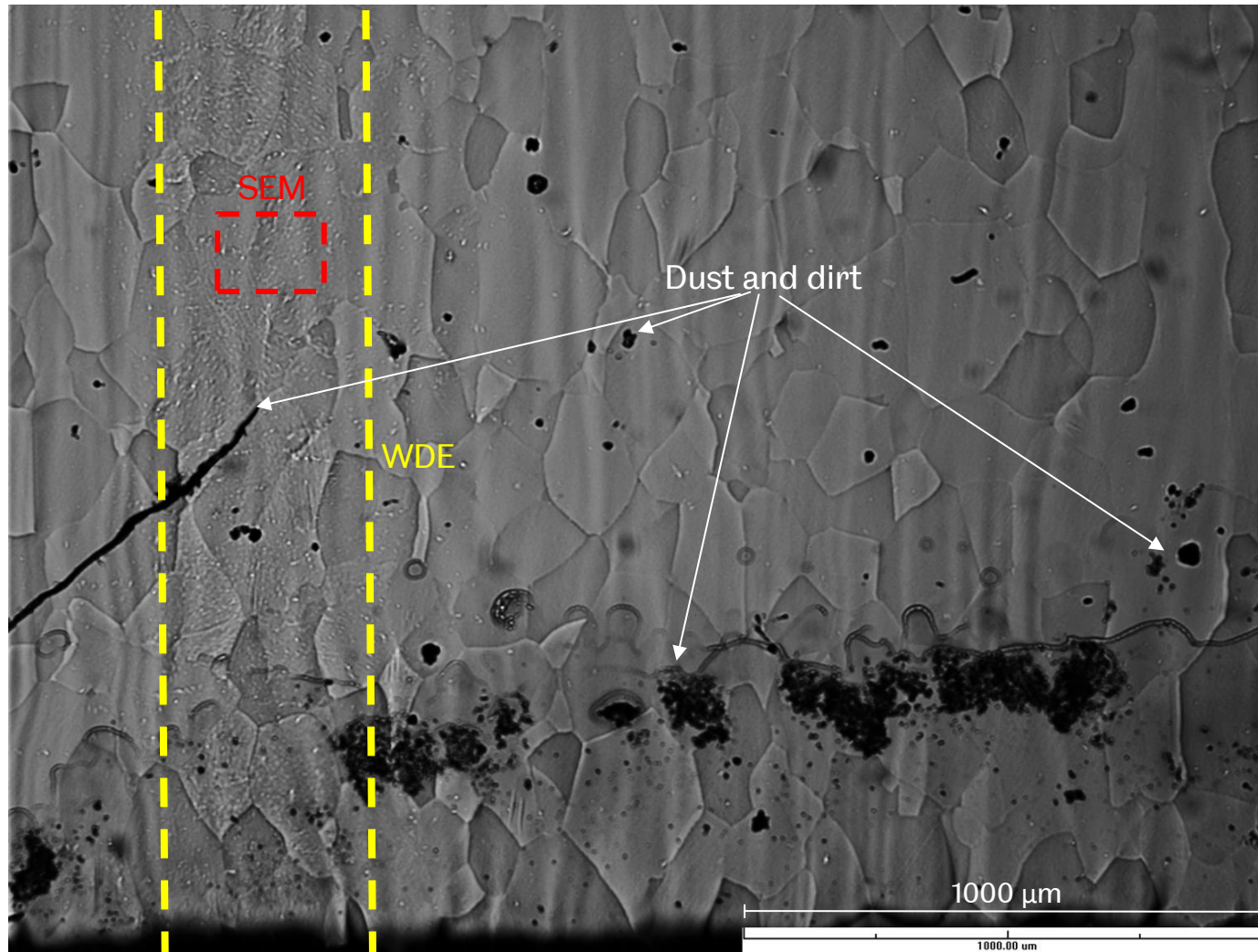
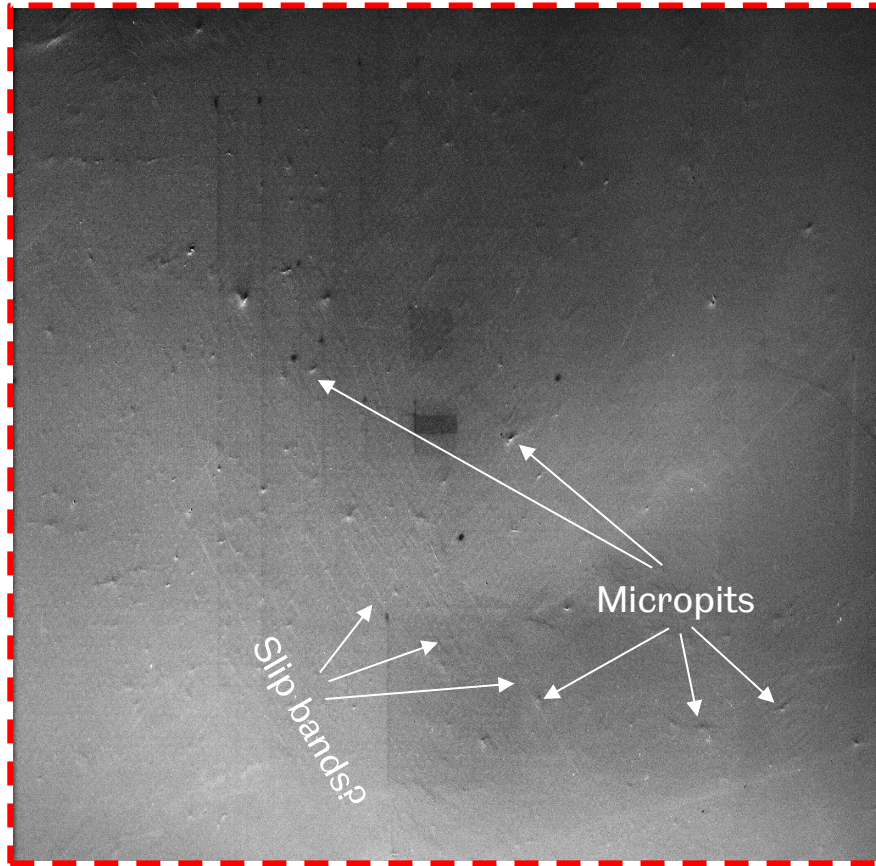
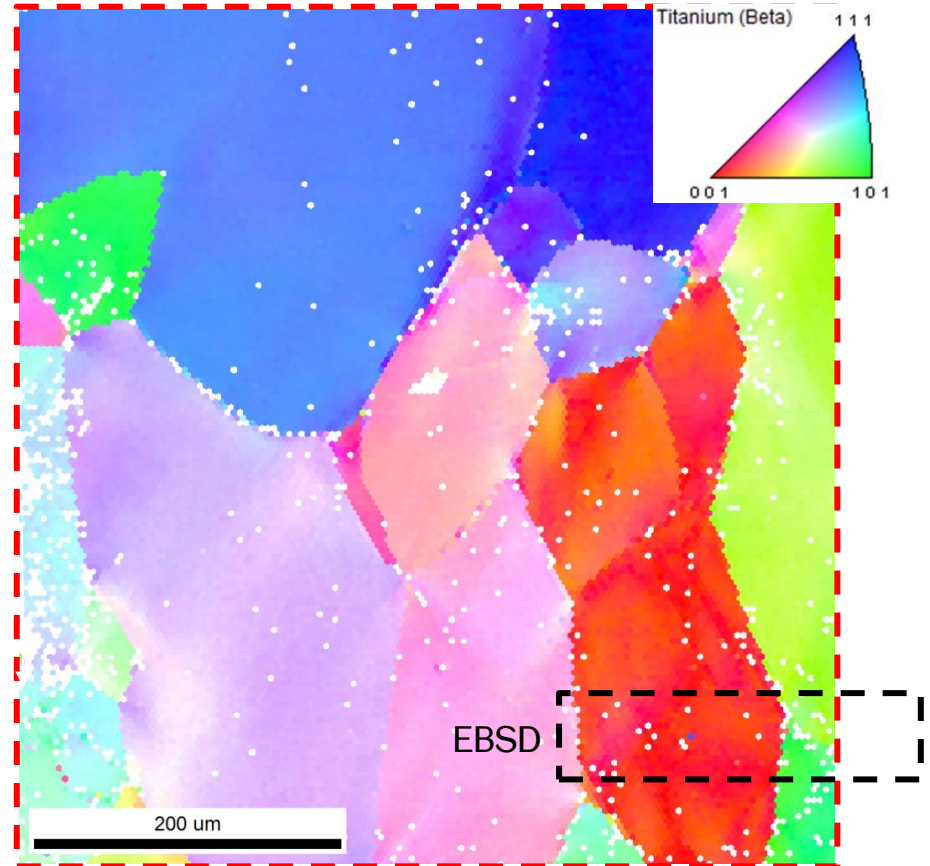


Figure 3.63 – Mid-section of coupon, edge furthest from nozzle. Ti-15Mo TD after 5 minutes WDE.

The SEM image in Figure 3.64 shows micropits and lines which could be slip bands. A large, low-resolution IPF map of the region doesn't reveal any further detail about the micropits, so a higher resolution scan was tried at the region marked "EBSD".



SEM image.



IPF scanned with a 2x2 binning rate and a step size of 4 μm .

Figure 3.64 – SEM & EBSD images of erosion scar at edge furthest from nozzle. Ti-15Mo TD after 5 minutes WDE.

A smaller step size scan produces higher resolution maps in Figure 3.65. The IPF does not clearly show micropits but the misorientation map shows misorientation around the pits. There are sub-grains and misorientation at grain boundaries, which was noted in the untested as-received microstructure and is thought to be residual from the materials manufacturing route.

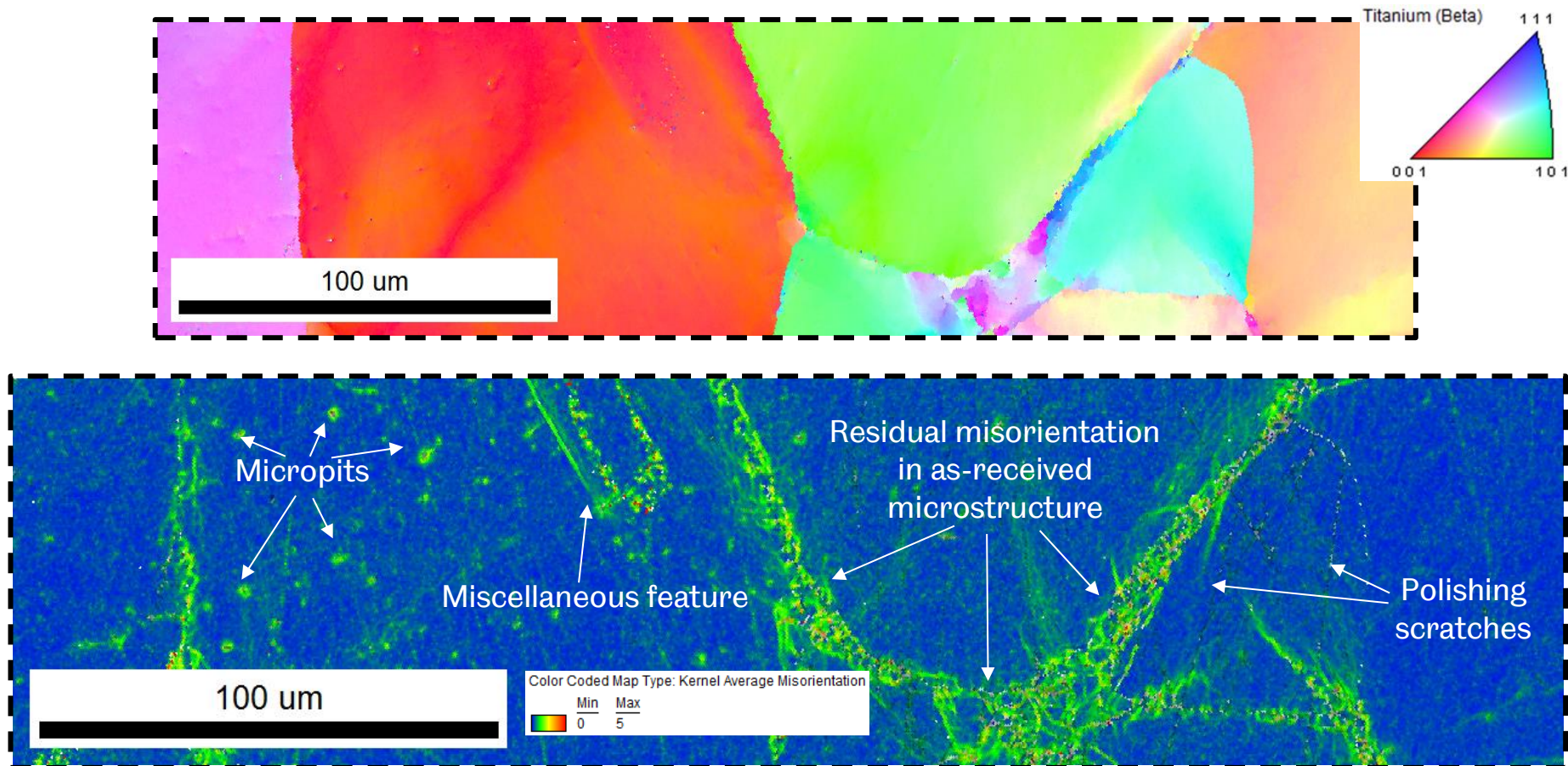


Figure 3.65 – Ti-15Mo TD after 5 minutes WDE. EBSD results with 2x2 binning rate, step size 0.5 μm. Top: IPF. Bottom: Misorientation map of the scan using Kernel Average 1st neighbour. Overlaid on IQ map.

An area of what appear to be slip bands (SEM Figure 3.66) was scanned at a high magnification with a small step size. The IPF does not show the slip bands at all and it is difficult to say if the misorientation map shows them either.

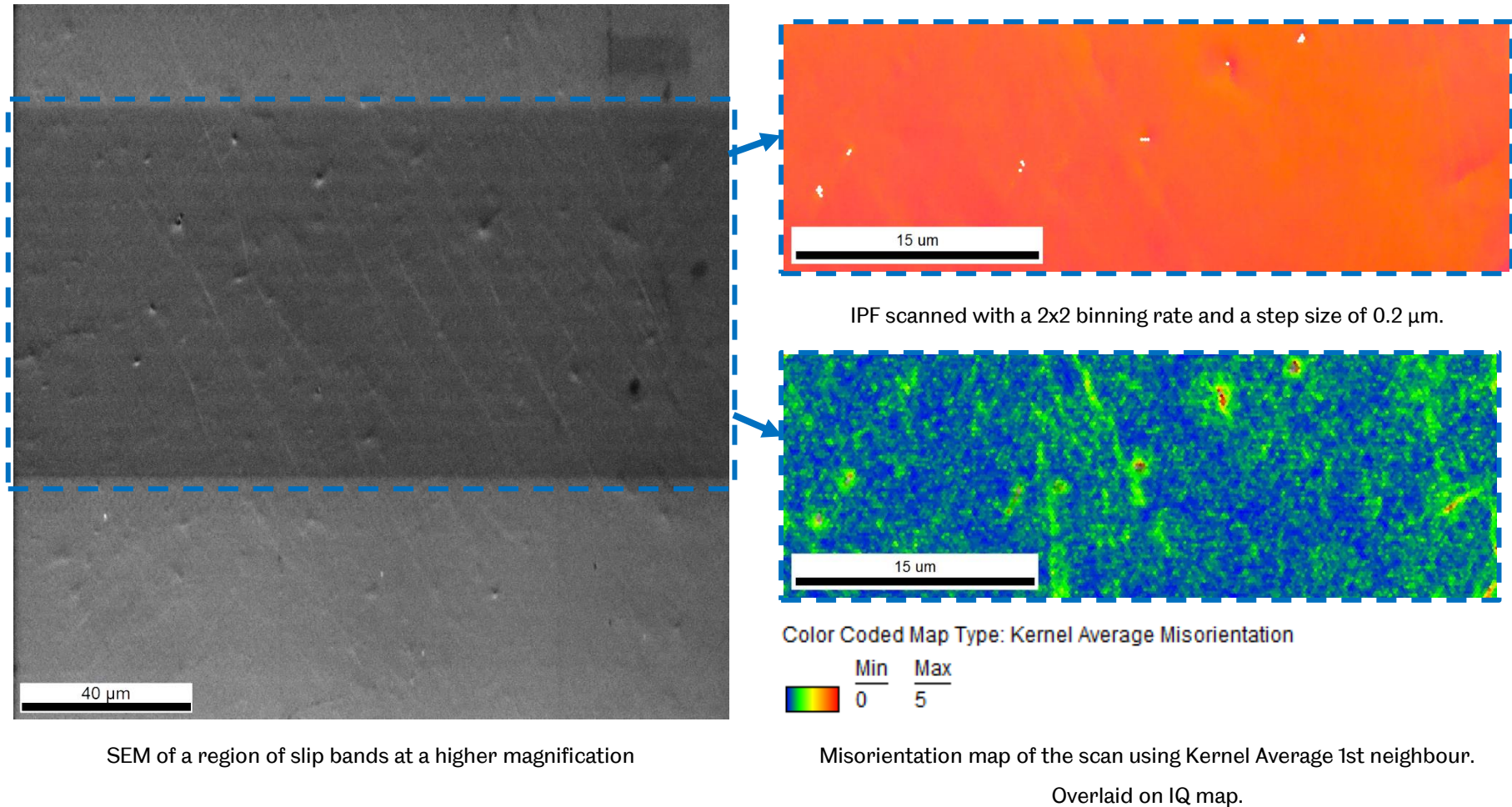


Figure 3.66 – Ti-15Mo TD after 5 minutes WDE. SEM & EBSD at a higher magnification of an area of slip bands.

3.4.5 5 minutes annealed Ti-6Al-4V

Annealed Ti-6Al-4V was tested alongside the Ti-15Mo. Again there was no measurable mass loss. Figure 3.67 is a series of light microscope images taken across the mid-section of the coupon before and after 5 minutes WDE testing. The erosion scar is identifiable approximately 1 mm left of the centre.

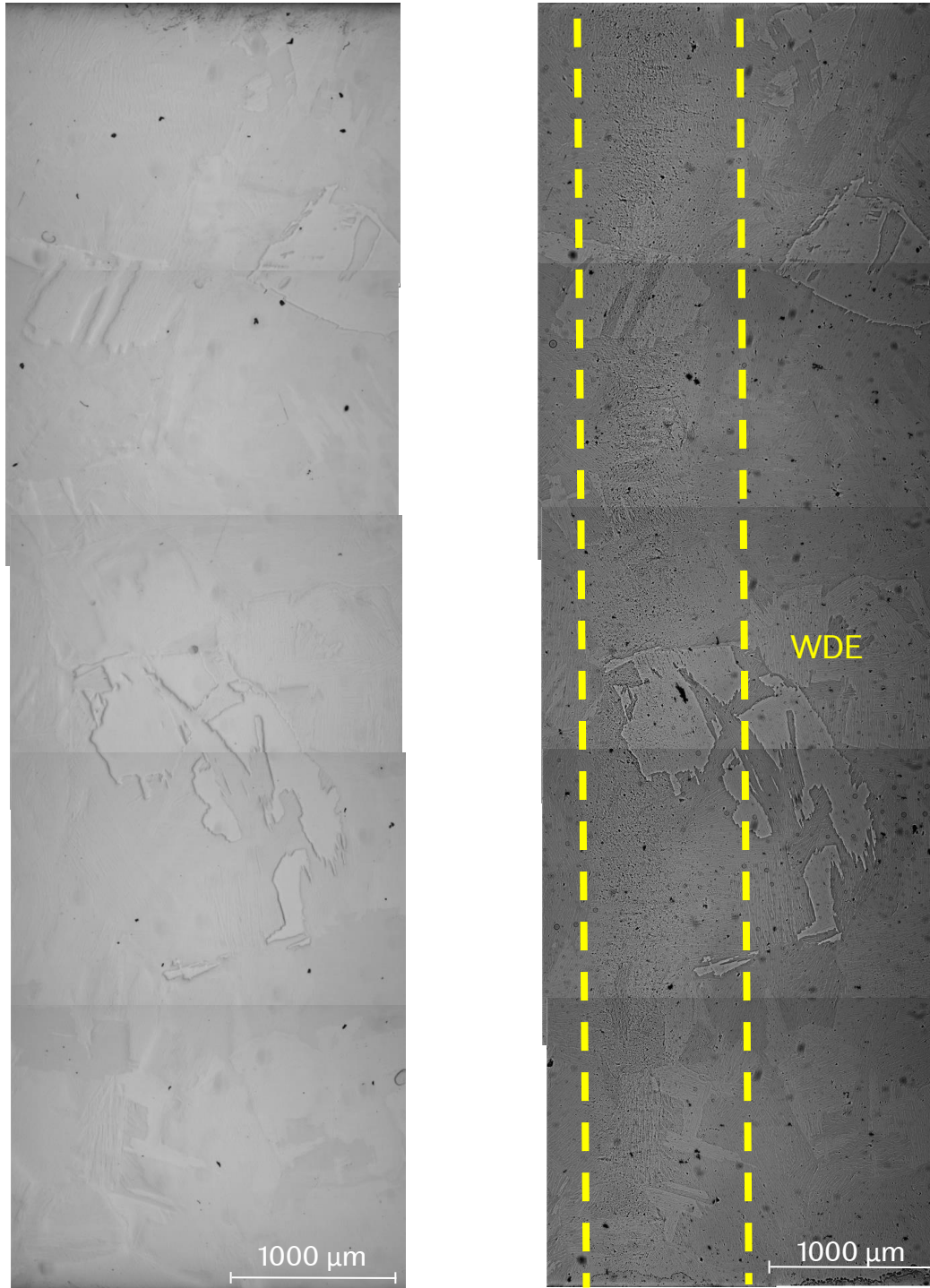


Figure 3.67 –Left: annealed Ti-6Al-4V RD before testing. Right: after 5 minutes WDE.

Figure 3.68 below is approximately 3 mm from the edge nearest to the nozzle, before testing. This location was chosen for analysis because some interesting features appeared here following testing.

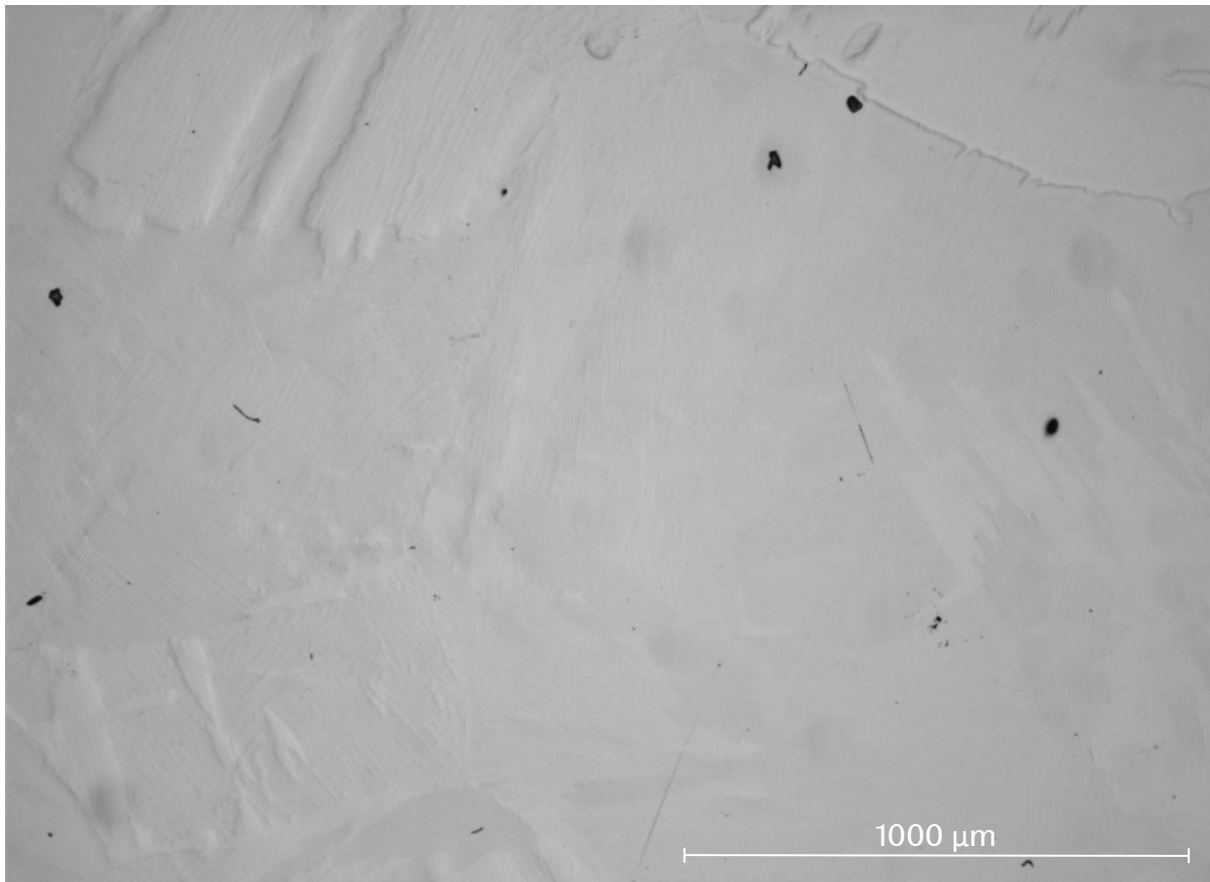


Figure 3.68 – Mid-section of coupon, 3 mm from edge nearest to nozzle. Annealed Ti-6Al-4V RD before WDE testing.

Figure 3.69 shows the area following the 5-minute test, taken in the same location as Figure 3.68. The erosion wear scar is slightly left of the mid-section. An area is highlighted where further analysis was conducted on an indentation.

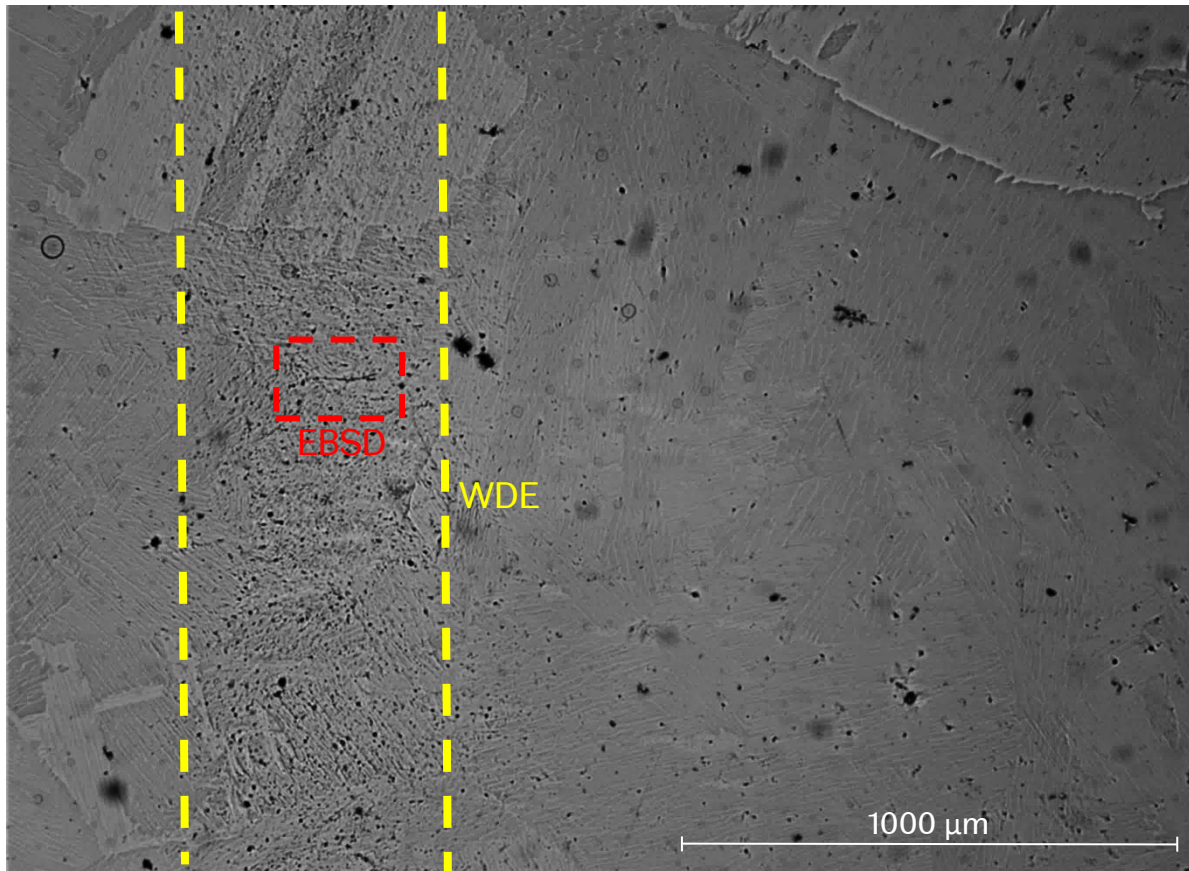
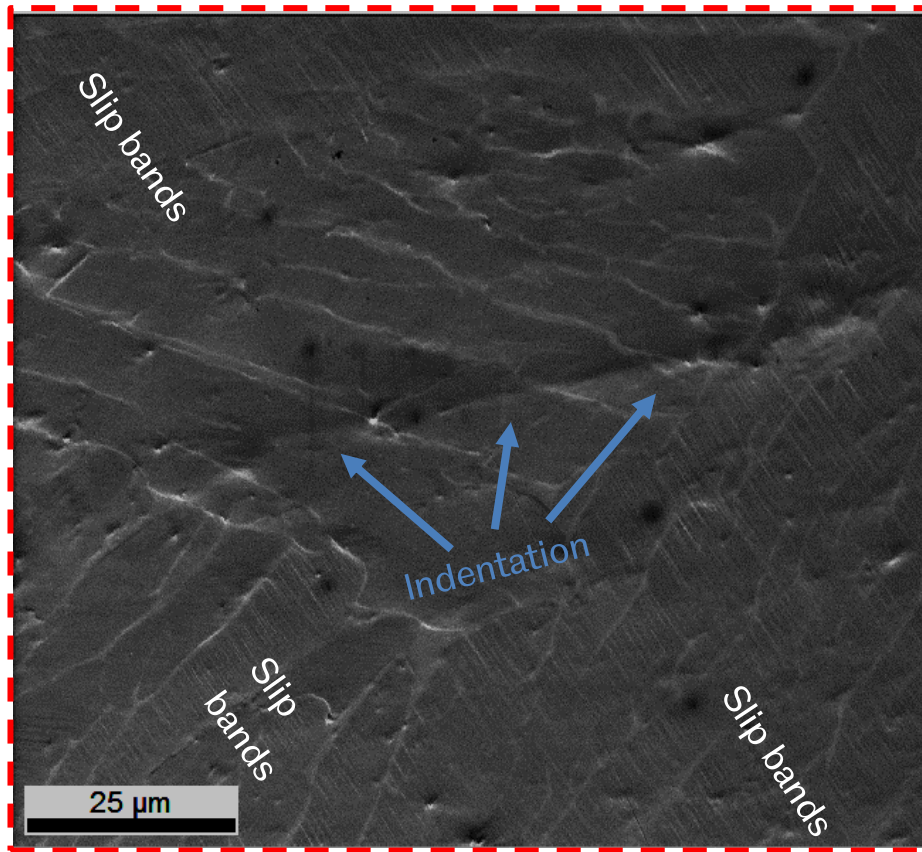
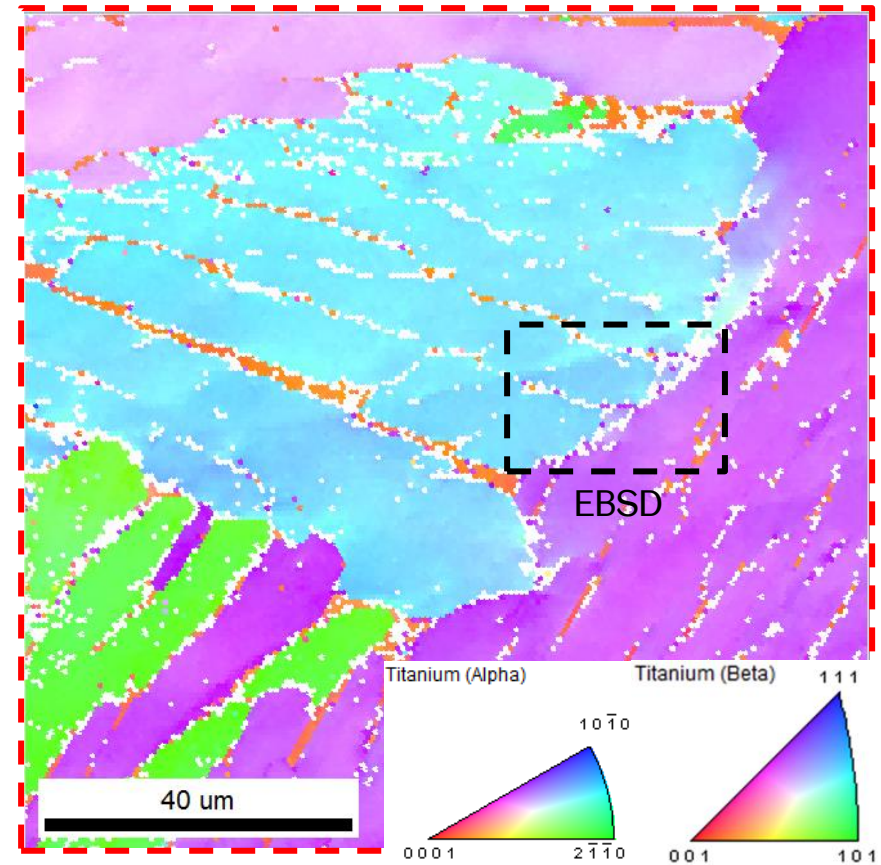


Figure 3.69 – Mid-section of coupon, 3 mm from edge nearest to nozzle. Annealed Ti-6Al-4V RD after 5 minutes WDE testing. Light microscope at low magnification. Scale bar is 1000 μm.

Figure 3.70 is an SEM image and IPF of a region of interest in the wear scar. The IPF shows the indentation is predominantly in the blue plane. The slip bands observed by SEM correspond to the purple plane.



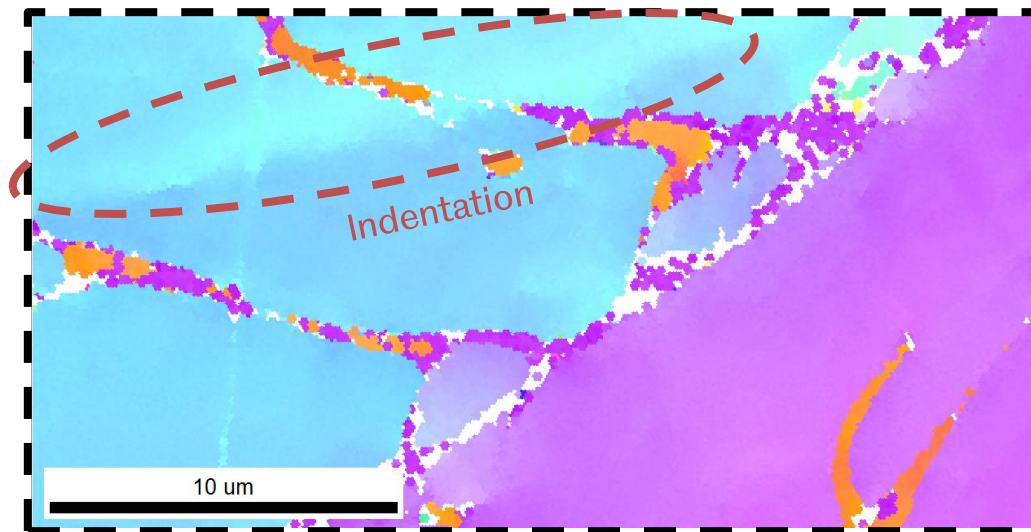
SEM image.



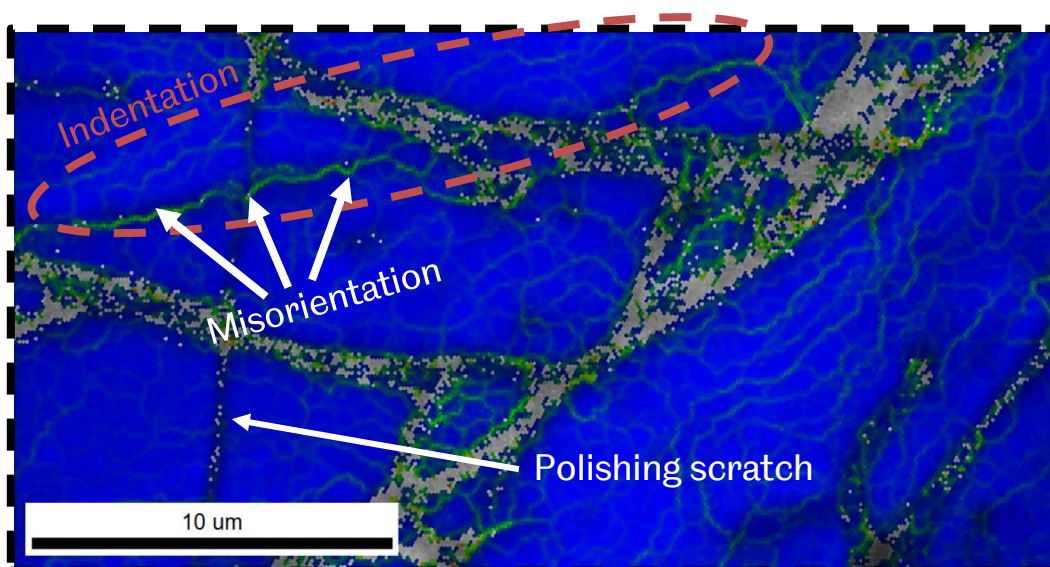
IPF scanned with a 2x2 binning rate and a step size of 0.7 μm. Grains of size less than 5 pixels removed.

Figure 3.70 – SEM & IPF images of mid-section of coupon, 3 mm from edge nearest to nozzle. Annealed Ti-6Al-4V RD after 5 minutes WDE testing.

A reduced step-size scan gives a higher resolution IPF in Figure 3.71, but does not reveal much further detail. However the misorientation map does suggest there is misorientation between the pixels where the indentation is located.



IPF. Grains of size less than 5 pixels removed.



Misorientation map of the scan using Kernel Average 1st neighbour. Data cleaned up by Kuwahara filter applied to first neighbour for two iterations. Grains of size less than 5 pixels removed. Overlaid on IQ map.

Figure 3.71 – IPF and Misorientation map for 5 minute WDE Annealed Ti-6Al-4V RD sample, scanned with a 2x2 binning rate and a step size of 0.1 μm .

3.4.6 10 minutes annealed Ti-6Al-4V

The annealed state Ti-6Al-4V was tested for 10 minutes with a 0.16 mm diameter, 0.5 mm thick sheet “diaphragm” nozzle. At a S.D. of 140 mm, droplets produced were on average 284 μm in diameter. Figure 3.72 below is the edge nearest to the nozzle, before testing. The total number of droplet impacts for the exposure time was 4.97×10^5 . Mass loss could not be detected with the $\pm 10^{-5}$ g precision mass balance used.

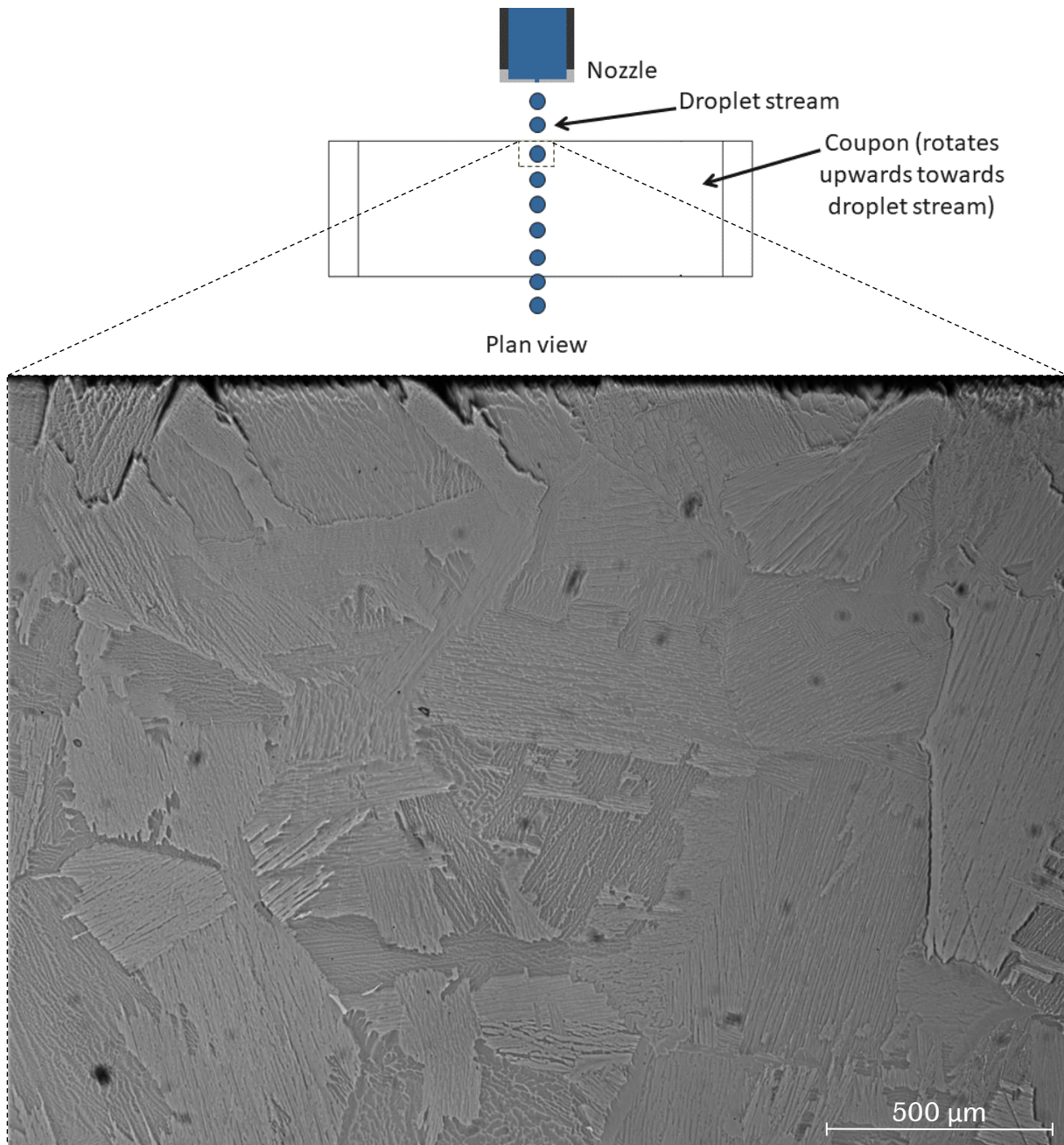


Figure 3.72 – Mid-section of coupon, edge nearest to nozzle. Annealed Ti-6Al-4V RD before WDE testing.

The same location after 10 minutes WDE testing is shown in Figure 3.73. The line of erosion is on the left of the image. Some regions have been annotated where further EBSD analysis was conducted.

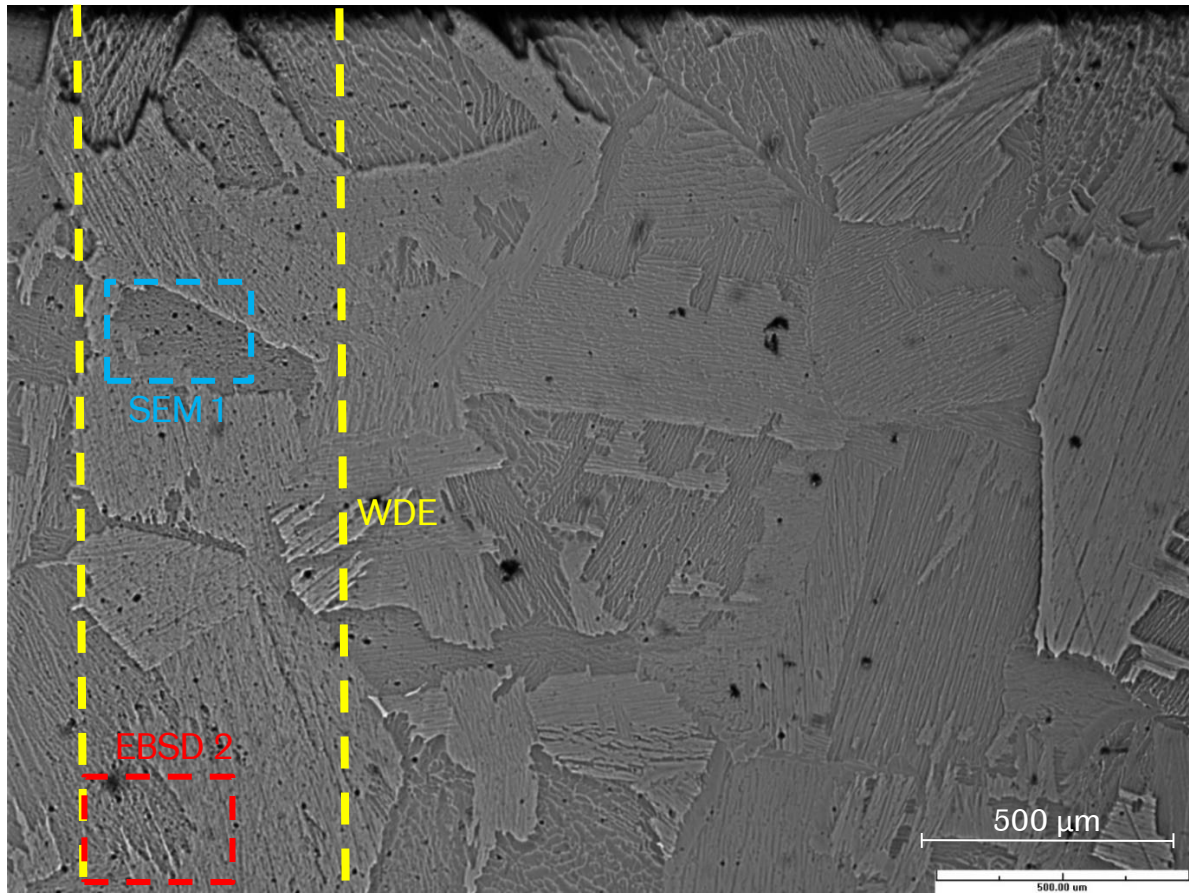
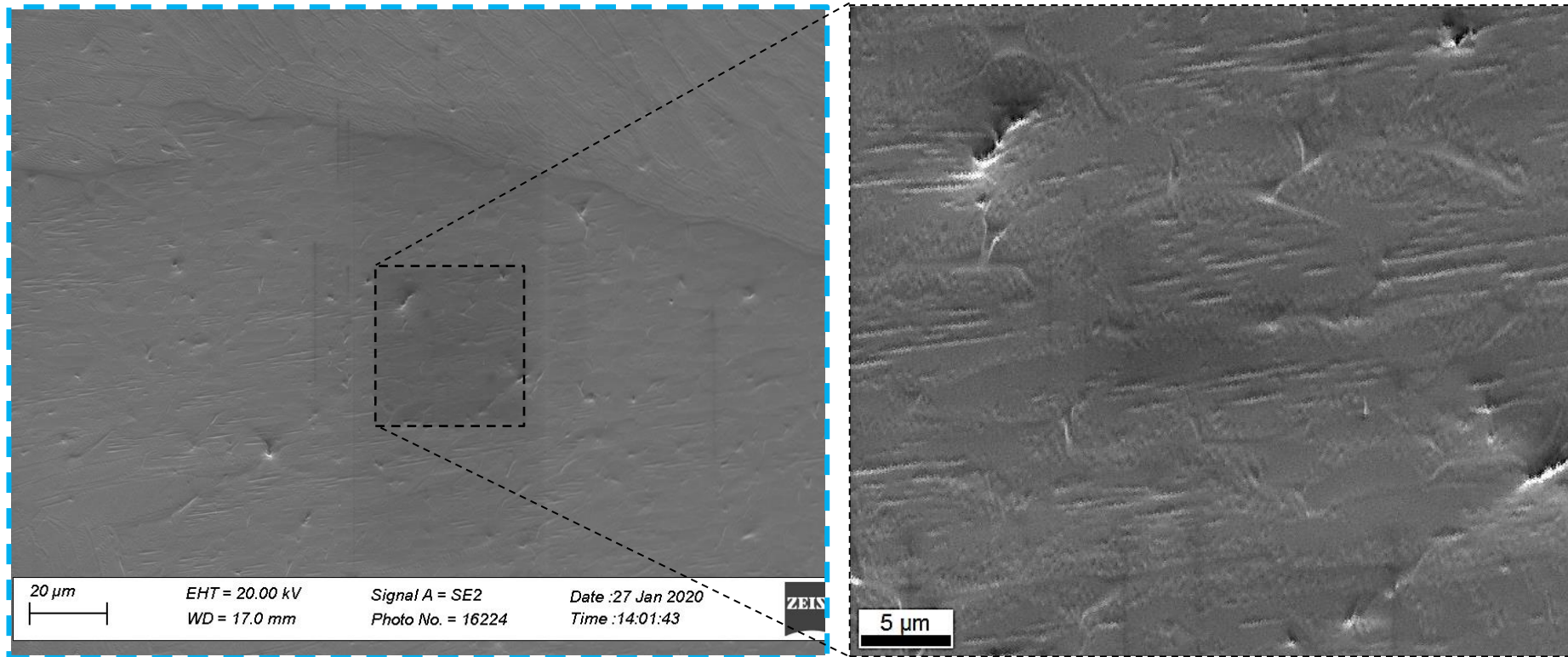


Figure 3.73 – Mid-section of coupon, edge nearest to nozzle. Annealed Ti-6Al-4V RD 10 minutes after WDE testing.

Figure 3.74 is SEM images of the “SEM 1” region noted in Figure 3.73, approximately 1 mm from coupon edge. Additionally to the micropits, there are highly directionalised lines which appear locally in this α colony.



SEM low magnification.

SEM at higher magnification.

Figure 3.74 – Erosion features at “SEM 1” region of Figure 3.73. Annealed Ti-6Al-4V RD 10 minutes after WDE testing.

The region at higher magnification in Figure 3.74 was examined with EBSD. However the results of the scan in Figure 3.75, below, do not show these features in any greater detail.

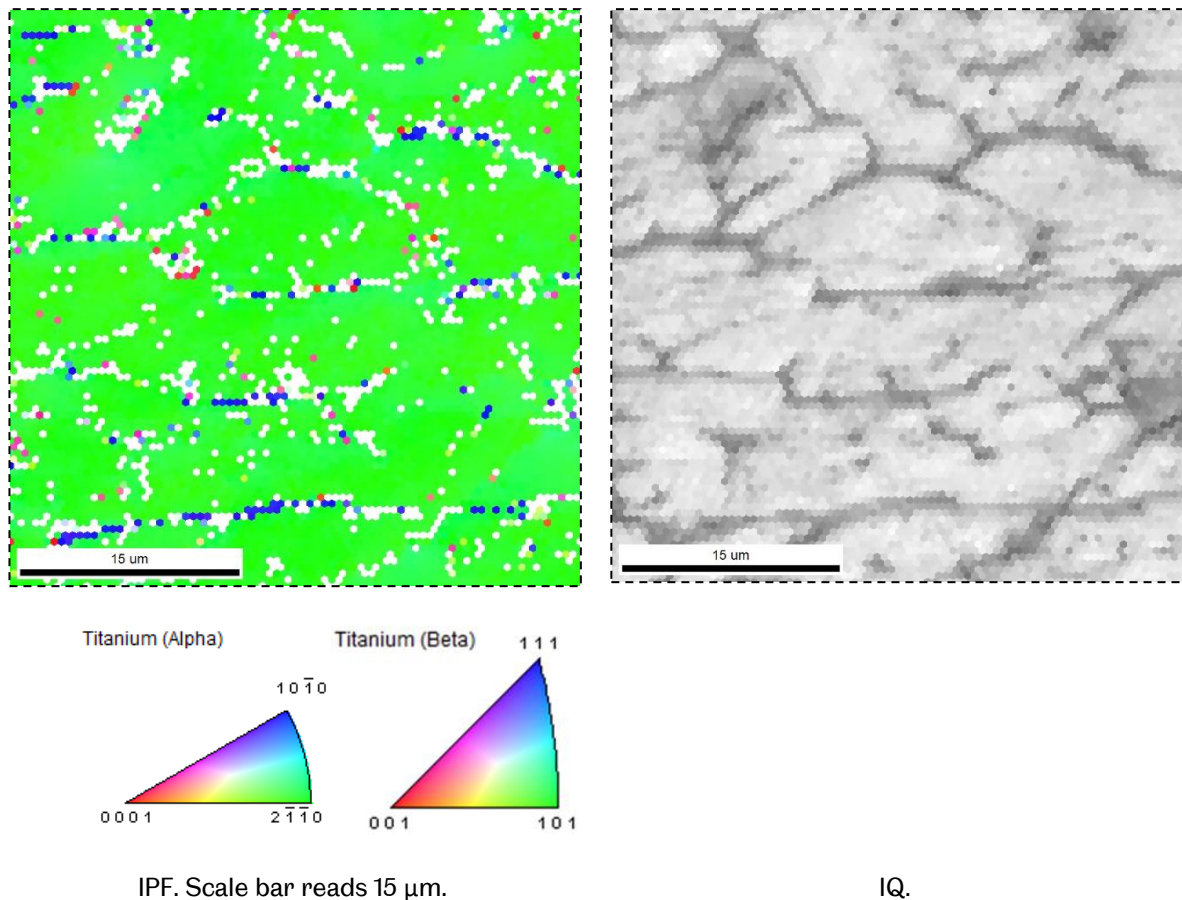


Figure 3.75 – IPF and IQ maps scanned with a 2x2 binning rate and a step size of 0.5 μm. EBSD of the higher magnification region of Figure 3.74. Annealed Ti-6Al-4V RD 10 minutes after WDE testing

SEM of the “EBSD 2” region of Figure 3.73, in Figure 3.76 below, shows micropits and possible twins or slip bands. EBSD confirms the straight lines are not twins so they’re possibly slip bands. The misorientation map does show misorientation (green) around deformed areas such as micropits. This map is overlaid on Image Quality (IQ) which is lighter where confidence in indexing is high, and darker where confidence index is poorer. The contrast is not related to the misorientation.

Further EBSD was conducted at a region of micropits and slip bands, labelled “EBSD 3” in Figure 3.76.

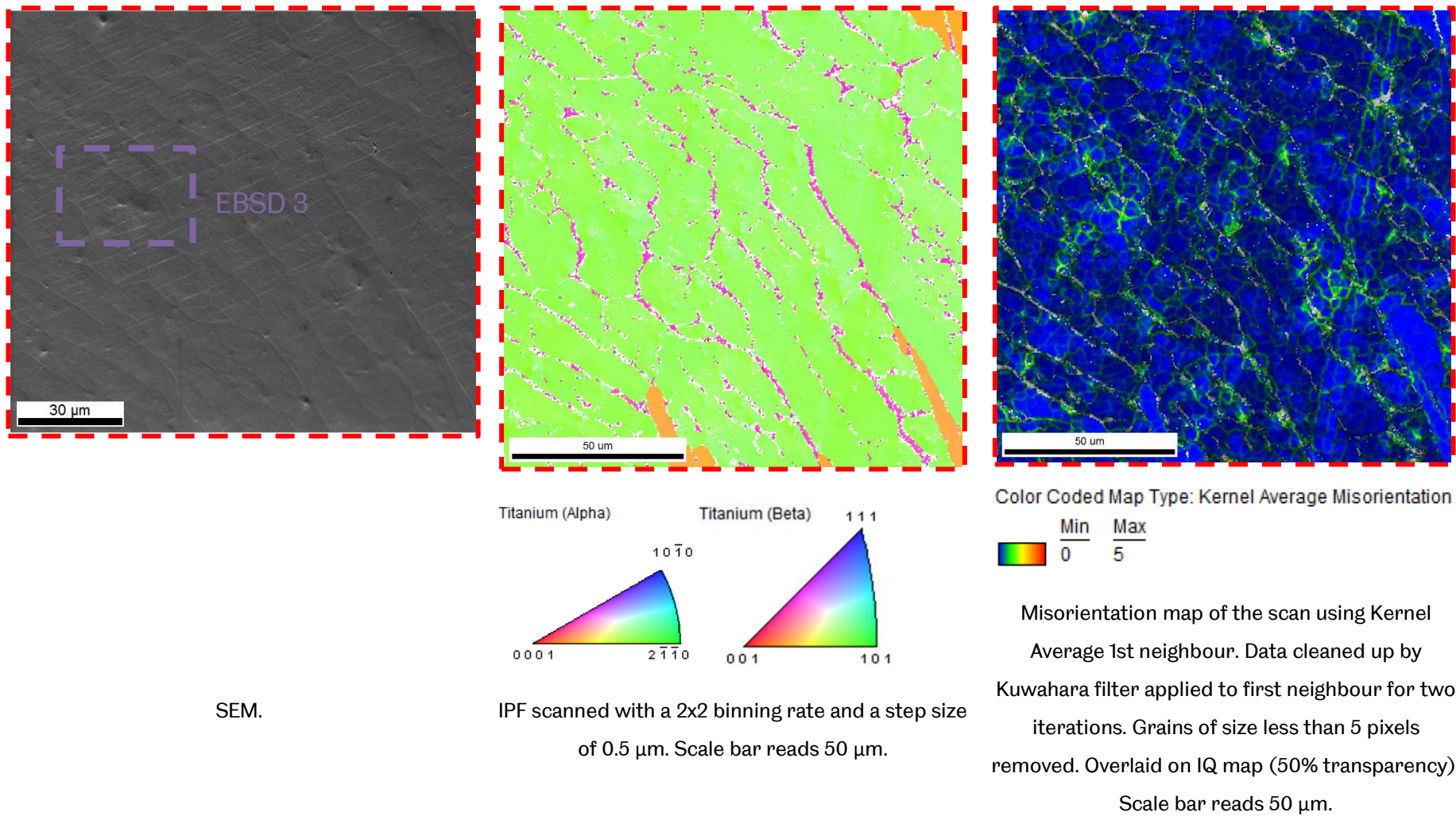
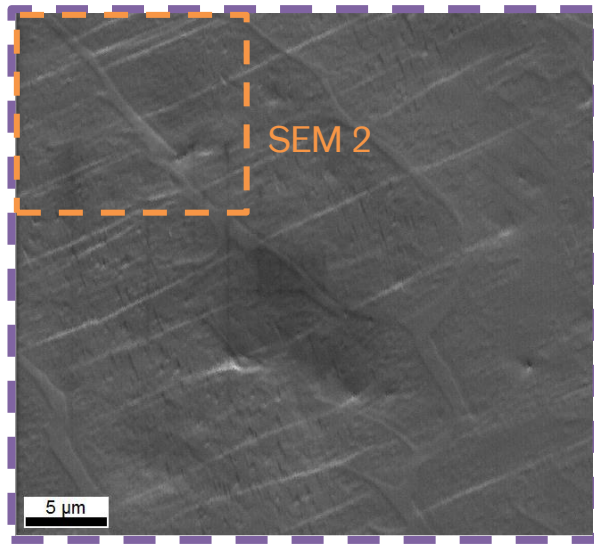
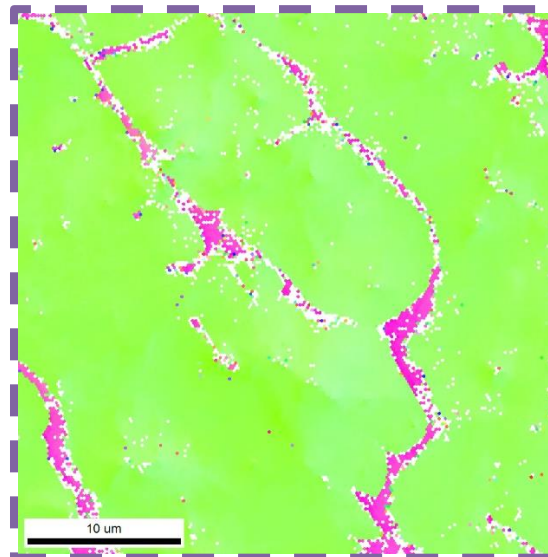


Figure 3.76 – SEM & EBSD images from “EBSD 2” region of Figure 3.73. Approximately 2.5 mm from the edge of the coupon. Annealed Ti-6Al-4V RD 10 minutes after WDE testing.

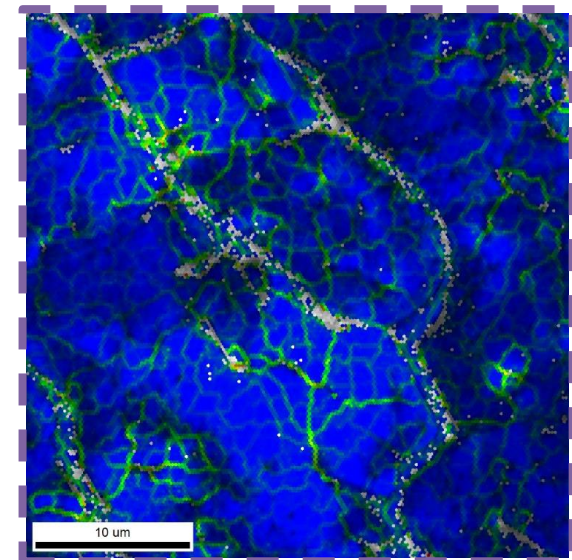
The “EBSD 3” location in Figure 3.76 was scanned at higher magnification and with a reduced EBSD step size, to produce higher resolution images in Figure 3.77. There is misorientation around micropits but the slip bands observed by SEM do not appear more clearly with EBSD techniques. Figure 3.77 also illustrates a region investigated at further increased magnification, labelled “SEM 2”.



SEM. Scale bar 5 μm



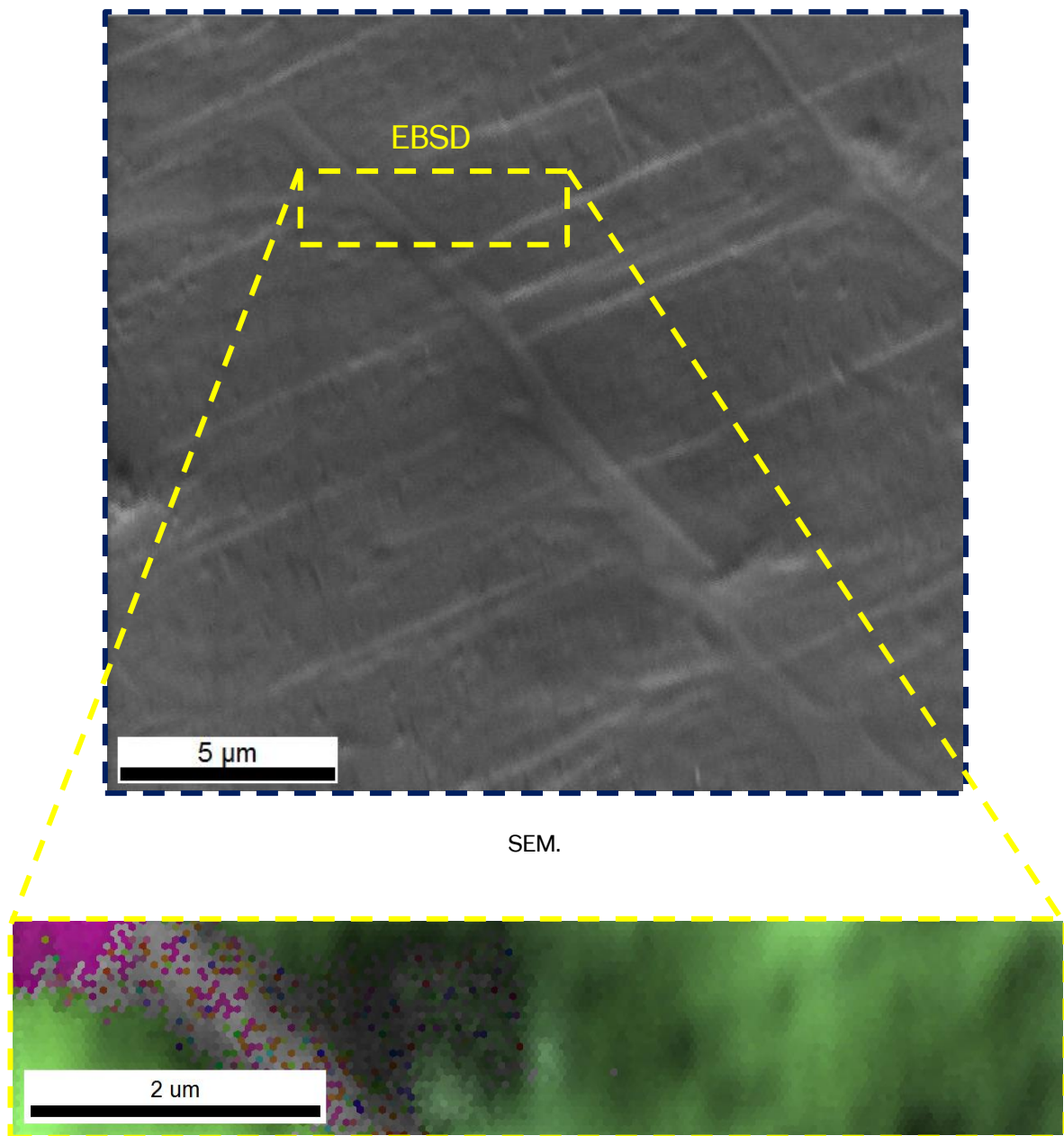
IPF. Scanned with a 2x2 binning rate and a step size of 0.2 μm . Scale bar 10 μm



Misorientation map of the scan using Kernel Average 1st neighbour. Data cleaned up by Kuwahara filter applied to first neighbour for two iterations. Grains of size less than 5 pixels removed. Overlaid on IQ map (50% transparency).

Figure 3.77 – Increased magnification SEM & EBSD images of erosion features. Approximately 2.5 mm from the edge of the coupon. Annealed Ti-6Al-4V RD 10 minutes after WDE testing.

Figure 3.78 shows the “SEM 2” region noted in Figure 3.77 at a higher magnification. Figure 3.78 also shows results of an EBSD scan with a small step size and a reduced binning rate, though this did not add any further detail.



IPF overlaid on an IQ map. Scanned with a 1x1 binning rate and a step size of 0.05 μm.

Figure 3.78 – Higher magnification images of the “SEM 2” area highlighted in Figure 3.77. Annealed Ti-6Al-4V RD 10 minutes after WDE testing.

3.5 Discussion

Although efforts were made to maintain a similar droplet size and flow characteristics, practicalities meant the original nozzle had to be changed following the 36-hour tests. However, consistency was maintained for the incubation period tests which used the same nozzle throughout. The effect of changing nozzle is not considered significant.

In the 36-hour advanced erosion tests, the Ti-6Al-4V crater surfaces (Figure 3.39) appeared rough, whereas the Ti-15Mo erosion scar displayed fatigue striations (Figure 3.42). This suggests the Ti-6Al-4V failed in a more brittle manner, in line with expectations as the predominantly α -phase alloy is strain-rate sensitive. The less strain-rate sensitive β -phase Ti-15Mo displays a more gradual, ductile failure. This appears to be reflected in the mass loss data in Figure 3.35 – the incubation period of Ti-6Al-4V ends suddenly when advanced erosion begins (mass loss increases rapidly), whereas mass loss increases more gradually in the incubation period of Ti-15Mo before transitioning into the advanced erosion regime. Many researchers focus on increasing the incubation period for as long as possible, ignoring the advanced erosion rate which could be high, such as the white squares in Figure 3.79. Alternatively, it may be beneficial to use a material with a more linear erosion rate (e.g. the orange squares in Figure 3.79), as this would be less prone to a rapid failure and more predictable when designing maintenance regimes.

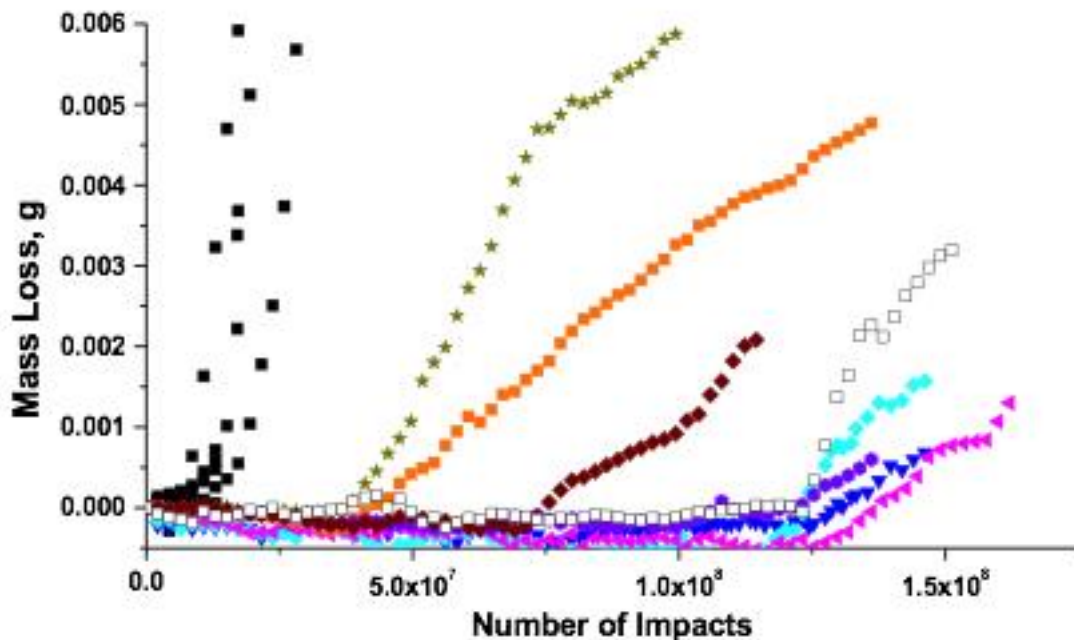


Figure 3.79 – Mass loss curves for various materials [77].

In the advanced erosion crater in Figure 3.45 there is limited evidence of localised deformation such as twinning or slip at the sectioned crater surface. Figure 3.46 shows there is little subsurface deformation, apart from cracks which appear to originate from the surface such as in Figure 3.47. This is in-line with theory; that advanced erosion is mechanically driven – hydraulic penetration forcing cracks wider and driving crack growth. This occurs rapidly and leads to material loss before other mechanisms can begin to cause other microstructural deformation. The analysis of eroded surfaces in this level of detail, in particular with EBSD, has not been researched elsewhere.

Short term tests in the incubation period produced erosion features similar to those observed in the literature, such as micropits and slip. Grain tilting, reported by some authors [9], [57], [59], was not noted in this work. However those researchers remark that grain tilting can transition into cracks or micropits rapidly, so it may be difficult to detect at the right moment.

Partial slip band (PSB) intrusions and extrusions, typically caused by fatigue loading, have been theorised for WDE before [55], [56]. There are indentations observed in the incubation period which may be PSB intrusions such as in Figure 3.51, although no extrusions have been observed. In general, there is localised misorientation within the indentations, as in Figure 3.71.

Slip bands appear to form in some grains during the incubation period, such as in Figure 3.64, an SEM image of a 5 minute test on Ti-15Mo. Slip bands were more apparent in the annealed Ti-6Al-4V alloy, as in Figure 3.70. Slip bands are most visible when using SEM, though EBSD was useful in identifying which crystallographic plane the slip was occurring in.

The use of EBSD for analysis of WDE is novel. EBSD was used because expected deformation mechanisms such as twinning would show up clearly. Twinning was not observed in either the advanced erosion or the incubation period tests. EBSD was useful for quantifying local effects around deformation, such as micropits, especially using misorientation maps. However the as-received microstructures of Ti-15Mo and Ti-6Al-4V had a large amount of residual misorientation. The annealed Ti-6Al-4V had a much less misoriented microstructure so proved useful for investigating early-stage WDE damage. For example, Figure 3.76 and Figure 3.77 show misorientation due to micropits very clearly.

Examining where and why erosion features begin has not been widely reported in the literature. Micropits often appeared to start in homogenous regions such as within grains, rather than at grain boundaries. Grain boundaries might have intuitively been

assumed to be initiation points since they represent an inhomogeneity in the material where the grain orientations change. Micropits formed in α phase rather than β in the bi-modal Ti-6Al-4V alloy Figure 3.60. However, this may just be chance, due to the abundance of α relative to β (roughly 95% of the alloy is α phase).

4 QUASI-STATIC MATERIAL TESTS

4.1 Background

Many researchers in WDE and cavitation note fatigue-like damage [3], [32], [48], [51], [55], [57], [58], [60], [75]. Thomas and Brunton [59] correlate erosion endurance with S-N fatigue life. In their work, they plot impact velocity with number of impacts to a material loss limit. Both the limit of the incubation period (when measurable weight loss occurs) and the limit when erosion depth reaches 100 μm produce trendlines similar in appearance to fatigue curves. In WDE, the loading is similar to low cycle fatigue (LCF) which involves repeated high strains, so LCF tests were planned [47], [51], [58].

A stress-strain curve is needed to plan the LCF tests. A conventional stress-strain curve for a material obtained from a tensile test will also aid in understanding that material's properties. Additionally, there is an element of tensile loading in WDE, perhaps importantly as a component in a Rayleigh wave. The annealed Ti-6Al-4V was tested. There was an abundance of the annealed Ti-6Al-4V because it was to be used for LCF testing. There was limited Ti-15Mo and limited as-received Ti-6Al-4V, so these materials would only have been tensile tested if there were enough material left over following other experiments such as WDE and high-strain rate tests.

4.2 Experimental methods

Tensile test coupons were of the same dimensions as LCF coupons, illustrated in Figure 4.1. Ultimately it was not possible to conduct LCF experiments due to a series of lab failures.

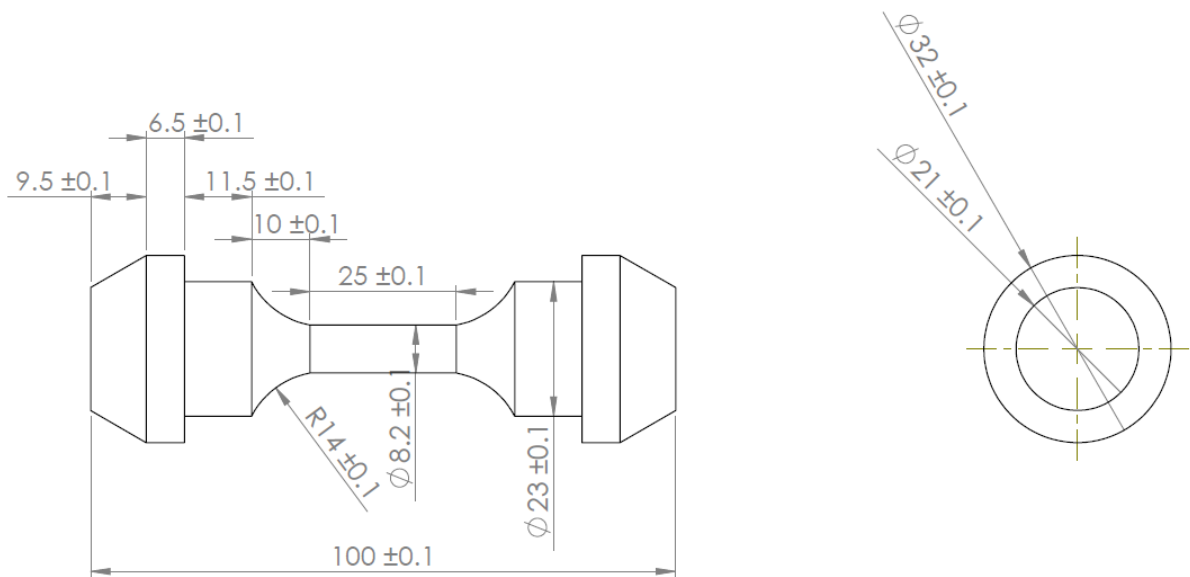


Figure 4.1 – Dimensions of the tensile test and low cycle fatigue test specimens (in mm).

Tensile testing was conducted on a Mates servo-hydraulic test machine with a 100 kN load cell. The test machine was controlled through a MOOG portable test controller. Testing was carried out under displacement control. Crosshead velocity was set to 1 mm·min⁻¹. For a gauge length of 25 mm, this equates to a strain rate of $4 \times 10^{-2} \text{ s}^{-1}$. Displacement was measured via an Epsilon 3542 extensometer with a gauge length of 25 mm. Force and extension data were logged in the controller and the test ran until failure.

Initially, the extensometer had to be calibrated. This was done by moving the extensometer in its range of ± 2.5 mm using a digital micrometer device with $\pm 0.01 \mu\text{m}$ precision. The extensometer was strain gauge based, so the voltage values were recorded in the test controller along with the corresponding extension in millimetres to produce a calibration gradient.

The load cell calibration was also checked by loading a reference load cell in compression and tension and comparing its readout to the controller's values. The load cell calibration was found to be incorrect so was adjusted accordingly.

A linear variable differential transformer (LVDT) is in-built in the machine to allow feedback control of the actuators position. The LVDT was checked using a 1 m rule with ± 1 mm precision. The position measured by the controller did not match the rule so the LVDT was calibrated against the ruler.

4.3 Analysis

Results were analysed using Mathworks MATLAB. Stress, σ , was calculated by $\sigma = \frac{F}{A}$ where F is the load cell force, and A the cross-sectional area in the sample gauge section. Strain, ε , was determined by $\varepsilon = \frac{x}{L}$ where x is the extension measured by the extensometer, and L is the gauge length over which the extensometer is measuring.

Young's modulus, E , is defined by $E = \frac{\sigma}{\varepsilon}$. Young's modulus is the linear gradient of the stress-strain plot. The gradient was calculated using a function called 'polyfit' in MATLAB for a 1st order polynomial. Because it was difficult to identify where the linear region ended, a 0.2 % proof stress was used as the linear limit.

Other properties could be extracted from the data. The offset yield strength is where the Young's modulus, offset by 0.2 % strain, intersects the stress-strain curve. The Ultimate Tensile Strength (UTS) is the maximum stress the sample supported. Resilience is the ability of a material to absorb energy when elastically loaded. It is the integral of the stress-strain curve in the elastic region. It can therefore be defined $U_r = \frac{\sigma_y \varepsilon_y}{2} = \frac{\sigma_y^2}{2E}$. Smart defined Ultimate Resilience as $U_{Sr} = \frac{\sigma_{UTS}^2}{2E}$ and stated materials with high ultimate resilience performed well in cavitation erosion [61].

Initially, the Hall-Petch equation relating yield strength to grain size was used to estimate yield strength, σ_Y , following annealing. Hall-Petch states $\sigma_Y = \sigma_i + kD^{-\frac{1}{2}}$ where D is the grain size, and σ_i and k are constants dependent on the material [78]. For titanium, σ_i is 80 MPa and k is 0.40 MPa·m^{-0.5}. Approximating the 500 μm size α colonies in the annealed Ti-6Al-4V to be equivalent to grains, Hall-Petch would estimate a yield strength of 818 MPa.

4.4 Results

Figure 4.2 is the stress-strain plot of the annealed Ti-6Al-4V tensile test.

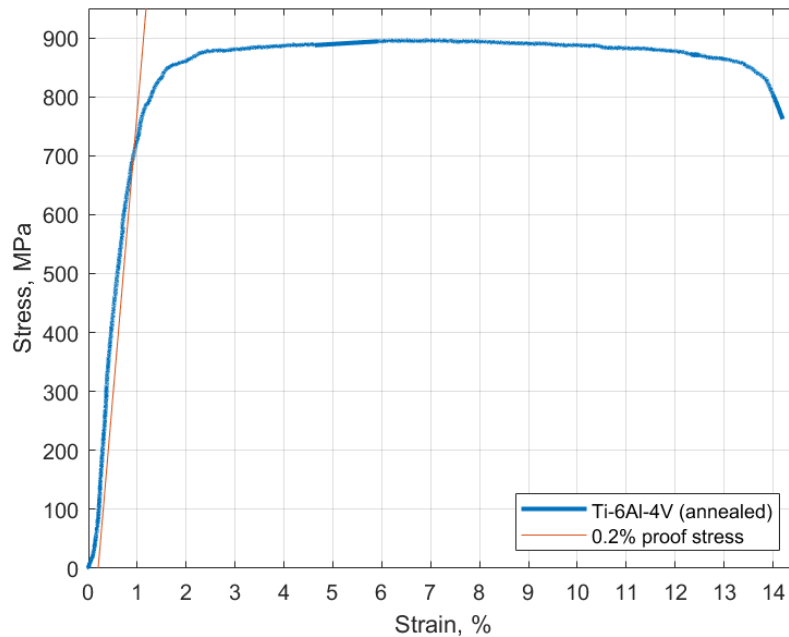


Figure 4.2 – Stress versus strain for the tensile test of annealed Ti-6Al-4V.

Material properties from the test are displayed in Table 4.1. For comparison, mechanical properties of the as-received alloys are also given.

Material property	Annealed Ti-6Al-4V	As-received Ti-15Mo	As-received Ti-6Al-4V
Young's modulus, GPa	97	78	107-122
Ultimate Tensile Strength (UTS), MPa	896	690	1068
Offset yield strength (0.2 % proof stress), MPa	710	483	999
Elongation, %	14	20	10
Smart's Ultimate Resilience, MPa	4.14	3.05	4.96
Resilience, MPa	2.60	1.50	4.36

Table 4.1 – Experimentally derived material properties of annealed Ti-6Al-4V, and properties of the as-received Ti-15Mo and Ti-6Al-4V from technical data sheets [79], [80].

4.5 Discussion

Although the LCF tests were not possible, due to extensive problems with the lab, LCF analysis might have been expected to find microstructural deformation such as slip and twinning, or crack growth rate might have been measured. Mechanical information such as strain hardening or softening due to strain loading could also have been extracted.

In the tensile testing, the Hall-Petch relation over-estimates the yield strength of the annealed Ti-6Al-4V slightly at 818 MPa, compared to the measured offset yield strength, 710 MPa. Callister and Rethwisch [81] note the Hall-Petch equation is not valid for very large grain materials so this may explain part of the discrepancy. Additionally, the colonies of similarly orientated α laths were approximated as 500 μm grains, when actually the α laths were lamellae interspersed by a β phase matrix.

Comparing the material properties; generally the Ti-15Mo appears to be the most ductile (having the greatest strain to failure), and as-received Ti-6Al-4V the least (with a 10% elongation to failure). The annealed Ti-6Al-4V sits almost halfway between the as-received alloys. Indeed most of its properties are around midway between the other alloys, so it should provide some basis of comparison between the two alloys.

The WDE test results are reflected in the material properties. The as-received Ti-6Al-4V performed better in terms of mass loss than the Ti-15Mo and had a higher Young's modulus, tensile strength and ultimate resilience. These properties may be important during the initial stages of erosion when the predominant mechanisms are direct deformation and stress wave propagation. Strength and resilience may be resisting the direct deformation. Many stress wave interactions involve a tensile component, particularly Rayleigh waves, which carry more than 60% of the impact energy [49], [50].

Ti-15Mo has a greater elongation to failure than the Ti-6Al-4V. In visual analyses of the eroded materials the Ti-15Mo appeared to fail gradually in a ductile fatiguing manner. A ductile failure is often preferable as brittle fractures can occur suddenly and rapidly, and are often difficult to account for in maintenance regimes. Smart's Ultimate Resilience takes into account the strain hardening ability of a material. This is important for water droplet erosion, where materials which strain harden appear to resist erosion. Strain hardening can be achieved by twinning, although the WDE tested materials in this work did not appear to twin.

The Ti-6Al-4V (annealed) was tensile tested to investigate the material's properties. The resulting stress-strain graph can also be used to plan the LCF tests.

5 HIGH STRAIN RATE MECHANICS

5.1 Background

Water droplet erosion occurs when droplets impact surfaces at high velocities, in some cases as high as $500 \text{ m}\cdot\text{s}^{-1}$. The speed of sound in air is around $340\text{-}350 \text{ m}\cdot\text{s}^{-1}$ under typical ambient conditions of temperature and pressure, so anything above this range is supersonic in nature. The strain rate due to impact at such velocities will therefore be high; some authors report it is greater than 10^6 s^{-1} [82].

Strain rate can be calculated knowing the velocity of one end of a deforming body relative to the other, and the length over which the deformation occurs. It is defined as $\dot{\epsilon} = \frac{v_2 - v_1}{L}$ where $\dot{\epsilon}$ is the rate of strain, v_2 and v_1 are the end velocities and L is the deformation length. If one end is fixed (i.e. $v_1 = 0$) then $\dot{\epsilon} = \frac{v_2}{L}$. For example, if the crosshead in a tensile test is moved at $50 \text{ mm}\cdot\text{s}^{-1}$ to deform a 25 mm gauge length testpiece, then the strain rate is 2 s^{-1} . Strain rate regimes, example test methods and example applications are given in Figure 5.1 below.

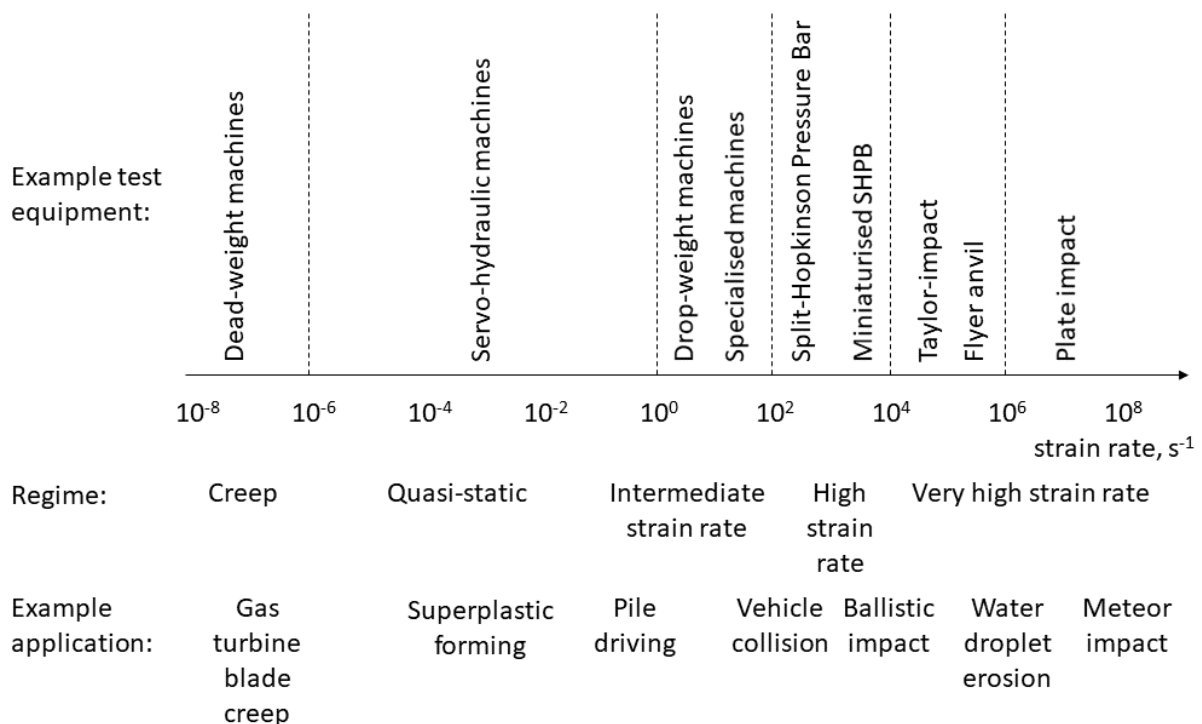


Figure 5.1 – Varying strain rate regimes, typical tests, and typical examples [83]–[85].

Materials perform differently at different strain rates. For example, Ti-6Al-4V performs well under low strain rates (creep) so is used in gas turbine fan and compressor

blades. The hcp structure of the predominantly α phase Ti-6Al-4V is able to slip or twin to accommodate deformation beyond the elastic limit (i.e. strain hardening). The material can also do this at high strain rate [86].

5.2 Literature review

5.2.1 High strain rate tensile testing

Resilience (the integral of a stress-strain curve, with the upper limit being either the Yield Stress, or sometimes the UTS) has been correlated with WDE before [47][61]. Tensile tests are usually conducted at strain rates between 10^{-5} s^{-1} to 10^{-3} s^{-1} [87]. It is possible to reach strain rates of 10^2 s^{-1} with a servo hydraulic machine by utilising a “slack adaptor”. The actuator must initially accelerate up to the constant velocity used for testing, so most authors use a lost motion device, or slack adaptor, to overcome inertia effects [88]–[90]. Figure 5.2 illustrates a typical device in the literature.

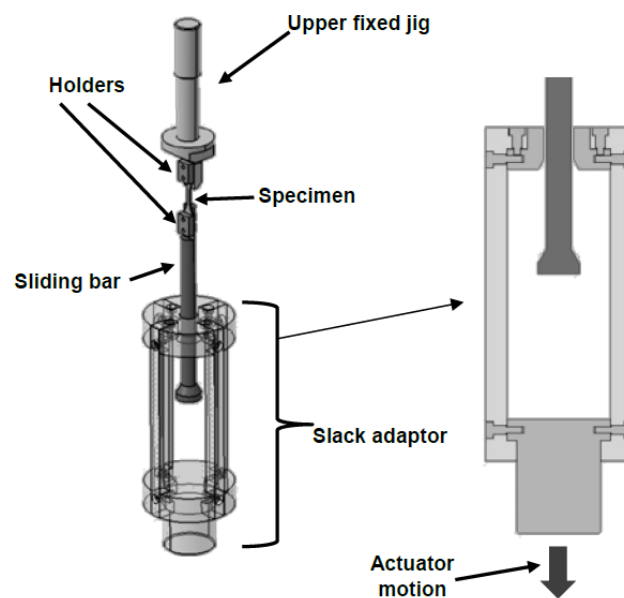


Figure 5.2 – Lost motion device or “slack adaptor” used to attain higher strain rates [88].

Strain rate can be calculated by dividing the velocity at which the deformation occurs by the length over which the deformation occurs. So a 10 mm gauge length deforming at $1 \text{ m}\cdot\text{s}^{-1}$ would theoretically deform at a strain rate of 100 s^{-1} . Realistically losses, due to machine compliance, mean actual strain rates are often lower than theoretically calculated.

5.2.2 Split Hopkinson pressure bar

A Split Hopkinson Pressure Bar (SHPB) may be able to produce strain rates on the order of 10^4 s^{-1} . A striker is used to impact an incident bar, as shown in Figure 5.3. The resultant stress wave travels through the bar and into the specimen. The wave can be measured by strain gauges which makes it possible to determine strain, strain rate and stress.

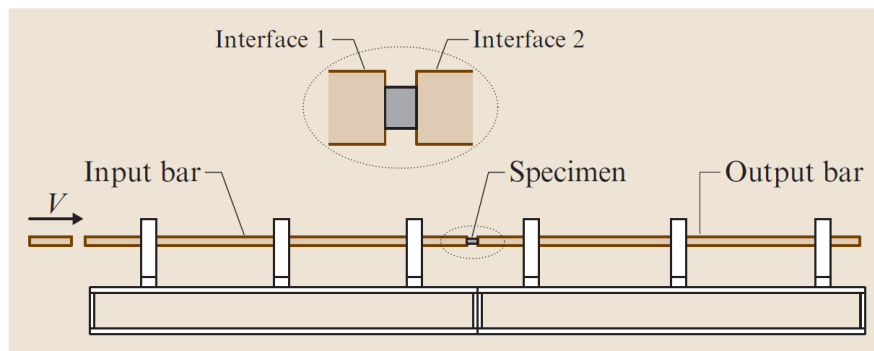


Figure 5.3 – Compressive Split Hopkinson Bar set-up [84].

WDE has elements of both compression and tension, particularly when considering stress wave interactions such as Rayleigh waves. The SHPB test is usually conducted in compression. It can be configured to load a specimen in tension, although this is a slightly more complex set-up.

The split Hopkinson pressure bar, also known as a Kolsky bar, was developed as a method of measuring the impact pressure of explosions or ballistic impacts [91]. Originally, the pressure from a blast or impact on one end of a long bar would be transmitted into another short bar which functioned as a momentum trap. The movement of this bar would indicate amplitude and time duration of the pressure wave. Kolsky [92] used two Hopkinson bars (so splitting the bar) and placed a small material specimen between the two bars. By measuring the stress pulse in the incident bar and stress pulse in the transmitter bar, the material specimen response could be inferred.

5.2.3 Other high-strain rate tests

Peak strain rates from defence related ballistics such as artillery shells (which may be travelling at velocities of $1000\text{-}2000 \text{ m}\cdot\text{s}^{-1}$) may be on the order of 10^5 s^{-1} to 10^6 s^{-1} [84]. Several methods fire a sample out of a barrel, usually attached to a larger flyer, to impact an anvil plate.

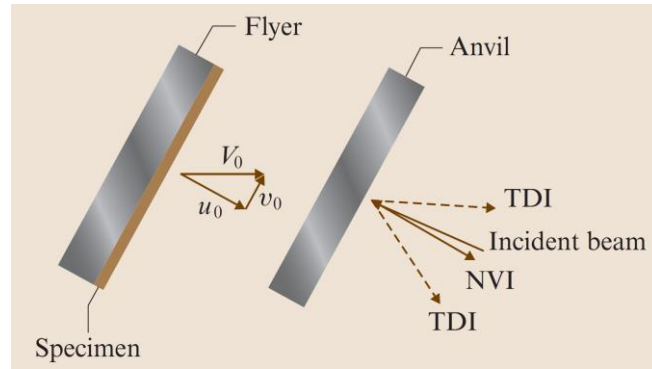


Figure 5.4 – A specimen mounted on a thick flyer plate, fired at an inclination to impact a parallel anvil [84].

5.3 Experimental methods

The Split Hopkinson Pressure Bar (SHPB) is used because of its robustness, straightforward set-up, and availability at the University of Sheffield. The analysis is also relatively simple, whereas higher strain rate tests cannot consider a 1D stress evaluation.

The SHPB test is usually conducted in compression, but can be configured to load a specimen in tension. A compressive SHPB test is shown schematically in Figure 5.3. A thin sheet metal diaphragm is tightened into the gas gun barrel, sealing a gas chamber. A nylon piston is positioned in the gun barrel. The striker bar is then placed in front of the piston. When the gas pressure is great enough to rupture the diaphragm, the gas pressure accelerates the piston, which launches the striker bar to impact the end of the incident bar once. This produces a compressive stress pulse, which is measured by the incident strain gauge. When the pulse reaches the end of the incident bar, part of the pulse is transmitted through the specimen and part of the pulse reflects, returning along the incident bar as a tensile pulse. The reflected, tensile pulse is measured by the incident strain gauge. The compressive stress pulse continues through the specimen and into the transmitter bar, where it is measured by another strain gauge.

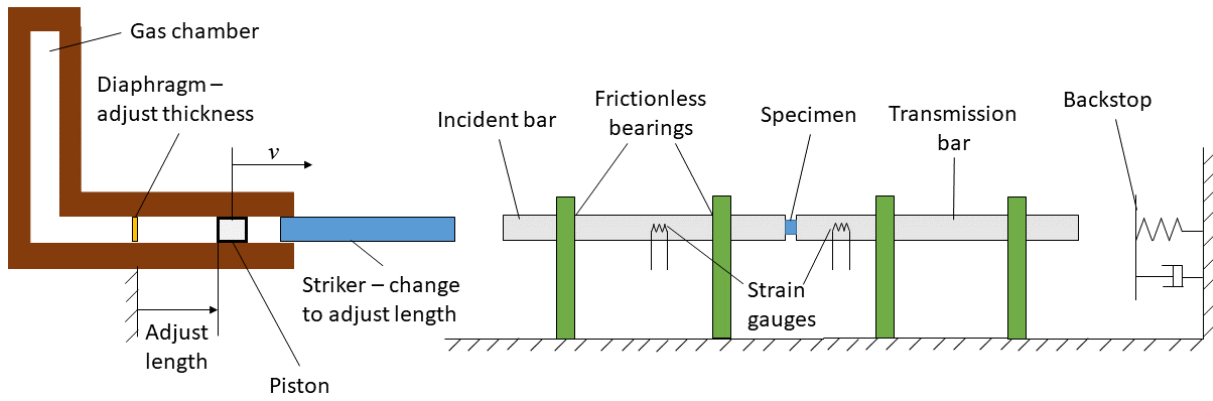


Figure 5.5 – Compressive Split Hopkinson Bar set-up.

The specimen is of a reduced diameter compared to the Hopkinson bars, so the stress pulse is amplified by a factor of $\frac{A_{Hopkinson}}{A_{sample}}$ where $A_{Hopkinson}$ is the cross-sectional area of the Hopkinson bar and A_{sample} is the cross-sectional area of the sample. Sample length is inversely proportional to strain rate, so sample length is kept to a minimum.

The test variables are stress, strain, and strain rate. There are several system parameters which can be varied to adjust these. For example, increasing the diaphragm thickness would require a greater gas pressure to rupture it, resulting in a larger stress pulse. This results in a larger stress, strain and strain rate applied to the sample. Other variables include the depth of the piston in the gun barrel, the initial depth of the striker in the barrel, length of the striker, the striker bar material, the distance from the striker bar to the incident bar, and other variables which couldn't be changed for this test such as Hopkinson bar material, length and diameter.

For tensile SHPB testing, the direction of the gas gun is reversed and a frame is used to connect the striker to the incident bar, as demonstrated in Figure 5.6.

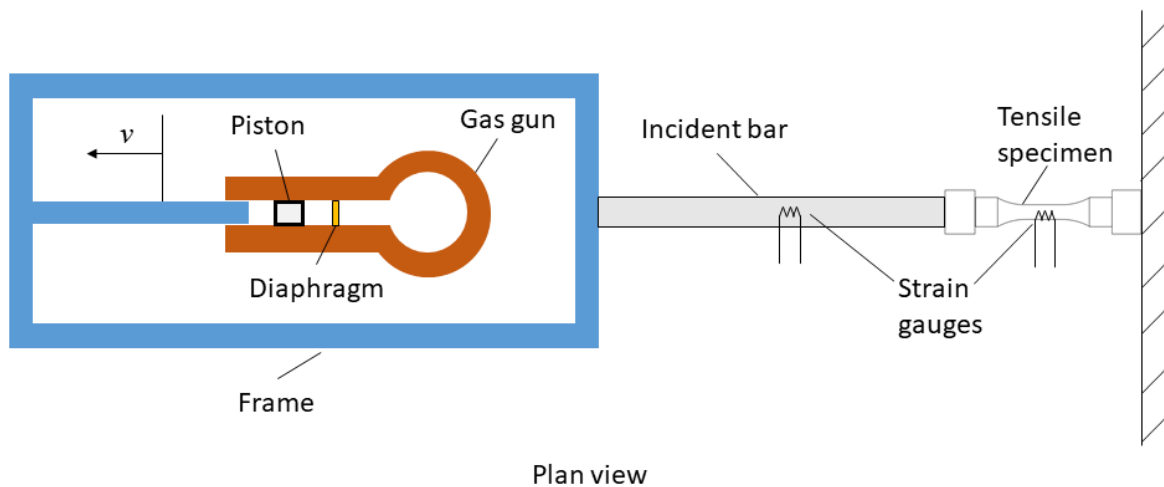


Figure 5.6 – Tensile SHPB set-up.

The gauge section of the tensile specimen allows a strain gauge to be bonded to the specimen and provide direct strain measurement. Kyowa KFEM-5-120-C1 high strain rate gauges were used, bonded with Kyowa CC36 adhesive. Due to the mass of the frame being greater than the compressive striker bar, and the longer length of the specimen, strain rates could not be expected to be as high as those developed in the compressive tests.

As-received Ti-15Mo and annealed Ti-6Al-4V were tested. Table 5.1 below summarises the test matrix for the samples available along with a range of strain rates it was possible to produce. Initially, six tests were planned; a tensile test for each of the two materials, a compressive test on 5 mm length samples of each material, and a compressive test on 2.5mm long samples of each material. Extra samples were prepared for trialling test conditions, hence several tests were actually possible, as detailed in Table 5.1.

Test	Strain rate	Material	Sample length	Number of tests
Compressive	High	Annealed Ti-6Al-4V	Short	3
			Long	1
		Ti-15Mo	Short	3
			Long	1
	Low	Annealed Ti-6Al-4V	Long	1
		Ti-15Mo		1
	Medium	Annealed Ti-6Al-4V	Long	1
		Ti-15Mo		1
Tensile	Constant	Steel	Constant	2
		Annealed Ti-6Al-4V		1
		Ti-15Mo		1

Table 5.1 – SHB test plan for the strain rates possible.

Compressive SHPB tests require a low length to diameter ratio (i.e. a short cylinder) – a longer specimen can lead to inertia errors since the stress wave needs to travel across the specimen near enough instantaneously. Dimensions of the compressive coupons are given in Figure 5.7. End friction can also be a problem, but careful specimen preparation can mitigate this by using an appropriate lubricant.

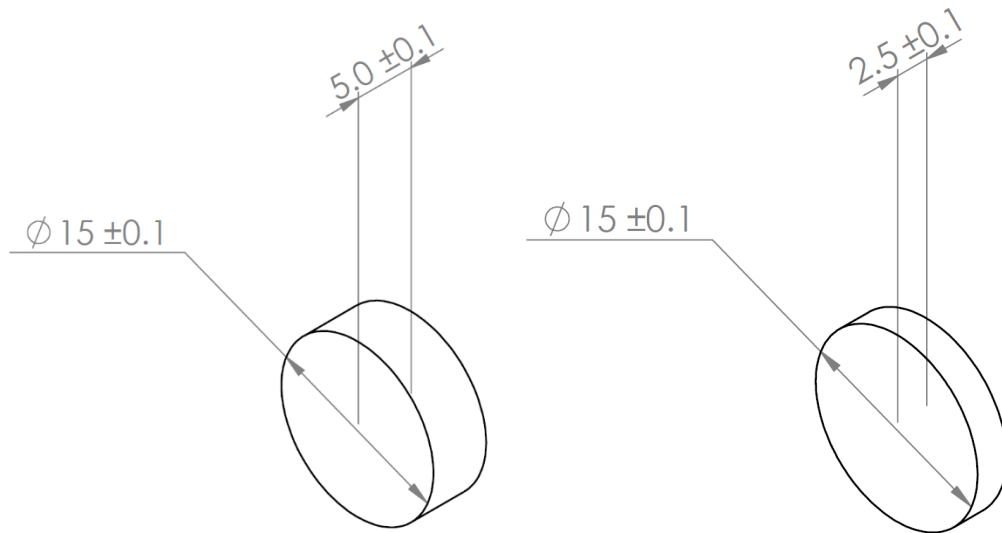


Figure 5.7 – The 'long' and 'short' SHB compressive test coupons.

Tensile tests require a small gauge diameter to concentrate stresses in the gauge. Dimensions of the tensile SHPB coupon are shown in Figure 5.8.

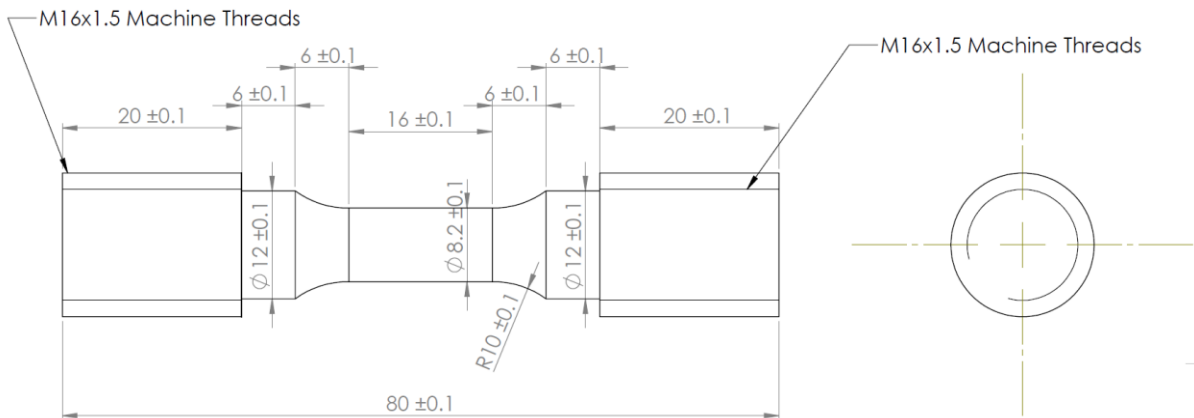


Figure 5.8 – SHB tensile test coupon dimensions.

5.4 Analysis

The measurement of the stress pulses by the strain gauges with time is illustrated in Figure 5.9. The compressive wave created by the striker's impact travels through the incident bar to the sample. Part of the compressive wave is reflected at the incident bar/sample interface as a tensile wave. Most of the compressive wave travels through the sample and into the transmission bar.

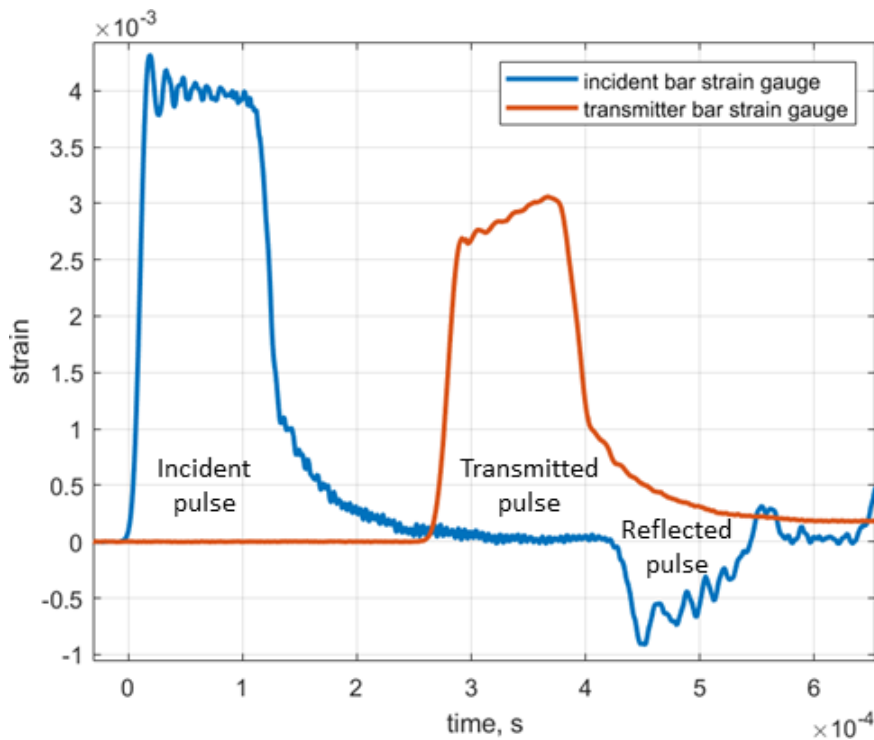


Figure 5.9 – Strain measurements from the strain gauges on the Hopkinson bars.

Assuming one-dimensional elastic wave theory, stress pulses travel in the Hopkinson bars at a velocity $c = \sqrt{\frac{E}{\rho}}$. Since the distance from the strain gauges to the bar ends is known, and the speed of sound in the bar materials is known, the strain at the bar ends (i.e. at the specimen faces) can be calculated. Provided the stress pulse remains within the elastic limit of the bar materials, the Young's modulus for the bars can be used to calculate stress from the strain values.

Stress at the incident bar/sample interface is calculated by $\sigma_{front} = \sigma_i + \sigma_r$ where σ_{front} is the front stress, σ_i is the incident stress and σ_r is the reflected stress. Stress at the sample-transmission bar interface is $\sigma_{back} = \sigma_t$ where σ_{back} is the back stress and σ_t the transmitted stress. Stress at the sample faces is amplified by the factor $\frac{A_{Hopkinson}}{A_{sample}}$. Sample axial stress is then assumed to be an average of the front and back stresses.

By calculating the Hopkinson bar displacements, the sample strain can be inferred. The derivation for bar displacements is given by Barr [83]. Incident bar displacement is calculated iteratively for each n^{th} element by $u_{i,n} = u_{i,n-1} + (\varepsilon_{i,n} - \varepsilon_{r,n})T_s c_i$ where u_i is incident bar displacement, ε_i is the incident strain pulse, ε_r is the reflected strain pulse, T_s is the timestep (the inverse of the sampling frequency), and c_i is the speed of sound in the incident bar. Cumulative transmission bar displacement is calculated in a similar manner by $u_{t,n} = u_{t,n-1} + \varepsilon_{t,n}T_s c_t$ where u_t is transmission bar displacement, ε_t is the transmitted strain pulse and c_t the wave speed in the transmission bar. Finally, axial strain in the sample is calculated element-by-element using $\varepsilon_{s,n} = \frac{u_{i,n} - u_{t,n}}{L}$ where ε_s is the sample strain and L is the initial sample length.

5.5 Results

Figure 5.10 below is the stress-strain plot for the compressive Ti-15Mo tests. Tests 2, 4 and 6 are performed under the same conditions; the highest strain rate possible and utilising a short sample length. Tests 2 and 4 show good agreement, test 6 is perhaps spurious in suggesting a greater strain to failure.

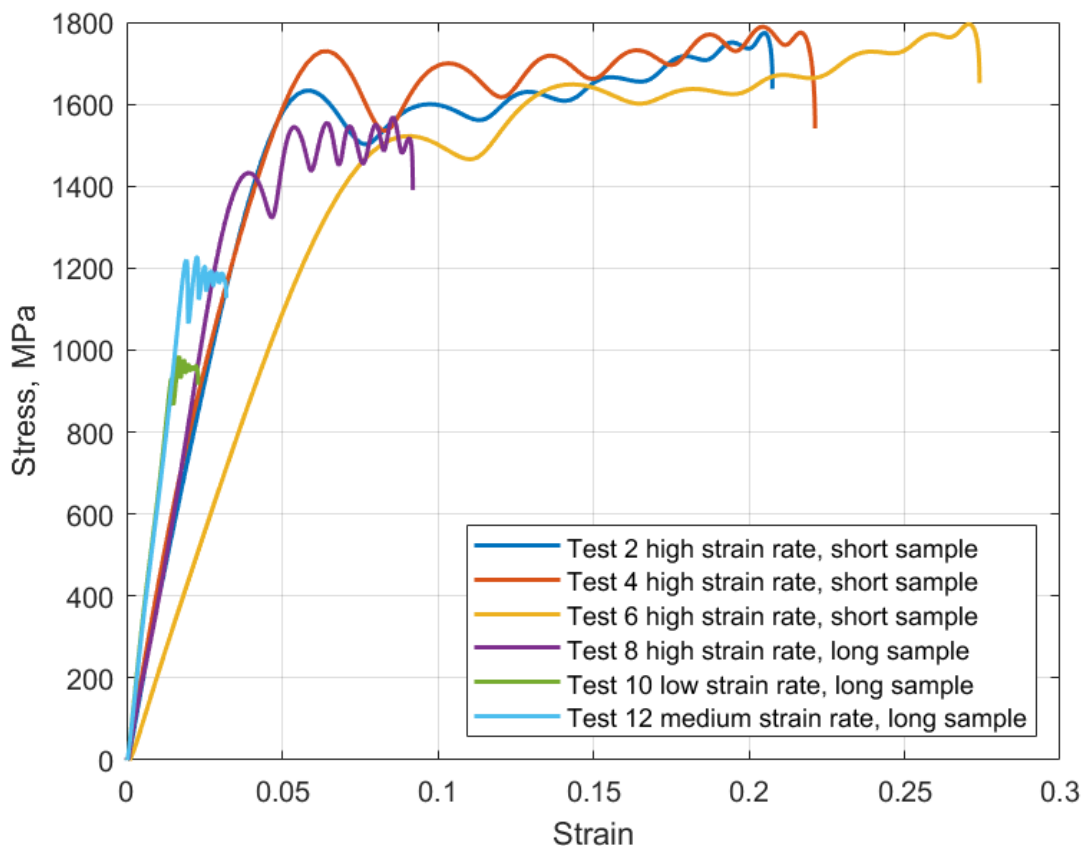


Figure 5.10 – Ti-15Mo samples tested at various strain rates.

Strain rate with time for the compressive Ti-15Mo tests is shown in Figure 5.11 below. The pulses all have common features; a nominal amplitude pulse for some duration (all approximately 1.3×10^{-4} seconds in length), higher frequency oscillations superimposed, and an initially high peak. The peak strain rate is probably the most significant, likely responsible for causing the microstructural deformation.

The highest strain rate tests reached 5500-6000 s^{-1} , although test 6 reached close to 8000 s^{-1} . Test 8 was performed under the same testing conditions as the high strain rate tests, but the sample length was twice as long at 5 mm, hence strain rate could be expected to be halved.

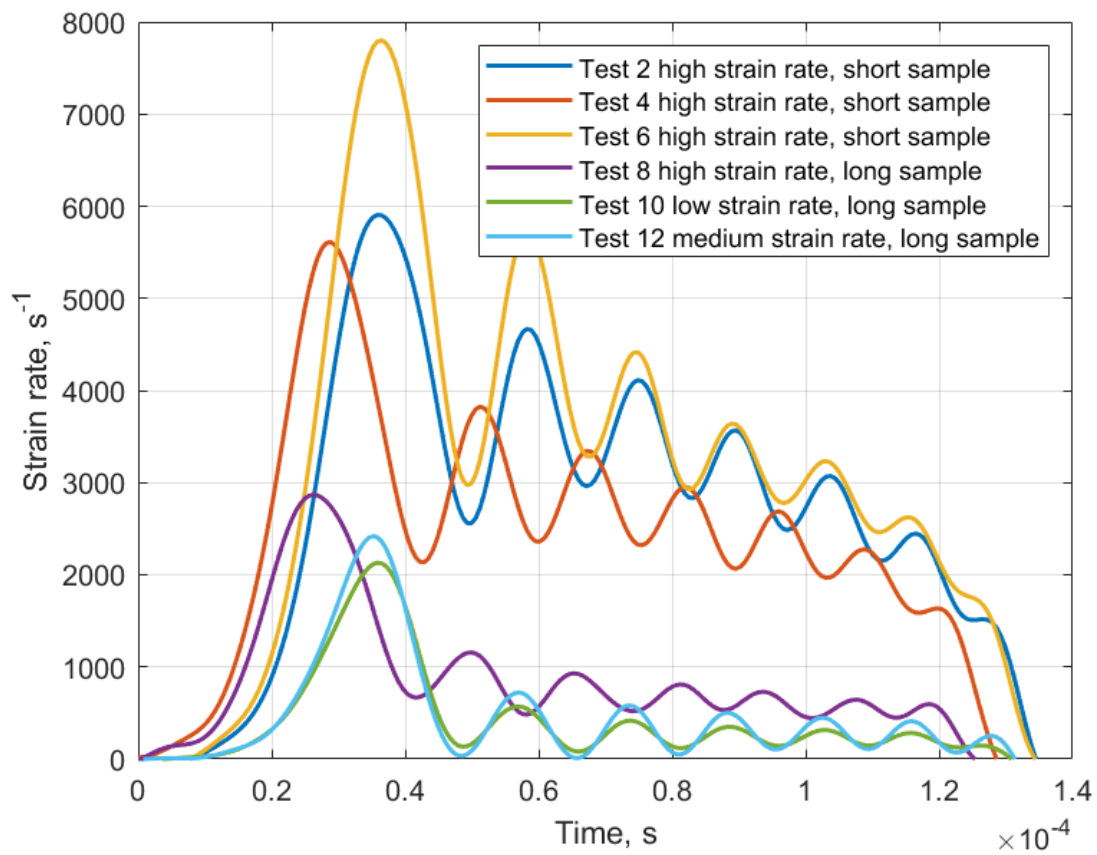


Figure 5.11 – Strain rate with time for the Ti-15Mo samples.

The stress versus strain plot for the compressive tests on annealed Ti-6Al-4V is shown below in Figure 5.12. Tests 3 and 5 were subject to the same conditions; the highest strain rate achievable on a 2.5 mm length sample. The results are similar, although test 5 records a higher strain to failure. Test 7 was also conducted at the highest strain rate but on a longer 5mm length sample.

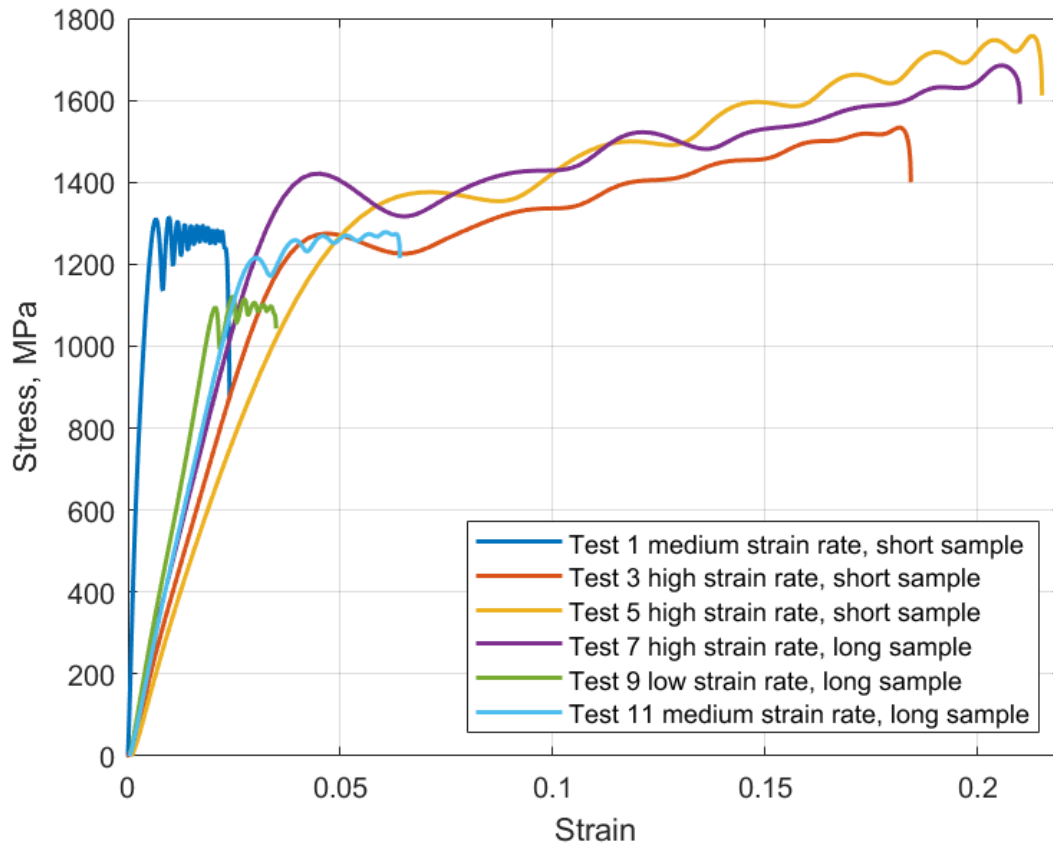


Figure 5.12 – Annealed Ti-6Al-4V samples tested at various strain rates.

Strain rate with time for the annealed Ti-6Al-4V is shown in Figure 5.13 below. Test 1 was the first test on any sample and utilised a longer striker bar in a different set-up. By changing to a shorter striker bar, a higher strain rate could be achieved, but for a shorter time period.

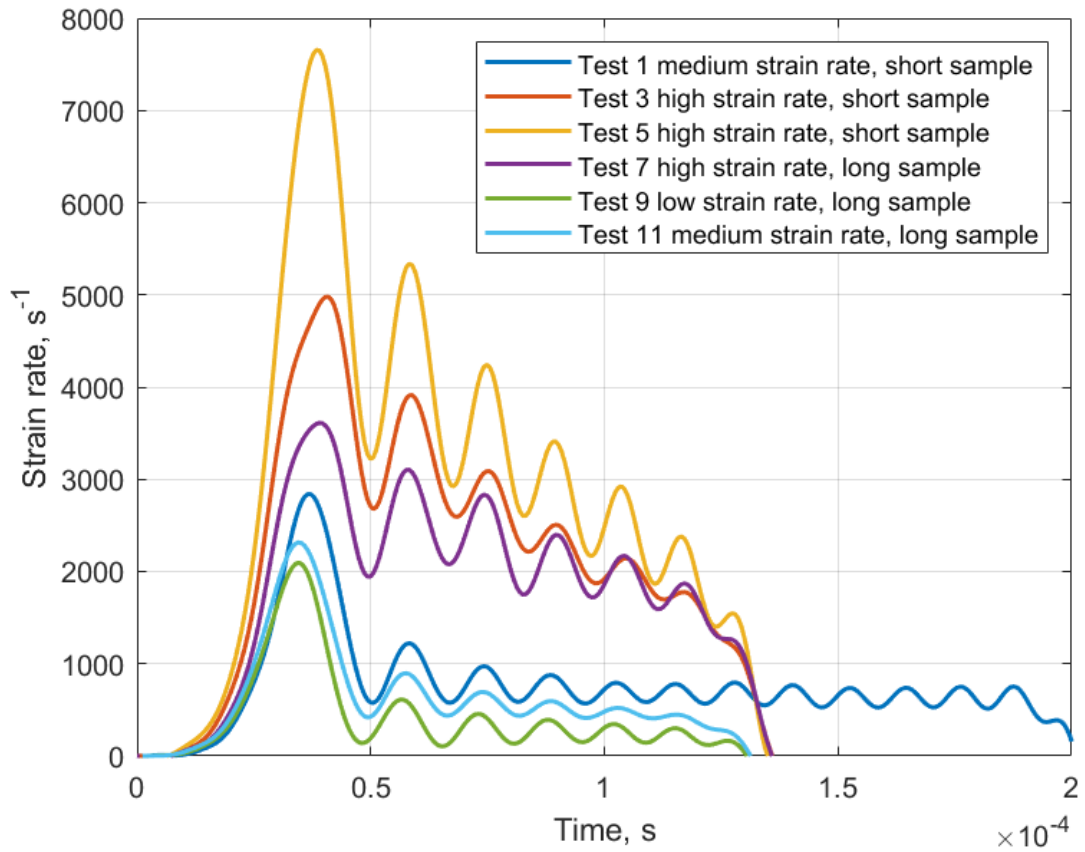


Figure 5.13 – Strain rate with time for the annealed Ti-6Al-4V samples.

The tensile set-up was slightly different; in this case a strain gauge on the sample could be used to measure strain directly. Figure 5.13 below is the stress-strain plot for the tensile SHPB tests. The quasi-static tensile test of the annealed Ti-6Al-4V is also plotted for comparison. The high strain rate tests can support a much greater stress before failure, but plastic strain to failure is a lot lower.

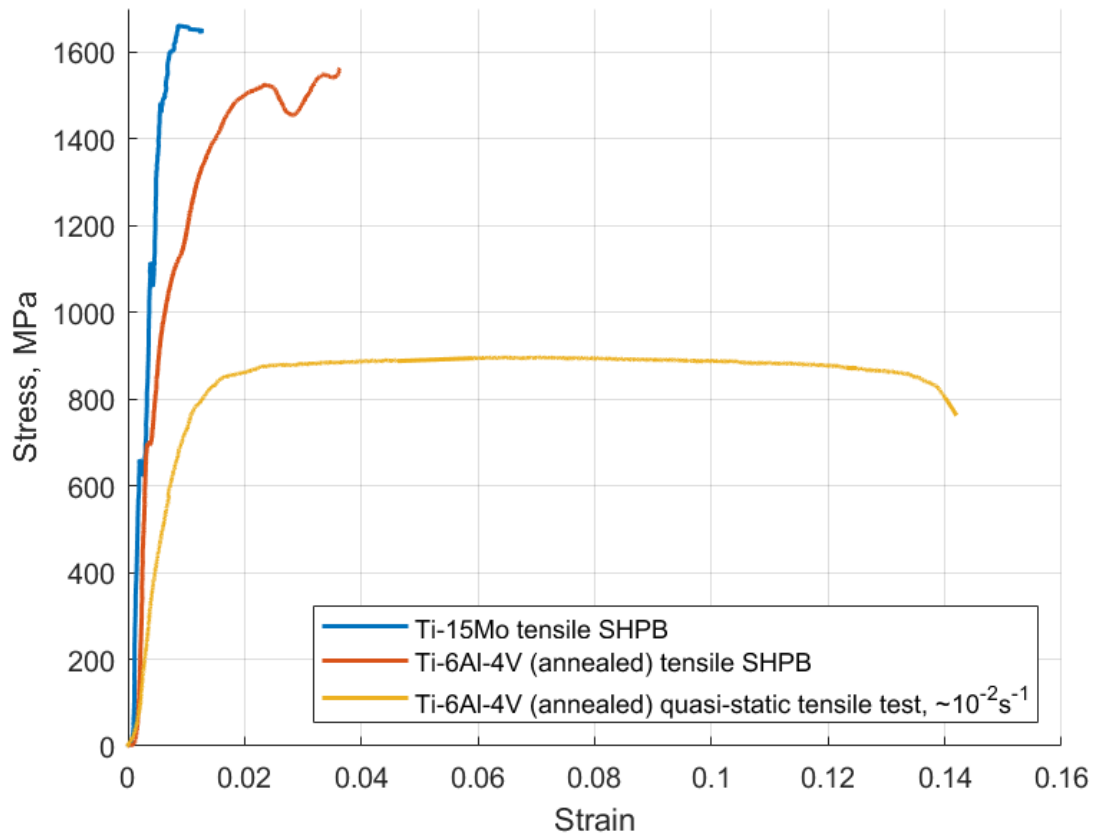


Figure 5.14 – Annealed Ti-6Al-4V and Ti-15Mo tested in tensile Split Hopkinson Pressure Bar. The result of the quasi-static tensile test is also included for comparison.

The strain rate against time for the tensile SHPB tests is shown in Figure 5.15 below. Annealed Ti-6Al-4V reached a maximum strain rate of approximately 280 s^{-1} ahead of failure; Ti-15Mo reached a strain rate of around 120 s^{-1} before failing. However, the Ti-15Mo was subject to a higher load (stress) than the annealed Ti-6Al-4V sample. This is reflected in the sample failure mechanisms; the Ti-15Mo sample failed by a brittle fracture, the annealed Ti-6Al-4V had some necking before failure.

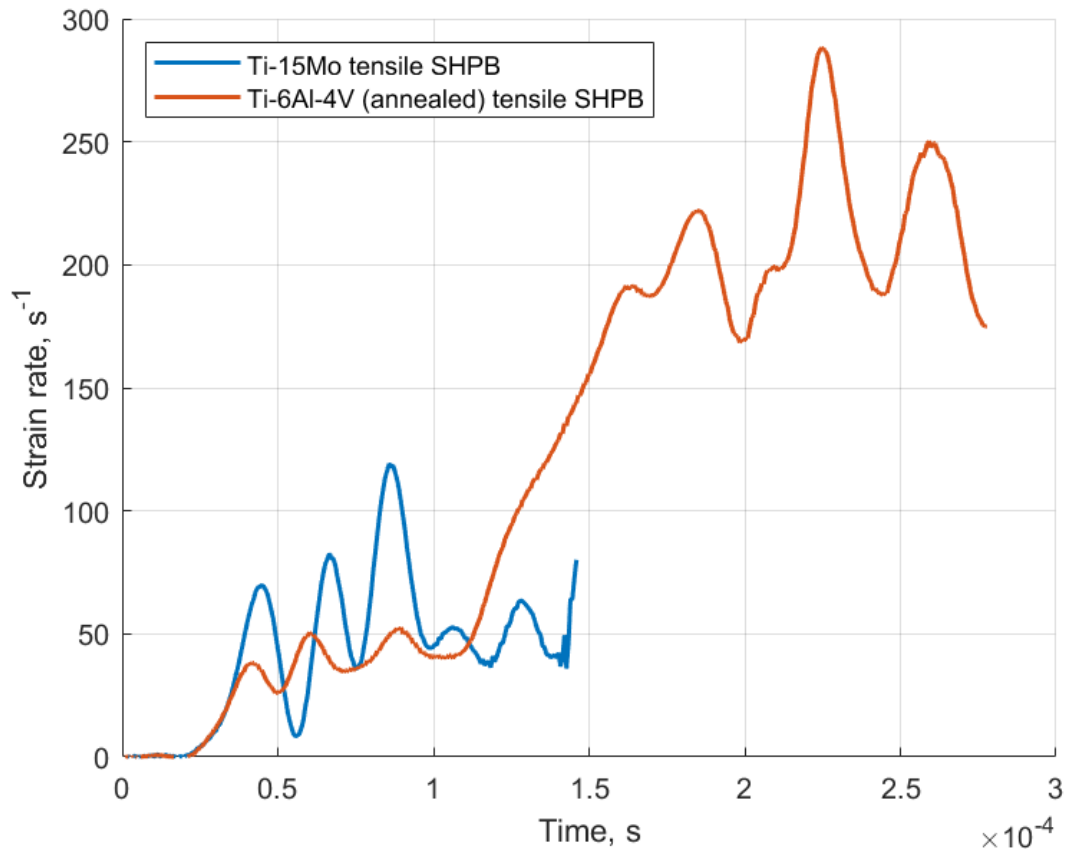
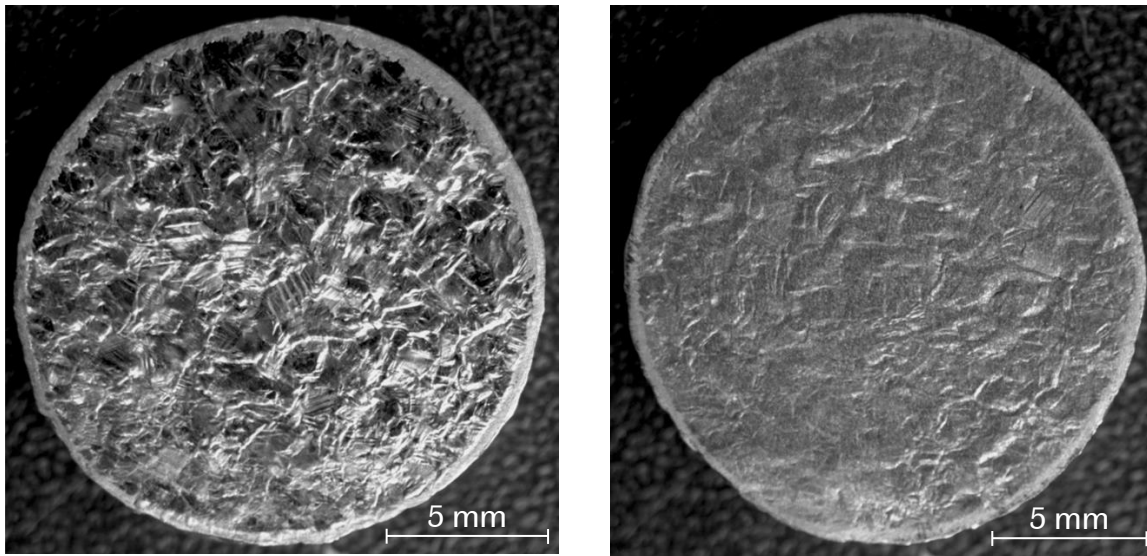


Figure 5.15 – Strain rate with time for the Ti-15Mo and annealed Ti-6Al-4V tensile SHPB tests.

5.5.1 Test 5 – annealed Ti-6Al-4V at ‘high’ strain rate

Further analysis of the compressive test coupons was performed using conventional light microscopy, Alicona focus variation microscopy and profilometry, SE microscopy and EBSD. Figure 5.16 below shows photographs of an annealed Ti-6Al-4V sample tested at high strain rate. Samples had initially been prepared for SHPB testing by metallographic polishing, to minimise loading on asperities. The side facing the incident stress pulse shows a lot of deformation resulting in surface texturing. The side which the stress pulse reaches last does not have as pronounced texturing and has also become duller and less reflective.



“Front” of sample.

“Back” of sample.

Figure 5.16 – Photographs of test number 5. Annealed Ti-6Al-4V tested at a peak strain rate of 7700 s^{-1} .
Peak strain 22 %. Peak stress 1750 MPa.

Figure 5.17 shows the Alicona image resulting from a scan of the “front” face, which illustrates the surface texture in more detail.

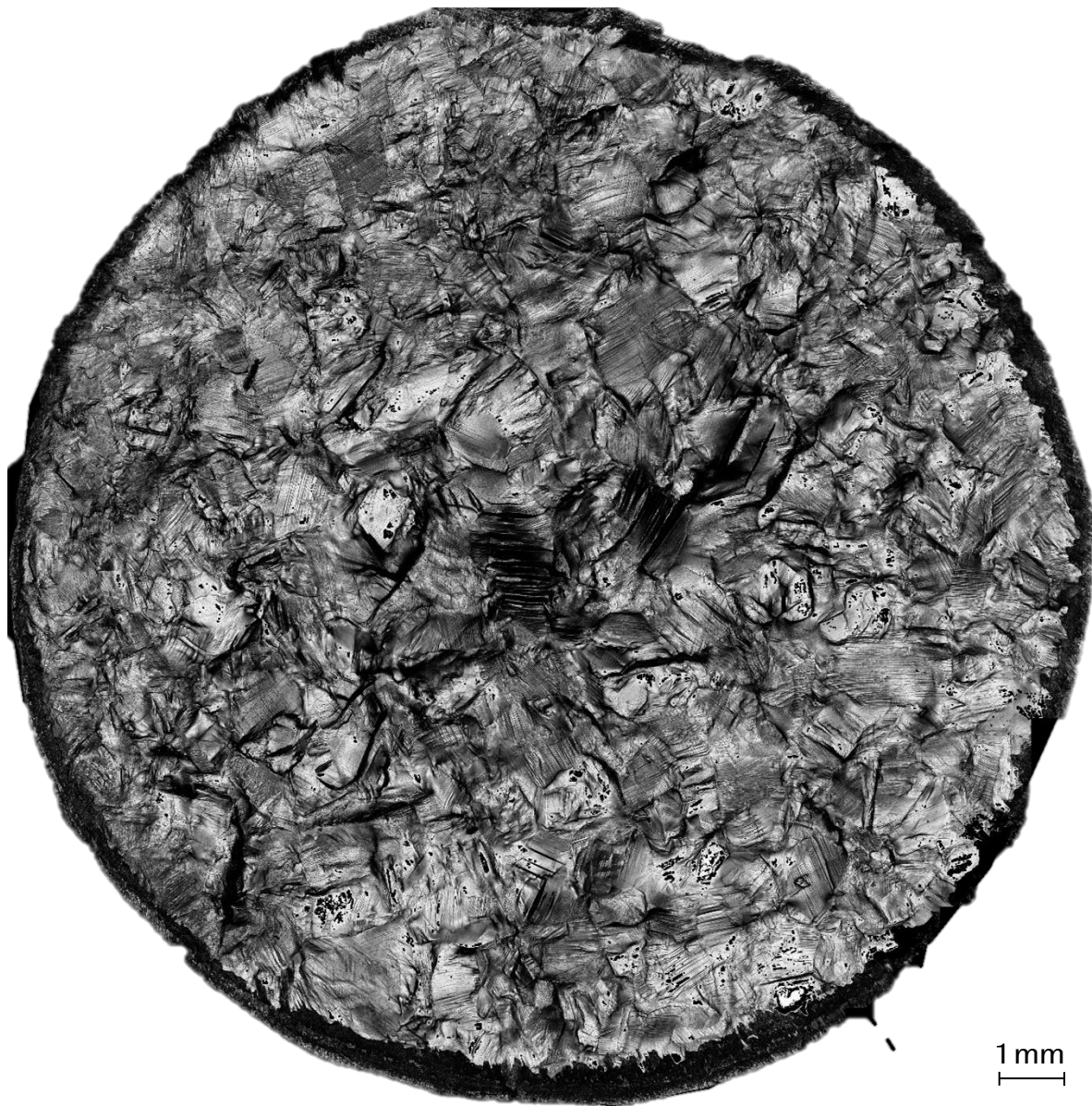


Figure 5.17 – Confocal microscopy of test number 5. Annealed Ti-6Al-4V tested at a peak strain rate of 7700 s^{-1} . Peak strain 22 %. Peak stress 1750 MPa.

SEM was used to characterise the surface at a higher magnification. Figure 5.18 and Figure 5.19 show a region of slip bands examined in increasing magnification.

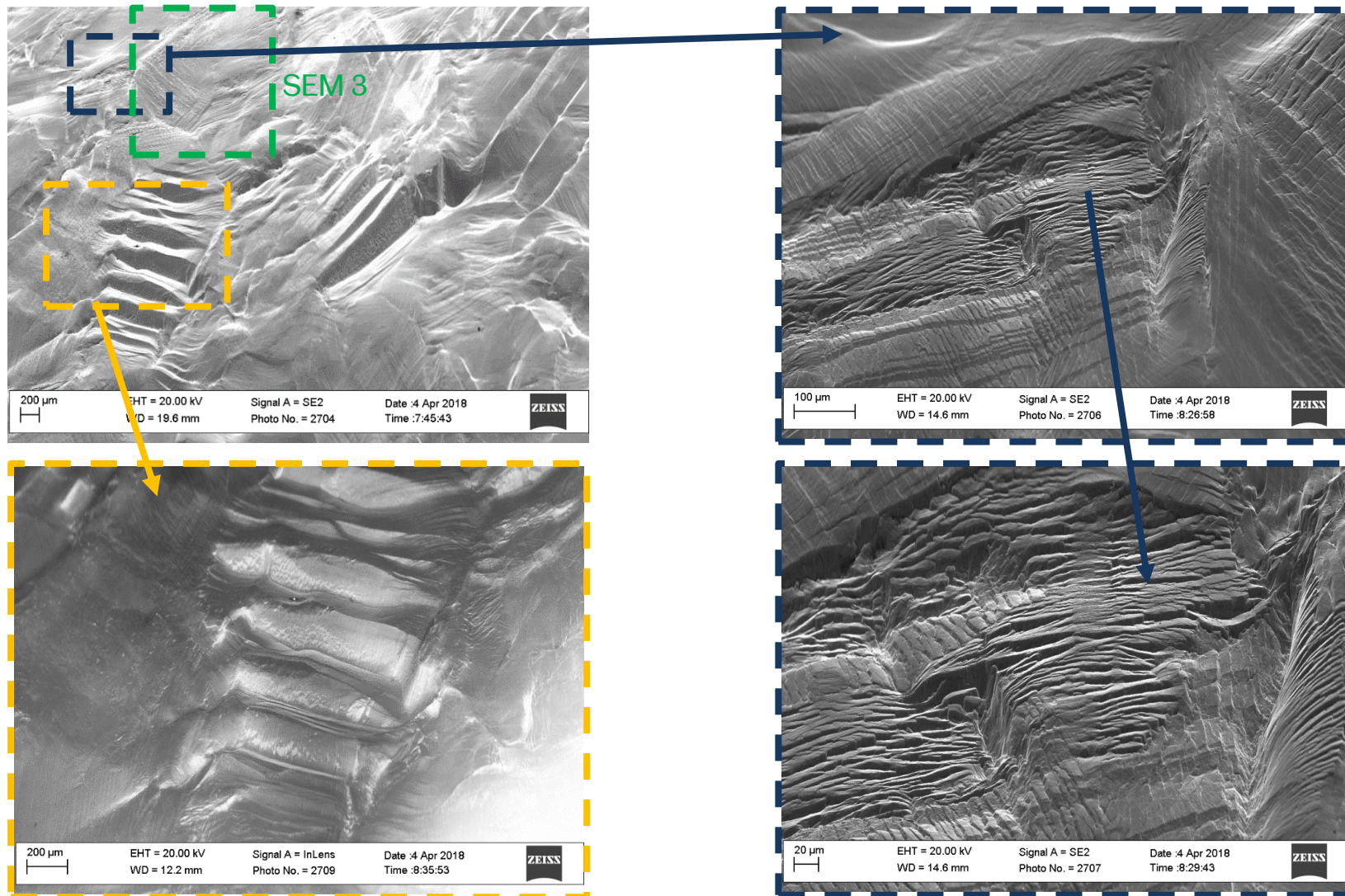


Figure 5.18 – SEM images of test number 5. Annealed Ti-6Al-4V tested at a peak strain rate of 7700 s^{-1} .

Figure 5.19 is a higher magnification image of the “SEM 3” area marked in Figure 5.18. Apart from slip bands there may also be twins. EBSD was attempted here but the confidence in indexing was extremely low.

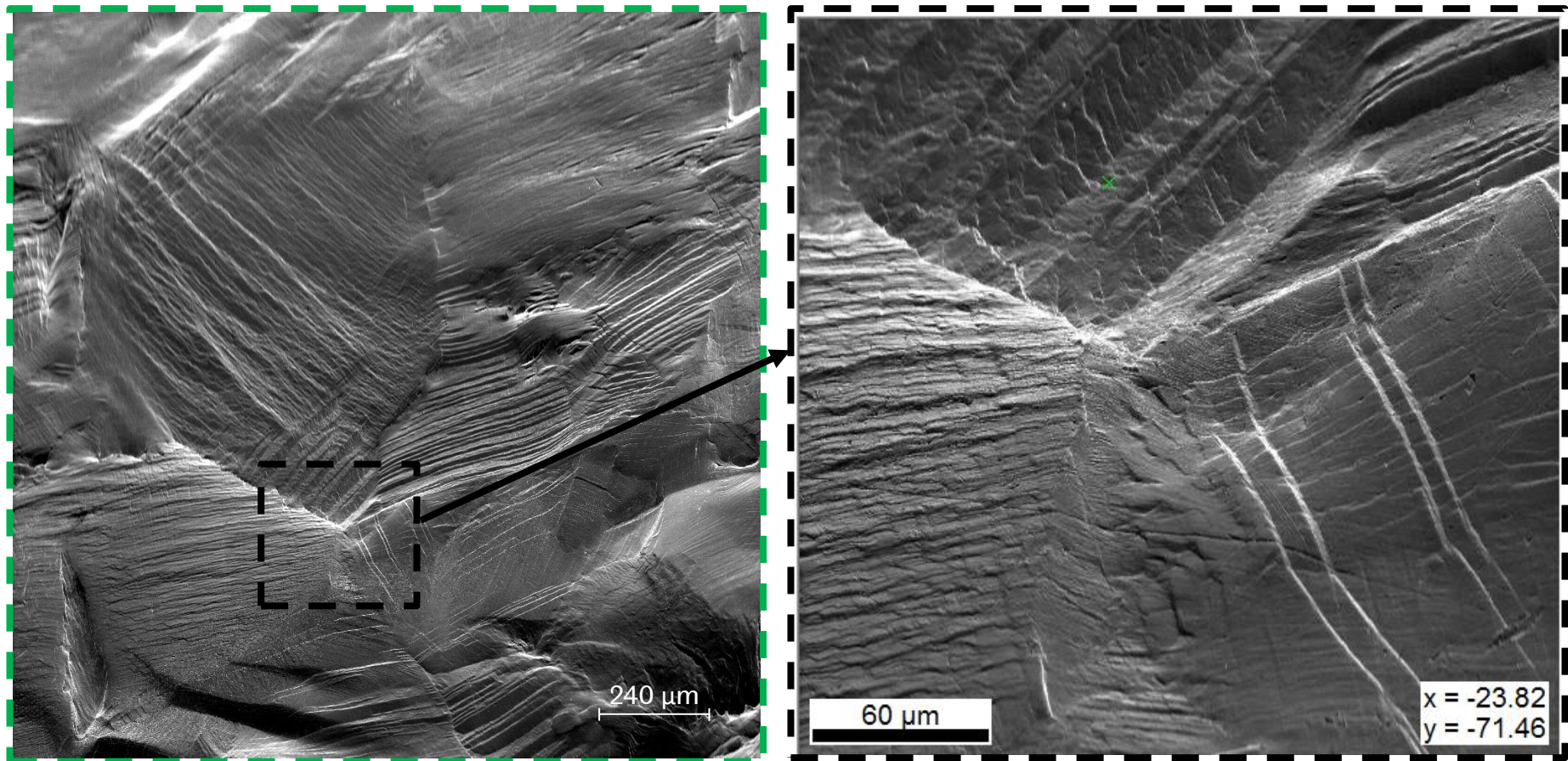
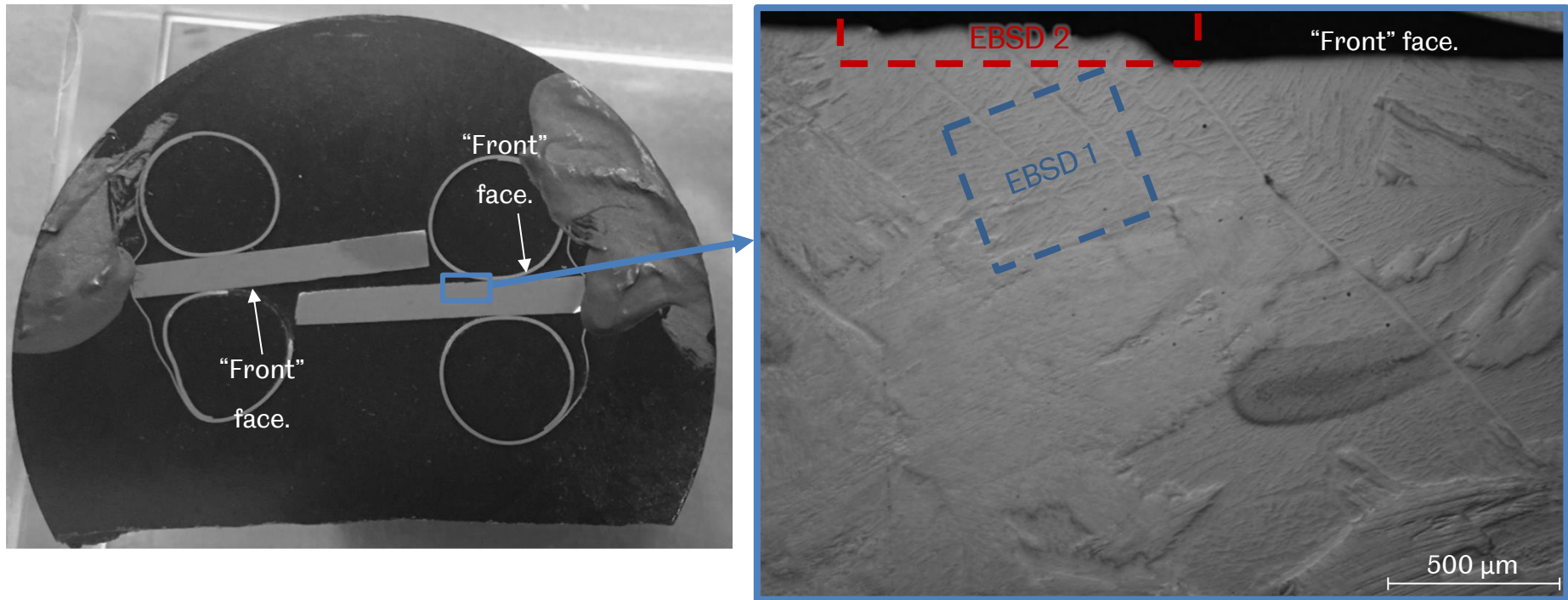


Figure 5.19 – Increased magnification images of “SEM 3” region in Figure 5.18. Annealed Ti-6Al-4V tested at a peak strain rate of 7700 s^{-1} .

The sample was sectioned and the two halves mounted as illustrated in Figure 5.20. Following metallographic polishing the samples could be examined. Figure 5.20 also shows a light microscope image, illustrating some regions of slip bands at the sample front face to be analysed by EBSD.

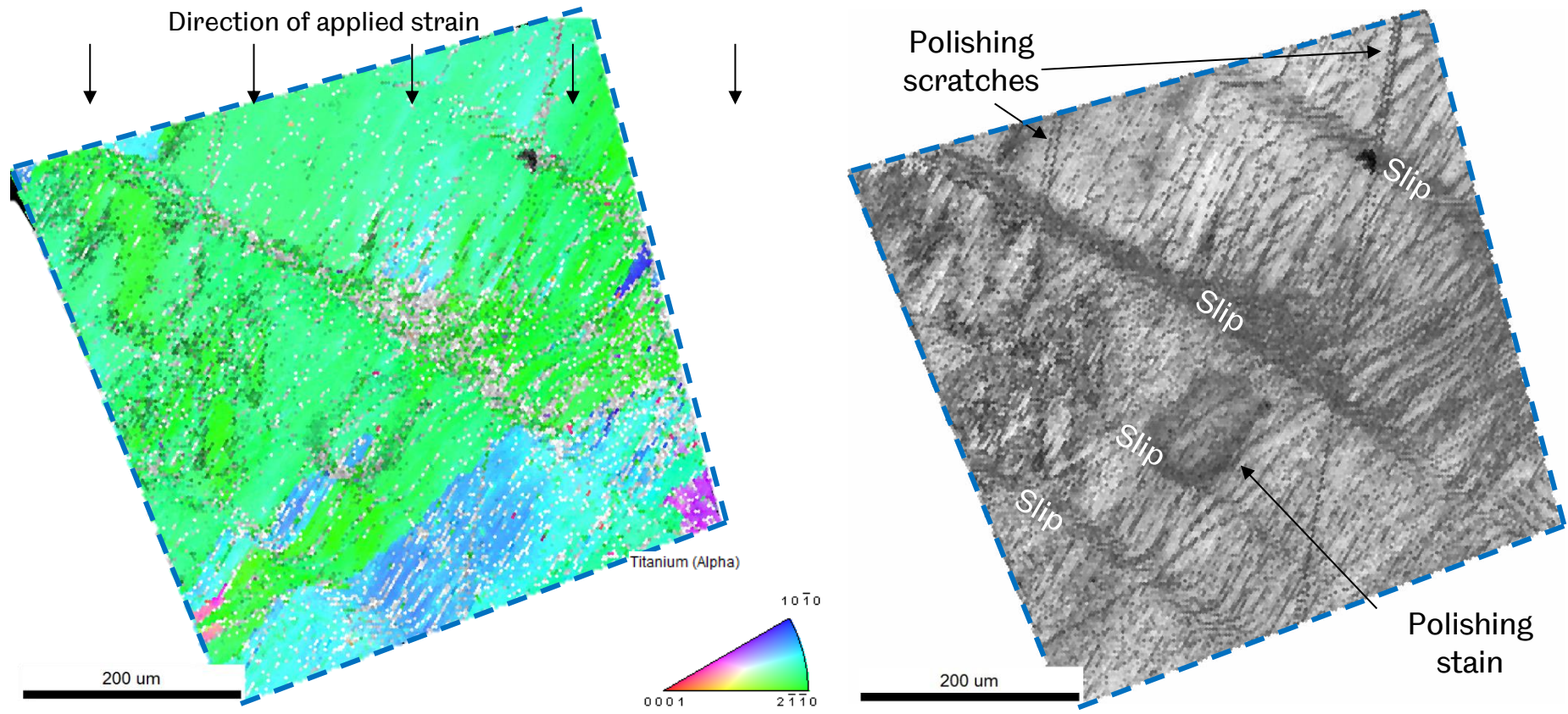


Sectioned and mounted with "Front" faces facing each other.

Light microscope image highlighting regions scanned by EBSD.

Figure 5.20 – Sectioning test number 5. Annealed Ti-6Al-4V tested at a peak strain rate of 7700 s^{-1} .

Figure 5.21 investigates the “EBSD 1” region circled in Figure 5.20. The IPF doesn't clearly show slip bands on its own, but overlaid on an Image Quality (IQ) map regions of slip become more obvious. The IQ map helps to identify the slip band regions a little more clearly.



Inverse Pole Figure (IPF) and Image Quality (IQ), scanned with a 2x2 binning rate and a step size of 3 μm . Grains of less than 2 pixels removed.

IQ map of the scan.

Figure 5.21 – EBSD near surface of “front” face of test number 5. Annealed Ti-6Al-4V tested at a peak strain rate of 7700 s^{-1} .

The “EBSD 2” region noted in Figure 5.20 was examined by EBSD, Figure 5.22 shows the results from a large EBSD scan at the surface where the stress pulse first reached the sample. The IQ map indicates the slip bands travel perpendicularly across the primary α laths. The IPF is particularly beneficial for establishing that the slip bands run through different orientations across grain boundaries.

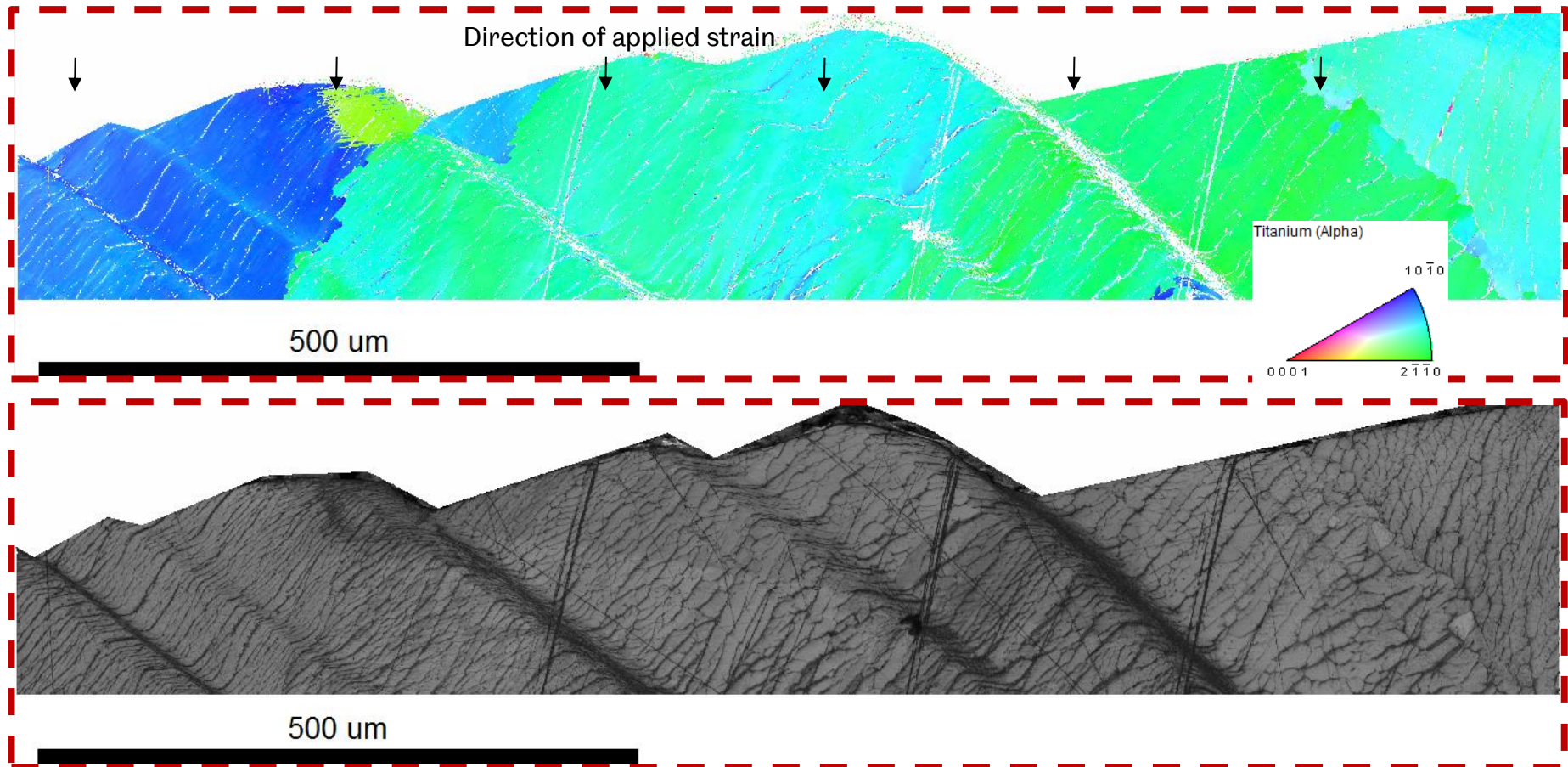
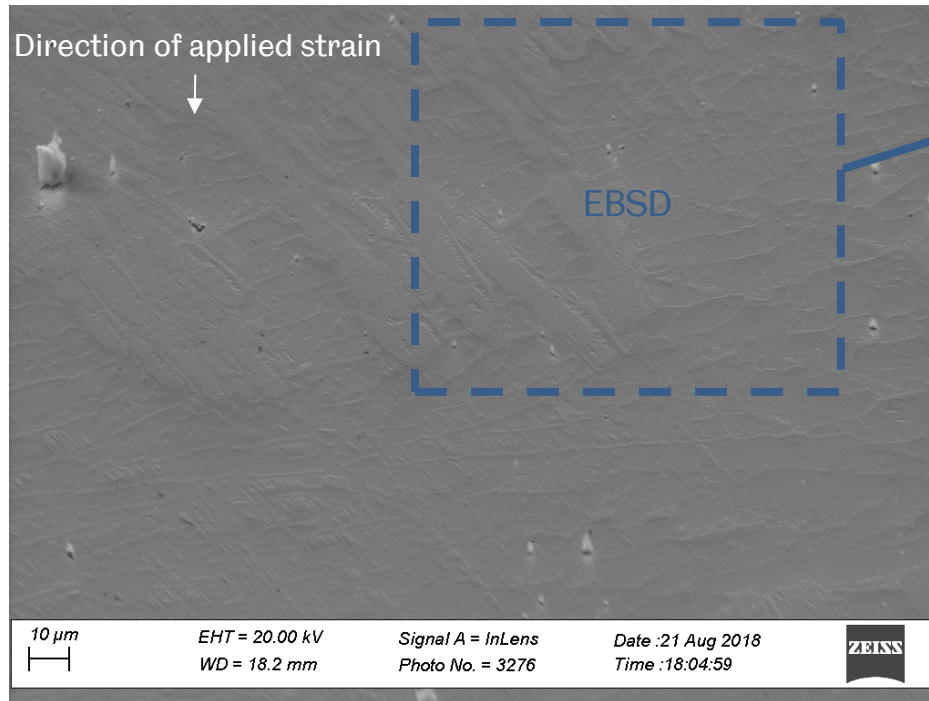
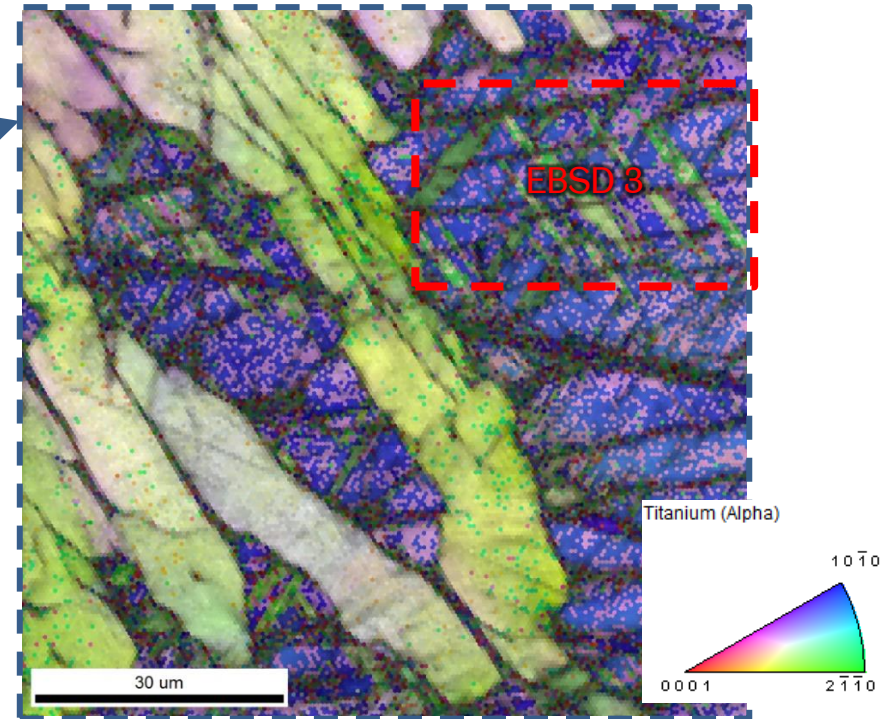


Figure 5.22 – IPF and IQ maps of “front” face of test number 5. Annealed Ti-6Al-4V tested at a peak strain rate of 7700 s^{-1} . Scanned with a 2×2 binning rate and a step size of 0.5 μm . Grains of less than 2 pixels size removed from the IPF.

Figure 5.23 shows SEM and EBSD images of a region within the sample bulk, approximately 1 mm away from the loading face. SEM identified patterns in the microstructure. The IPF overlaid on the IQ map revealed an area, marked “EBSD 3”, which may be heavily twinned. This was analysed further with EBSD using a smaller scan step size to acquire a higher resolution image.



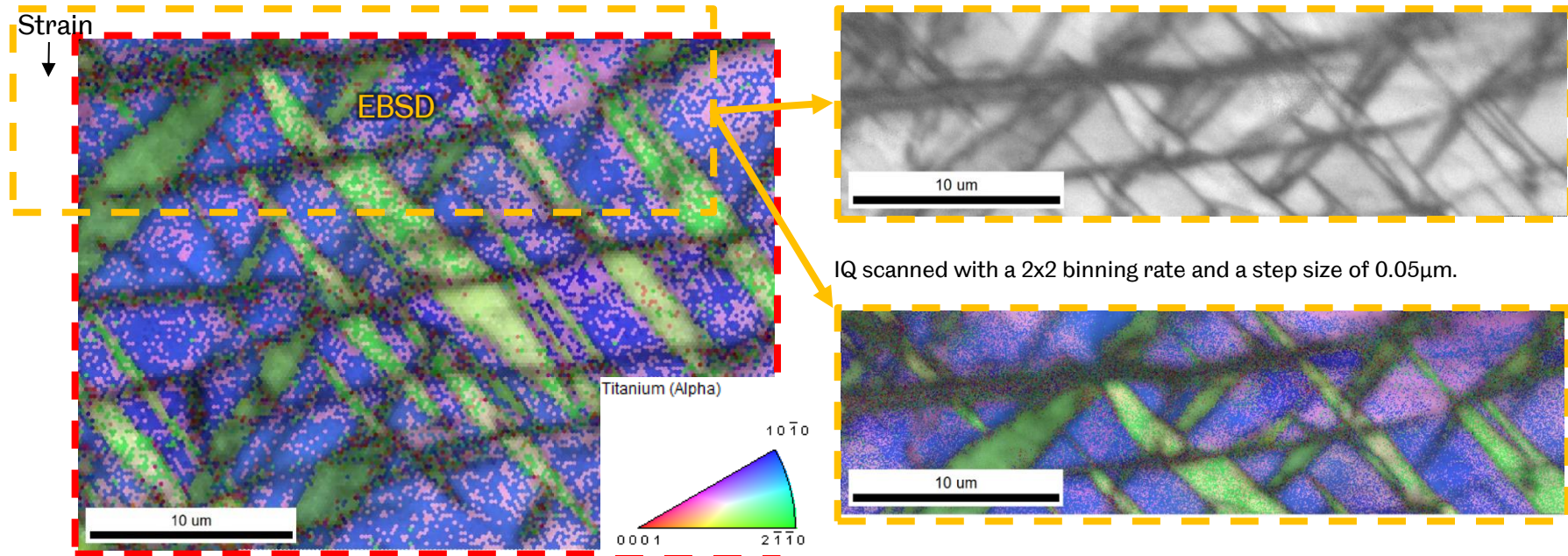
SEM image where a region of interest was identified for EBSD analysis.



IPF overlaid on IQ map, scanned with a 2x2 binning rate, step size 0.5 μm.

Figure 5.23 – EBSD of a location within the sample, ~1 mm from the loading face, of test number 5. Annealed Ti-6Al-4V tested at a peak strain rate of 7700 s⁻¹.

Figure 5.24 shows the results of higher resolution EBSD scans of the “EBSD 3” location marked in Figure 5.23. The results show twinning at two perpendicular angles, crossed by horizontal slip bands.

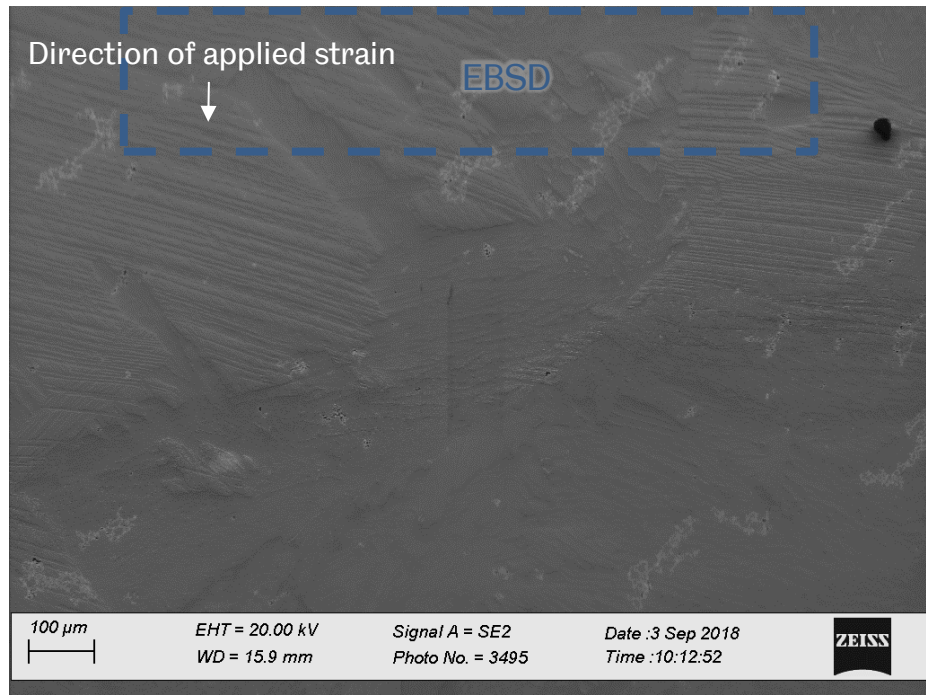


IPF overlaid on an IQ map. Scanned with a 2x2 binning rate and a step size of 0.2 μm . Scale bar 10 μm .

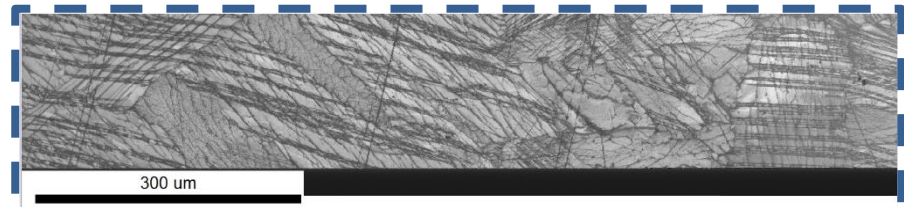
IPF overlaid on an IQ map. Scanned with a 2x2 binning rate and a step size of 0.05 μm . Scale bar 10 μm .

Figure 5.24 – EBSD of a location deeper in the sample, away from the loading faces, of test number 5. Annealed Ti-6Al-4V tested at a peak strain rate of 7700 s^{-1} .

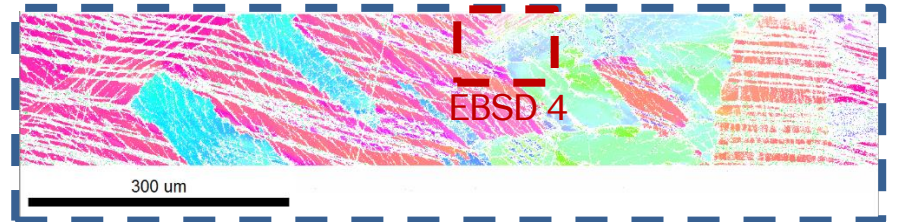
Figure 5.25 shows images from another location in the sample, again deep within the bulk, more than 1 mm away from the loading faces. SEM revealed what may be slip or twinning here so EBSD was conducted in the area outlined. The IPF indicates there are several crystal lattice planes intersecting in this region. A location in the microstructure where several grain boundaries appear to meet is marked “EBSD 4” on the IPF map. This was further investigated in Figure 5.26.



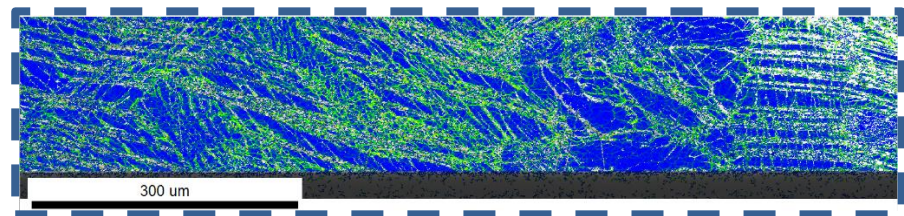
SEM. Scale bar 100μm.



IQ scanned with a 2x2 binning rate and a step size of 0.75 μm.



IPF scanned with a 2x2 binning rate and a step size of 0.75 μm. Pixels of less than 0.1 confidence index removed.



Misorientation map of the scan using Kernel Average 1st neighbour. Data cleaned up by Kuwahara filter applied to first neighbour for two iterations. Grains of size less than 5 pixels removed. Overlaid on IQ.

Figure 5.25 – SEM and EBSD of another location in the sample, away from the loading faces, of test number 5. Annealed Ti-6Al-4V tested at a peak strain rate of 7700 s⁻¹.

The “EBSD 4” location marked in Figure 5.25 was investigated with a higher magnification, small Further step size EBSD scan. The results in Figure 5.26 show a lot of twinning deformation.

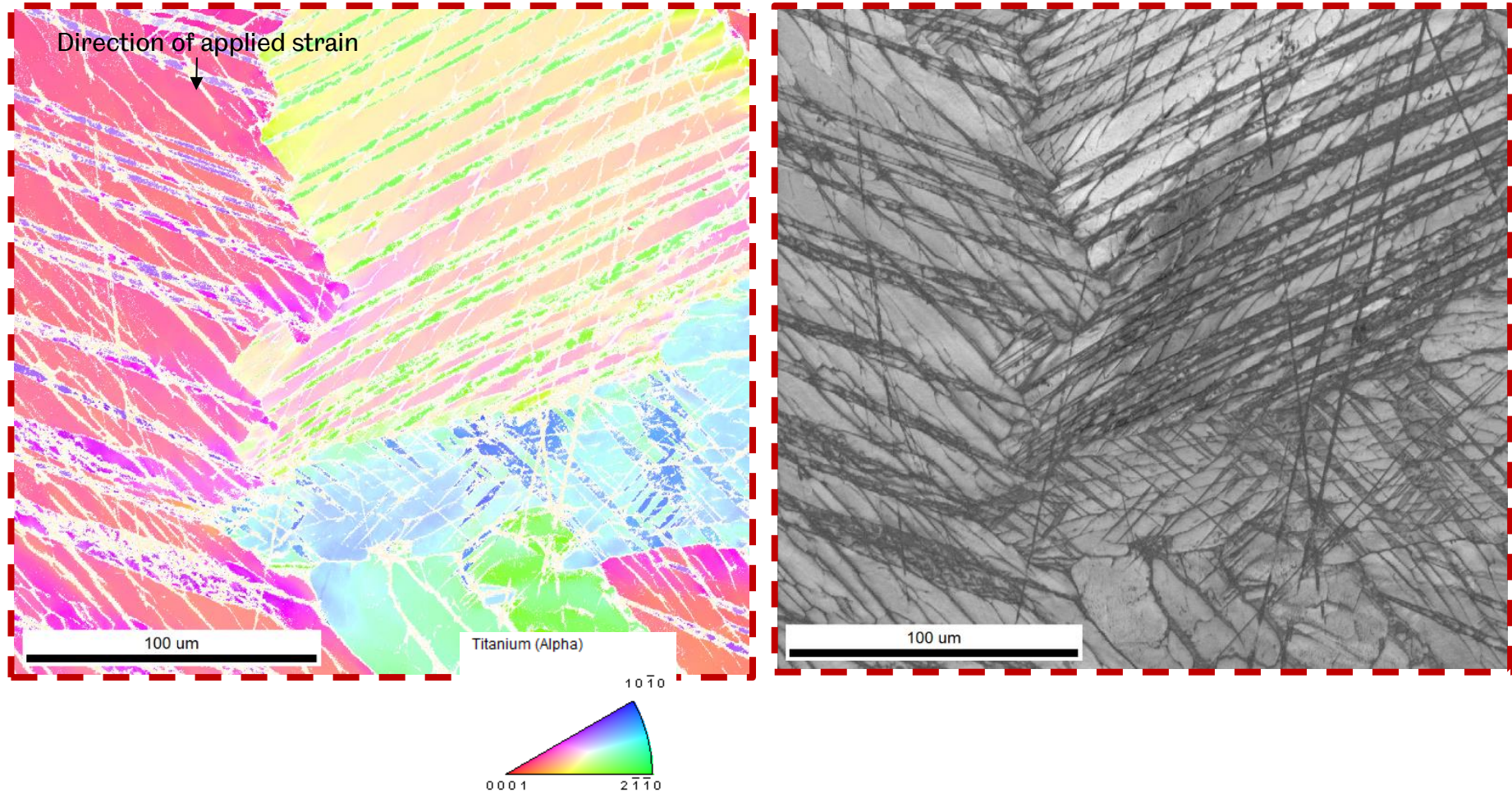
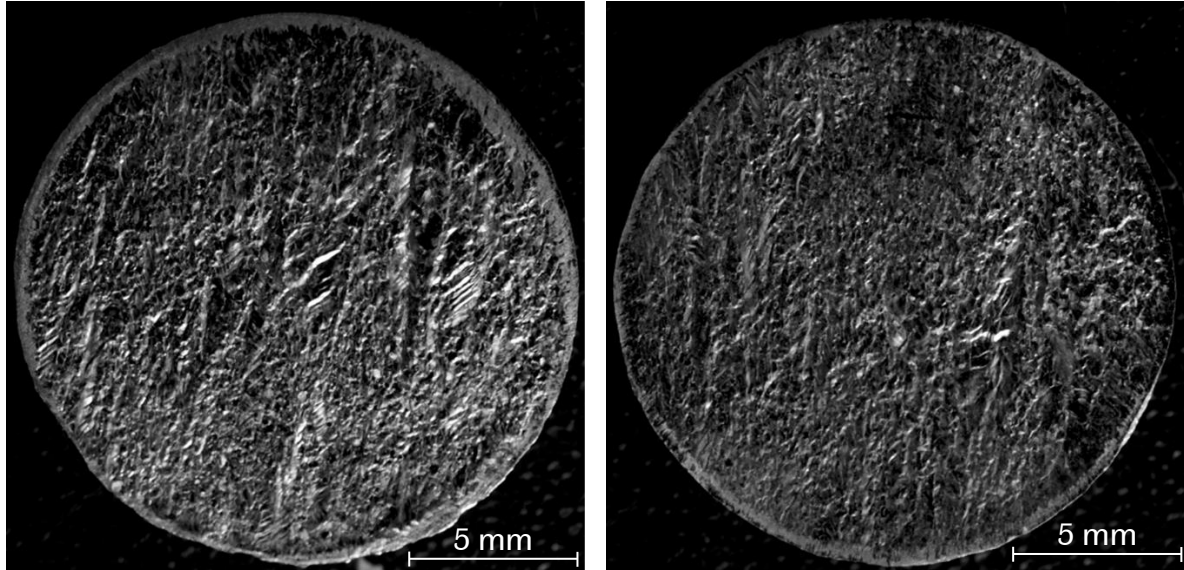


Figure 5.26 – IPF and IQ maps of the region highlighted in Figure 5.25. Scanned with a 2x2 binning rate and a step size of 0.2 μm, Pixels of less than 0.1 confidence index removed from the IPF map.

5.5.2 Test 6 – Ti-15Mo at ‘high’ strain rate

Figure 5.27 shows the two faces of a Ti-15Mo sample compressed at high strain rate. Microstructural deformations have led to a significantly textured surface. The texturing follows the direction of large laths previously noted in the as-received microstructure in Figure 2.13.



Side 1 of sample.

Side 2 of sample.

Figure 5.27 – Photographs of test number 6. As-received Ti-15Mo tested at a peak strain rate of 7800 s^{-1} . Peak strain 27 %. Peak stress 1800 MPa.

Confocal microscopy was also used to characterise the surface. Figure 5.28 shows side 1, which appeared to be the more deformed side.

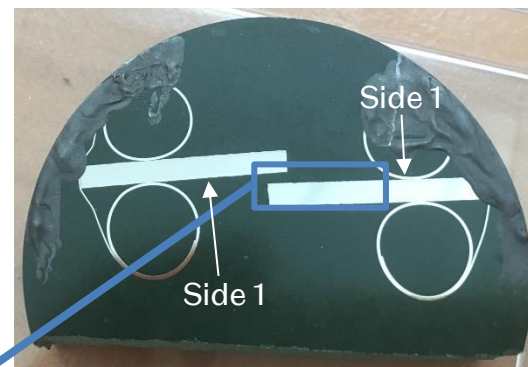


Figure 5.28 – Alicona image of side 1 of test number 6. As-received Ti-15Mo tested a peak strain rate of 7800 s^{-1} . Peak strain 27 %. Peak stress 1800 MPa.

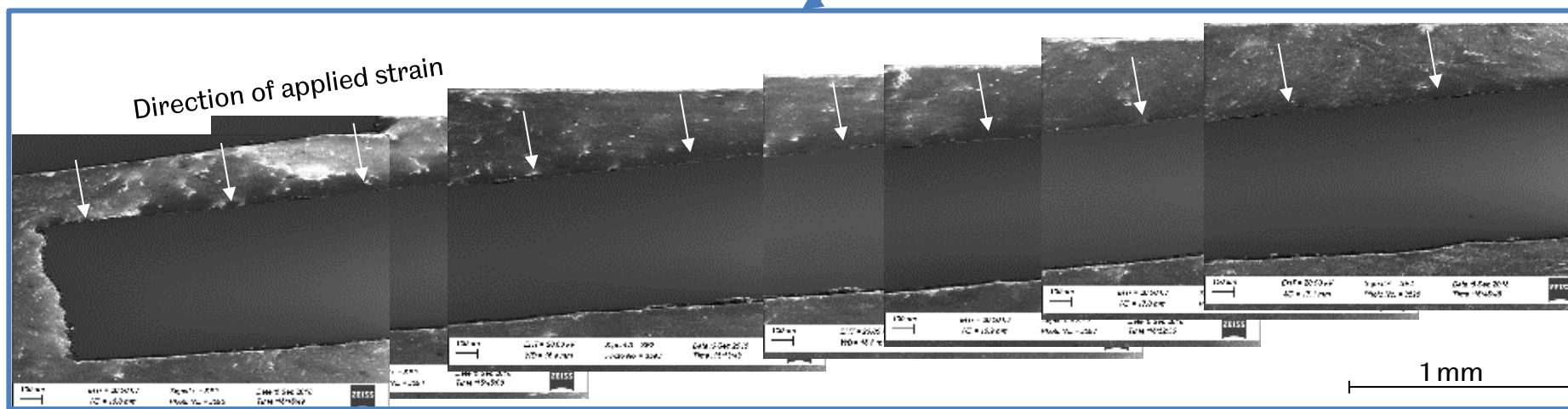
The sample was sectioned in two, mounted and polished for EBSD analysis. This is illustrated in Figure 5.29. SEM images in Figure 5.29 also show where EBSD analysis was conducted.



Side 1 face. Sample sectioned across predominant lines of macrozones.



Sectioned and mounted with "Side 1" faces facing each other.



SEM images "stitched" together to show the region EBSD scans were taken in.

Figure 5.29 – Photographs & SEM images of test number 6 sectioned. As-received Ti-15Mo tested at a peak strain rate of 7800 s^{-1} .

Figure 5.30 shows the IPF maps generated from EBSD scans in the regions highlighted in Figure 5.29. The large macrozones already exist in the untested alloy. However there appear to be new features in some grains which may be twins, so this region (outlined in Figure 5.30) was investigated further with a higher resolution EBSD scan.

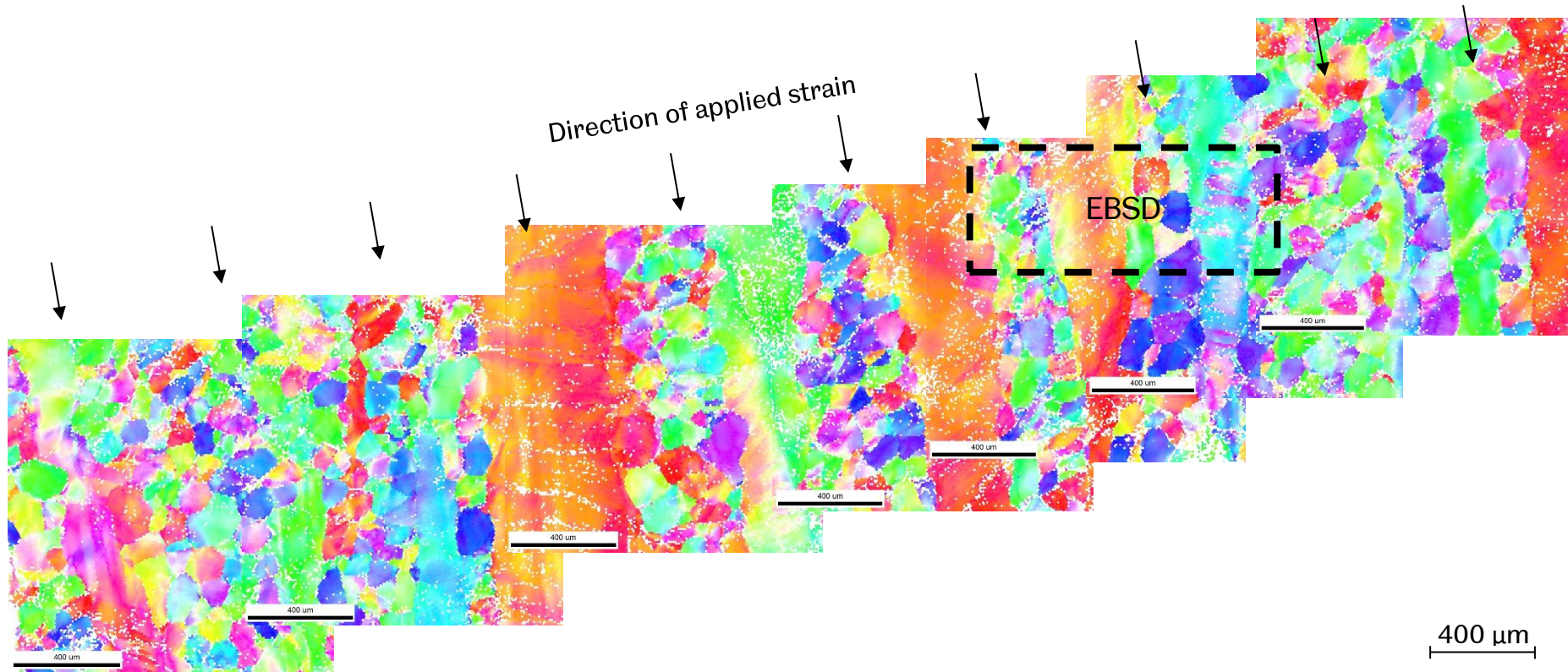


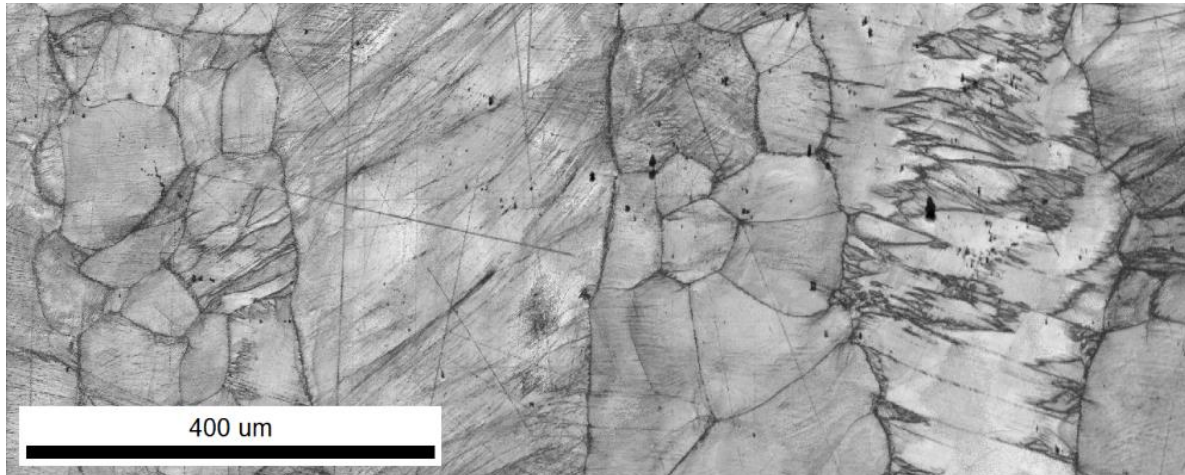
Figure 5.30 – IPF maps “stitched” together, taken in the regions highlighted in Figure 5.29. Scanned with 2x2 binning rate, step size 8 μm . Pixels of less than 0.1 confidence index removed. Test number 6 - as-received Ti-15Mo tested at a peak strain rate of 7800 s^{-1} .

Figure 5.31 is the resulting IPF from a smaller step size scan of the area highlighted in Figure 5.30. It shows what appears to be twinning.

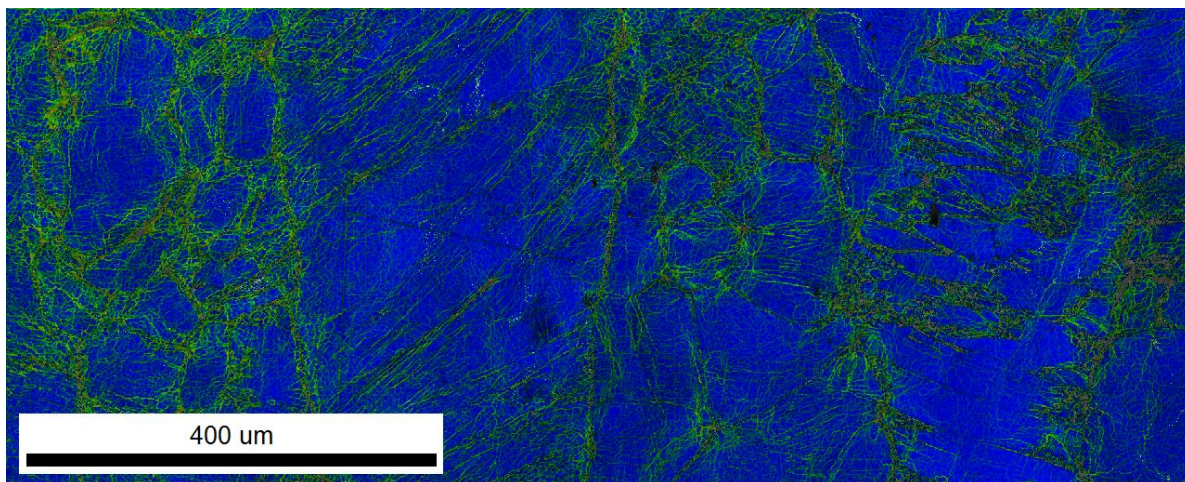


Figure 5.31 – IPF scanned with a 2x2 binning rate, step size 0.7 μm. Pixels of less than 0.1 confidence index removed. Test number 6 - as-received Ti-15Mo tested at a peak strain rate of 7800 s⁻¹.

The IQ map of the EBSD scan in Figure 5.32 shows grain boundaries more clearly, but there doesn't appear to be any other obvious deformations like slip bands or microcracks. The misorientation map also in Figure 5.32 shows a similar result to the untested as-received Ti-15Mo. There is a lot of misorientation at grain boundaries and some misorientation within grains, residual from the materials forming and processing route.



IQ map.



Misorientation map of the scan using Kernel Average 1st neighbour. Data cleaned up by Kuwahara filter applied to first neighbour for two iterations. Grains of size less than 5 pixels removed. Overlaid on Image Quality map.

Figure 5.32 – IQ and Misorientation map. Scanned with 2x2 binning rate, step size 0.7 μm . Test number 6 - as-received Ti-15Mo tested at a peak strain rate of 7800 s^{-1} .

5.5.3 Test 2 – Ti-15Mo at ‘high’ strain rate

Figure 5.33 shows the incident face of sample 2; Ti-15Mo tested at the highest strain rate. Alicona uses confocal microscopy to achieve a large depth of field when capturing images, such as the image on the left. Simultaneously, optical interferometry captures the surface height profile, as the right-hand image illustrates. The pseudocolour height map reveals ring features across the surface. Ring markings appear on all the samples.

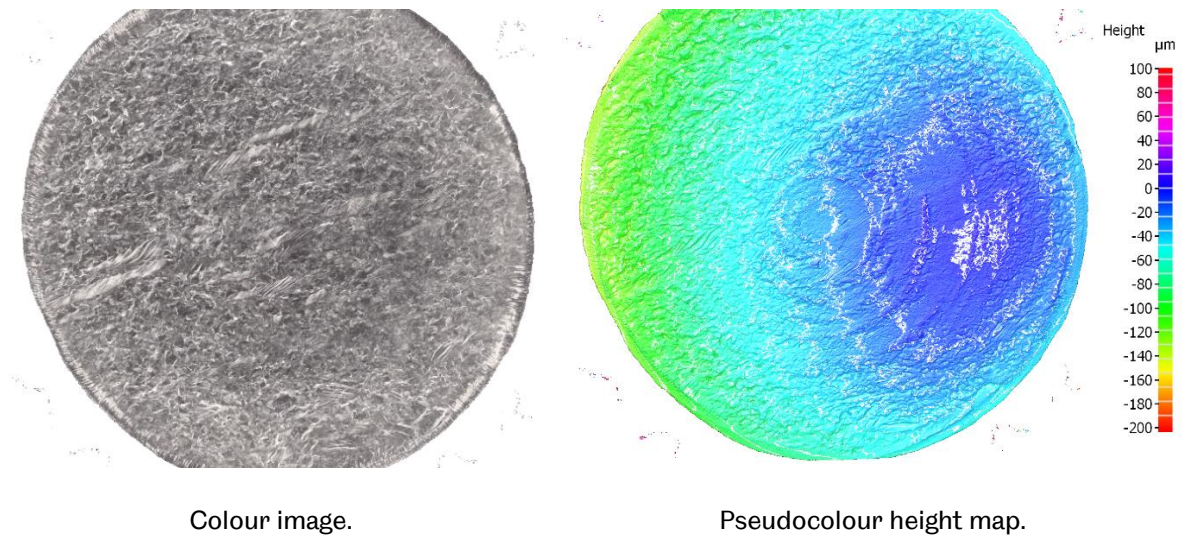


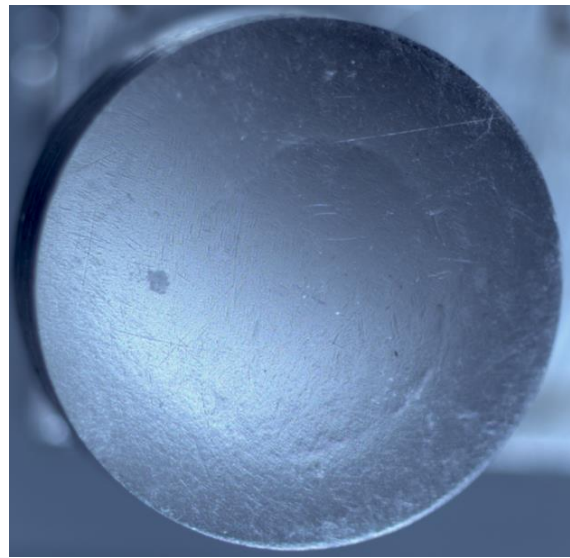
Figure 5.33 – Alicona results of the “front” of sample 2. As-received Ti-15Mo tested at a peak strain rate of 6000 s^{-1} . Peak strain 21 %. Peak stress 1800 MPa.

5.5.4 Test 10 – Ti-15Mo at ‘low’ strain rate

Photographs of the incident face of test 10 are shown in Figure 5.34 below, a 5 mm length Ti-15Mo sample, tested at the lowest achievable strain rate. There is an indentation in a ring shape on this specimen which is visible when the light source is at a slight angle to the specimen. The ‘long’ (5 mm) sample experienced a lower strain rate than ‘short’ (2.5 mm) specimens. The test was also set up to produce the lowest strain rate possible with the available test equipment. The lower strain rate resulted in less visible deformation, so the ring features are more obvious in the lower strain rate tests.



Front face.

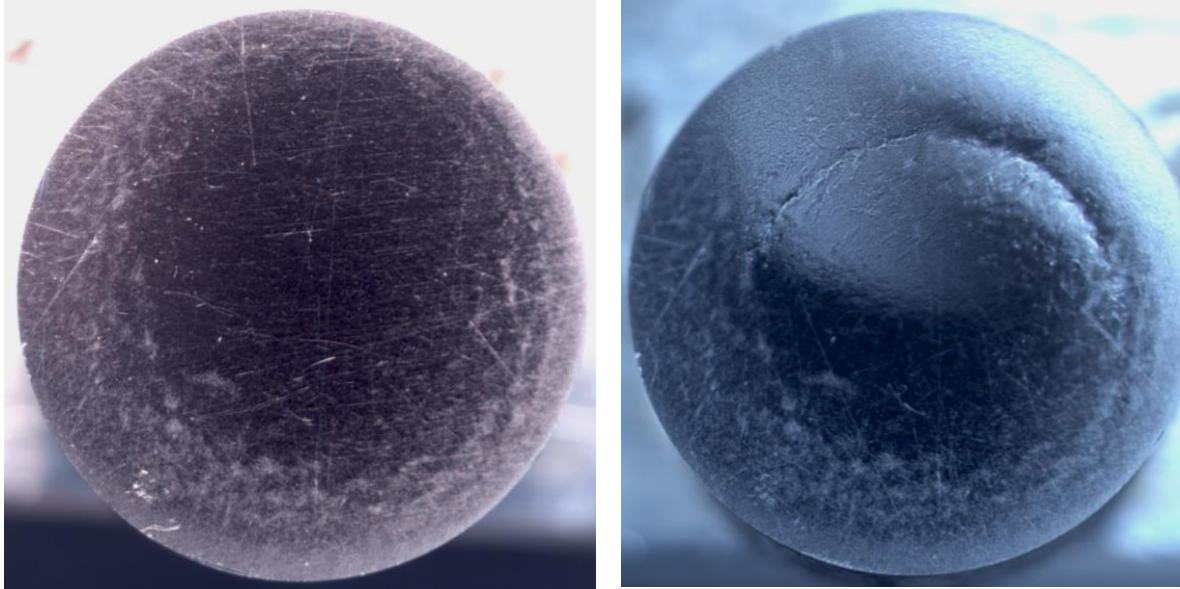


Front face (tilted at angle to light).

Figure 5.34 – Photographs of test number 10. As-received Ti-15Mo tested at a peak strain rate of 2000 s^{-1} . Peak strain 2.5 %. Peak stress 1000 MPa.

5.5.5 Test 12 – Ti-15Mo at ‘medium’ strain rate

The ring feature is clearly visible in Figure 5.35 below, a ‘long’ (5 mm) Ti-15Mo sample tested at a medium-range strain rate.



Front face.

Front face (tilted at angle to light).

Figure 5.35 – Photographs of test number 12. As-received Ti-15Mo tested at a peak strain rate of 2400 s^{-1} . Peak strain 3 %. Peak stress 1200 MPa.

Surface profilometry was conducted with Alicona. Figure 5.36 shows an approximately $10 \mu\text{m}$ height difference between the centre of the sample and the bottom of the indentation.

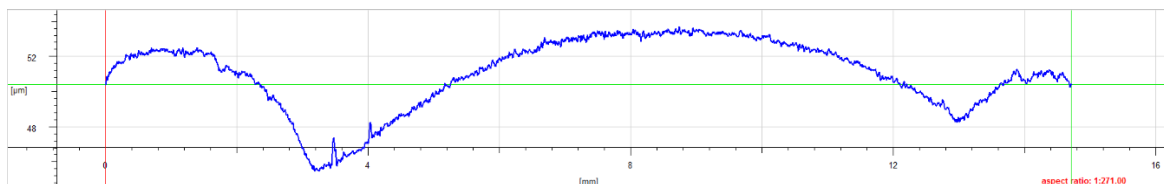
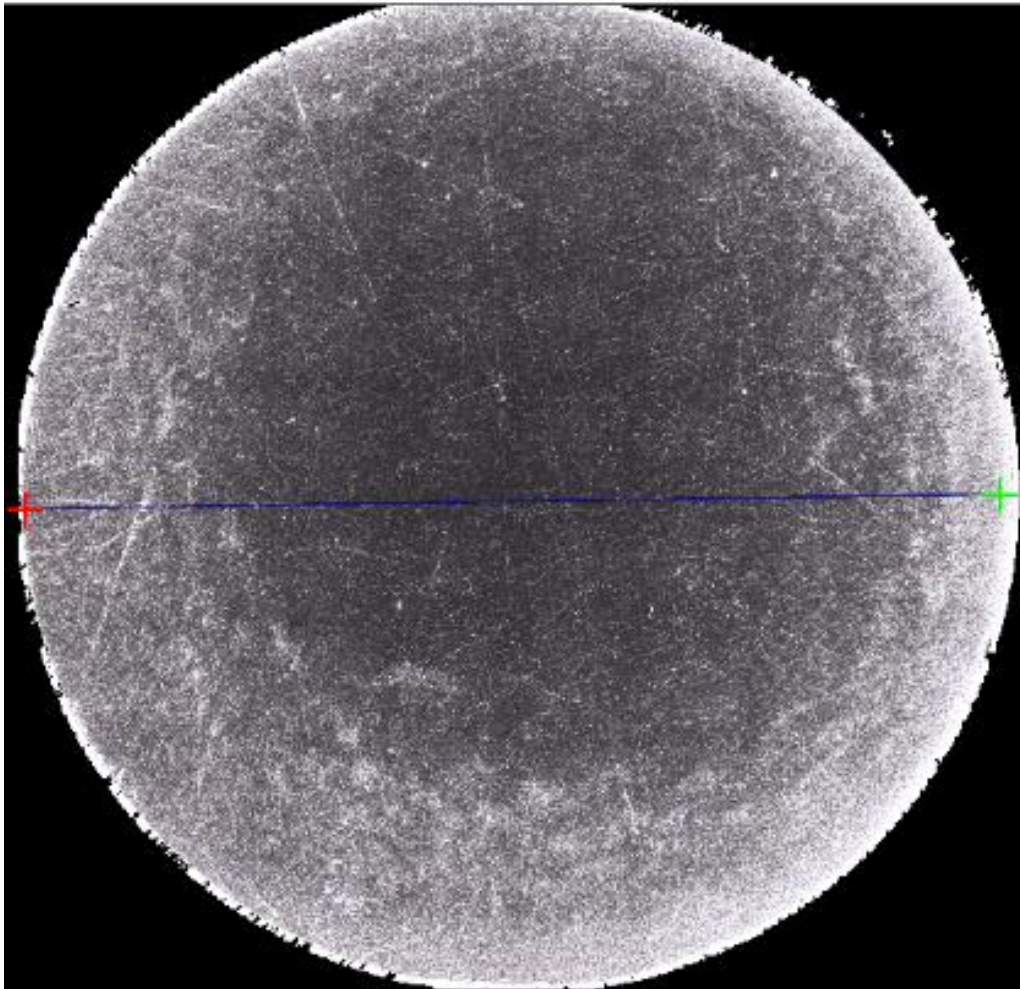


Figure 5.36 – Profile path from left to right of the sample. The red cross is where the profile measurement begins, corresponding to the left of the diagram.

5.6 Discussion

In compressive high strain rate testing, both Ti-15Mo and the annealed Ti-6Al-4V performed similarly in terms of the stress amplitudes supported (up to 1800 MPa) and strain accommodated (maximum around 22 %). Strain hardening was apparent.

By the nature of the test set-up, reducing strain rate would also reduce the maximum stress amplitude and total strain applied. Therefore the stress-strain curves of compressive SHPB tests all have a similar shape, but are scaled to smaller stresses and strains with smaller strain rates. Plastic deformation was observed in all the samples,

so it is reasonable to state that all tests exceeded the yield stress for the given strain rate.

In common with the compressive tests, the tensile high strain rate tests were able to reach a stress much higher than the quasi-static UTS. The quasi-static UTS of Ti-15Mo is 690 MPa whereas the maximum stress at high strain rate was 1650 MPa, a factor of 2.4 larger. The quasi-static UTS of annealed Ti-6Al-4V is 896 MPa (as noted in Table 4.1 earlier) but the maximum stress at high strain rate is 1550 MPa – 1.7 times larger.

Despite the high strain rates and loads, both materials were able to accommodate compressive deformation by slip and twinning, rather than failing by macro-scale cracking. Some microcracks could be observed in the annealed Ti-6Al-4V microstructure deformed at 7700 s^{-1} in Figure 5.26, but these seemed to be arrested by grain boundaries.

These high strain rate tests produced deformation mechanisms as seen in WDE, and the stress-strain results illustrate strain hardening – indicating work hardenability is an important property for materials in WDE.

6 CAVITATION EROSION

6.1 Literature review

Cavitation erosion occurs when cavities in a liquid collapse, producing high velocity jets, as well as pressure waves, which damage the surface. The cavities are caused by rarefactions (a pressure drop) in the wake of a high pressure compressive wave. Cavitation occurs in a number of applications, from ship propellers to lubricated bearings. Cavitation in WDE has been both observed in experiment and predicted by simulation [13], [16], [53].

Brunton & Camus [11] note that attempts to correlate material properties with water droplet erosion fail to predict performance. This may be because researchers typically only consider one erosion mechanism. Among some mechanisms they consider, they show that even at low droplet impingement velocities, cavitation is powerful enough to produce stress waves when the main impact stress wave is too weak to be visible. The superposition of many small impacts from cavitation contribute to overall damage.

Hattori and Takanami [93] compared cavitating submerged impingement jet (SIJ) erosion and impingement jet erosion and found similar erosion features in the early onset of damage. Keil et al. [94] compare cavitation with a whirling arm water jetting rig and note similar micropits and grain tilting in the early stages of erosion. Preece and Brunton [32] compared WDE (conducted on a wheel and jet rig) with cavitation erosion. The results were similar to WDE in the early stages of erosion, but three to four orders of magnitude more impacts by cavitation were required to produce similar erosion to advanced WDE. They concluded that although the early stages of cavitation and WDE appear similar, lateral outflow jetting is key to higher rates of material removal than cavitation once the surface is roughened [32].

Richman and McNaughton [60] have established a correlation between cavitation erosion resistance and fatigue. Preece and Brunton [32] also noted fatigue striations in cavitation erosion.

6.2 Experimental methods

Two methods of inducing cavitation were investigated; a submerged impingement jet (SIJ) and a sonotrode (or ultrasonic horn).

6.2.1 Submerged impingement jet

When a high velocity water jet strikes a surface at normal incidence, the sudden arresting of the flow results in a pressure drop. Cavities are formed which collapse

and cause cavitation damage. ASTM G134 describes the standard test method for erosion by a cavitating liquid jet [95]. The test can be interrupted periodically to weigh samples to track erosion rate.

The Institute of Functional Surfaces at the University of Leeds offered the use of their SIJ rigs, which are predominantly used with sand circulating in the flow to produce slurry erosion – a common problem for the oil and gas industry. Figure 6.1 illustrates the set-up. The sample was fixtured perpendicular to the nozzle at a constant stand-off distance of 5 mm. Water was recirculated; pumped through the nozzle with the nozzle tip positioned below the surface of the water in a tank. The nozzle diameter was 4 mm.

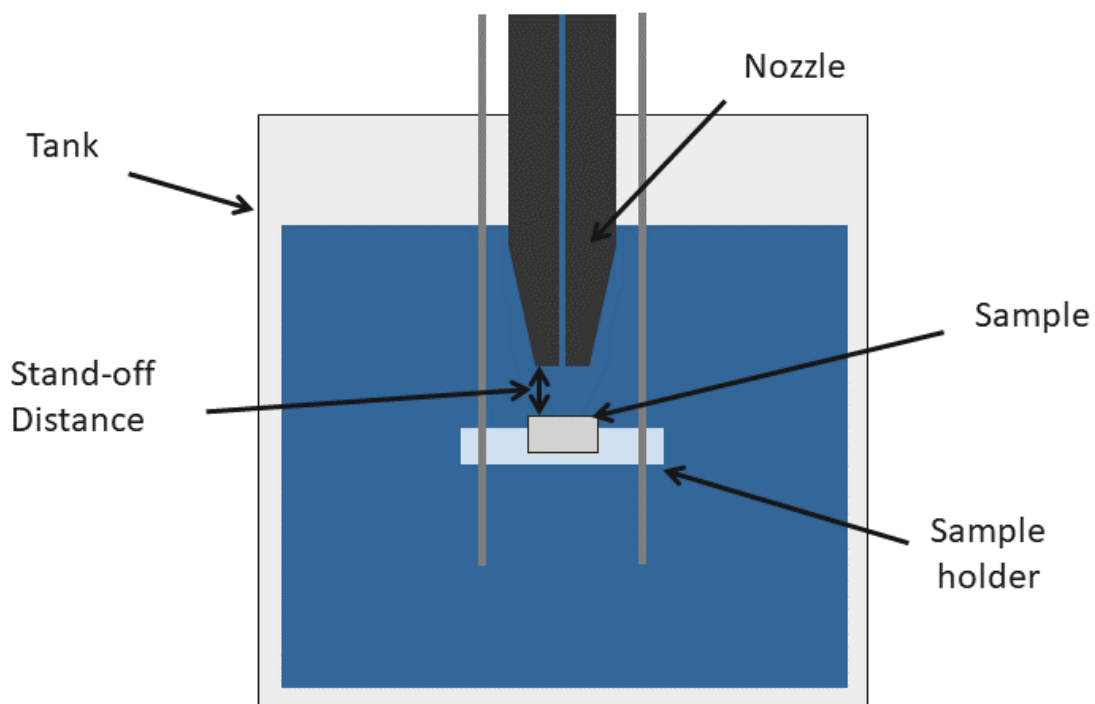


Figure 6.1 – Schematic of the submerged impingement jet (SIJ) rig.

The motor frequency determined the flow rate and hence the speed. At the maximum frequency the speed was determined to be $24.6 \pm 0.9 \text{ m}\cdot\text{s}^{-1}$. The water was drained and refilled multiple times with tap water in an attempt to flush sand, residual from previous testing, out of the system. 25 mm diameter test samples were manufactured from annealed Ti-6Al-4V and prepared by metallographic polishing to remove defects and roughness.

6.2.2 Sonotrode

A sonotrode utilises an ultrasonic horn to create cavities within a liquid, which subsequently collapse and result in cavitation. ASTM G32 describes how to use the

apparatus for cavitation erosion testing [96]. The sonotrode used in this work operated at a constant natural frequency of 20 kHz. Amplitude was set to 35 % which corresponds to a displacement of 50 μm , as recommended by the manufacturer. A 50 % duty cycle was recommended, i.e. 0.5 s running followed by a 0.5 s pause, so the equipment did not overheat. This meant that actual cavitation exposure time was 50 % of the time interval of the test. The stand-off distance from the horn tip to the sample was held constant at 1 mm \pm 0.5 mm. The sample was completely submerged in a container of tap water and the horn partially submerged to a depth of 12 mm \pm 2 mm. The flat-ended horn tip was 0.75 in (19.05 mm) in diameter. Test sample material, size, and preparation methods were identical to those for SIJ experiments.

6.3 Results

6.3.1 Submerged impingement jet

The effectiveness of the SIJ rig was initially checked with a stainless steel sample. The sample was prepared for testing by metallographic polishing. Figure 6.2 shows part of the circular wear scar resulting from a 30 minute test, imaged by a light microscope. There was no measurable difference in mass loss when using the laboratory's $\pm 10^{-5}$ g precision mass balance.



Figure 6.2 – Light microscope images stitched together of a stainless steel sample after 30 min in SIJ rig.

Figure 6.3 shows the resulting damage from a 10 minute test on annealed Ti-6Al-4V. The erosion scar shows pits so damage was thought to be in the advanced stage, rather than the (desired) incubation period. However, the damage looks like solid particle impingement, i.e. due to sand particles residual in the system from it's previous use. The system was flushed several times more in an attempt to remove these.

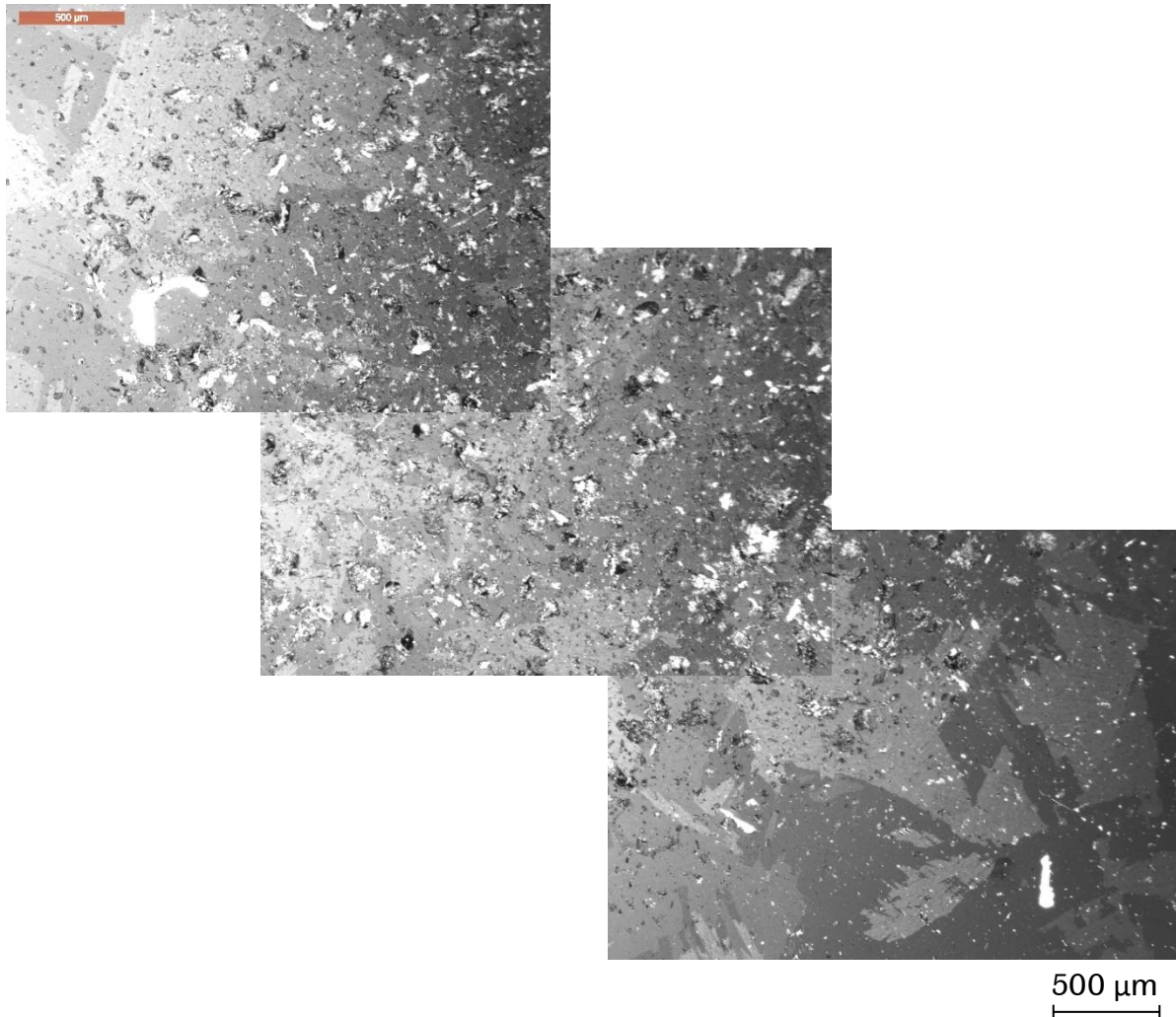
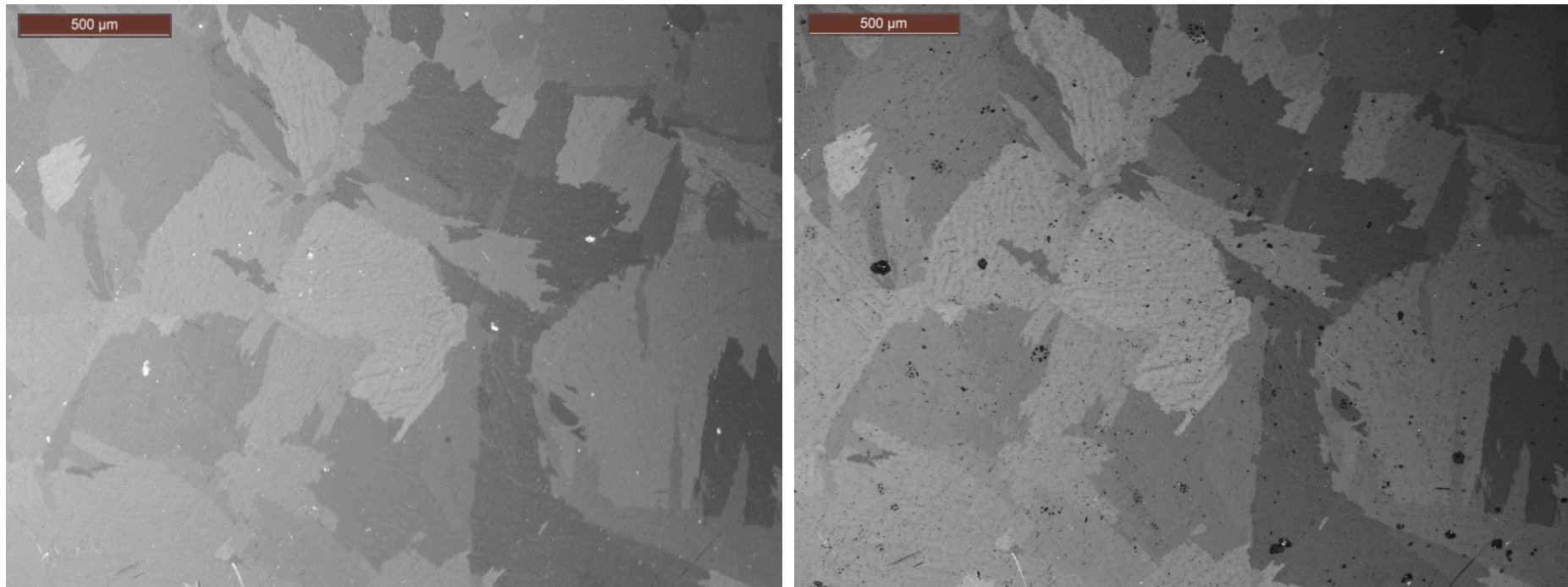


Figure 6.3 – Annealed Ti-6Al-4V after 10 minutes in SIJ rig. Wear scar is approximately 4 mm in diameter.

A shorter-term 10 second test is shown in Figure 6.3 below. The DRO on the microscope stage meant the location of the wear scar region could be imaged both prior to and then after testing. There was still some solid particle sand damage, but it appears significantly less since the system was flushed.



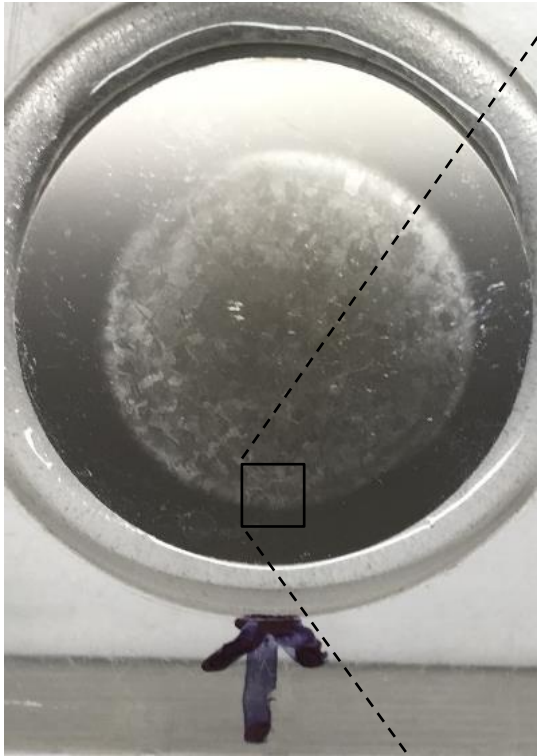
Centre of wear scar region before testing.

Centre of wear scar region after 10s testing.

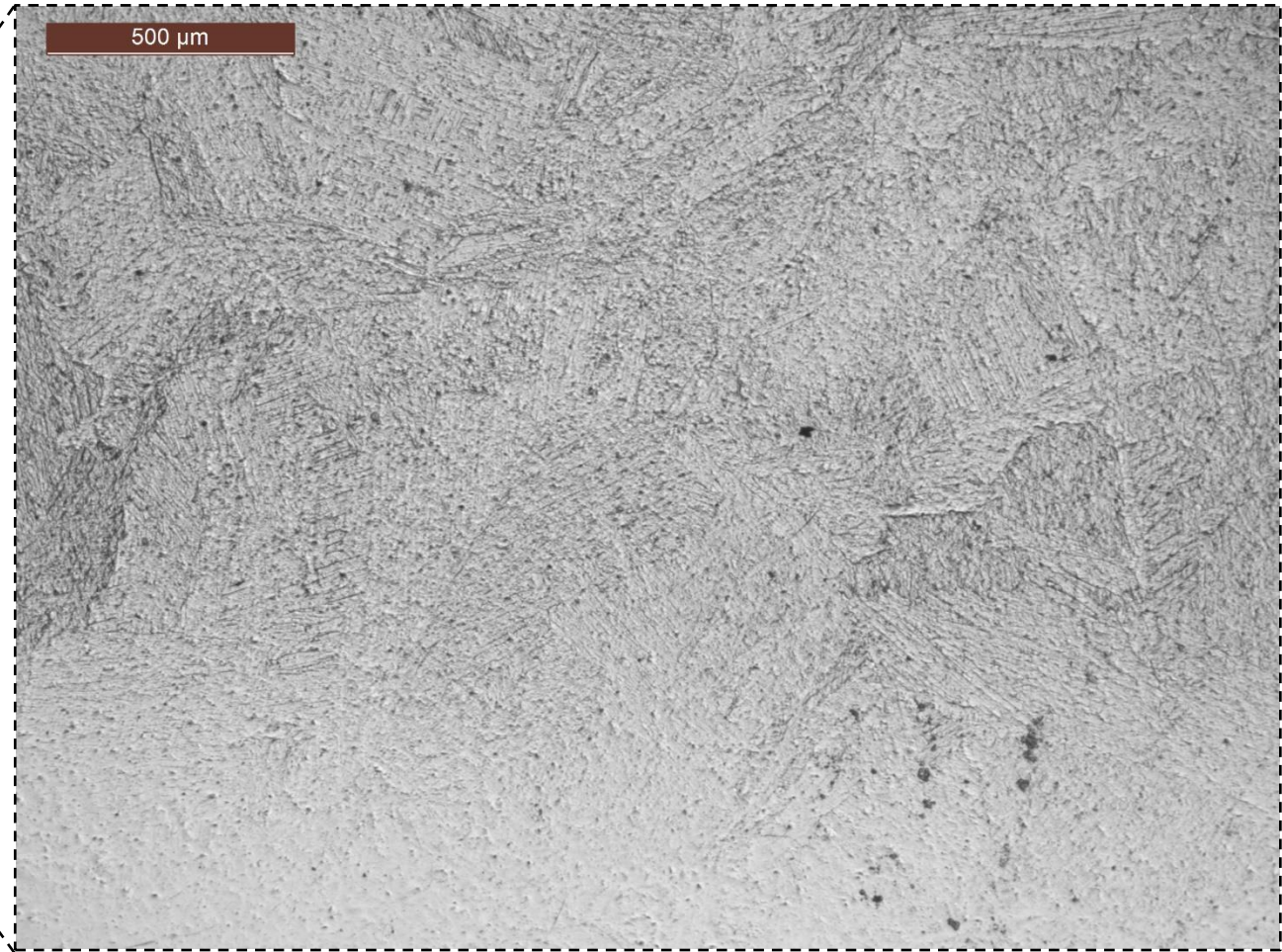
Figure 6.4 – Annealed Ti-6Al-4V before and after 10s in SIJ rig.

6.3.2 Sonotrode

Because the SIJ rig suffered contamination from residual sand in the system, a different cavitation rig was tried. Results from a 1 hour test are shown in Figure 6.5 below. Grain tilting is visible at grain boundaries, which gives the surface an etched appearance in normal light. There was no measurable mass loss.



Photograph.



Light microscope image. Taken at the edge of the damaged region, the bottom is outside the region where cavitation occurred.

Figure 6.5 – Annealed Ti-6Al-4V after 1 hour in sonotrode rig.

Figure 6.6 shows the edge of the damaged region scanned with Alicona focus variation microscopy. Again, grain tilting and protrusions are visible, however the surface profilometry was not able to measure a difference in roughness, nor a difference in surface height, between the polished and damaged regions.

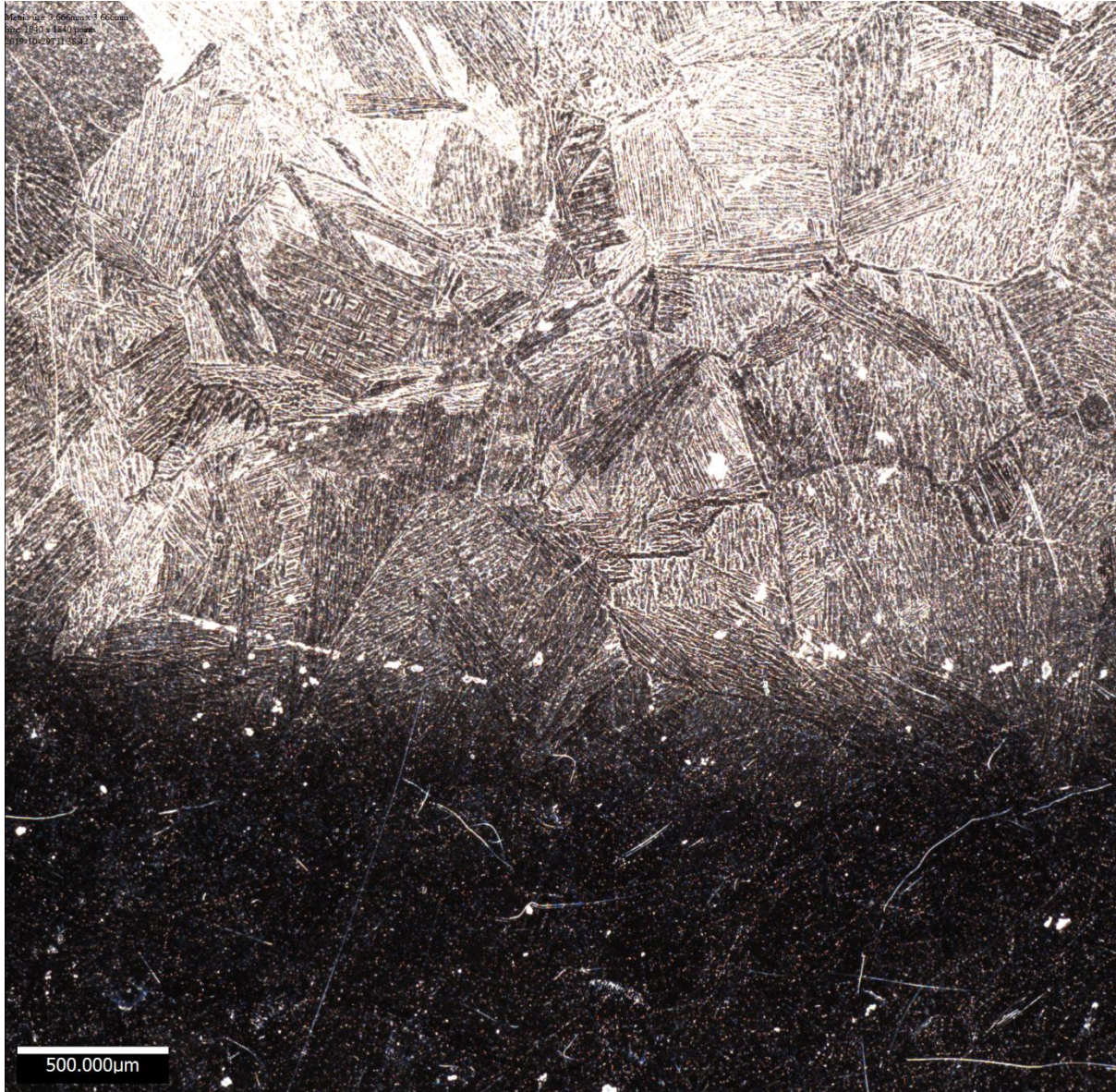


Figure 6.6 – Alicona image of annealed Ti-6Al-4V sample after 1 hour in cavitating sonotrode rig.

Figure 6.7 is an Alicona image of the sample following another hour in the sonotrode cavitation rig. The sonotrode was not realigned precisely so there is a visible overlap between the first hour and second hour of testing results, though this helps to illustrate the increase in cavitation deformation. No difference in mass loss could be measured.

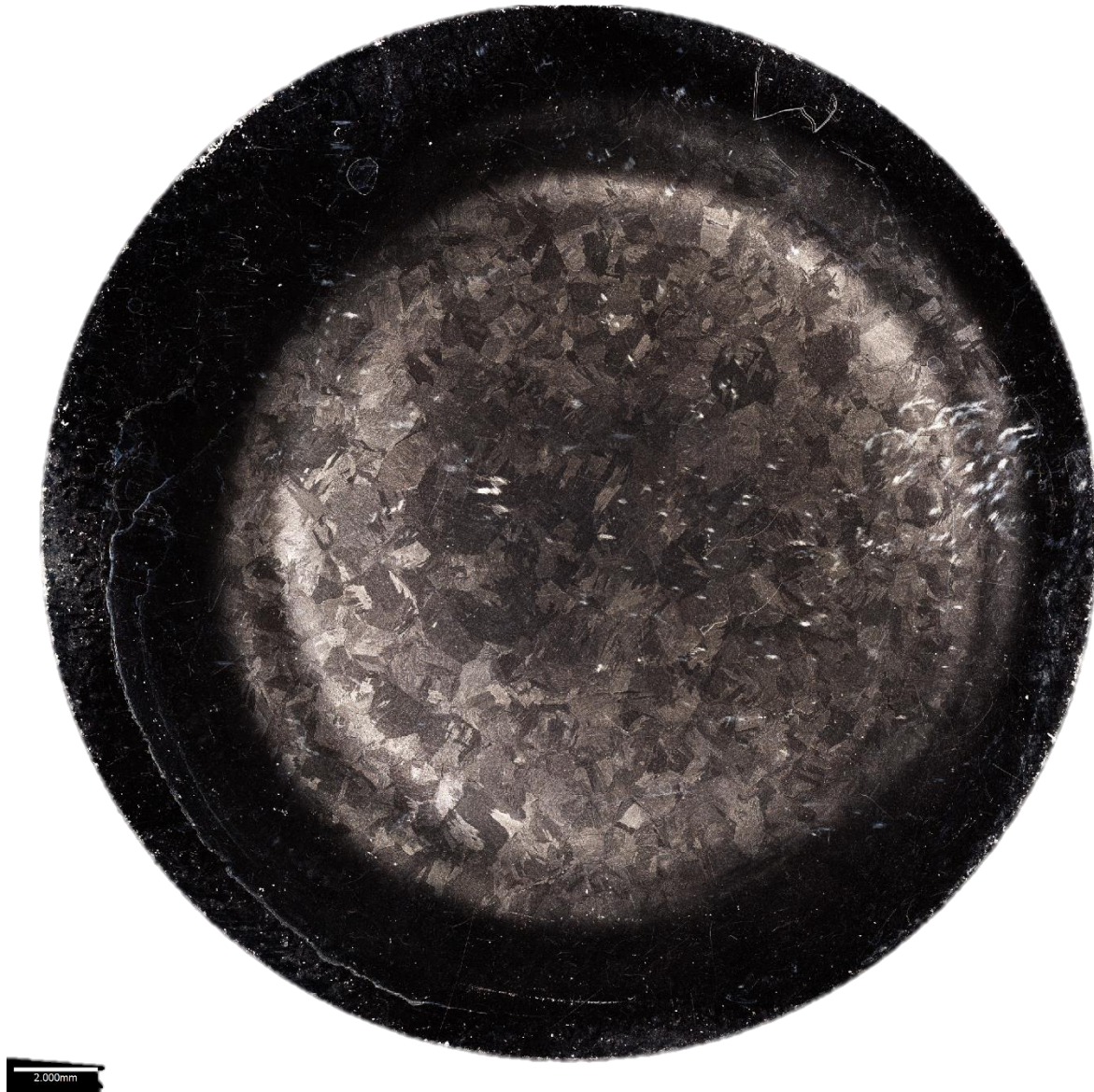


Figure 6.7 – Alicona image of annealed Ti-6Al-4V sample after 2 hours in cavitating sonotrode rig. 2mm scale bar.

Higher magnification imaging of the damaged region was possible using SEM. Figure 6.8 shows micropits initiating at grain boundaries. The region labelled “SEM” was investigated at increasing magnification.

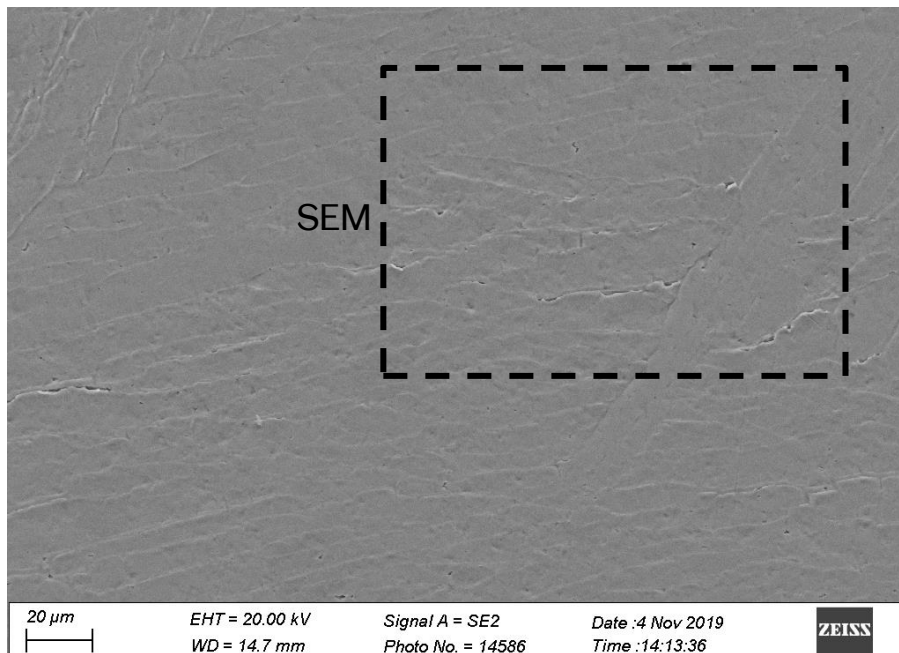


Figure 6.8 – SEM image of annealed Ti-6Al-4V sample after 2 hours in cavitating sonotrode rig.

Figure 6.9 is the area noted in Figure 6.8. The micropits are more discernible. They occur within grains, not just at grain boundaries.

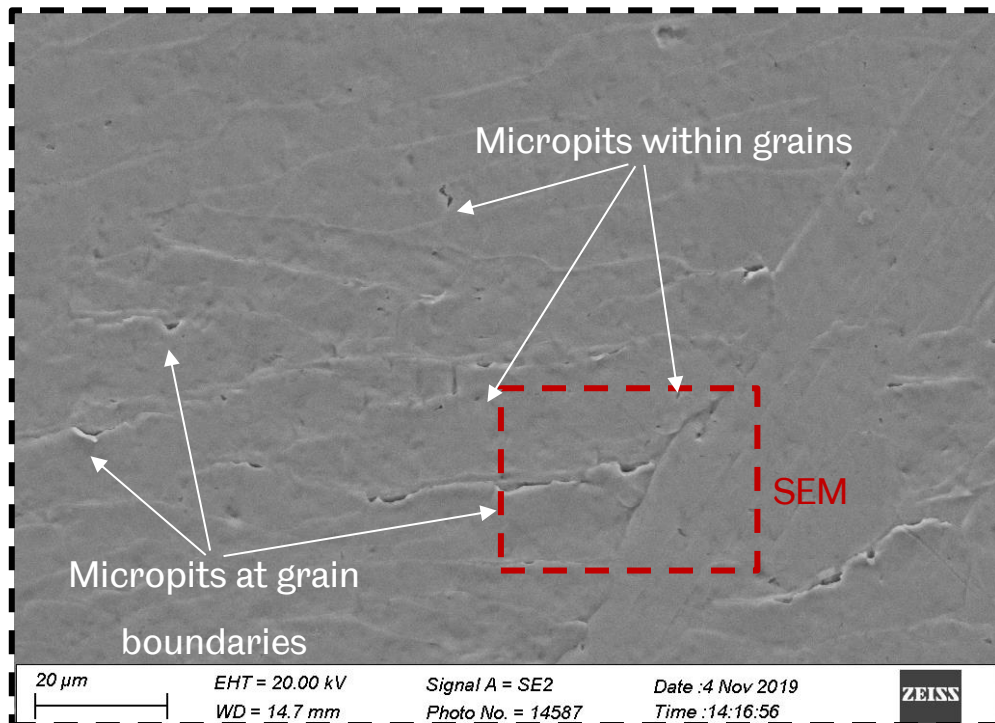


Figure 6.9 – SEM image of annealed Ti-6Al-4V sample after 2 hours in cavitating sonotrode rig.

A further location is marked in Figure 6.9 where higher magnification analysis was conducted. Figure 6.10 indicates brittle fractures where protruding material has been eroded at grain boundaries.

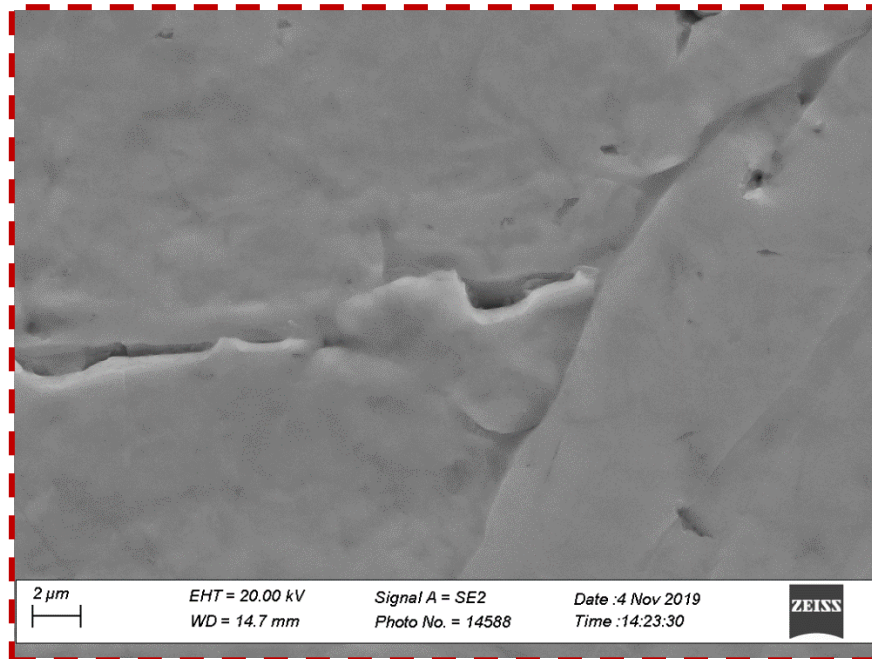


Figure 6.10 – SEM image of annealed Ti-6Al-4V sample. 2 hours in cavitating sonotrode rig.

Figure 6.11 is another location, which further demonstrates micropits occurring not just at grain boundaries, but also at locations within grains.

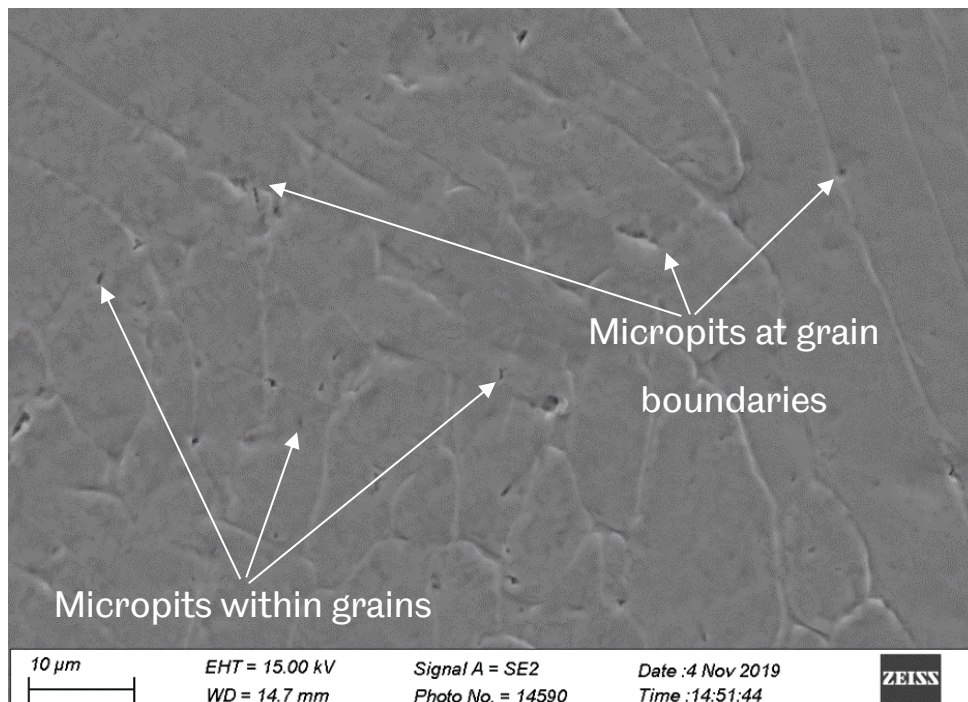


Figure 6.11 – SEM image of annealed Ti-6Al-4V sample. 2 hours in cavitating sonotrode rig.

EBSD was attempted, but was not possible due to extremely poor indexing, on both the tested and undeformed regions. Even a polished, but untested sample had poor indexing. This suggested the polishing technique was not optimal for EBSD, despite giving results acceptable for optical and even SE microscopy.

6.4 Discussion

Submerged Impingement Jetting (SIJ) cavitation proved unreliable in this case due to sand contamination from the equipment's previous use for slurry erosion. Ultrasound induced cavitation proved much more controllable.

The literature indicated initial cavitation erosion provided damage similar in appearance to WDE in the early stages. Compared to literature findings of early stage WDE, similar deformation was observed for cavitation erosion such as grain tilting and micropitting.

Cavitation could therefore be used as a simple but effective indicator of initial WDE performance. Materials could be ranked, and the best performing put forward for WDE testing on more complicated equipment such as whirling arm impact rigs. There are limited numbers of whirling arm WDE test rigs which limits accessibility and availability. Whirling arm rigs can also have complicated maintenance requirements and are not easy to troubleshoot.

It may be possible to simulate advanced WDE damage on samples using other methods. In the literature, after firstly using a pressure wave in a column of water to produce deformation similar to initial WDE, Thomas and Brunton [59] reproduced advanced erosion by using high velocity jetting at an oblique angle to the surface, to simulate lateral outflow jetting.

7 STRAIN RATES IN THIS INVESTIGATION

7.1 Summary table

Strain rate can provide a useful comparator for the different types of test conducted. Table 7.1 summarises the experiments, resulting strain rates, maximum stresses they produced, and microstructural features the materials exhibited.

Test	Material	Strain rate, s ⁻¹	Stress, MPa	Microstructural features observed
WDE	Ti-15Mo	10 ⁵	444	Slip bands, micropits, fatigue striations, brittle faceted fracture
	Annealed Ti-6Al-4V	10 ⁵	444	Slip bands, micropits
	As-received Ti-6Al-4V	10 ⁵	444	Micropits, ductile tearing
Tensile test	Annealed Ti-6Al-4V	4×10 ⁻²	896	Necking
LCF	Annealed Ti-6Al-4V	10 ⁻³	–	–
SHPB (compressive)	Ti-15Mo	2×10 ³ – 7.8×10 ³	1000 – 1800	Slip bands, possible twinning
	Annealed Ti-6Al-4V	2×10 ³ – 7.7×10 ³	1100 – 1800	Slip bands, twinning
SHPB (tensile)	Ti-15Mo	1.25×10 ²	1650	Brittle fracture
	Annealed Ti-6Al-4V	2.8×10 ²	1550	Necking
Cavitation	Annealed Ti-6Al-4V	4.93×10 ⁵	250	Grain tilting, micropits

Table 7.1 – Maximum strain rates, stresses and microstructural features observed for the experiments in this investigation.

The table helps illustrate that although WDE occurred at a very high strain rate, this may not have been high enough to produce the characteristic grain tilting noted by other researchers in the literature. Cavitation erosion was at a slightly greater strain rate and this did produce grain tilting.

Interestingly, although the Ti-15Mo behaves plastically at low strain rates (e.g. a large strain-to-failure under quasi-static conditions) the reverse seems to be true at high

strain rates as the alloy fails in a brittle manor. Lainé suggested there is likely a strain rate limit in titanium, above which twinning does not occur [97].

High strain rate SHPB tests produced features such as slip bands and twinning. However, the very high strain rate WDE tests didn't appear to produce twinning features. It is possible that WDE is occurring at a strain rate too great for twinning to occur, and deformation may be accommodated in some other diffusionless transformation mechanism such as martensitic transformation.

7.2 Supporting calculations

Strain rate for the water droplet erosion tests was calculated by considering a droplet deforming the coupon front-face relative to the back-face, as Figure 7.1 demonstrates.

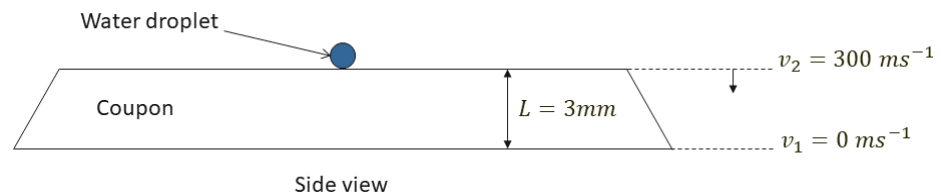


Figure 7.1 – Schematic for the calculation of the strain rate of a droplet impacting a coupon.

Stress for the WDE experiments was calculated using the water hammer equation, $p = \rho cv$, using a fluid density ρ of $1000\text{ kg}\cdot\text{m}^{-3}$, the speed of sound c in water as $1480\text{ m}\cdot\text{s}^{-1}$, and by considering the velocity v of a droplet was $300\text{ m}\cdot\text{s}^{-1}$.

Although LCF testing was not completed, strain rate is included for reference and comparison.

Strain rate in the cavitation erosion tests was calculated in a similar manner to WDE, by considering the velocity of sound waves in water; $1480\text{ m}\cdot\text{s}^{-1}$, applied over a 3 mm thick sample. Maximum stress due to cavitation erosion was estimated from Preece and Brunton's work [32] which used a 20 kHz vibratory device at a $45\text{ }\mu\text{m}$ amplitude.

8 CONCLUSIONS

The aim of this work was to better understand the initiation of water droplet erosion (WDE). Coating failures are difficult to study, so uncoated titanium alloys were investigated to simplify the tracking of damage. Two titanium alloys were used; Ti-15Mo and Ti-6Al-4V. Additionally some Ti-6Al-4V was annealed to a larger grain size.

8.1 Water droplet erosion

An objective of this study was to review the mechanisms of erosion in the literature. Common mechanisms reported are direct deformation, stress wave propagation, hydraulic penetration, and lateral outflow jetting. Hydraulic penetration and lateral outflow jetting are secondary mechanisms, only occurring when surfaces have been roughened or cracked by primary mechanisms. Impact pressures below material yield strength are still able to cause deformation, suggesting direct deformation alone is not responsible for erosion. WDE is thought to be a synergy of mechanisms.

Erosion damage seen in the literature was reproduced here. Deep craters, characteristic of advanced erosion, were formed in long term 36-hour tests, and the mass loss with time data resulted in a typical erosion S-curve. Another objective was to investigate the early stages of erosion, as this is not explored much in the literature. Some WDE deformations reported in the literature were observed experimentally, such as slip bands, micropits and fatigue striations. Grain tilting due to WDE was not found, but occurred in cavitating sonotrode erosion. Slip band extrusions and intrusions were theorised for WDE in the literature but weren't observed in this work, however they were obvious in high strain rate split Hopkinson pressure bar testing.

EBSD of WDE has not been reported in the literature, so this was utilised in the hope that it may reveal where and why certain initial deformation mechanisms, such as twinning or grain tilting, occur. EBSD requires a high (30 kV) accelerating voltage. One potential reason grain tilting was not observed is that most tests were examined at high voltage. Electron energy will penetrate deeper into the surface, and therefore finer surface details (such as grain tilting) may not be as apparent. That said, grain tilting due to cavitating sonotrode erosion was visible at high (20 kV) accelerating voltage and also with light microscopy techniques.

Twinning due to droplet impingement is also described in the literature. Twinning was not apparent in the 36-hour advanced erosion tests which were sectioned for EBSD, nor in the incubation period results.

8.2 Quasi-static material tests

Some microstructural deformations in WDE are similar to features reported for low cycle fatigue: striations, slip bands, extruded slip bands, twinning. Conducting low cycle fatigue tests (where the controlling variable is strain, rather than stress, as in HCF) was originally an objective of this work, but could not be conducted within the time.

8.2.1 Tensile test

Some material properties in the literature have been found to correlate with WDE resistance, so a further objective was to explore certain relations. Smart's ultimate resilience did indeed correlate with erosion resistance, but the current work used a small sample size of three materials so this result should be treated cautiously. Of the materials tested in WDE, Ti-6Al-4V had the greatest Young's modulus, strength, and resilience, which lead to a lower erosion rate than Ti-15Mo. However Ti-15Mo, had the greater elongation to failure, allowing for more ductile material removal mechanisms.

8.3 High strain rate tests

WDE occurs at a high strain rate, so an objective of this study was to investigate the test material response at high strain rates. Split Hopkinson Pressure Bar (SHPB) tests demonstrated that the materials deform by slip or twinning under high strain rate loading. The compressive specimens plastically deformed but did not appear to reach failure by fracture; no cracks were observed. This strain hardening behaviour was also observed in the data, as both materials tested were able to support the maximum stress applied (up to 1800 MPa) and accommodate high strain (around 22%). Strain hardening is a desirable property for WDE applications, as the material can absorb energy beyond the elastic yield limit. Tensile specimens also supported a high stress, much higher than under quasi-static conditions, though strain to failure was much less than in quasi-static tests.

8.4 Cavitation erosion

Cavitation is thought to contribute to the early stages of WDE, and in fact other researchers have recreated early stage WDE features using cavitation. An objective was to explore cavitation as an alternative method to replicate initial WDE. Cavitation erosion produced initial damage similar in appearance to initial WDE such as micropits and grain tilting. This demonstrates simple benchtop equipment could be used to simulate the early stages of WDE, to either study the incubation period, or

rank material responses before committing to testing in more representative (but complex) equipment, such as whirling arm-type rigs.

8.5 Further work

Grain tilting in the initial stages of WDE has been reported in the literature but not observed here. More thorough analysis with SEM at lower accelerating voltage might be able to reveal further surface detail. It is also possible that grain tilting has been missed, as it's a short-lived phenomenon which rapidly leads to microcracks and micropits forming, so more thorough analysis before micropits form may be required.

Twinning was expected in WDE but not observed. Twinning occurred in at least one of the materials tested at high strain rate in SHPB. Sectioning of erosion incubation phase tests would give subsurface information and may be able to find twins. Focussed Ion Beam (FIB) milling could also assist in revealing subsurface deformation, but without the mechanical damage which is associated with metallographic polishing.

While twinning wasn't observed in WDE with EBSD, other techniques may be able to give information on microstructural changes. X-ray diffraction (XRD) can indicate phase change. Transmission electron microscopy (TEM) or electron channeling contrast imaging (ECCI) can provide finer detail such as dislocations or stacking faults. X-ray computed tomography (XCT) is useful for providing a three-dimensional view of the microstructure.

Investigation of LCF was planned for this work but not completed due to problems with the laboratory. Fatigue is thought to play a role in WDE so would be pertinent to investigate further, particularly low cycle fatigue, where localised plastic deformation plays a significant role.

Cavitation erosion has proven to be an effective method to recreate the early stages of WDE with off-the-shelf equipment. In the literature, Thomas and Brunton [59] went a step further to recreate advanced erosion following simulated initial damage. They used high velocity jets at a low impingement angle, to simulate lateral outflow jetting produced by impacting droplets. Their results were in good agreement with WDE tests conducted in parallel. Future work could consider using such benchtop methods to accelerate cavitation-induced incubation phase erosion toward advanced erosion in a manner representative of WDE, utilising simpler apparatus than the specialist, whirling-arm type of rig.

REFERENCES

- [1] M. G. Gee and I. M. Hutchings, "General Approach and Procedures for Erosive Wear Testing," no. 56.
- [2] O. Gohardani, "Impact of erosion testing aspects on current and future flight conditions," *Prog. Aerosp. Sci.*, vol. 47, no. 4, pp. 280–303, 2011, doi: 10.1016/j.paerosci.2011.04.001.
- [3] Q. Zhou, N. Li, X. Chen, T. Xu, S. Hui, and D. Zhang, "Liquid drop impact on solid surface with application to water drop erosion on turbine blades, Part II: Axisymmetric solution and erosion analysis," *Int. J. Mech. Sci.*, vol. 50, no. 10–11, pp. 1543–1558, 2008, doi: 10.1016/j.ijmecsci.2008.08.002.
- [4] Q. Zhou, N. Li, X. Chen, T. Xu, S. Hui, and D. Zhang, "Analysis of water drop erosion on turbine blades based on a nonlinear liquid-solid impact model," *Int. J. Impact Eng.*, vol. 36, no. 9, pp. 1156–1171, 2009, doi: 10.1016/j.ijimpeng.2009.02.007.
- [5] N. Li, Q. Zhou, X. Chen, T. Xu, S. Hui, and D. Zhang, "Liquid drop impact on solid surface with application to water drop erosion on turbine blades, Part I: Nonlinear wave model and solution of one-dimensional impact," *Int. J. Mech. Sci.*, vol. 50, no. 10–11, pp. 1526–1542, 2008, doi: 10.1016/j.ijmecsci.2008.08.001.
- [6] S. Soni and J. P. Pandey, "Erosion Behaviour Of Steam Turbine Blades Of Glass-Epoxy," *Int. J. Adv. Eng. Technol.*, vol. II, no. II, pp. 110–117, 2011.
- [7] F. P. Bowden and J. E. Field, "The Brittle Fracture of Solids by Liquid Impact, by Solid Impact, and by Shock," *Proc. R. Soc. A Math. Phys. Eng. Sci.*, vol. 282, no. 1390, pp. 331–352, 1964, doi: 10.1098/rspa.1964.0236.
- [8] Y. I. Oka and H. Miyata, "Erosion behaviour of ceramic bulk and coating materials caused by water droplet impingement," *Wear*, vol. 267, pp. 1804–1810, 2009, doi: 10.1016/j.wear.2009.02.009.
- [9] L. Huang, J. Folkes, P. Kinnell, and P. H. Shipway, "Mechanisms of damage initiation in a titanium alloy subjected to water droplet impact during ultra-high pressure plain waterjet erosion," *J. Mater. Process. Technol.*, vol. 212, no. 9, pp. 1906–1915, 2012, doi: 10.1016/j.jmatprotec.2012.04.013.
- [10] Y. I. Oka, S. Mihara, and H. Miyata, "Effective parameters for erosion caused by water droplet impingement and applications to surface treatment technology," *Wear*, vol. 263, pp. 386–394, 2007, doi: 10.1016/j.wear.2006.11.022.
- [11] J. H. Brunton and J. J. Camus, "The flow of a liquid drop during impact," in *Proceedings of the 3rd International Conference on Rain Erosion and Associated Phenomena*, 1970, pp. 327–352.
- [12] I. Y. Gavrillov, V. V. Popov, I. Y. Sorokin, V. a. Tishchenko, and S. V. Khomyakov, "A contactless technique for determining the average sizes of erosion-hazardous droplets in polydisperse wet steam flow," *Therm. Eng.*, vol. 61, no. 8, pp. 577–584, 2014, doi: 10.1134/S0040601514080072.
- [13] K. K. Haller, "High-velocity impact of a liquid droplet on a rigid surface," Swiss

Federal Institute Of Technology Zurich, 2002.

- [14] E. F. Tobin, T. M. Young, D. Raps, and O. Rohr, "Comparison of liquid impingement results from whirling arm and water-jet rain erosion test facilities," *Wear*, vol. 271, no. 9–10, pp. 2625–2631, 2011, doi: 10.1016/j.wear.2011.02.023.
- [15] Q. Zhou, N. Li, X. Chen, A. Yonezu, T. Xu, S. Hui, and D. Zhang, "Water Drop Erosion on Turbine Blades: Numerical Framework and Applications," *Mater. Trans.*, vol. 49, no. 7, pp. 1606–1615, 2008, doi: 10.2320/matertrans.MRA2008025.
- [16] J. E. Field, J. P. Dear, and J. E. Ogren, "The effects of target compliance on liquid drop impact," *J. Appl. Phys.*, vol. 65, no. 2, pp. 533–540, 1989, doi: 10.1063/1.343136.
- [17] M. H. Keegan, D. H. Nash, and M. M. Stack, "On erosion issues associated with the leading edge of wind turbine blades," *J. Phys. D. Appl. Phys.*, vol. 46, no. 38, p. 20, 2013, doi: 10.1088/0022-3727/46/38/383001.
- [18] M. H. Keegan, D. Nash, and M. Stack, "Modelling rain drop impact on offshore wind turbine blades," 2012.
- [19] M. H. Keegan, D. Nash, and M. M. Stack, "NUMERICAL MODELLING OF HAILSTONE IMPACT ON THE LEADING EDGE OF A WIND TURBINE BLADE," 2013.
- [20] A. H. Whitehead, H. Simunkova, P. Lammel, J. Wosik, N. Zhang, and B. Gollas, "Rain erosion characteristics of electrodeposited Ni-SiC metal-matrix composite layers," *Wear*, vol. 270, no. 9–10, pp. 695–702, 2011, doi: 10.1016/j.wear.2011.02.001.
- [21] P. Lammel, L. D. Rafailovic, M. Kolb, K. Pohl, A. H. Whitehead, G. Grundmeier, and B. Gollas, "Analysis of rain erosion resistance of electroplated nickel-tungsten alloy coatings," *Surf. Coatings Technol.*, vol. 206, no. 8–9, pp. 2545–2551, 2012, doi: 10.1016/j.surfcoat.2011.11.009.
- [22] P. Lammel, a. H. Whitehead, H. Simunkova, O. Rohr, and B. Gollas, "Droplet erosion performance of composite materials electroplated with a hard metal layer," *Wear*, vol. 271, no. 9–10, pp. 1341–1348, 2011, doi: 10.1016/j.wear.2010.12.034.
- [23] M. M. Stack, Y. Purandare, and P. Hovsepian, "Impact angle effects on the erosion-corrosion of superlattice CrN/NbN PVD coatings," *Surf. Coatings Technol.*, vol. 188–189, no. 1-3 SPEC.ISS., pp. 556–565, 2004, doi: 10.1016/j.surfcoat.2004.07.075.
- [24] "2012 Chen, Jedrzejowski, Medraj - Appl of Stress Wave analys in multi-layer coating design - Concordia and R-R.pdf." .
- [25] V. P. "Swami. Swaminathan, R. Wei, and D. W. Gandy, "Nanotechnology Coatings for Erosion Protection of Turbine Components," *J. Eng. Gas Turbines Power*, vol. 132, no. 8, p. 082104, 2010, doi: 10.1115/1.3028567.
- [26] M. S. Mahdipoor, D. Kevorkov, P. Jedrzejowski, and M. Medraj, "Water droplet

- erosion behaviour of gas nitrided Ti6Al4V,” *Surf. Coatings Technol.*, vol. 292, no. March, pp. 78–89, 2016, doi: 10.1016/j.surfcoat.2016.03.032.
- [27] M. Duraiselvam, R. Galun, S. Siegmann, V. Wesling, and B. L. Mordike, “Liquid impact erosion characteristics of martensitic stainless steel laser clad with Ni-based intermetallic composites and matrix composites,” *Wear*, vol. 261, pp. 1140–1149, 2006, doi: 10.1016/j.wear.2006.03.024.
- [28] G. DeBotton, “The interaction of a coated target and an impinging waterdrop,” *Wear*, vol. 219, pp. 60–72, 1998, doi: 10.1016/S0043-1648(98)00226-9.
- [29] N. K. Bourne, T. Obara, and J. E. Field, “High-speed photography and stress gauge,” *Phil. Trans. R. Soc. Lond. A*, vol. 355, pp. 607–623, 1997.
- [30] H. S. Kirols, D. Kevorkov, a. Uihlein, and M. Medraj, “The effect of initial surface roughness on water droplet erosion behaviour,” *Wear*, vol. 342–343, pp. 198–209, 2015, doi: 10.1016/j.wear.2015.08.019.
- [31] W. F. Adler, “Waterdrop impact modeling,” *Wear*, vol. 186–187, pp. 341–351, 1995, doi: 10.1016/0043-1648(95)07176-8.
- [32] C. M. Preece and J. H. Brunton, “A comparison of liquid impact erosion and cavitation erosion,” *Wear*, vol. 60, no. 2, pp. 269–284, 1980, doi: 10.1016/0043-1648(80)90227-6.
- [33] S. S. Cook, “Erosion by water-hammer,” *Proc. R. Soc. London, Ser. A*, vol. 119, pp. 481–488, 1928.
- [34] A. Leyland and A. Matthews, “Thick Ti/TiN multilayered coatings for abrasive and erosive wear resistance,” *Surf. Coatings Technol.*, vol. 70, no. 1, pp. 19–25, 1994, doi: 10.1016/0257-8972(94)90069-8.
- [35] M. Thomas, “On the characterisation of subsurface deformation microstructures in aerostructural titanium alloys,” University of Sheffield, 2012.
- [36] M. Motyka, K. Kubiak, W. Ziaja, and S. Jan, “Hot Plasticity of Alpha Beta Alloys,” in *Towards Achieving Enhanced Properties for Diversified Applications*, A. K. M. Nurul Amin, Ed. 2012, pp. 87–116.
- [37] E. O. Hall, *Twinning and Diffusionless Transformations in Metals*. London: Butterworths Scientific Publications, 1954.
- [38] R. Cochrane, “Annealing twins in alpha brass,” *DoITPoMS*, 2002. https://www.doitpoms.ac.uk/miclib/full_record.php?pid=430 (accessed Aug. 05, 2021).
- [39] E. Plancher, C. C. Tasan, S. Sandloebes, and D. Raabe, “On dislocation involvement in Ti-Nb gum metal plasticity,” *Scr. Mater.*, vol. 68, no. 10, pp. 805–808, 2013, doi: 10.1016/j.scriptamat.2013.01.034.
- [40] Y. Al-Zain, H. Y. Kim, H. Hosoda, T. H. Nam, and S. Miyazaki, “Shape memory properties of Ti-Nb-Mo biomedical alloys,” *Acta Mater.*, vol. 58, no. 12, pp. 4212–4223, 2010, doi: 10.1016/j.actamat.2010.04.013.
- [41] T. Ozaki, H. Matsumoto, S. Watanabe, and S. Hanada, “Beta Ti Alloys with Low

- Young's Modulus," *Mater. Trans.*, vol. 45, no. 8, pp. 2776–2779, 2004, doi: 10.2320/matertrans.45.2776.
- [42] Y. L. Zhou and D. M. Luo, "Microstructures and mechanical properties of Ti-Mo alloys cold-rolled and heat treated," *Mater. Charact.*, vol. 62, no. 10, pp. 931–937, 2011, doi: 10.1016/j.matchar.2011.07.010.
- [43] W. F. Ho, C. P. Ju, and J. H. C. Lin, "Structure and properties of cast binary Ti-Mo alloys," *Biomaterials*, vol. 20, no. May, pp. 2115–2122, 1999.
- [44] I. M. Ivasishin, "Mechanism Of Beta-Grain Growth In Alpha/Beta Titanium Alloys During Continuous, Rapid Heating," Kiev, 2001.
- [45] O. M. Ivasishin, S. L. Semiatin, P. E. Markovskiy, S. V. Shevchenko, and S. V. Ulshin, "Grain growth and texture evolution in Ti-6Al-4V during beta annealing under continuous heating conditions," *Mater. Sci. Eng. A*, vol. 337, no. 1–2, pp. 88–96, 2002, doi: 10.1016/S0921-5093(01)01990-6.
- [46] F. P. Bowden and J. H. Brunton, "The Deformation of Solids by Liquid Impact at Supersonic Speeds," *Proc. R. Soc. A Math. Phys. Eng. Sci.*, vol. 263, no. 1315, pp. 433–450, 1961, doi: 10.1098/rspa.1961.0172.
- [47] M. S. Mahdipoor, H. S. Kirols, D. Kevorkov, P. Jedrzejowski, and M. Medraj, "Influence of impact speed on water droplet erosion of TiAl compared with Ti6Al4V," *Sci. Rep.*, vol. 5, p. 14182, 2015, doi: 10.1038/srep14182.
- [48] D. Ma, A. Mostafa, D. Kevorkov, P. Jedrzejowski, M. Pugh, and M. Medraj, "Water Impingement Erosion of Deep-Rolled Ti64," *Metals (Basel)*, vol. 5, no. 3, pp. 1462–1486, 2015, doi: 10.3390/met5031462.
- [49] H.-H. Shi, K. Takayama, and N. Nagayasu, "The measurement of impact pressure and solid surface response in liquid-solid impact up to hypersonic range," *Wear*, vol. 186–187, pp. 352–359, 1995, doi: 10.1016/0043-1648(95)07141-5.
- [50] W. F. Graff, "Wave motion in elastic solids." Oxford University Press, 1975.
- [51] J. E. Field, J. J. Camus, M. Tinguely, D. Obreschkow, and M. Farhat, "Cavitation in impacted drops and jets and the effect on erosion damage thresholds," *Wear*, vol. 290–291, pp. 154–160, 2012, doi: 10.1016/j.wear.2012.03.006.
- [52] D. Obreschkow, N. Dorsaz, P. Kobel, A. De Bosset, M. Tinguely, J. Field, and M. Farhat, "Confined shocks inside isolated liquid volumes: A new path of erosion?," *Phys. Fluids*, vol. 23, no. 10, pp. 2–5, 2011, doi: 10.1063/1.3647583.
- [53] J. J. Camus, "High-Speed Flow in Impact and its Effect on Solid Surfaces," University of Cambridge, 1971.
- [54] G. S. Springer, *Erosion by Liquid Impact*, 1st ed. Washington: Scripta Publishing, 1976.
- [55] M. S. Mahdipoor, D. Kevorkov, P. Jedrzejowski, and M. Medraj, "Water droplet erosion mechanism of nearly fully-lamellar gamma TiAl alloy," *Mater. Des.*, vol. 89, no. October, pp. 1095–1106, 2016, doi: 10.1016/j.matdes.2015.10.077.
- [56] J. Polák and J. Man, "Mechanisms of extrusion and intrusion formation in

- fatigued crystalline materials,” *Mater. Sci. Eng. A*, vol. 596, no. February 2014, pp. 15–24, 2014, doi: 10.1016/j.msea.2013.12.005.
- [57] N. P. D. Kamkar, “Water droplet erosion mechanisms of Ti-6Al-4V,” École De Technologie Supérieure Université Du Québec, 2014.
- [58] A. W. Momber, Y. C. Wong, R. Ij, and E. Budidharma, “Hydrodynamic profiling and grit blasting of low-carbon steel surfaces,” *Tribol. Int.*, vol. 35, no. 4, pp. 271–281, 2002, doi: 10.1016/S0301-679X(02)00009-9.
- [59] G. Thomas and J. Brunton, “Drop impingement erosion of metals,” *Proc. R. Soc. Lond. A. Math. Phys. Sci.*, vol. 314, no. 1519, pp. 549--565, 1970, [Online]. Available: <http://rspa.royalsocietypublishing.org/content/314/1519/549.short>.
- [60] R. H. Richman and W. P. McNaughton, “Correlation of cavitation erosion behavior with mechanical properties of metals,” *Wear*, vol. 140, no. 1. pp. 63–82, 1990, doi: 10.1016/0043-1648(90)90122-Q.
- [61] R. F. Smart, “Selection of surfacing treatments,” *Tribol. Int.*, vol. 11, no. 2, pp. 97–104, 1978, doi: 10.1016/0301-679X(78)90136-6.
- [62] S. Osgerby, “SUSCOAT 31-10-2013 Alstom technical meeting.” Rugby, 2013.
- [63] W. F. Adler, “Rain impact retrospective and vision for the future,” *Wear*, vol. 233–235, pp. 25–38, 1999.
- [64] N. L. Hancox and J. H. Brunton, “The erosion of solids by the repeated impact of liquid drops,” *Philos. Trans. R. Soc. London. Ser. A, Math. Phys. Sci.*, vol. 260, no. 1110, pp. 121–139, 1966.
- [65] J. H. Brunton, “The physics of impact and deformation: single impact,” *Philos. Trans. R. Soc. A Math. Phys. Eng. Sci.*, vol. 260 A, pp. 79–85, 1966.
- [66] M. C. Rochester, “The impact of a liquid drop with a solid surface and the effects of the properties of the liquid on the erosion of the solids,” *Univ. Cambridge*, 1977.
- [67] M. B. Lesser and J. E. Field, “The Impact of Compressible Liquids,” *Annu. Rev. Fluid Mech.*, vol. 15, no. 1, pp. 97–122, 1983, doi: 10.1146/annurev.fl.15.010183.000525.
- [68] J. E. Field and N. K. Bourne, “Bubble Collapse and the Initiation of Explosion,” *Proc. Math. Phys. Sci.*, vol. 435, no. 1894, pp. 423–435, 1991.
- [69] J. E. Field, “The physics of liquid impact, shock wave interactions with cavities, and the implications to shock wave lithotripsy,” *Phys. Med. Biol.*, vol. 36, no. 11, pp. 1475–1484, 1991, doi: 10.1088/0031-9155/36/11/007.
- [70] R. J. Hand, J. E. Field, and D. Townsend, “The use of liquid jets to simulate angled drop impact,” *J. Appl. Phys.*, vol. 70, no. 11, pp. 7111–7118, 1991, doi: 10.1063/1.349793.
- [71] T. Obara, N. K. Bourne, and J. E. Field, “Liquid-jet impact on liquid and solid surfaces,” *Wear*, vol. 186–187, pp. 388–394, 1995, doi: 10.1016/0043-1648(95)07187-3.

- [72] C. R. Seward, E. J. Coad, C. S. J. Pickles, and J. E. Field, "The liquid impact resistance of a range of IR-transparent materials," *Wear*, vol. 186–187, pp. 375–383, 1995, doi: 10.1016/0043-1648(95)07150-4.
- [73] J. E. Field, "ELSI conference: Invited lecture liquid impact: Theory, experiment, applications," *Wear*, vol. 233–235, pp. 1–12, 1999, doi: 10.1016/S0043-1648(99)00189-1.
- [74] ASTM, "G73 Standard Test Method for Liquid Impingement Erosion Using Rotating Apparatus," 2010. doi: 10.1520/G0073-10.2.
- [75] A. K. Gujba, L. Hackel, D. Kevorkov, and M. Medraj, "Water droplet erosion behaviour of Ti-6Al-4V and mechanisms of material damage at the early and advanced stages," *Wear*, vol. 358–359, no. April, pp. 109–122, 2016, doi: 10.1016/j.wear.2016.04.008.
- [76] M. C. Kong, D. Axinte, and W. Voice, "Aspects of material removal mechanism in plain waterjet milling on gamma titanium aluminide," *J. Mater. Process. Technol.*, vol. 210, no. 3, pp. 573–584, 2010, doi: 10.1016/j.jmatprotec.2009.11.009.
- [77] M. Gee, "Assessing the risk to engineering materials from water impact," *Open Access Government*, 2017. <https://www.openaccessgovernment.org/assessing-risk-engineering-materials-water-impact/31741/> (accessed May 14, 2020).
- [78] G. Dieter and D. Bacon, *Mechanical Metallurgy. SI Metric Edition*. 1988.
- [79] ATI, "ATI 15Mo™ Titanium Alloy Technical Data Sheet," vol. 2. Allegheny Technologies Incorporated, Pittsburgh, USA, pp. 1–4, 2014, [Online]. Available: https://www.atimetals.com/Documents/ati_15Mo_Titanium_Alloy_en_v4_final.pdf.
- [80] TIMET, "TIMETAL® 6-4, 6-4 ELI & 6-4-.1RU." Titanium Metals Corporation, pp. 1–2, 2000.
- [81] W. Callister and D. Rethwisch, *Materials Science and Engineering*, 8th Editio. Wiley, 2011.
- [82] G. F. Schmitt Jr., "Liquid and Solid Particle Impact Erosion," Wright-Patterson Air Force Base, Ohio, 1979. [Online]. Available: <http://www.dtic.mil/dtic/tr/fulltext/u2/a080607.pdf>.
- [83] A. D. Barr, "Strain rate effects in quartz sand," University of Sheffield, 2016.
- [84] K. T. Ramesh, "33 High Strain Rate and Impact Experiments," in *Springer Handbook of Experimental Solid Mechanics*, W. N. Sharpe Jr., Ed. 2008, pp. 1–31.
- [85] Kalpakjian and Schmid, *Manufacturing Processes for Engineering Materials*, 5th ed. Pearson Education, 2008.
- [86] D. R. Chichili, K. T. Ramesh, and K. J. Hemker, "The high-strain-rate response of alpha-titanium: Experiments, deformation mechanisms and modeling," *Acta Mater.*, vol. 46, no. 3, pp. 1025–1043, 1998, doi: 10.1016/S1359-6454(97)00287-

5.

- [87] BS EN 10002-1:2001 / ISO 6892-1, "Metallic materials - Tensile testing - Part 1: Method of test at room temperature.," *British Standards Institution*, 2009.
- [88] J. B. Kwon, H. Huh, and C. N. Ahn, "An improved technique for reducing the load ringing phenomenon in tensile tests at high strain rates," *Conf. Proc. Soc. Exp. Mech. Ser.*, vol. 1, pp. 253–257, 2015.
- [89] C. Fichera, "High Strain-Rate And Temperature Behaviour Of Metals: Advanced Testing And Modelling," Politecnico di Torino, 2015.
- [90] M. J. Cox, "Development of high strain rate mechanical testing for metallic materials," Imperial College London, 2013.
- [91] B. Hopkinson, "A Method of Measuring the Pressure Produced in the Detonation of High Explosives or by the Impact of Bullets," vol. xiv, no. 1907, pp. 437–456, 1914.
- [92] H. Kolsky, "An investigation of the mechanical properties of materials at very high rates of loading," *Proc. Phys. Soc. Sect. B*, vol. 62, no. 11, pp. 676–700, 1949, doi: 10.1088/0370-1301/62/11/302.
- [93] S. Hattori and M. Takinami, "Comparison of cavitation erosion rate with liquid impingement erosion rate," *Wear*, vol. 269, no. 3–4, pp. 310–316, 2010, doi: 10.1016/j.wear.2010.04.020.
- [94] T. Keil, P. F. Pelz, J. Kadavelil, J. Necker, W. Moser, and D. Christ, "Droplet Impact vs . Cavitation Erosion," in *WIMRC 3rd International Cavitation Forum 2011*, 2011, pp. 1–8.
- [95] ASTM International, "G134 - 17 Standard Test Method for Erosion of Solid Materials by Cavitating Liquid Jet," 2017. doi: 10.1520/G0134-95R10E01.1.6.
- [96] ASTM International, "G32 - 16 Standard Test Method for Cavitation Erosion Using Vibratory Apparatus," 2016. doi: 10.1520/G0032-10.bility.
- [97] S. J. Lainé, "The Role of Twinning in the Plastic Deformation of Alpha Phase Titanium," *Univ. Cambridge*, 2017.